THE UNIVERSITY *of* EDINBURGH

Physical and chemical effects of CO_2 storage in saline aquifers of the southern North Sea

Niklas Heinemann

Thesis submitted in fulfilment of
the requirement for the degree of
Doctor of Philosophy

School of Geosciences

University of Edinburgh

2012

Declaration

I declare that, except where explicit reference is made to the contribution of others, that this dissertation is the result of my own work and has not been submitted for other degree at the University of Edinburgh or any other institution.

Signature: _____ 5nd December, 2012

(Niklas Heinemann)

Data and conclusions of this thesis have been presented at the following conferences:

- Goldschmidt Conference; Prague, Czech Republic, August 2011
  "Stepwise C & O Stable Isotope shows little detectable CO_2 Sequestration by Cements in Analogue for Engineered Storage"

- Geological Society of London Conference: Carbon Storage Opportunities in the North Sea; London, UK, March 2010
  "CO_2 Storage Capacity in the Bunter Sandstone limited by Local Pressure Development, UK Southern North Sea"

- 17th North Britain Student Forum; Edinburgh, UK, February 2010
  "CO_2 Storage in the Bunter Sandstone Formation, UK Southern North Sea: Storage Capacity and Injectivity"

- BSRG Conference; Bangor, UK, December 2009
  "CO_2 Storage Capacity of the Bunter Sandstone Formation, UK Southern North Sea"

The following publications have been published:

- Heinemann, N., Wilkinson, M., Pickup, G.E., Haszeldine, R.S. & Fallick, A.E. 2012. CO_2 sequestration in UK North Sea analogue for geological carbon storage. (accepted, Geology)

- Heinemann, N., Wilkinson, M., Pickup, G.E., Haszeldine, R.S. & Cutler, N.A. 2012. CO_2 storage in the offshore UK Bunter Sandstone Formation. International Journal of Greenhouse Control, 6, 210-219.

Table of Contents

Figures

Acknowledgements

I would like to thank my two main supervisors Mark Wilkinson and Gillian Pickup for their support over the last years. Thanks for constant advice and efforts, for the incredible amount of time and for the help which made the completion of this thesis possible. Additionally, I would like to thank my supervisor Stuart Haszeldine for his reliability and support and for having given me the opportunity to become part of the Edinburgh SCCS group.

Furthermore, I would like to thank Tony Fallick and Terry Donnelly from SUERC for supporting the experimental work - without their support and generosity a major part of this thesis could not have been realised at all!

Endless conversations, discussions and arguments, sometimes followed by an enlightenment concerning geology and CCS were being held with my colleagues and office mates Jennifer Roberts and Grant Nicoll over the last years. I want to thank them for always being interested and interesting, thought-provoking and critical as well as patient and humorous.

Finally, but not less sincerely, many thanks to Matt Booth, Rachel Kilgallon, Jamie Stewart, Andrew Miles, Mike Edwards, Simon King, Juliane Pohl, Jennifer Roberts, Grant Nicoll and Edward Hoskin for proofreading a countless number of reports, drafts and applications. I will never be able to repay you!

Abstract

One of the most promising mitigation strategies for greenhouse gas accumulation in the atmosphere is carbon capture and storage (CCS). Deep saline aquifers are seen as the most efficient carbon dioxide (CO_2) storage sites, mainly because of their vast size and worldwide distribution. Injecting CO_2 into brine filled media will cause a physical and chemical disequilibrium in the formation. This PhD thesis documents the investigation of some of the resulting effects which occur at the beginning of the injection, during the injection period and millions of years after injection.

When CO_2 is injected into a brine filled reservoir, large amounts of *in situ* brine will be displaced away from the injection well. This causes a pressure increase in the vicinity of the well which may compromise the injection process. The simulation of this pressure increase was performed with the black-oil simulator Eclipse100 (Schlumberger) while using a number of recent formulas to predict the mutual dissolution and the fluid properties of CO_2 and brine. The results show that the pressure increase can exceed the maximum sustainable pore pressure and will cause fracturing of the reservoir formation. The pore pressure increase is dependent on parameters such as temperature and salinity because they change the fluid properties of the CO_2 and brine, but also the capability of the fluids to dissolve mutually. The mutual dissolution has generally a pressure reducing effect although its impact is regarded to be overestimated. This is mainly because reservoir engineering software cannot simulate the shock front realistically. Undulations, which appear on the injection pressure profile are not a result of model instabilities but can either be related to enhanced mutual dissolution due to grid effects, or to the software which may overestimate or underestimate the pressure and dissolution. A detailed investigation of those undulations is vital for the interpretation of the injection pressure.

High fluid pressure can be an important parameter for the estimation of the CO_2 storage capacity of saline aquifers such as the offshore Bunter Sandstone Formation,

in the UK southern North Sea. Based on fluid pressure, the storage capacity was calculated using the ECLIPSE compositional simulation package and a simple analytical equation. The estimated storage capacity is 6.55 to 7.17 Gt of CO_2 calculated with the analytical and the numerical approach respectively. By comparing the results, the differences are relatively moderate and therefore the application of the numerical simulator is not regarded as necessary. This is mainly due to the effective pressure flow which prevents pressure accumulations underneath the cap rock. Although the CO_2 storage capacity of the Bunter Sandstone Formation remains high, a previous survey, which was not based on fluid pressure, calculated a storage capacity approximately twice as high as the results presented here.

In theory, due to the increase in CO_2 concentration, CO_2 bearing carbonate minerals could precipitate when CO_2 is injected into an aquifer such as the Rotliegend aquifer in the southern North Sea. Geochemical models often predict a relatively rapid growth of carbonate minerals as the most secure form of long term engineered CO_2 storage. But validation of model-results remains difficult due to the long periods of time involved. Natural analogue studies can bridge the gap between experiments and real-world storage. The Fizzy field, a southern North Sea (UK) gas accumulation with a high natural CO_2 content (c. 50%) provides an ideal opportunity to study the long term effect of CO_2 related mineral reaction. However all such reservoirs contain 'normal' diagenetic dolomite, so that distinguishing sequestration related dolomite is a challenge. CO_2 was stepwise extracted from dolomite from both the Fizzy field and the Orwell Rotliegend sandstone in order to reveal any zonation of the crystals which could be related to enhanced dolomite precipitation due to the high CO_2 concentration. According to the method between 0 and 22 % of the dolomite in the Fizzy field precipitated due to the high CO_2 concentration. Therefore, between 0 and 19 % of the CO_2, which is related to the relatively recent high CO_2 concentration, is 'trapped' in the 'sequestration dolomite'. The wide range of this estimate is mainly related to rock heterogeneity.

1 Chapter: Introduction

1.1 The concept of subsurface carbon storage

Data from sediment records, ice cores and other scientific investigations have revealed that the global climate has varied considerably during geological times. Over the past 6,000 years, the earth has been gradually cooling, with a new glacial period expected within tens of thousands of years (Jenkins 2001). Nevertheless, it is generally accepted that overall global temperature has risen in an unprecedented way since the middle of the past century. Contemporaneously, the atmospheric amount of carbon dioxide (CO_2) has increased over the past 200 years. The analyses of ice cores has shown that atmospheric concentration of CO_2 is nearly 100 ppm higher than in the 420,000 years prior to the industrial revolution, and has risen to that level at a rate at least 10 and possibly 100 times faster than any previous increase during the same 420,000 year time interval (Falkowski et al. 2000). Scientists have concluded that this increase in CO_2 concentration has triggered the increase in temperature (Crowley 2000). Although rapid temperature changes without an increase of CO_2 are suggested to be possible, the converse does not appear to be true (Smith et al. 1999).

There is little doubt now that human socioeconomic activities have lead to the enrichment of CO_2 in the atmosphere. Anthropogenic CO_2 emissions are primarily caused by energy consumption and 85% of primary power is supplied by the combustion of fossil fuel, the reduction of CO_2 emissions is a major challenge for society today (Orr 2004). One significant impact is that CO_2 is a greenhouse gas and therefore an important contributor to global warming (Falkowski et al. 2000). Current climate simulations predict a change in climate will severely impact humanity all over the world. The actual amount of temperature increase is still under debate, but values ranging from a global average increase of 2.5 centigrade (IPCC 2001) up to 5.5 centigrade (Cox 2000) before the end of this century seem to be possible in a 'business-as-usual' scenario. Despite the growing concern about the global climate problem, it is very unlikely that the world wide dependence on fossil fuels will decrease. This is mainly due to the economic growth of developing

countries such as China and India. The pressure to maintain or even increase wealth and industrial productivity on the one hand and restrict fossil fuel usage on the other hand creates a challenge for researchers to develop new technologies.

One of the most promising strategies to prevent greenhouse gas accumulation in the atmosphere is the capture of CO_2 from combustion power plants and storage in the subsurface (Lindeberg & Bergmo 2002). The implementation of this technology has been successful for several small and intermediate size projects (e. g. Sleipner/Norway, In Salah/Algeria, Weyburn/Canada). However, large-scale emission reduction implies CO_2 injection into the subsurface at volumes much greater than what has been previously been achieved. One opportunity is to store CO_2 in depleted gas fields because of their proven ability to store gas over geological time scales. However, their world wide distribution is inhomogeneous and their regional storage capacity is too limited to reduce global CO_2 emissions significantly. The cumulative annual CO_2 emissions in 2002 from the United Kingdom's major industrial sources were approximately 125 million tonnes of CO_2 whereas the estimated storage capacity of the Leman gas field, by far the biggest gas field in the southern North Sea, is estimated to be around 870 million tonnes of CO_2 (Holloway et al. 2006; Bentham 2006). Another promising option is the storage in deep saline aquifers, vast permeable rock units filled with brine that are located in globally distributed sedimentary basins with storage capacities in the range of many Gt of CO_2 (Bradshaw et al. 2007). In order not to encounter public concern typical storage sites are below the depth of fresh water resources.

The major concern in any CO_2 storage project is a potential leakage of the gas into the atmosphere. Possible pathways are pre-existing fractures, the loss of the integrity of the cap rock due to CO_2 injection or abandoned injection/production wells (Rutqvist & Tsang 2002; Jimenez & Chalaturnyk 2002; Nordbotten et al. 2004). Once injected into the formation, the CO_2 can be trapped by four different storage mechanisms. The dominant physical processes of these mechanisms during and after the injection of CO_2 into a geological formation vary significantly over time. A

general assumption of the time dependence is shown on figure 1.

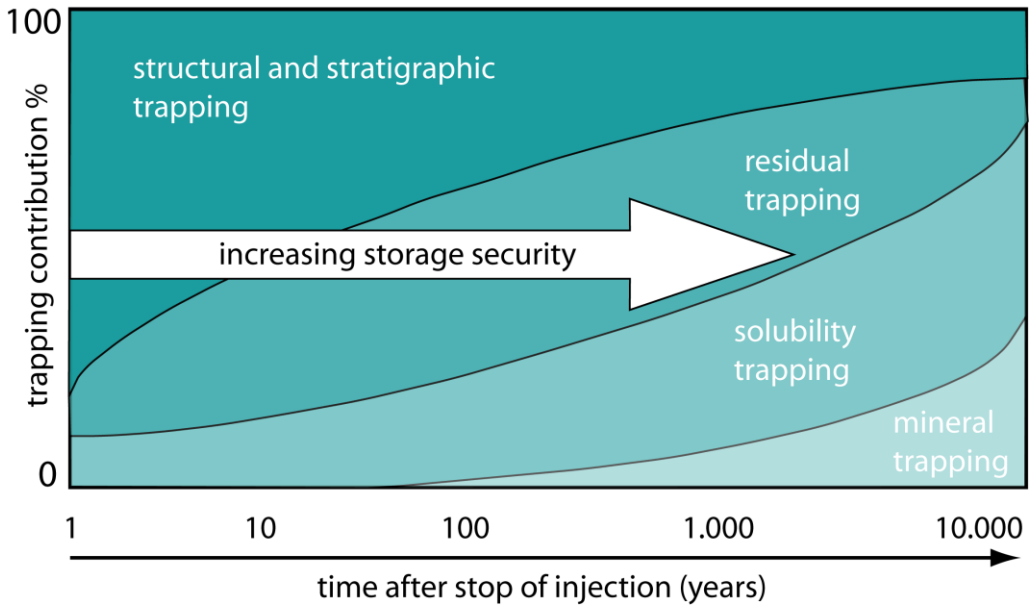

Figure 1.1: Relationship of the trapping contribution of different mechanisms and the increasing storage security as a function of time after injection (modified after http://www.geos.ed.ac.uk/sccs/storage/howstored.html)

The main four storage mechanisms are:

1) Structural and stratigraphic trapping

After injection the CO_2 plume migrates upwards due to its lower density and remains in a mobile phase. It migrates until it reaches an impermeable layer that prevents the CO_2 from flowing back to the surface (Bachu et al. 1994). The dynamic development of the CO_2 plume during the injection period and shortly after the injection has ceased is investigated in chapter 4.

2) Relative permeability hysteresis trapping (residual trapping)

During injection of CO_2 into a brine saturated formation, the brine is displaced by the CO_2 in a drainage-like process. After injection is ceased, the CO_2 migrates laterally and upwards and is displaced by water in an imbibition-like process. The water cannot replace all the CO_2 from the pores and small amounts of CO_2 remain

effectively immobile (Juanes et al. 2006).

3) Solubility trapping

One of the first chemical reactions of CO_2 will be its dissolution into the formation water (Rochelle et al. 2004). This reaction provides a relatively large sink for CO_2. The limited influence of solubility trapping on the injection process will be discussed in chapter 4.

4) Mineral trapping

Mineral trapping is the precipitation of CO_2 bearing minerals due to a high CO_2 concentration. Over very long timescales mineral trapping reactions may be the key trapping mechanism for CO_2 (e.g. Baker et al. 1995; Gunter et al. 1997, 2000). However, the types and magnitude of reactions that will occur depend on a variety of factors. For example, the mineralogical composition of the host rock, formation water chemistry, in-situ pressure and temperature, groundwater flow rates, and the relative rates of the dominant reactions (Rochelle et al. 2004). Many of these parameters are not yet well understood or are based on characteristic regional properties that must be investigated in detail. An overall prediction of the role of mineral trapping, especially for small and middle timescales, is still difficult. In chapter 5, the precipitation of CO_2 as dolomite, one of the most abundant carbonate minerals in the southern North Sea aquifers, will be discussed.

To ensure safe CO_2 storage, the injection process as well as the long-term migration of the CO_2 plume have to be taken into consideration. Since trapping mechanisms such as solubility trapping, capillary trapping and mineral trapping are either not capable of retaining large amounts of gas or take a very long time to gain a significant storage contribution, the focus should concentrate on the ability of overlying impermeable rock units under which the CO_2 plume accumulates. The cap rock must prevent vertical buoyancy driven CO_2 migration in order to provide sufficient time for additional trapping mechanisms to contribute to the overall trapping process. If it fails, any leakage could pollute freshwater aquifers at

structurally higher levels. A worst case scenario would be CO_2 degassing in highly populated areas where life threatening situations may develop.

1.2 Introduction to pressure increase during CO_2 injection and its impact on storage capacity estimation

There have been numerous studies, both analytical and numerical, related to the storage of CO_2 in the subsurface (e. g. Johnson et al. 2004; Bickle et al. 2007; Ukaegbu et al. 2009; Singh et al. 2010), and several workshops (e. g. Class et al. 2009) on the migration of CO_2 in the subsurface. A variety of methods have been tested, dependent on the aim of the study including; analytical solutions of the spreading of the CO_2 plume (e. g. Nordbotten et al. 2005), artificial 'what happens if' leakage scenarios modelled with numerical simulators (e. g. Pruess 2008), injection simulations into a geological model (e. g. Vandeweijer et al. 2009) or into simple geometries with (e. g. Doughty & Pruess 2004) or without heterogeneities (e. g. Ghanbari et al. 2006; Hurter et al. 2007).

Recent work on high resolution models of the Sleipner field and other injection sites have introduced a new chapter for modelling the fate of injected CO_2. The 4D Sleipner seismic data has been used to estimate velocity and thickness changes within the CO_2-saturated layers in several studies. The use of pre-stack stratigraphic inversion has proved to be especially useful to characterize the CO_2 plume in CCS operations (Clochard et al. 2010). But an accurate visualization of the plume is still difficult, mainly due to the pushdown effects associated with the gas injection, the uncertain prediction of rock properties (such as P-wave impedance and porosity) and the generally low resolution of seismic data (Clochard et al. 2010). An additional limitation is that once CO_2 dissolves into the pore water it is impossible to detect by acoustic methods. D**e**spite the uncertainties, researchers have attempted to match their modelled plume development with what is interpreted to be the plume (Singh et al. 2010; Chadwick et al. 2009; Arts et al. 2008).

Studies concerning the plume migration are not the only important areas of research to investigate. The idea that injected CO_2 requires space in the subsurface has become important. Some researchers criticised CO_2 storage capacity estimations which did not take pressure into account as 'somewhat naïve approach(es)' (van der Meer & Egberts 2008). At about the same time, 'solubility trapping', which involves the dissolution of CO_2 into brine as a permanent storage mechanism, was seen in a more realistic way: It came to be regarded as a slow chemical process, with the potential for only a small reduction in pressure , and with very little impact on injection and storage (e. g. van der Meer & van Wees 2006).

Pressure increase due to CO_2 injection is directly related to the geological formation in which the injection takes place. The two end-members of these considerations are injection into a fully closed system and injection into an entirely open system. Unfortunately, both scenarios have problems and it is difficult to deliberate about which scenario should be preferred. A closed system is regarded as a compartmentalised rock formation surrounded by low permeability zones. This includes a top seal as well as an underlying rock unit with low permeability. In the North Sea, these formations are likely to consist of evaporates or mudstones. Additionally, the formation has to be confined laterally. Structures that guarantee no horizontal hydraulic conductivity are either faults (whether the fault disconnects the formation entirely by an offset that exceeds the formation thickness or whether it is a sealing fault does not matter) or heterogeneities such as facies changes. Typical confined structures are hydrocarbon fields with no aquifer support. The confined system approach becomes more unlikely with increasing aquifer size but it is clear that not all brine saturated formations have a hydraulic conductivity to the surface like the Bunter Sandstone aquifer. If CO_2 is being injected into a closed system, the CO_2 requires space which will be provided by the compressibility of the rock formation and the in situ pore fluid. Since those compressibilities are low, the pressure will increase and limit the storage potential so that the pore pressure does not exceed the fracture pressure of the host rock (Holloway et al. 1996; Rutquist et al. 2007).

In an open system, the pressure increase will be less of a problem because the in situ pore fluid can migrate vertically or horizontally to generate space for the injected CO_2. The pressure increase will be lower and it will be dependent on the hydraulic diffusivity. The general problem concerning pressure increase is rather the pressure increase in the vicinity of the injection well at the beginning of the injection. Open aquifers would allow vast CO_2 injection and storage operations but the general concern is that in situ brine will be displaced uncontrollably. Large scale pore fluid displacements could cause environmental issues such as mixing of deep saline brine with drinking water or increasing water table levels (Bergman & Winter 1995). The level of impact depends on the pressure build up (which is also a function of the volume of injected CO_2) and the hydraulic communication with overlying freshwater aquifers (Birkholzer & Zhou 2009).

When pressure is taken into account within a closed system, pressure is the parameter that limits the storage capacity because it reduces the available pore space fraction for CO_2 to a minimum value, typically ~1 % of the total porespace (e. g. van der Meer 1995) or even less (Ehlig-Economides & Economides 2010; Heinemann et al. 2012). Other studies, as pointed out by Cavanagh et al. (2010), have calculated higher numbers but those are inappropriate if a closed system is considered. Critical researchers often regard the closed system approach to be a 'simplification (that) is inappropriate for regional CO_2 storage modelling …' (Cavanagh et al. 2010) and disregard the fact that the idea of an open system is an equally naïve simplification.

Whether an aquifer is closed or open depends on the regional geology. A careful interpretation of pressure data can be used to answer this important question. If the aquifer is open, increased pressure due to CO_2 injection is still an issue because large-scale pressure changes may have environmental impacts on shallow groundwater resources, causing water table rise, increased rates of discharge into lakes or streams, and/or mixing of displaced native brine into drinking water aquifers (Bergman & Winter, 1995). Taking all the risks and uncertainties into consideration,

the closed system approach provides a conservative estimate for CO_2 storage capacity which is not determined by optimistic assumptions.

Recent work on CO_2 storage has focused on methods to control the pressure that may limit the storage capacity. At the CO_2 modelling workshop on Svalbard in 2009, Eric Lindeberg from SINTEF Petroleum Research discussed the possibility of a simultaneous production of brine during CO_2 injection to prevent the pressure from damaging the formation. According to his theoretical considerations, the Utsira Formation, a relatively shallow aquifer in the North Sea could store 40 Gt of CO_2 if 210 CO_2 injection and a further 210 water production wells were used (Lindeberg et al. 2009). In a subsequent publication, 'it is assumed that the water can be released in the ocean (after suitable treatment)' (Bergamo et al. 2011).

1.3 Introduction to southern North Sea aquifers as CO_2 storage sites

The location of the southern North Sea makes it an ideal target for CO_2 storage particularly for several industrialised European countries such as the UK, Germany and France. The area is close to most of the main industrial CO_2 emitters or hubs and is interconnected by pipelines and terminals which are still used for hydrocarbon extraction. Two large scale aquifers are present, the Rotliegend Formation and the Bunter Sandstone Formation (Fig. 2.1).

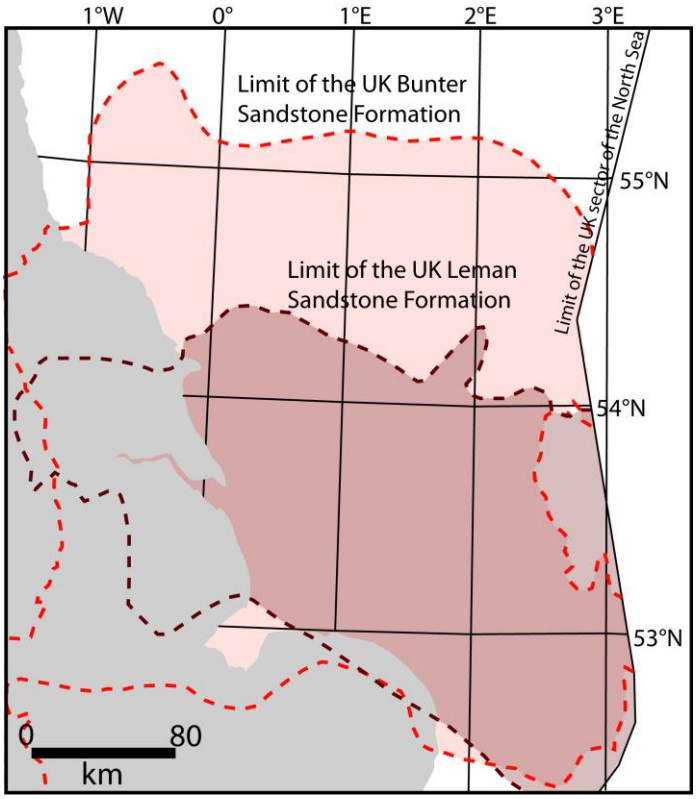

Figure 1.2: Map showing the distribution of the two main aquifers in the southern North Sea: The Permian Leman Sandstone Formation (brown) and the Triassic Bunter Sandstone Formation (red).

The Rotliegend Sandstone Formation

The Rotliegend Sandstone aquifer is one of the main targets for CO_2 storage in Europe. Numerous gas fields located in the Rotliegend Formation prove that injected CO_2 will be retained in the formation over geological timescales. Unfortunately, the Rotliegend Formation is highly compartmentalised by sealing faults (Leveille et al. 1997). It is therefore questionable, whether the Rotliegend Formation should be seen as a suitable aquifer for CO_2 storage.

The proposed Rotliegend CO_2 storage site is the Leman sandstone Formation which consists predominantly of porous and permeable aeolian sandstones (for more detailed information: Holloway et al. 2006; Ziegler 2006; Sullivan 1991). The average thickness of the formation is 110 m and it has a horizontal extent of 27,510

km^2 (Holloway et al. 2006). The overlying unit is the Upper Permian Zechstein evaporite sequence which is typically several hundred meters thick. The existence of many gas fields in the area proves the excellent sealing capability of this formation. The transition horizon is the Kupferschiefer, a thin organic rich shale. This is then overlain by a thick evaporitic formation, mainly derived of Halite and Anhydrite, with minor carbonate horizons (McCrone et al. 2003). The underlying Carboniferous sequence mainly consists of low permeability mudstones. They are an important source rock for gas reservoirs in the southern North Sea and are, on aggregate in excess of 9000 m thick (Glennie 1998).

The Bunter Sandstone Formation

The Bunter Sandstone Formation is generally regarded as a potential aquifer for CO_2 storage (Holloway et al. 2006; Vandeweijer et al. 2009; Heinemann et al. 2012). Due to many years of hydrocarbon exploration, especially from the deeper Permian sandstone, a reasonable amount of information is available to evaluate the long term evolution of injected CO_2. The intrinsic idea is that huge amounts of CO_2 will be injected into the sandstone which will then migrate into several large scale anticlines where it will be stored over geological timescales. Holloway et al. (2006) estimated the storage capacity of the Bunter Sandstone Formation of the southern North Sea to be up to 15 Gt. If the Bunter Sandstone Formation were determined to be a safe storage site its contribution to the carbon reduction process would be significant.

The Bunter Sandstone Formation consists of red, orange and white sandstones which are predominantly fine grained with localised medium or coarse grained horizons (Rhys 1974). The average thickness of the unit in the UK part of the North Sea is 140 m and it covers an area of 56,660 km^2 (Holloway et al. 2006). It is underlain by the Bunter Shale which is several hundred meters thick and consists of mudstone, with (an assumed) very low permeability. The overlying unit is the Dowsing Dolomitic Formation which comprises a thick sequence of mudstone, evaporate and limestone with low permeabilities (Cameron et al. 1992). Several dome structures have formed in the Bunter Sandstone Formation due to salt tectonics from the underlying

Zechstein units. Most of these anticlines are filled with brine and only a few of the structures are gas bearing (e. g. the Hewett and Orwell gas fields). The reason is not an absence of caprocks (e.g. Heinemann et al. 2012) but rather a migration problem. The gas producing formations of the southern North Sea are coal bearing units of the Carboniferous which are located beneath the impermeable Zechstein evaporites. Thus, gas migration through the Zechstein evaporites into the Triassic (Rotliegend) reservoir rocks was only possible through areas of salt withdrawal or extensive faulting.

1.4 Dolomite

Introduction to dolomite

Dolomite is a common mineral that is difficult to define precisely. It is insufficient to regard dolomite as a secondary carbonate mineral with a composition of equal Ca and Mg concentrations. First of all, dolomite can be of primary or secondary origin: It can either precipitate out of a solution or it can be generated by the chemical alteration of other carbonate minerals (mainly calcite).

Additionally, important variations occur both in the degree of cation order and concentration (Goldsmith & Graf 1958a; Reeder & Wenk 1979). A definition for dolomite is required in order to avoid 'grey zones' where the usage of the term dolomite is dependent on the point of view of the scientist. Lynton Land (1980) used the name dolomite for minerals which:

- Have a Ca-Mg composition ratio near 50/50.
- Have indisputable evidence of order (crystal symmetry higher than that of calcite ... (Land 1980)). If the double carbonate phase is not ordered, it is not dolomite.

Hence dolomite cannot be regarded as one composition but rather as a compositional series, comparable with feldspar (Land 1980). The different dolomite variations have

different thermo chemical properties depending on the degree of lattice ordering and non-stoichiometry (Warren 2000).

Ideal stoichiometric (Ca=Mg) sedimentary dolomite is the exception, not the rule (Land 1980). Such ideal dolomite has a crystal lattice consisting of alternating calcium and magnesium layers, separated by CO_3 layers. Dolomite in post-Palaeozoic rocks shows a generally greater compositional variation than older dolomite. Together with the observation that more disordered phases and Ca-rich phases are more soluble than ordered stoichiometric dolomite (Folk & Land 1975), one could conclude that dolomite does not preferentially form as a stoichiometric phase but that it is the stoichiometric dolomite part that survives over geological time. Additionally, a very slow diffusion based substitution towards the ideal Ca=Mg composition is also possible and would also describe why recent dolomite is commonly poorly ordered. More recently, Warren (2000) made it very clear that dolomite is a metastable mineral which undergoes so called 'Ostwald ripening' via several replacement reactions in order to reach a higher stoichiometry. A more straightforward explanation was given by Morrow (1978) who proposes that the composition of the dolomite is controlled by the composition of the acting fluid.

The root of the problem can be summarized relatively briefly. 'Nobody has yet synthesized dolomite either by replacement or by direct nucleation under conditions typical of sedimentary depositional environments, (Land 1980)', a statement which is already quite old but still relevant. Interestingly, dolomite formation under elevated temperature and pressure is uncomplicated and rapid. The simple conclusion of those two facts could be that dolomite does not form (by precipitation or by replacement) under surface conditions. This has been contradicted by the description of dolomite which clearly formed under surface or shallow subsurface conditions in the past.

Dolomite as a primary mineral

Dolomite is not necessarily a secondary mineral. In other words, it does not necessarily require a combination of carbonate minerals, such as calcite, and magnesium rich fluids to generate dolomite. How high the amount of 'primary' dolomite actually is, is debatable. After a presentation given by Prof. Judith McKenzie (ETH Zurich), she answered the question of a sceptical Professor ("So Judith, what do you think, how many percent of the world wide dolomite is 'primary' dolomite?") with a smile and a provocative: "I would say most of the worldwide dolomite is 'primary' dolomite". Nevertheless, most geologists agree that most dolomite is secondary in that some sort of carbonate precursor existed prior to the replacement by dolomite.

Primary dolomite, which formed by direct nucleation out of the pore water will always be bound to the initial porosity of the surrounding sediments and acts as a cement in formations such as the southern North Sea Rotliegend Formation (e.g. Purvis 1992, Wilkinson et al. 2009). However, the cliffs of the Dolomites in Italy, which consists of hundreds of meters of dolomite, require a different explanation. Their formation is explained by the alteration of massive calcite cliffs, the formation of which can be witnessed all over the world under subsurface conditions. Under subsurface conditions, dolomite forms under a broad range of geochemical environments and under all saline conditions; the elementary requirement only seems to be an oversaturation of the pore water with dolomite.

For primary dolomite, the problem can be shown by expressing the precipitation reaction:

$$Ca^{2+} + Mg^{2+} + 2(CO_3^{2-}) = CaMg(CO_2)_2 \qquad (1)$$

The equilibrium constant K for this reaction is:

$$K = ([Ca^{2+}][Mg^{2+}][(CO)_3^{2-}]^2) / [CaMg(CO_3)_2] \quad (2)$$

where the denominator is per definition 1. Estimations for K are in the order of $K \approx 10^{-17}$ (Hsu 1967) and $K \approx 10^{-16.5}$ (Hardie 1987). Even if the error of the K values is relatively large, the approximate activity product of Ca^{2+}, Mg^{2+} and CO_3^{2-} in seawater lies in the order of 10^{-15}. Hence, seawater is supposed to be highly supersaturated with respect to dolomite. These theoretical considerations, together with Lynton Land's patient experiment where he unsuccessfully tried to precipitate dolomite over 32 years at 25°C (and the conclusions of many more studies), allowed Land to state that '… we all (?) now agree that 'the dolomite problem' is one of the kinetics' (Land 1998).

The environmental conditions of dolomite formation at the Earth's surface are therefore extremely difficult to determine. The oxygen isotope fractionation factor between dolomite and the solution from which it precipitated at surface conditions has been especially difficult to calibrate experimentally. Whereas fractionation factors for calcite are easy to determine (simply because calcite can be precipitated out of a solution at virtually any temperatures) dolomite fractionation factors have to be extrapolated from high temperature experiments. To circumvent the uncertainties of extrapolating fractionation factors, scientists measured the isotopes of coexisting dolomite/calcite formations (where dolomite was actually 'primary' dolomite and precipitated simultaneously with the calcite). Together with the known fractionation factors of calcite/solution, the dolomite/solution factors could be calculated theoretically.

The determination of isotopic fractionation factors for dolomite is what Land (1980) calls the 'Δ problem'. The fractionation factor for oxygen of phase A and B in equilibrium is defined as:

$$\alpha_{A-B} = \frac{\delta^{18}O_A + 1000}{\delta^{18}O_B + 1000} \qquad (3)$$

The relationship of reaction temperature and fractionation factor is given by:

$$1000 \ln \alpha = X(10^6 T_{(K)}^{-2}) + Y \qquad (4)$$

Here *X* and *Y* are constants which have to be measured experimentally. Additionally, the isotopic composition of one phase can be calculated if the reaction temperature is known.

Several approaches to determine a fractionation factor, such as high temperature experiments, studies of coexisting dolomite/calcite formations, precipitation of 'proto-dolomite', studies on low-temperature hydrothermal dolomite (see Land (1980) and Vasconcelos et al. (2005) for references) give $\Delta\ \delta^{18}$O (Dol-Cal) values which spread from 0 ‰ to 9 ‰; a rather unsatisfying outcome. A more recent study, published by Vasconcelos et al. (2005), has claimed to have solved the 'Δ problem' by using microbes as catalysts for dolomite precipitation experiments under low temperature conditions. Although microbes are present, they assume dolomite precipitates in equilibrium with the solutions because 'the precipitation is not biologically controlled but simply biologically induced …'. The outcome of their study for dolomite precipitated out of pore water, the temperature/fractionation factor is:

$$1000 \ln \alpha = 2.73(10^6 T_{(K)}^{-2}) + 0.26 \qquad (5)$$

1.5 Outline of the thesis

The thesis will touch on several aspects concerning carbon storage which were introduced in chapter 1.1 to chapter 1.3. Structural trapping, solubility trapping and mineral trapping will be discussed in greater detail; only ‘capillary trapping’ will not be further investigated.

This chapter is followed by a chapter on the ‘Technical background’. It introduces two important parts of the simulation of CO_2 injection. Firstly, the Darcy flow based fluid flow equation is introduced. The second part introduces the concept of equation of states that are used to calculate the pressure, volume and temperature (PVT) relationship of fluids, in the case of CO_2. The basic idea behind the ‘technical background’ is to provide an overview on how results presented in chapter 3 and chapter 4 were generated and how they are to be interpreted.

Whereas chapter 3 and chapter 4 describe studies that were mainly based on the simulation of CO_2 injection into aquifers such as the ones in the southern North Sea, chapter 5 describes a project on the precipitation of dolomite due to a high CO_2 concentration. The basic introduction to dolomite and the challenges that the research on dolomite precipitation provides were introduced in chapter 1.4. For this study, rock samples were analysed to investigate whether CO_2 precipitated as dolomite in a southern North Sea gas field with a relatively high CO_2 concentration.

2 Technical background

To accurately simulate the injection and migration of CO_2 through porous media in the subsurface, a fluid flow simulator has to calculate the flow and the PVT (pressure-volume-temperature) conditions of both the aqueous and the gaseous phase. This chapter introduces the two theories behind these fundamental aspects of reservoir engineering, the fluid flow equation and the equation of state, and will provide the technical background information to understand and interpret the results of the two following research chapters (chapter 3 and 4). The focus of this chapter lies on the theoretical and mathematical introduction of the theories. No further aspects concerning the numerical implementation or how to code the equation in a software package will be discussed.

The fluid flow equation that will be introduced here is based on Darcy's law. It assumes a relationship between flow velocity and pressure gradients. The sub-chapter starts with the basic single phase one dimensional flow and subsequently introduces the more complicated scenarios such as three dimensional flow and multi-phase flow.

The second part of the chapter introduces equation of states (EoS). Because the reservoir engineering section of this thesis focusses on injection and flow of CO_2 in brine, the chapter introduces the EoS for these two phases only. The prediction of brine/water properties is relatively simple. The behaviour of CO_2 in the subsurface is difficult predict at depths which are potentially interesting for CO_2 storage because CO_2 will undergo phase changes. The chapter introduces the EoS which were used in this project and describes a way of solving the equations. It also points out where uncertainties are and introduces alternative EoS.

2.1 Introduction to multi-phase flow modelling

2.1.1 Nomenclature

(Units may vary and are defined in the text)

d	particle diameter
g	gravity
h	pressure head
k	permeability
k_r	relative permeability
np	cap-pressure coefficient
mp	pore size distribution factor
q	volumetric flow rate
r	radial distance
t	time
u	Darcy velocity
x	distance
z	depth
x, y, z	principle direction
A	area
D_h	hydraulic diffusivity
B	formation volume factor
P	pressure
P_{ca}	capillary pressure
P_{c0}	strength coefficient
P_w	pressure of the wetting phase
P_{nw}	pressure of the non-wetting phase
$R_1; R_2$	radii of curvature
Re	Reynold number
S	saturation
S_r	residual saturation

S^*	effective saturation of the liquid phase
S'	effective saturation of the gas phase
αp	fitting parameter for capillary pressure
β	inertial effect coefficient/Forchheimer parameter
θ	wettability contact angle
κ	displacement/threshold pressure
λ	Brooks-Corey exponent
μ	viscosity
ρ	density
ϕ	porosity
γ	interfacial tension
v	fluid velocity

2.1.2 Single phase flow

One dimensional flow

Pressure migration is based on single-phase fluid flow. The most common method which is used for reservoir engineering purposes is the pressure diffusion equation which is based on a simple mass conservation. Here, the mass accumulation (given by the volumetric flow rate q and the density of the fluid ρ), which can be positive or negative of a certain volume (the grid block i) over a specific time:

$$= \left[(q\rho)_{i-1/2} - (q\rho)_{i+1/2}\right]\Delta t \qquad (1)$$

is equal to the difference between the mass (defined by the density ρ and the volume ϕ), entering and the mass leaving the volume (length Δx and surface A) over the specific time.

$$= \left[(\rho\phi)_{t+\Delta t} - (\rho\phi)_t\right]\Delta x \cdot A \qquad (2)$$

By dividing (1) and (2) by Δx, Δt and A and assuming Δx and Δt tend to zero, the general equation becomes:

$$\frac{\partial}{\partial t}(\rho\phi) = -\frac{\partial}{\partial x}(\frac{q\rho}{A}) \qquad (3)$$

Flow rate through an area is the crucial auxiliary parameter. Most reservoir engineering software defines 'q/A' via the Darcy equation, but alternative theories are available and, dependent on the application, can be reasonable.

Darcy flow was 'discovered' by the French engineer Henry Darcy in 1855. It describes the relationship of parameters which control the flow through an area. It can be written as:

$$u = \frac{q}{A} = -\frac{k}{\mu}(\frac{\partial P}{\partial x}) \qquad (4)$$

where k is permeability, μ is viscosity, P is the pressure gradient over x (a particular distance). The Darcy equation is an empirical relationship based on experimental observations of 1-dimensional water flow through packed sands at relatively low velocity (Zeng & Grigg 2006). The important relationship of Darcy's law is that the pressure gradient is linearly proportional to the fluid velocity in the porous media. To make the simulation more realistic, gravity can be added. It describes the influence of the gravity on the density for changing elevations. The resulting equation is:

$$u = -\frac{k}{\mu}\left[(\frac{\partial P}{\partial x}) - \rho g \frac{\partial z}{\partial x}\right] \qquad (5)$$

The gravity term should be included to describe realistic fluid flow but it will be neglected until the end of this chapter in order to keep the equations simple.

As a second step, pressure as a function of distance and time, has to appear on the left hand side of equation (1), too. Since density and porosity are dependent on pressure, the chain rule may be applied, as follows:

$$\frac{\partial}{\partial t}(\rho\phi) => \frac{\partial(\rho\phi)}{\partial P}(\frac{\partial P}{\partial t}) \qquad (6)$$

By using (6) on the LHS of equation (3) and including the Darcy term into the RHS of (3), equation (3) becomes:

$$\frac{\partial(\rho\phi)}{\partial P}(\frac{\partial P}{\partial t}) = \frac{\partial}{\partial x}(\frac{\rho k}{\mu}(\frac{\partial P}{\partial x})) \qquad (7)$$

The first term of the left hand site of the equation describes the change of pore space and density (in other words: the fluid volume) during pressure changes. Hence, it describes compressibility.

At this stage, an important hydrological parameter can be introduced. If it is assumed that viscosity, porosity, total compressibility (or fluid density) and permeability are constant, these constants can be isolated. The ratio is called the 'hydraulic diffusivity' (D_h):

$$D_h = \frac{k}{\mu\phi\rho} \qquad (8)$$

Radial flow

To simulate radial flow, which is necessary to show fluid flow in the vicinity of an injection well, a radial component has to be added. Equation (3) becomes:

$$\frac{\partial}{\partial P}((2\pi r)\rho\phi)\cdot(\frac{\partial P}{\partial t}) = -\frac{\partial}{\partial r}(u\rho) \qquad (9)$$

and equation (4) becomes:

$$u = -\frac{k(2\pi r)}{\mu}(\frac{\partial P}{\partial r}) \qquad (10)$$

which then, if (10) is included into (9), becomes

$$\left(\frac{\partial}{\partial P}\rho\phi\right)\left(\frac{\partial P}{\partial t}\right) = \frac{1}{r}\frac{\partial}{\partial r}\left[\frac{\rho k r}{\mu}\left(\frac{\partial P}{\partial r}\right)\right] \qquad (11)$$

Multi-phase flow

In order to describe the migration of CO_2 through brine filled porous media two phase fluid flow has to be applied. To describe two phase fluid flow, several important parameters have to be taken into account. The fundamental idea is to calculate the flow and the change in mass of the two phases independently and add parameters and terms which deal with the connection of the different phases.

Necessary adjustments and parameters

Since CO_2 sequestration operations deal with at least a liquid and a gaseous phase the following explanation describes a water-gas system. Another possible phase would be oil which has to be taken into account for enhanced oil recovery scenarios combined with CO_2 storage. The possible phase transition of gaseous CO_2 to supercritical CO_2 within a depleted, low pressure gas reservoir, or the reverse transition in the case of CO_2 leaking out of the reservoir and migrating towards the

surface is conveniently described with the same approach. Supercritical CO_2 is usually seen as a version of gaseous CO_2 with elevated density and viscosity.

The first important parameter which connects the two phases is the phase saturation, the fraction of pore space that is occupied by either the first or the second phase. Since pore space has to be always 'full', phase saturation is defined as:

$$S_G + S_L = 1 \qquad (12)$$

where S_G is the gas saturation and S_L the liquid saturation.

The second parameter is the formation (or reservoir) volume factor or its inverse, the expansion factor. The formation volume factor (B) is defined as the volume of a phase at reservoir conditions required to produce a certain volume of gas (e. g. 1 m^3) at the surface. The formation volume factor for the liquid and the gaseous phase can be expressed with:

$$B_G = \frac{V_{res}}{V_{sc}} = \frac{\rho_{sc}}{\rho_{res}} \ , \ B_L = \frac{V_{res}}{V_{sc}} = \frac{\rho_{sc}}{\rho_{res}} \qquad (13)$$

Finally, two important parameters have to be introduced which have direct impact on the fluid flow, the relative permeability and the capillary pressure. Both parameters are connected and dependent on phase saturation but can be explained separately. Relative permeability controls how much fluid flows (relative to the permeability) whereas capillary pressure defines the pressure difference between the fluids.

Relative permeability

Relative permeability is a parameter which describes how different phases, dependent on their saturation, impair the fluid flow. It varies between 0 and 1 and can therefore reduce the permeability of the porous media but does not increase it. It

also controls the residual saturation, remnants of the initially present phase, which was forced out by an injected second phase. Relative permeability data can either be taken from experimental studies or they can be determined analytically.

If relative permeability curves are not available, linear flow relationship (here called 'linear relative permeability') is assumed for a multi-phase flow system. Linear relative permeability means that the flow of two phases is linearly dependent on their saturation. Linear relative permeability can be depicted with Stone's relative permeability function (Stone 1970), which is as follows:

$$k_{rx} = \left(\frac{S_x - S_{xr}}{1 - S_{xr}} \right)^{np} \qquad (14)$$

k_r is the relative permeability, S_x the saturation of the phase x and S_{xr} the residual saturation. If the residual saturation is neglected (S_{xr}=0) and the exponent (np) is set to 1, the sum of the permeability of both phases is always 1 and its value is linearly dependent on the saturation (Fig. 2.1).

Bennion and Bachu (2006) conducted several experiments to determine relative permeability for CO_2 and brine. Their results for a core sample from the Cardium Formation in Wabamun Lake area, Alberta, Canada at 43°C, a water salinity of 0.27096 kg/l and an IFT of 19.8 mN/m (which corresponds to a pressure of 200 bar) are presented in Fig. 2.2.

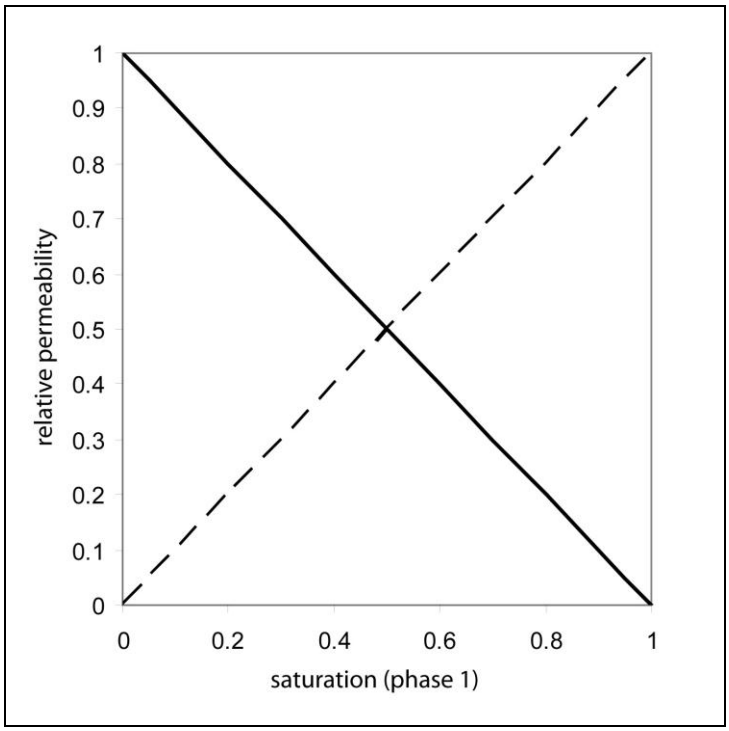

Figure 2.1: Linear relative permeability.

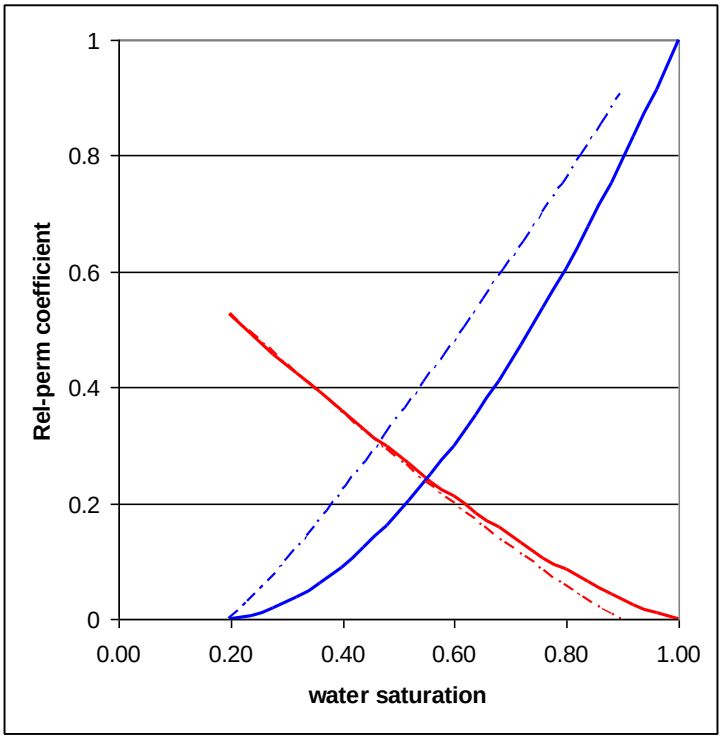

Figure 2.2: Relative permeability curves of CO_2 (red) and brine (blue) for a core sample from the Cardium Formation in Wabamun Lake area, Alberta, Canada at in-situ temperatures of 43°C, water salinity of 27.096 ppm and 200 bar. Taken from Bennion and Bachu (2006).

The residual brine saturation, the fraction of brine which cannot be pushed out by the invading CO_2, is 0.197. That means 19.7 % of the available pore space will always be occupied with brine (if water dissolution into CO_2 is not taken into account). If no CO_2 is present, the relative permeability for brine is 1 and migrating brine, which can be seen as pressure migration, can 'use' the entire available permeability. On the other side, if CO_2 saturation is maximum, in this case 80.3 %, no water flow will occur and CO_2 flow will be constrained by 47.35 %.

The dotted lines show the relative permeabilities for the imbibition process which controls the hysteresis effect. Imbibition occurs if brine, after being replaced by CO_2, re-enters the pores after CO_2 moves on due to buoyancy forces. The invading brine reduces the CO_2 saturation and the relative permeability for brine increases more rapidly than it decreases during drainage. A residual CO_2 saturation will remain and is in this case 10.2 %. Hence, around 10 % of the pore space will remain occupied by CO_2. At this stage, this fraction of CO_2 is seen as permanently stored CO_2 and the storage mechanism is called capillary trapping. With time, the amount of capillary trapped CO_2 decreases because the CO_2 fraction dissolves into the brine. The hysteresis effect and capillary trapping is not of particular importance for the following studies and will therefore not be explained any further.

A common method to calculate liquid phase relative permeability (k_{rl}) of hydrocarbons and CO_2 is the van Genuchten (1980) method:

$$k_{rl} = (S^*)^{\alpha p}[1-(1-(S^*)^{1/m})^m]^2 \qquad (15)$$

where S^*, the effective saturation, is:

$$S^* = (S_1 - S_{lr})/(1-S_{lr}) \qquad (16)$$

S_l is the saturation and S_{lr} the residual saturation of the liquid phase. The exponent 'αp' is a fitting parameter accounting for the effects of tortuosity and connectivity with respect to the wetting phase. Mualem (1976) found that a value of 0.5 provided an appropriate average of the relative water permeability for many soils. The parameter *mp* depends on the lithology. As an example, Pruess et al. (2003) listed *mp* values for several types of porous media such as sand (0.6269), sandy loam (0.4709) and sandy clay (0.187). Appropriate residual saturations for brine as the wetting liquid phase were 0.105, 0.158 and 0.263, respectively.

A common model for the calculation of gaseous relative permeability was presented by Corey (1954):

$$k_{rg} = (1 - S')^2 (1 - S'^2) \qquad (17)$$

where S' is:

$$S' = (S_1 - S_{lr}) / (1 - S_{lr} - S_{gr}) \qquad (18)$$

Pruess et al. (2003) proposes the S_{gr} (residual gas saturation) to be 0.05 throughout. If the previously mentioned data are applied, the relative permeability curves calculated with the two equations are show in Fig. 2.3.

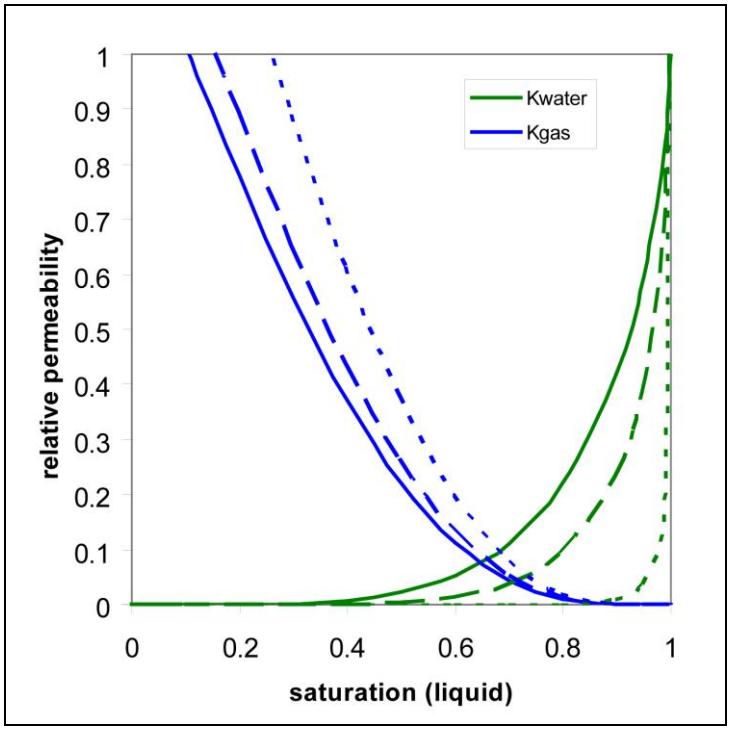

Figure 2.3: Calculated relative permeability curves for an aqueous phase and gas phase system. Aqueous phase relative permeability (water, green) was calculated after van Genuchten (1980) and gas phase permeability (blue) was calculated after Corey (1954). Data were calculated for sand (solid lines), sandy loam (dashed lines) and sandy clay (dotted line); according to Pruess et al. (2003).

Modelled relative permeability curves such as those presented in Fig. 2.3 are extensively used for CO_2 storage simulation. An interesting difference can be recognized if compared with experimental data. The gas relative permeability reaches 1 at the residual water saturation. In other words, gas can flow by using the entire available permeability although a fraction of the pore space is occupied by residual water. The experimental data show that CO_2 flow would still be constrained and the relative permeability will never reach 1 in a water wet system with residual saturation.

Capillary pressure

Capillary pressure defines the entry pressure of a phase which enters a pore filled with a different phase. It can be expressed by the equation (Purcell 1949):

$$P_c = \frac{2\gamma \cos\theta}{r} \qquad (19)$$

P_c is the capillary pressure, γ the interfacial tension, $\cos\theta$ is the wettability term (θ is the contact angle) and r determines the radius of the set of pores with the largest pore throats. The equation (22) derives directly from the Young-Laplace equation (42). The following section summarizes the three parameters (interfacial tension, wettability and pore throat radius) very briefly.

The interface between two immiscible fluids is under a certain tension that arises from the unbalanced cohesional forces on molecules at the interface (Adam 1968). This tension, the interfacial tension (IFT) causes the interface to contract creating an interface as small as possible (McWhorter & Kueper 1996). It is the result of differences between the mutual attraction of molecules within each fluid and the attraction of dissimilar molecules across the interface of the fluids. Gas water IFT decreases with increasing temperature depending on the pressure and decreases with increasing pressure depending on the temperature (Hough et al. 1951). The IFT of a gas-liquid system or in other words, the displacement pressure of CO_2 (the non-wetting phase) and brine (the wetting phase) is relatively high (compared with e. g. oil-water IFT) and therefore reduces the migration potential of CO_2 in the subsurface.

Wettability describes the contact between two immiscible fluids and the solid. It can be defined as the work necessary to separate a wetting fluid from a solid. It is a result of the combined interfacial energy of the system. The unit is the contact angle between the solid and fluid.

The size of the pore throat is the third parameter which defines the capillary pressure. Although it is a simple parameter it is actually very difficult to determine. Due to the pore size distribution, the 'one' pore throat radius is also rather a distribution than a particular length. Generally, the largest connected pore throats are estimated and taken for the capillary pressure. Two ways to obtain capillary pressure data are available laboratory experiments or modelled values.

Capillary pressure measurements are usually performed as mercury-air displacement tests, then converted to appropriate scenarios using a scaling factor (Purcell 1949, Schowalter 1979):

$$P_{c(CO2-brine)} = \left[\frac{\gamma_{(CO2-brine)} \cos\theta_{(CO2-brine)}}{\gamma_{(mercury-air)} \cos\theta_{(mercury-air)}} \right] P_{c(mercury-air)} \qquad (20)$$

where the term in brackets is the scaling factor for a CO_2-brine system.

Several models are available to calculate the capillary pressure. Brooks and Corey (1964) introduced an equation which can be used to calculate the capillary pressure:

$$P_c = \kappa \left[\frac{S_w - S_{rw}}{1 - S_{rw} - S_{rg}} \right]^{-\frac{1}{\lambda}} \qquad (21)$$

where S_w is the wetting phase saturation, S_{rw} the residual wetting phase saturation, the κ is the 'displacement (or threshold) pressure' and λ the Brooks-Corey exponent which has a value between 1 and 4. Pruess et al. (2002) use the equation:

$$P_c = P_{c0} \left(\left(\frac{S_w - S_{rw}}{1 - S_{rw}} \right)^{-1/mp} - 1 \right)^{1-mp} \qquad (22)$$

P_{c0} is here called the 'strength coefficient' with a pressure unit and '*mp*' is an exponent, similar to the Brooks-Corey exponent. This equation derives from van Genuchtens (1980) original paper where the original equation [24] is:

$$\alpha = \frac{1}{h}\left(S*^{(-1/m)} - 1 \right)^{1-m} \qquad (23)$$

where *h* is the pressure head in cm. Fig 2.4 shows capillary pressure curves calculated with the two models. Both types of capillary pressure curves have similar residual water saturation (S_{rw}) and P_{c0}. Appropriate values for the other parameters were chosen to create two comparable capillary pressure curves. The important difference between the two models is that Brook-Corey defines a necessary capillary pressure for invading CO_2 in an entirely brine filled formation. The van Genuchten model defines this capillary pressure to be zero, but only for a relatively small CO_2 fraction (Fig. 2.4).

In common reservoir engineering software packages relative permeability and capillary pressure is inserted into the Darcy flow equation as follows:

$$u_{aq} = -\frac{k \cdot k_{raq}}{\mu_{aq}}\left[\left(\frac{\partial P_{aq}}{\partial x}\right) - \rho_L g \frac{\partial z}{\partial x} \right] \qquad (24)$$

and

$$u_g = -\frac{k \cdot k_{rg}}{\mu_g}\left[\left(\frac{\partial P_g}{\partial x}\right) - \rho_L g \frac{\partial z}{\partial x} \right] \qquad (25)$$

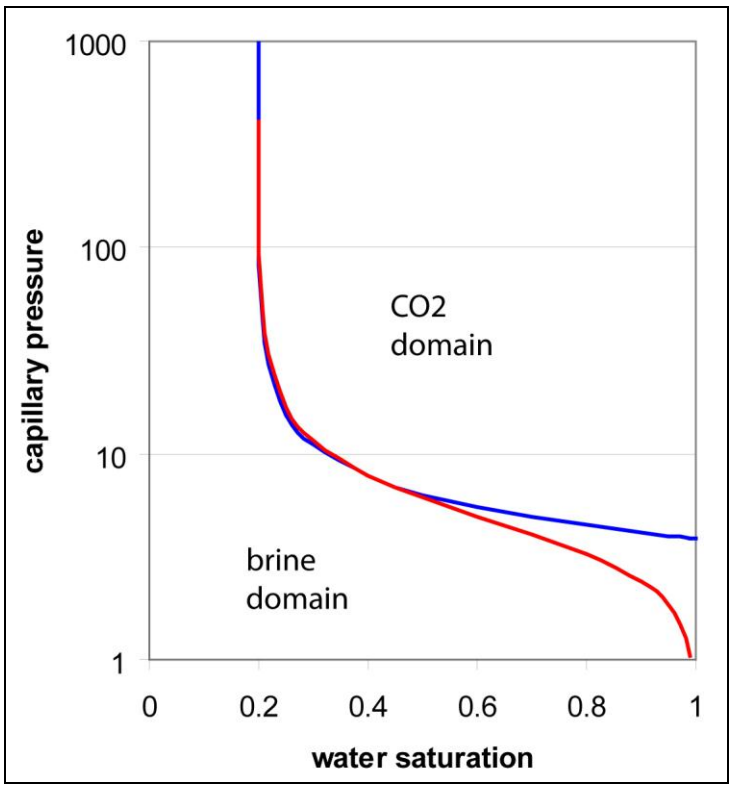

Figure 2.4: Comparison between capillary pressure curves modelled with van Genuchten (1980, red) and Brook and Corey (1964, blue).

where k_{raq} and k_{rg} are the relative permeability of the aqueous phase (brine) and the gas phase (CO_2) respectively. P_{aq} and P_g are the pressure of the different phases and are described by the relationship:

$$P_c = P_{nw} - P_w \qquad (26)$$

where P_{nw} is the pressure of the non-wetting phase (CO_2 or P_g in this case) and P_w the pressure of the wetting phase (brine or P_{aq} in this case).

The two phase fluid flow equation

Two equations can be written one for the liquid phase:

$$\frac{\partial}{\partial t}\left(\frac{\rho_{aqsc} S_{aq} \varphi}{B_{aq}}\right) = -\frac{\partial}{\partial x}\left(\frac{u_{aq} \rho_{aqsc}}{B_{aq}}\right) \quad (27)$$

and one for the gas phase:

$$\frac{\partial}{\partial t}\left(\frac{\rho_{gsc} S_g \varphi}{B_g}\right) = -\frac{\partial}{\partial x}\left(\frac{u_g \rho_{gsc}}{B_g}\right) \quad (28)$$

Here again, pressure is missing on both sites. On the left hand side, it is again assumed that compressibility and the formation volume factor is pressure dependent. Additionally, the reference density of both the gas and the liquid phase is constant and can therefore be discarded. Because gas phase pressure is regarded as the reference pressure,

$$\frac{\partial}{\partial t}\left(\frac{S_X \varphi}{B_X}\right) = \varphi S_X \frac{\partial}{\partial P_g}\left(\frac{1}{B_X}\right)\left(\frac{\partial P_g}{\partial t}\right) + \frac{\varphi}{B_X}\left(\frac{\partial S_X}{\partial t}\right) + \frac{S_X}{B_X}\frac{\partial}{\partial P_g}\varphi\left(\frac{\partial P_g}{\partial t}\right) \quad (29)$$

This can be simplified to:

$$\frac{\partial}{\partial t}\left(\frac{S_X \varphi}{B_X}\right) = \frac{\varphi}{B_X}\left(\frac{\partial S_X}{\partial t}\right) + \left[\varphi S_x \frac{\partial}{\partial P_g}\left(\frac{1}{B_X}\right) + \frac{S_x}{B_X}\left(\frac{\partial \varphi}{\partial P_g}\right)\right]\frac{\partial P_g}{\partial t} \quad (30)$$

The gas phase pressure is the reference pressure whereas P_X is either the gas or the aqueous phase pressure. The two saturations are by definition 1 if added. Hence the addition of their derivatives becomes 0:

$$\frac{\partial S_{aq}}{\partial t} + \frac{\partial S_g}{\partial t} = 0 \qquad (31)$$

In order to dispose of the saturation, both sides have to be added after the isolation of the saturation term via the multiplication of $(\frac{B_g}{\phi})$. Additionally, the two saturations of the term:

$$\frac{S_{aq}}{\phi}\left(\frac{\partial \phi}{\partial P_g}\right) + \frac{S_g}{\phi}\left(\frac{\partial \phi}{\partial P_g}\right) \qquad (32)$$

become 1 if added. Hence what is left from the left hand sides of equations (27) and (28) is:

$$= \left[B_g S_g \frac{\partial}{\partial P_g}\left(\frac{1}{B_g}\right) + B_{aq} S_{aq} \frac{\partial}{\partial P_g}\left(\frac{1}{B_{aq}}\right) + \frac{1}{\varphi}\left(\frac{\partial \varphi}{\partial P_g}\right)\right] \frac{\partial P_g}{\partial t} \qquad (33)$$

where the first part represents the compressibility of the gas phase, the second part the compressibility of the liquid phase and the third part the compressibility of the rock. This is the LHS of the two phase flow equation.

The right hand site consists of the addition of the two equations with inserted Darcy-flow and the definition of the capillary pressure term. Since the pressure of the non-wetting phase is seen as the reference pressure, the pressure of the wetting phase can be defined as:

$$(\frac{\partial P_{aq}}{\partial x}) = (\frac{\partial P_g}{\partial x}) - (\frac{\partial P_c}{\partial x}) \qquad (34)$$

This assumption eliminates the pressure of the liquid phase. Additionally, the RHS has to be multiplied by ($\frac{B_g}{\varphi}$) like the LHS before. The complete two phase fluid flow equation for one dimension which takes gravity, compressibility and capillary pressure into account is:

$$\begin{aligned}
&\left[B_g S_g \frac{\partial}{\partial P_g}\left(\frac{1}{B_g}\right) + B_{aq} S_{aq} \frac{\partial}{\partial P_g}\left(\frac{1}{B_{aq}}\right) + \frac{1}{\varphi}\left(\frac{\partial \varphi}{\partial P_g}\right)\right] \frac{\partial P_g}{\partial t} \\
&= \frac{B_g}{\varphi} \frac{\partial}{\partial x}\left[\frac{k \cdot k_{rg}}{\mu_g B_g}\left(\left(\frac{\partial P_g}{\partial x}\right) - \rho_g g\left(\frac{\partial z}{\partial x}\right)\right)\right] \\
&+ \frac{B_{aq}}{\varphi} \frac{\partial}{\partial x}\left[\frac{k \cdot k_{raq}}{\mu_{aq} B_{aq}}\left(\left(\frac{\partial P_g}{\partial x}\right) - \left(\frac{\partial P_C}{\partial x}\right) - \rho_L g\left(\frac{\partial z}{\partial x}\right)\right)\right]
\end{aligned} \tag{35}$$

2.1.3 **Non-Darcy flow**

Introduction

Experimentally, fluid flow deviations from Darcy flow have long been observed and several terms such as inertial flow, turbulent flow or non-Darcy flow are in use to describe them (Firoozabadi & Katz 1979). Two kinds of deviations are possible: either flow rates become too high or modifications such as inertial or turbulence corrections have to be applied to guarantee a 'realistic' description of the processes. For CO_2 storage scenarios, high flow rates are expected in the vicinity of the injection well where CO_2 flow and water displacement are highest. On the other hand fluid flow rates can become too low so that the contribution of the viscosity is negligible and the viscous-dominated Darcy flow approximation becomes inappropriate. This occurs if buoyancy driven CO_2 migrates through brine saturated porous media and is supposed to be accurately described by the 'invasion percolation' theory.

High velocity fluid flow: Forchheimer flow

The fluid flow regime that requires the Forchheimer parameter to be represented accurately, is here called 'Forchheimer flow'.

If CO_2 is being injected into the subsurface under a certain injection pressure, it is logical that the fluid flow rate will be relatively high. Hence, it is expected that Darcy flow will not occur but Forchheimer flow (or even turbulent flow) might take over. Forchheimer flow is named after Phillip Forchheimer, an Austrian hydrologist and engineer, who expanded the Darcy flow equation by a term which describes the inertial effect of the flowing fluid (Forchheimer 1901):

$$-\frac{dP}{dx} = \frac{\mu v}{k} + \beta \rho v^2 \qquad (36)$$

Where β is the 'inertial effect' coefficient (also called the Forchheimer parameter). The application of the Forchheimer equation for well performance simulations can be important because it could reduce the effective fracture conductivity and the gas production (Holditch & Morse 1976). Some analytical models for pressure build up due to CO_2 injection also use the Forchheimer equation (Mathias et al. 2009).

To include Forchheimer flow into a numerical model, a value for the Forchheimer parameter has to be defined. The main problem for the implementation of Forchheimer flow in a CO_2 injection model (instead of invasion percolation flow, see next paragraph) is that inertial influenced flow only occurs at certain locations of the model, e.g. in the vicinity of the injection well. A zone where Forchheimer flow occurs has to be picked and adjusted with the appropriate parameter in order not to simulate non-Darcy flow over the entire grid.

Buoyancy driven fluid flow: Invasion percolation (IP) flow

At very slow multi-phase fluid flow rates the viscosity forces can be neglected and the flow is dominated by capillary forces. For buoyancy driven subsurface CO_2 flow,

it means that the invasion of a brine filled pore with CO_2 will be determined by the Laplace equation which describes the capillary pressure (The equation is named after Thomas Young and Pierre-Simon Laplace who deduced it in 1805 independently).

$$\Delta P_c = \gamma \cdot \left(\frac{1}{R_1} + \frac{1}{R_2} \right) \qquad (37)$$

where R_1 and R_2 are the principle radii of curvature. If a pore (or in the simulation a cell) has been invaded, the saturation increases and increases the effective permeability by increasing the saturation related relative permeability. It leads 'to the dynamical rule of advancing the interface at the point of least resistance, as opposed to advancing all interfaces up to some chosen threshold resistance, …' (nels instead of a broad area. A pressure gradient, for example due to CO_2 injection or oil production is not included in the theory, and fluid flow that is pressure driven, such as Darcy flow, can only be approximately simulated - a fact that makes the simulator unsuitable for many economically related scenarios.

2.2 Equation of States (EoS) for CO_2

2.2.1 Introduction

The simulation of injection and migration of CO_2 sequestration processes is typically performed by numerical codes such as Eclipse (Schlumberger), GEM-GHG (Nghiem et al. 2004)) or TOUGH2 (Pruess et al. 1999). The core of the simulators, together with the fluid-flow algorithm, is the equation of state (EoS) algorithm which computes the several thermophysical properties of different phases and phase mixtures under different conditions.

The overall task of an EoS is to represent the properties of different phases of one (or for a mixture for several) component. The problem is that components can exist as a liquid, a gas or as a supercritical fluid (i.e. at temperature and pressure conditions above the critical point, where there is no phase distinction between a gas and a liquid). The properties of the gas phase compared with a liquid phase are very different, mainly because the molecules in gas are much further apart than in a liquid. Therefore, a component in the gas phase is much more compressible than the same component in a liquid phase. Hence, the characterization of a gas as a homogenous fluid with low density and low viscosity is usually insufficient because the phase characteristics as well as phase transitions have to be taken into account

To predict the properties of fluids such as CO_2 accurately (but for other fluids too) an EoS has to be established which describes these properties as a function of pressure and temperature. EoS's have two main objectives: Firstly, they should reproduce fluid properties derived from experiments. Experimental data are always the base for EoS, or, in other words, the quality of an EoS will be confirmed by its ability to match experimental data. Hence, inaccuracies in an EoS are actually second order errors because by validating EoS with experimental data, uncertainties which derive from the experiments are generally not taken into account. The second objective is

more relevant for geological processes which occur deep in the crust/upper mantle rather than CO_2 storage engineering. Experiments can hardly represent fluid properties accurately under these conditions, so an EoS is used to predict fluid properties under conditions unachievable in the lab. In such cases, the EoS cannot be a purely empirical based equation because such an 'arbitrary' equation with no fundamental thermodynamic basis would be unreliable for extrapolating data beyond the reliable experimental data range. As mentioned before, carbon storage is not considered to be implemented under middle or lower crustal conditions but under conditions which are well covered with experimental data. An application of non-thermodynamic based EoS could therefore be possible although the problem of fitting fluid properties of gas mixtures remains. In order to apply mixing rules, all gases should be fitted to polynomials of the same form. This is difficult to achieve if the properties of different pure gases are calculated with their own 'arbitrary' equation (Kerrick & Jacobs, 1981).

Introduction to 2-parameter EoS

The properties of an ideal gas (theoretical idea of a gas with independent, non-interacting molecules) can be predicted with a simple EoS based on the fundamental laws from Boyle, Charles and Avogadro and is written as:

$$PV = nRT \qquad (38)$$

where P is the pressure, V the volume, n the number of moles of the gas, R the Avogadro constant and T the temperature. No 'ideal' gas exists and mathematical modifications based on thermodynamic properties are necessary to predict the behaviour of real gas. As a first modification, the compressibility factor or z-factor was introduced which is the ratio of the volume of a real gas and the volume of an ideal gas under the same conditions. It is not constant and varies with changes in gas composition, temperature and pressure and must be determined experimentally. The corresponding EoS, the so called 'compressibility EoS' is:

$$PV = znRT \quad (39)$$

In 1873, the Dutch scientist and later Nobel Prize winner Johannes Diderik van der Waal introduced an EoS without experimentally derived z-factors. It can be seen as the fundamental EoS with foundations relating to molecular thermodynamics. He proposed the following equation:

$$\frac{RT}{V - b} - \frac{a}{V^2} = P \quad (40)$$

This EoS is the fundamental template for a whole range of '2-constant' EoS. The first term is called the ‘repulsive term’ and the second the ’attractive term’. Van der Waals extended the traditional equation by two constants *a* and *b* (*a* in (bar·cm^6)/mol^2, *b* in cm^3/mol (units are taken from literature (Spycher et al. 2003)), they are dependent on the units of pressure, temperature and *R*) which are characteristics of the particular gas and can be calculated with the critical properties. The term a/V^2 is a correction for the attraction between the molecules and the constant *b* is regarded as the correction to the molar volume due to the volume occupied by the molecules. The cubic or expanded version is:

$$V^3 - \left(b + \frac{RT}{P}\right)V^2 + \left(\frac{a}{P}\right)V - \frac{ab}{P} = 0 \quad (41)$$

The van der Waal EoS was an important step forward in calculating fluid properties, but from a modern point of view was too basic. The main limitation of the van der Waal’s EoS is its poor accuracy at intermediate and high pressures and the poor accuracy of predicting strongly non-ideal gases. However, the basic structure and general form is still the template for most of the recent EoS.

One of the most famous modifications of the van der Waals equation was introduced and published by O. Redlich and J. N. S. Kwong in 1948. It is still in use because of its accuracy to predict phase behaviour and its simple implementation. Richard B. Stein (1982) pointed out three computational advantages and stated that (a) 'it requires only values of T_c, P_c and ω (whereas the acentric factor in this quoting is misleading, it is usually not used for calculations of gas properties with the Redlich-Kwong EoS for each component,' (b) 'it converges to real roots for Z_V and Z_L in every case, even at or near the critical point, which is not always the case for other more complicated equations,' and (c) 'it requires minimum computer time for highly iterative processes …'. The general formula of the Redlich-Kwong EoS is:

$$P = \frac{RT}{(V-b)} - \left(\frac{a}{T^{1/2}V(V+b))} \right) \qquad (42)$$

where:

$$a = 0.4278\frac{R^2T_c^{2.5}}{P_c} \quad (49) \text{ and } b = 0.0867\frac{RT_c}{P_c} \qquad (43)$$

The coefficient a represents a correction for low pressure. The coefficient b represents a correction for high pressure. It accounts for gas behaviour at high pressures where the volume of gas approaches a practically temperature-independent limiting value which is close to $0.26V_c$, with V_c as the critical volume.

The Redlich-Kwong equation did not offer more accurate predictions of properties compared with the van der Waal equation, partly because of the lack of accuracy in

expressing the influence of temperature. This was mainly due to the fact that neither of the coefficients was temperature dependent.

Soave presented an improvement version of the Redlich-Kwong EoS in 1972 replacing $a/T^{1/2}$ with α_T which is a temperature dependent term (Soave 1972). The new coefficient (α_T) is defined by:

$$a_T = a_c \alpha \qquad (44)$$

where a_c is α_T at the critical temperature and α is the temperature modification (which is 1 at the critical temperature). The coefficients (a_c, b) are defined to be:

$$a_c = 0.42747 \frac{R^2 T_c^2}{P_c} \quad (52) \text{ and } b = 0.0867 \frac{RT_c}{P_c} \qquad (45)$$

The Soave equation uses almost similar coefficients to Redlich-Kwong equation. $T_c^{2.5}$ becomes T_c^2 because Soave removed $T_c^{1/2}$ from the formula and added $T_r^{1/2}$ (which is the reduced temperature) to the coefficient. The new coefficient is a, which is temperature dependent and shall act as a temperature correction. The coefficient is defined to be:

$$a^{1/2} = 1 + m1 - T_r^{1/2} \qquad (46)$$

where:

$$m = 0.480 + 1.574\omega - 0.176\omega^2 \qquad (47)$$

ω is the acentric factor, which is defined as:

$$\omega = -(\log P_{vr} + 1) \text{ at } T_r = 0.7 \qquad (48)$$

P_{vr} is the reduced vapour pressure. The acendric factor is a characteristic constant for a fixed temperature and is a measure of the non-sphericity (acentricity) of the molecules.

2.2.2 The Redlich-Kwongs EoS

Some of the models presented in this thesis were performed with the Redlich-Kwong EoS or modified equivalents. This paragraph shall introduce a simple way to solve it and to use it for predicting CO_2 properties. Note here that better (or more accurate, especially close to the critical point) EoS's are available, but these are either not valid over a wide range of conditions or their numerical implementation is difficult and complicated. The Redlich-Kwong EoS is:

$$P = \frac{RT}{(V-b)} - \left(\frac{a}{T^{1/2} V (V+b)} \right) \qquad (49)$$

In order to convert this equation into its cubic form, the RHS has to be expanded by its numerators to:

$$P = \frac{\left\{ \left[RT \right] \left[T^{1/2} V \left(V + b \right) \right] \right\} - \left[a(V-b) \right]}{(V-b) \left[T^{1/2} V (V+b) \right]} \qquad (55)$$

By multiplying the equation by the RHS's numerator and subtracting the LHS the equation becomes:

$$0 = \left\{\left[RT\right]\left[T^{1/2}V(V+b)\right]\right\} - \left[a(V-b)\right] - P\left\{\left[V-b\right]\left[T^{1/2}V(V+b)\right]\right\} \qquad (51)$$

It can be rearranged to:

$$0 = V^3PT^{1/2} - V^2RT^{1,5} - VRT^{1.5}b - VPTb^2 + Va - ab \qquad (52)$$

In order to isolate the volume, the equation has to be divided by $PT^{1/2}$ so that cubic version of the Redlich-Kwong EoS can be written as:

$$0 = V^3 - V^2\left(\frac{RT}{P}\right) - V\left(\frac{RTb}{P} + b^2 - \frac{a}{PT^{1/2}}\right) - \frac{ab}{PT^{1/2}} \qquad (53)$$

Now the EoS has a form which can be solved non-iteratively. The general way of solving a cubic equation of state is based on the general form of cubic equation which is for this particular case:

$$0 = aV^3 + bV^2 + cV + d \qquad (54)$$

where a is always 1. With the substitution of:

$$V = y - \frac{b}{3a} \qquad (55)$$

The so called ‘reduced form’ can be written as:

$$0 = y^3 + py + q \qquad (56)$$

where:

$$p = \frac{3ac - b^2}{3a^2} \quad (65) \qquad \text{and} \qquad q = \frac{2b^2}{27a^3} - \frac{bc}{3a^2} + \frac{d}{a} \quad (57)$$

By taking this steps, a cubic equation with no squared component is achieved. Since every cubic equation has three solutions (at least one is always real) the discriminant *D*, which is defined to be:

$$D = \left(\frac{q}{2}\right)^2 + \left(\frac{p}{3}\right)^3 \qquad (58)$$

determines the next step.

If $D>0$, one solution (*y1*) is real and is defined to be:

$$y1 = \left[\sqrt[3]{-\frac{q}{2} + \sqrt{D}}\right] + \left[\sqrt[3]{-\frac{q}{2} - \sqrt{D}}\right] \qquad (59)$$

If $D=0$, two solutions (*y1*, *y2*) are real (actually, the third solution (*y3*) is real too but is similar to *y2*) and are defined to be:

$$y1 = \sqrt[3]{-4q} \quad (60) \quad \text{and} \quad y2 = \sqrt[3]{\frac{q}{2}} \quad (61)$$

If $D<0$, three solutions ($y1$, $y2$, $y3$) are real and are defined to be:

$$y1/\,y2/\,y3 = 2\sqrt{-\frac{p}{3}\cos\left(\frac{\wp}{3} + k\cdot 120°\right)} \quad (62)$$

where:

$$k = 0,1,2 \quad \text{and} \quad \wp = \cos^{-1}\left[\frac{-q}{\sqrt[2]{-\left(\frac{p}{3}\right)^3}}\right] \quad (63)$$

The maximum root gives the density of the liquid phase, and the volume of the gaseous phase is given by the minimum root.

One of the important achievements of this EoS is the accuracy in the vicinity of the critical points or along two phase lines (e. g. dew point curve, the curve which defines the phase transition from liquid to gas and vice versa). In temperature-pressure phase diagrams the phase transition is illustrated as a simple line but in a pressure-density diagram it is defined to be an area which does not physically exist. Theoretically, the transition can occur under conditions below the critical pressure and the critical temperature. Mathematically, it is constrained to the conditions under which the cubic EoS provides three real solutions.

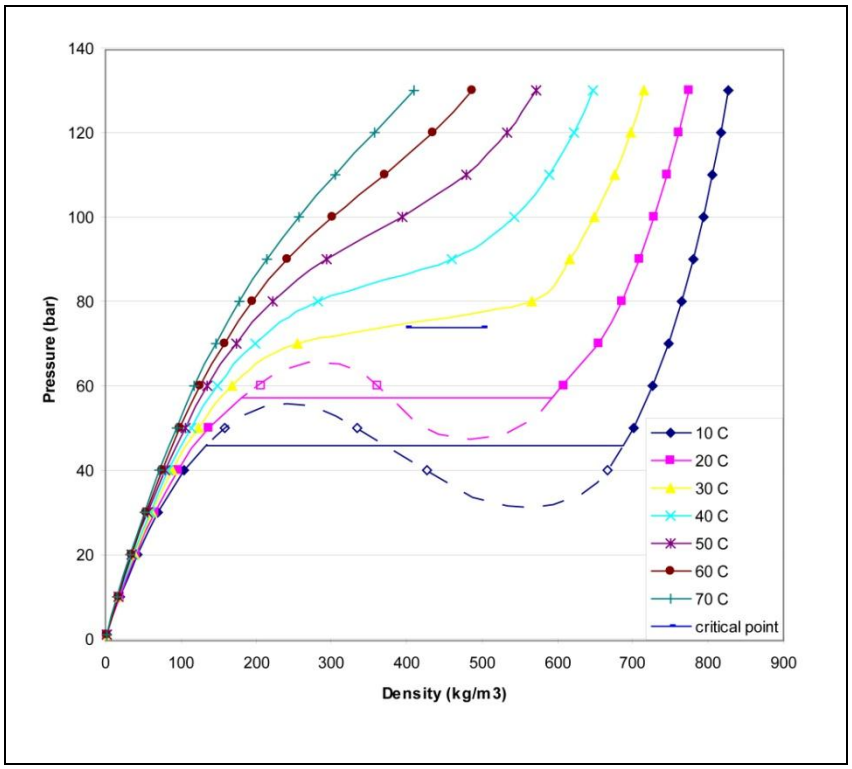

Figure 2.5: Illustration of the P-V-T relationships of pure CO_2 calculated with the Redlich-Kwong EoS. Solid symbols represent 'actual' values and empty symbols represent 'theoretical values. See further information in the text about the phase change calculation. Note that the curve which describes the 30°C density-pressure relationship is at higher pressure than the assumed critical density and has only one solution, not three. This is a clear example for the inaccuracy of this EoS in the vicinity of the critical point. The sine-shaped dashed curves which illustrate the phase transition are interpreted and the hinges are assumed.

The density of CO_2 dependent on pressure and temperature can then be calculated with appropriate software (Excel, MatLab) over the range of conditions of interest. Figure 2.4 shows the density of CO_2 for temperatures between 10°C and 70°C and pressure up to 130 bar with the Redlich-Kwong EoS. The critical point of CO_2, the *T*/*P* condition where CO_2 is (theoretically) present in three of the four possible phases (gaseous, liquid, supercritical) is approximately at 31.1°C and 73.8 bar. On the phase diagram the real critical pressure is marked by a blue line whereas the critical density is unknown (the NIST-website provides a critical density of 467.6 kg/m3 calculated with the Span and Wagner EoS (Span & Wagner 1996)). The inaccuracy of the Redlich-Kwong EoS in the vicinity of the critical point is

illustrated by the fact that the 30°C curve goes above the line which defines the area of the critical pressure/density.

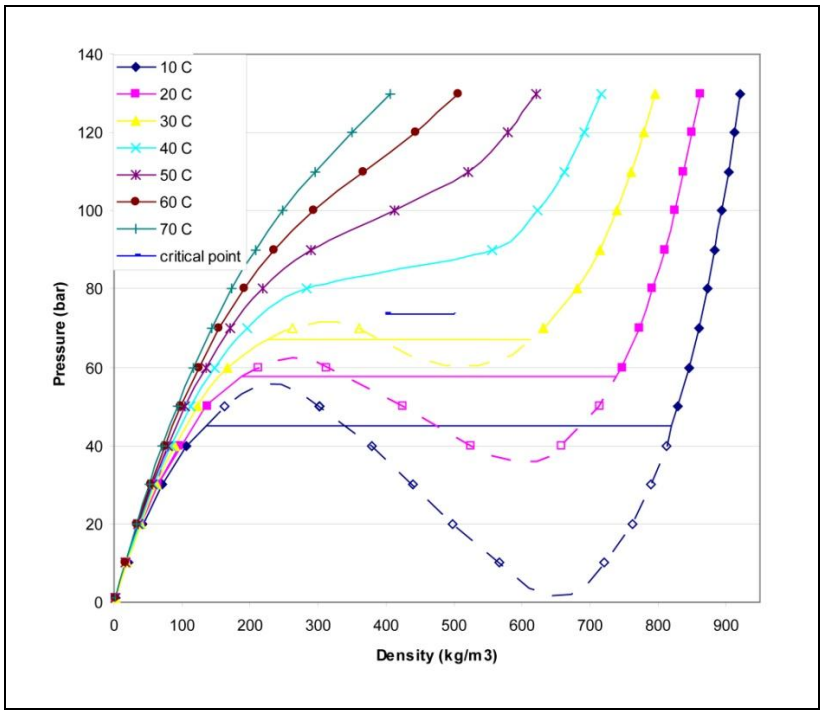

Figure 2.6: Illustration of the P-V-T relationships of pure CO_2 calculated with an improved Redlich-Kwong EoS based on new coefficients implemented by Spycher et al. (2003). Solid symbols represent 'actual' values and empty symbols represent 'theoretical values and the sin-shaped dashed curves whose illustrate the phase transition are drawn by hand and the hinges are assumed. Note that the curve which describes the 30°C density-pressure relationship is just below the critical pressure, an example for how Spycher's coefficients have improved the accuracy of the EoS in the vicinity of the critical point.

Since the critical temperature of CO_2 is ~31.1°C, the 30°C curve should remain below the 'critical area'. Such inaccuracy is a problem pervasive to all '2-parameter' EoS, but improvements, which have been achieved will be discussed later in this chapter, are possible. For temperatures above the critical temperature the EoS provide one density for every pressure. For temperatures below the critical temperature an appropriate EoS should provide either one or three solutions, dependent on the pressure. If there are three results, the lower density is the gas

density and the high density is the liquid density for the same pressure; in other words, the equation defines a phase jump with an instantaneous density increase due to the transformation of gas to liquid. The two sides of the half-circle, the saturated gas line and the saturated liquid line, are one vapour pressure line in a temperature-pressure phase diagram. The intermediate density, which is only mathematically important, is usually discarded.

It can be seen on Fig. 2.4 and Fig. 2.5 that the two phase solution occurs over a wide range of pressure/temperature conditions. The range is not only dependent on the EoS itself but also on the value of the parameters chosen for the EoS (Fig. 2.5 which shows data calculated with a Redlich-Kwong EoS but with modified coefficients, will be introduced further down. The diagram is presented here to show the diversity of the data).

One method of determining which of the two solutions is 'true' and which one is theoretical can be achieved by comparing the 'work done' (*w1*) for the condensation and the 'work done' (*w2*) along a path depicted by the EoS itself (e.g. Adamson 1979). Work, which is defined by the first law of thermodynamic for a reversible process in a closed system, can be expressed as:

$$w1 = P(V_G - V_L) \qquad (64)$$

By differentiating the Redlich-Kwong EoS between the volume of gas and liquid *w2* can be obtained:

$$w2 = RT \cdot \ln\left(\frac{V_G - b}{V_L - b}\right) + \frac{a}{T^{1/2} b} \ln\left(\frac{(V_G + b)V_L}{(V_L + b)V_G}\right) \qquad (65)$$

Figure 2.6 illustrates the change from liquid to gas phase as a function of pressure and 'work-ratio' for different temperatures. The phase change is defined to occur where *w1* and *w2* are equal. If *w1* is bigger than *w2*, the root which provides the high density is true and CO_2 is present as a liquid phase. If *w1* is smaller than *w2*, the low density root is true and CO_2 is present as a gas phase.

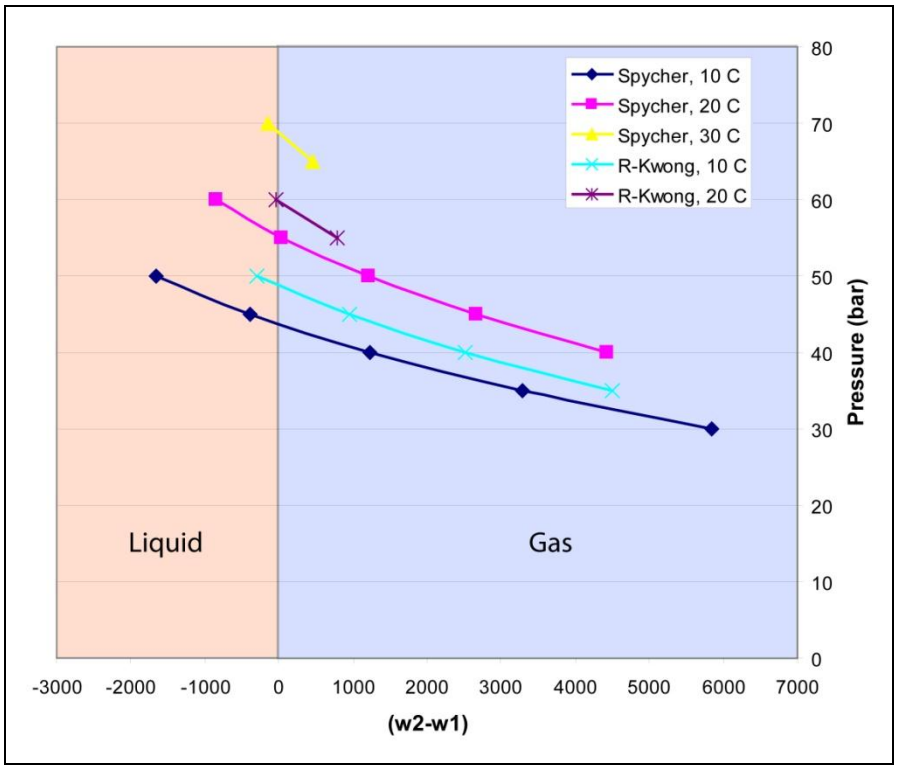

Figure 2.7: Illustration of the phase change from gas and liquid. The vertical line (where *w*1 and *w*2 are equal) defines the pressure at which the phase transition occurs. See text for more information.

Numerical implementation

All thermodynamic properties are connected by the integrated EOS algorithms. Figure 2.7 (adopted from Han & McPherson 2008) shows this interrelation graphically. It also illustrates how errors which are always present, multiply due to the several interrelated calculation steps. For example the calculation of the mole fraction is clearly affected by all the uncertainties which influence the fugacity

coefficient. As Han and McPherson pointed out, interrelated errors can cause different results if different EoS are compared. Although their study used models which were chosen to present the differences as clearly as possible, their conclusions are certainly generally consistent.

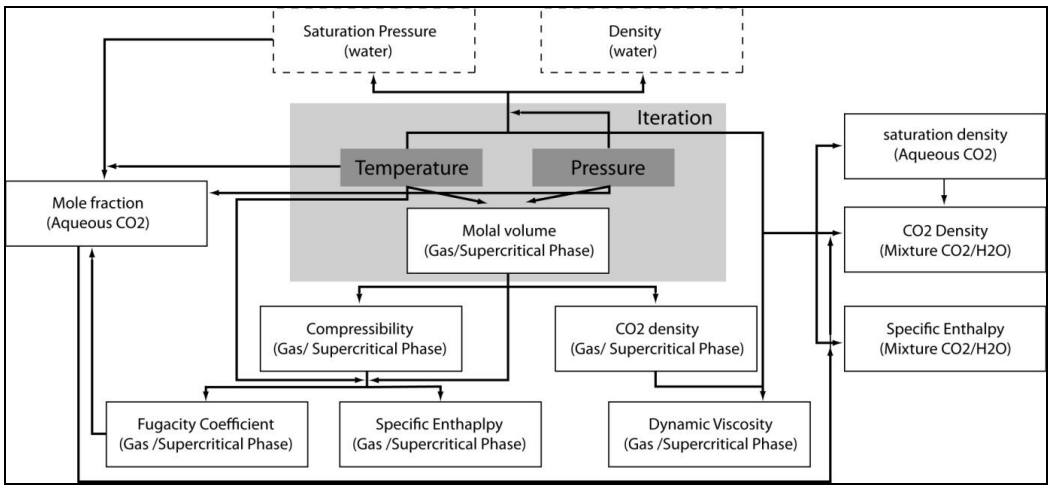

Figure 2.8: Schematic representation of the interrelation of parameters of a modified Redlich-Kwong EoS presented by Han and McPherson (2008). The boxes with dotted and solid lines express the thermodynamic properties of water, mixture (CO_2/H_2O), and separate-phase CO_2. Arrows indicate the direction of the input parameters for the subsequent calculation of thermophysical properties. The box with grey colour shows the location where the primary variables are switched. The idea of the figure in this context is to provide an overview of how different parameters are connected and dependent on each other.

2.2.3 New Redlich-Kwong coefficients for CO_2

Whereas the original Redlich-Kwong EoS has coefficients independent of pressure and temperature, many Redlich-Kwong EoS modifications assume that the coefficient *a* is dependent on temperature (e. g. Soave (1972)). Additionally, as Kerrick and Jacobs (1981) pointed out, 'the assumption of isothermal invariance of *a* with volume will introduce an error in the fugacity coefficients (…)'. Considerations concerning the coefficient b have been simpler. The coefficient *b* is usually assumed to be independent of *P* and *T* and can be fixed for a component in order to obtain an

a which is then dependent on temperature or temperature and pressure and yields the best fit to experimentally derived gas properties. This is a simplification; *b* should be temperature and pressure dependent (Vera & Prausnitz 1972; Jueza 1966) and appropriate modifications of Redlich-Kwong have been developed (e. g. Touret & Bottinga, 1979). Kerrick and Jacobs (1981) describe the choice of *b* to be a compromise between the following: Low *b* values yield a complex *a* versus volume curve whereas high *b* values yield steep *a* versus volume curves at high pressures. In other words, the choice of *b* depends on the equation itself and the *b* which yields the simplest *a*-function will be chosen.

Spycher et al. (2003) used the Redlich-Kwong EoS with an intermolecular attraction coefficient *a*, which is temperature dependent, and a non-temperature dependent repulsion coefficient *b*. They fitted the parameters to available P-V-T data for pure CO_2 (Span & Wagner 1996) and to a broad range of experimental derived data. Their approach has been calibrated and seems to have produced consistent results for temperatures between 283°K and 380°K and pressures up to 600 bar.

Spycher et al. (2003) proposed the following parameters:

$$a_{CO2} = 75400000 - 10000T(K) \qquad (66)$$

$$b_{CO2} = 27.8 \qquad (67)$$

This is an important improvement to the traditional temperature independent Redlich-Kwong coefficient *a*. Fig. 2.8 shows the density of CO_2 for three temperatures (10°C, 30°C and 70°C) calculated with the 'traditional' Redlich-Kwong EoS and the Redlich-Kwong EoS with the Spycher coefficients. It can be seen that the disparities, especially for higher pressures and in the vicinity of the critical point, are significant.

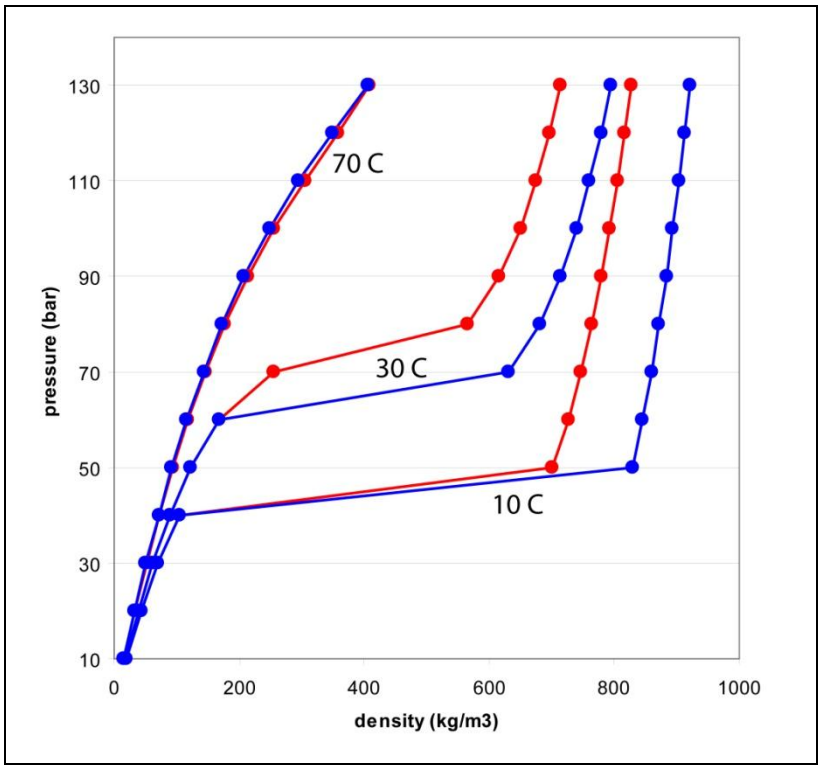

Figure 2.9: Illustration of P-V-T relationships calculated with the Redlich-Kwong EoS (red) and the Redlich-Kwong EoS with modified coefficients (Spycher et al. 2003, blue).

The modification of the coefficients by Spycher et al. (2003) is what Kerrick and Jacobs (1981) called an 'arbitrary' equation. With the modifications, the Redlich-Kwong equation is only applicable for CO_2 and only valid for certain temperature and pressure conditions. The advantage of the modification is that it produced the density and volume of CO_2 more accurately of the temperature and pressure conditions which are relevant for hypothetical subsurface carbon storage projects.

2.2.4 Alternative EoS

There have been numerous modifications of the Redlich-Kwong EoS to improve the accuracy by turning some or all of the parameters into temperature dependent variables, typically as functions of T_r. In general, modified Redlich-Kwong EoSs can be divided into those which have adjustments of the attractive or the repulsive term

and those with adjustments of both terms. One of the earliest modifications of the attractive term, the Soave modification, has already been introduced. Another famous EoS modification of the same kind was published by Peng and Robinson (1976). Their modification of the attractive term is equally simple as Redlich-Kwong but reproduces the liquid-vapour boundary much more accurately. An example for the adjustment of the repulsive term is the Carnahan and Starling modification (1972). Kerrick and Jacobs (1981) used this modification of the repulsive term and they adjusted the attractive term to a form in which the coefficient 'a' is additionally pressure and temperature dependent. Other well-known Redlich-Kwong modifications were presented and published by Graboski and Daubert (1978), Zudkevitch and Joffe (1970) and Stein (1982).

Eclipse300, the reservoir engineering software that has been used for this study offers a choice of four EoS. These are Redlich-Kwong, Soave-Redlich-Kwong, Peng-Robinson and Zudkevitch-Joffe-Redlich-Kwong. The latter is being ignored here because it requires two coefficients which are multiplied with Redlich-Kwong parameters *a* and *b* and act as a temperature correction. Figure 2.9 shows density data calculated with these EoS and shows how extreme the variations are. The data calculated by the Redlich-Kwong EoS with Spycher parameters, which were fitted to the Span & Wagner EoS (Span & Wagner 1996), are included and can be seen as the 'most realistic' result (see previous chapter).

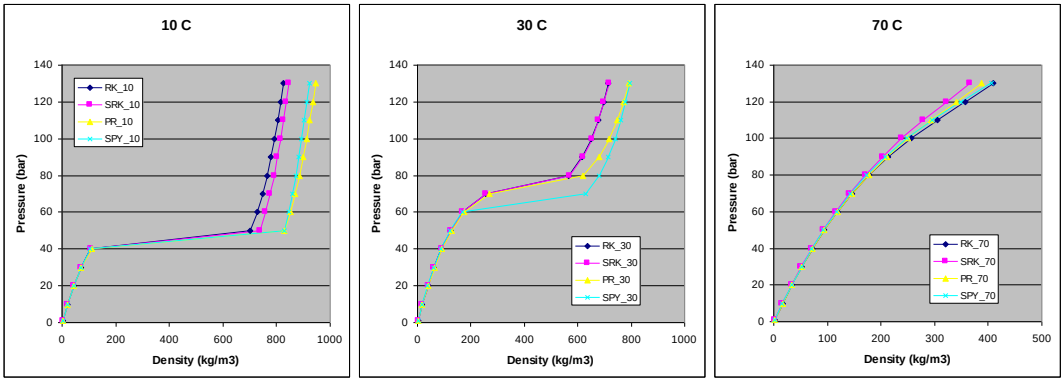

Figure 2.10: Illustration of P-V-T relationships calculated with different EoS which can be chosen in the Eclipse software. Note the dramatic variations at higher pressures and lower

temperatures. Blue – Redlich-Kwong EoS; pink – Redlich-Kwong-Soave EoS; yellow – Peng-Robinson EoS; green – Redlich-Kwong EoS with Spycher coefficients.

Instead of solving the EoS independently a general form is proposed by the Eclipse user manual. The general cubic version of the 2-parameter EoS can be written as:

$$Z + E_2 Z^2 + E_1 Z - E_0 = 0 \qquad (68)$$

with

$$Z = \frac{PV}{RT} \qquad (69)$$

$$E_2 = (m_1 + m_2 - 1)B - 1 \qquad (70)$$

$$E_1 = A - (m_1 + m_2 - m_1 m_2)B^2 - (m_1 + m_2)B \qquad (71)$$

$$E_0 = -[AB + m_1 m_2 B^2 (B + 1)] \qquad (72)$$

The coefficients *m1* and *m2* are defined for the different EoS (Redlich-Kwong: m_1=0, m_2=1; Soave-Redlich-Kwong: m_1=0, m_2=1; Peng-Robinson: m_1=1+$2^{0.5}$, m_2=1-$2^{0.5}$) and *A* and *B* can be calculated for every EoS. Note here that this relatively simple way of solving the EoS is only possible because they are all based on the same polynomial function.

More recent EoS do not follow the polynomial of the 2-parameter EoS. One of the currently most famous EoS is the one introduced by Span and Wagner (1996). Their equation predicts the thermodynamic properties of CO_2 (and only of CO_2) accurately for pressures between 0.1-800 MPa and temperatures between 273.15-800°K, including a high accuracy in the near-critical region. The equation is mathematically

complex and is more difficult to solve than the traditional 2-parameter EoS. The fluid properties calculated with the Span & Wagner EoS are so far the state of the art over such a broad range of temperature and pressure conditions. And indeed, by comparing their results with results calculated by a 2-parameter EoS and applying these results on a simulated CO_2 storage operation, the differences are significant (Han & McPherson 2008).

3 Simulation of pressure accumulation in the vicinity of a well during CO_2 injection into brine filled porous media

3.1 Introduction

3.1.1 Introduction to the problem

If CO_2 is injected into a confined reservoir, the average pressure is highest at the end of the injection period. Whether the local pressure, i.e. the pressure in the vicinity of the injection well, is also highest at the end of the injection period is dependent on the injection rate and on the reservoir properties. If, for example, the permeability is low the pressure could theoretically be highest at the beginning of the injection in the vicinity of the injection well. If the aquifer is 'open', no major average pressure increase is expected, the highest pressure will occur in the vicinity of the injection at the beginning of the injection. Various research studies have been conducted to evaluate the long term pressure development related to CO_2 injection into saline aquifers (e.g. van der Meer & van Wees 2006; Birkholzer et al. 2009). However, there has been comparatively little numerical work involving the parameters which affect the pressure in the vicinity of the injection well. In order to avoid rock fracturing during any kind of injection into permeable rocks, the injection rate has to be kept low at the beginning. A better understanding of injection pressure modelling will increase the confidence of designing CO_2 injection plans and will help to make CO_2 sequestration safer.

The injection of CO_2 into brine filled porous media will lead to an increase of the fluid pressure. If the pressure increases, rock stability will be decreased and fluid pathways may open and compromise the storage operation. In order to avoid this scenario, two investigations have to be conducted: Firstly, the fracture pressure has to be determined and secondly, an accurate simulation of the pressure increase in the vicinity of the injection well has to be performed. These two parameters can be used to help critically evaluate a CO_2 injection scenario which otherwise might be risky or inefficient.

The aim of this study is to improve the understanding of these two complex issues that help to guarantee a safe CO_2 injection process. The theoretical determination of the fracture pressure will be reviewed and the pressure build up in the vicinity of the injection well will be simulated with reservoir engineering software. Special focus lies on the impact of varying temperature and salinity and the mutual dissolution of H_2O and CO_2 on the simulated injection pressure.

3.1.2 Parameters determining the pressure increase in the vicinity of the injection well

Several parameters have major or minor effects on the pressure buildup. These parameters can be approximately divided into two groups:

1. Parameters concerning technical reservoir engineering factors. These parameters can be manipulated directly by the engineer in order to guarantee a safe and efficient injection process. Examples are injection rate or the length of the well perforation.

2. Physical and chemical parameters concerning fluid and rock properties. These parameters are usually not manipulated by the engineer because they are derived directly from interactions between the 'CO_2 – brine – reservoir rock' system.

Although technical parameters are important and their adjustments are crucial for safe CO_2 injection they are not taken into account in this study. The physical and chemical parameters can be interpreted as two important processes that control the pressure increase and these include:

- Single and two phase fluid flow: The fluid flow of a CO_2 – brine system is the major mechanism that determines the pressure accumulation. Key parameters include fluid density, rock permeability, viscosity, relative permeability, rock compressibility, capillary pressure, salinity and temperature.

- Mutual dissolution of CO_2 and brine: CO_2 is relatively soluble in brine and its impact on pressure development may be important. H_2O is less soluble in CO_2 and this process has no significant effect on the pressure development.

- Factors including the simulation setup and numerical codes that are used for fluid flow simulation with reservoir engineering software are also important. Possible parameters are the size of the cells or the choice of a radial or cubic model. These affects are different from the others because they do not influence the injection process directly but they have a significant impact on the simulation results. They occur when fluid flow is simulated and do not derive from physical or chemical properties of the fluid – rock system.

It is apparent that multiple processes interact with each other. Some parameters, for example the mutual dissolution of a $CO_2 – H_2O$ water system, could be deactivated in a simulation whereas other parameters, such as grid effects (e.g. numerical dispersion), will always occur (although the severity of their effects may vary with cell size).

3.1.3 Pressure increase in the vicinity of the injection well

In the literature, numerical pressure simulations in the vicinity of a CO_2 injection well are rare. This is mainly because fluid flow around the injection well is not clearly understood yet and its simulation is difficult and requires a careful interpretation of the results.

If CO_2 is injected into porous media, it will displace the *in situ* fluid. When injection starts, brine in the vicinity of the injection well will be displaced almost instantaneously by an expanding bubble of CO_2 (Chadwick et al. 2009). The size of the CO_2 bubble and its rate of expansion mainly depend on the injection rate, the temperature of the injected CO_2 and the pressure of the reservoir. Additionally, the pressure will rise because of the relative permeability of CO_2 which is low at the beginning and increases gradually as the saturation increases (Ukaegbu et al. 2009).

Chadwick et al. (2009) performed a study on pressure increase in the vicinity of the injection well and concluded that it is dependent on formation permeability and injection rate if simulated with a Darcy flow based reservoir simulation software. They conducted their simulations using TOUGH2 software (Pruess et al. 1999). All these aspects are well explained and have been quantified in the literature. An interesting feature in Chadwick's at al. (2009) injection pressure results is a distinct pressure decrease followed by a pressure increase and a subsequent short, erratic pressure profile becoming smoother over time (Fig. 3.1). Unfortunately, this is neither described nor explained although it might be an important issue for the interpretation of the maximum pressure.

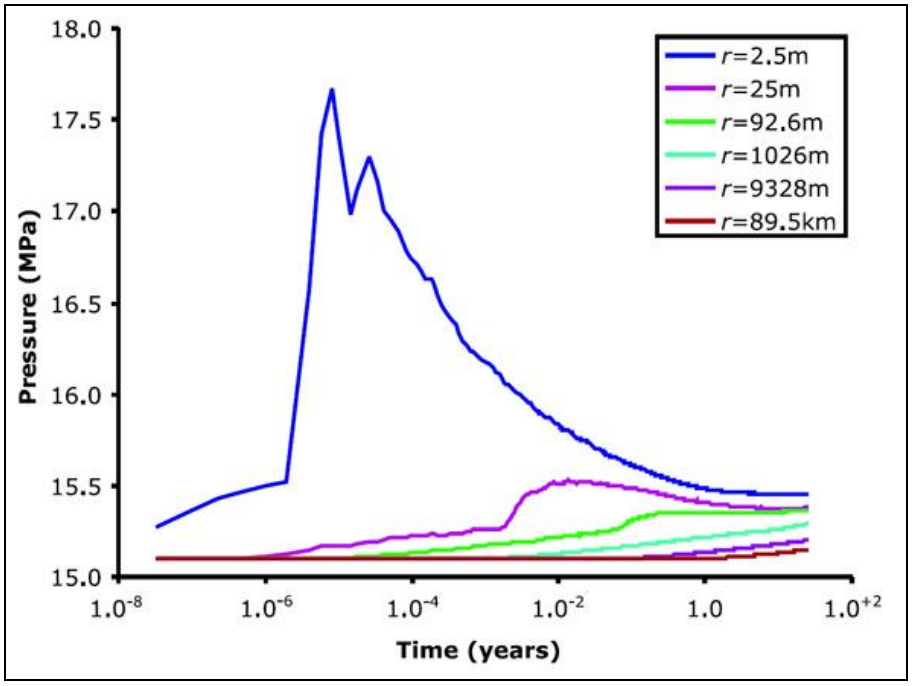

Figure 3.1: Detail of early time pressure responses using logarithmic time-scale (taken from Chadwick et al. 2009). Note the distinct pressure decline and subsequent pressure increase shortly after the maximum pressure as well as the undulations of the pressure profile.

3.1.4 Problem description

This study focuses on two aspects concerning a manageable injection pressure. For determination of the fracture pressure, a review of hydro fracturing and different ways to calculate fracture pressures is presented and finally the most realistic one is chosen and used for the study.

Secondly, by using the reservoir engineering software Eclipse (Schlumberger) a radial model was designed to model the injection pressure. The focus of the model lies on the influence of fluid properties on the injection pressure. The influence of the two parameters, temperature and salinity, on the CO_2 and brine are calculated and used for the simulation. Temperature and salinity were selected because they are often sources of uncertainties for simulations because they can have a significant impact on the fluid properties of both CO_2 and brine (in the case of temperature) or on the properties of brine (in the case of salinity).

A special focus lies on the effect of mutual dissolution on the injection pressure. Mutual dissolution, calculated with Spycher et al. (2003) and Spycher and Pruess (2005), was included in the model to determine, by how much it could reduce the simulated pressure. Since mutual dissolution is dependent on temperature and salinity, sensitivity tests were performed to achieve a better understanding of how dissolution and fluid flow interact.

Finally, the origin of the undulations, illustrated in Chadwick's at al. (2009) pressure profile, are described and discussed. A careful interpretation of those is important to ascertain whether they are real or simulation artefacts and if the latter is likely, do they lead to an underestimation or an overestimation of the pressure.

3.1.5 Introduction to the method

CO_2 injection was simulated with the Eclipse black oil reservoir simulator (E100). In a black oil simulator, the water phase is simulated together with an oil phase and a gas phase. Gas is allowed to dissolve into the oil phase and oil may vaporize into the gas phase. The accurate simulation of a CO_2 injection into brine requires the simulation of the mutual dissolution of CO_2 and brine. To model the dissolution of CO_2 into brine and the evaporation of H_2O into CO_2, brine has to be modeled as the oil phase. The Eclipse reservoir engineering software is based on flow equations introduced in Chapter 2.1.

The accurate interpretation of model results requires a high degree of understanding of the input parameters. Therefore, all fluid properties which were used for the simulation were calculated and the calculation methodology is documented in chapter 3.2. Basic CO_2 properties were calculated with the Redlich-Kwong EoS as described in Chapter 2.2.

Although fluid flow in the vicinity of the injection or production wells is presumably influenced by inertial effects (Mathias et al. 2009), a Forchheimer correction was not taken into account (see chapter 2.1). The numerical simulation of the injection pressure based on Darcy flow is already difficult to simulate and discuss. The Forchheimer flow parameters would have made it even more complicated. Therefore, the attempt to simulate the pressure increase more realistically was sacrificed in favour of a better and clearer understanding of a simpler simulation. If a Forchheimer correction was applied, the modelled pressure increase would be higher.

Several simulations were conducted to study the impact of different parameters on the pressure increase. The ‘base case model’ is the reference model and represents a likely scenario for injection in a 1 km deep, southern North Sea aquifer. The salinity of the ‘base case model’ is 0.15 kg/l which lies in the range of the Triassic Bunter

Sandstone reservoirs (Ketter 1991). To investigate the impact of salinity on the injection pressure, sensitivity models were conducted with pure water ('pure H_2O model') and a salinity of 0.3 kg/l ('0.3 kg/l model'). The temperature of the 'base case model' is 35°C. Two sensitivity tests were conducted to study the impact of varying temperature: A low temperature model with an isothermal temperature of 30°C ('30 C model') and a high temperature model with 40°C ('40 C model'). All models were conducted with and without mutual dissolution of CO_2 and H_2O/brine.

3.1.6 Nomenclature

(Units may vary and are defined in the text).

a	fitted Redlich-Kwong parameter
a_{mix}	Redlich-Kwong parameter (Spycher et al. 2003)
b	fitted Redlich Kwong parameter
b_{mix}	Redlich-Kwong parameter (Spycher et al. 2003)
BHP	bottom-hole pressure
c	compressibility
C_s	solute concentration of sodium chloride
C_c	cohesion
d	stoichiometric number
g	gravity
D	material dependent dissolution coefficient
D_h	hydraulic diffusivity
B	formation volume factor
H'	inverse of the soil compressibility
P	pressure
P_0	reference pressure
P_{c0}	strength coefficient for capillary pressure
P_p	pore pressure
P_l	lithostatic pressure
P_w	fluid pressure

1	P_c	fracture pressure
2	P_{ca}	capillary pressure
3	P_{co}	confining pressure
4	k	permeability
5	K_r	relative permeability
6	K	equilibrium constant
7	K_0	reference equilibrium constant
8	K_m	macroscopic bulk modulus
9	m_{ps}	pore size distribution index
10	m	mass
11	m_l	molality
12	mp	pore size distribution factor
13	M	molar mass
14	r	radius
15	R	universal gas constant
16	R_x	radial extent
17	S	phase saturation
18	S_r	residual phase saturation
19	S^*	effective saturation of the aqueous phase
20	S'	effective saturation of the gas phase
21	t	time
22	T	temperature
23	T_s	tensile strength
24	V	volume
25	V_{ap}	partial molar volume
26	V_w	shear wave velocity
27	w	mass ratio
28	x	CO_2 mole fraction in the H_2O rich phase
29	y	H_2O mole fraction in the CO_2 rich phase
30	z	depth
31	αa	activity
32	α_b	Biot coefficient
33	αp	fitting parameter for capillary pressure

1	β	pore pressure fraction
2	$\Delta\sigma_x$	injection induced horizontal stress
3	θ	angle to the maximum principle stress
4	κ	depth-fracture ratio
5	λ	pore fluid factor
6	μ_f	coefficient of friction
7	μ_v	viscosity
8	v	Poisson's ratio
9	ρ	density
10	σ_1	maximum principle stress
11	σ_2	intermediate principle stress
12	σ_3	minimum principle stress
13	σ_d	differential stress
14	σ_H	maximum horizontal stress
15	σ_h	minimum horizontal stress
16	σ_v	vertical stress
17	σ_n	normal stress
18	σ'_n	effective normal stress
19	σ_w	principle stress away from the borehole
20	τ	frictional shear stress
21	ϕ	angle of the failure envelope
22	ϕ	porosity
23	f	fugacity
24	fc	fugacity coefficient
25	Ψ	salt impact ratio
26	λ_l, G	Lame parameters
27		
28		
29		
30		
31		
32		

3.2 Fluid properties

3.2.1 PVT data predicting the properties of CO_2 and H_2O/brine

The black oil simulator requires direct information about gas and liquid phase properties, such as density, volume, viscosity and compressibility. This chapter reviews the PVT data of CO_2 and H_2O/brine which are used for the simulation. All equations are given in a non iterative form and can be solved with common calculation software (such as Excel or Matlab). Mixtures of the gas and the fluid phase are not yet accounted for.

Density of CO_2

The density and volume of CO_2 is directly calculated by an equation of state (EoS). The black oil simulator does not calculate the CO_2 properties itself but uses PVT tables with the information. CO_2 densities have been calculated with the Redlich-Kwong EoS (Redlich & Kwong 1949) with coefficients '*a*' and '*b*' suggested by Spycher et al. (2003). Fig. 3.2 illustrates the CO_2 properties over the temperature and pressure range of interest for this study. As a comparison, data calculated with the Peng-Robinson EoS (Peng & Robinson 1976) and those taken from the NIST website (calculated with the Span & Wagner EoS; NIST-website) are also presented.

The Span and Wagner EoS is one of the most elaborate equations and the density of CO_2 calculated with it provides an accurate prediction in comparison with the experimental data. The CO_2 densities calculated with the modified Redlich-Kwong EoS are closer to the Span and Wagner densities (relative to the Peng-Robinson EoS) for realistic geological subsurface conditions (35˚C and 100 bar at a depth of 1000 m). If pressure increases, the Peng-Robinson EoS appears to predict the density more accurately.

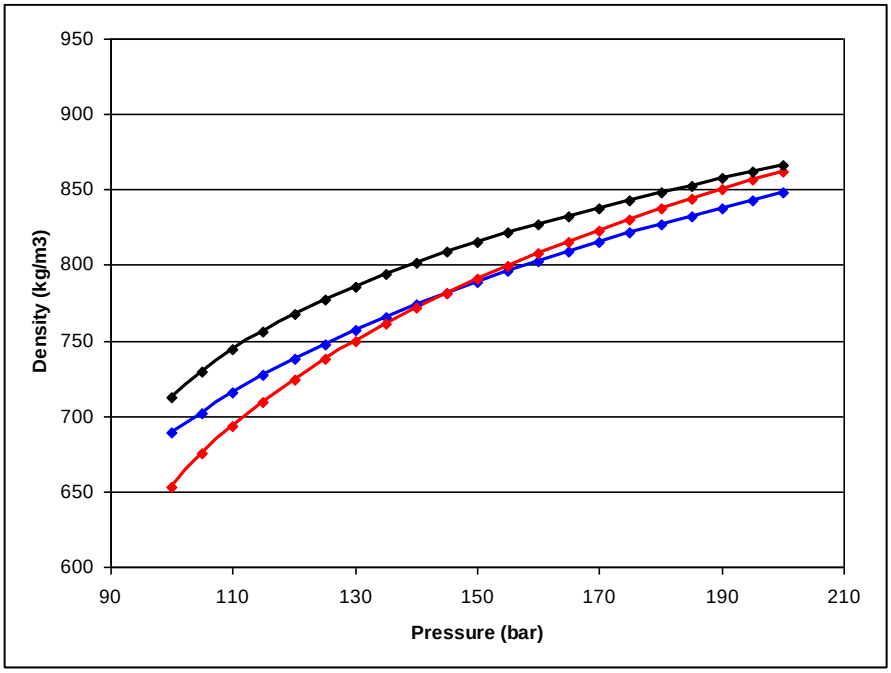

Figure 3.2: Density of CO_2 for a temperature of 35°C calculated with the Redlich-Kwong EoS (with Spycher coefficients, blue) and Peng-Robinson (red). Densities calculated with the Span and Wagner EoS (black) were taken from the NIST website.

Density of H_2O and brine

The density of H_2O was calculated using the approach of Batzle and Wang (1992). H_2O density data taken from the NIST-website are also presented for reference. The estimated uncertainty of the density data ranges from ± 0.001 % to ± 0.02 % in the most important part of the liquid region (Wagner & Pruss 2002; Fig. 3.3). The H_2O densities predicted by Wagner and Pruss (2002) are approximately 0.8 kg/m^3 higher than the Batzle and Wang (1992) data. The impact of pressure on the H_2O density is almost equal under the given temperature and pressure conditions.

Water properties generally do not vary significantly if calculated with different approaches. The differences between the Batzle and Wang (1992) predictions and those predicted by Pruss and Wagner (2002) are small and water properties are not regarded as a major source of uncertainty here.

If salt is added, the density of H_2O will be increased. To calculate the impact of salinity on the density of H_2O, this study uses the Batzle and Wang (1992) approach. Figure 3.4 shows the density of H_2O and brine with a salinity of 0.15 kg/l and 0.3 kg/l. The density increase due to salinity is higher if the salinity is high (Fig. 3.4). The average increase in density of H_2O and brine (0.15 kg/l) is ~108 kg/m^3 and the average density increase of brine (0.15 kg/l) and brine (0.3 kg/l) is 122 kg/m^3. Additionally, the impact of pressure on the density is relatively low for H_2O (4.26 kg/m^3 for a pressure range between 100 and 200 bar). This impact decreases with increasing salinity (3.86/3.12 kg/m^3 for the same pressure range and salinities of 0.15/0.3 kg/l).

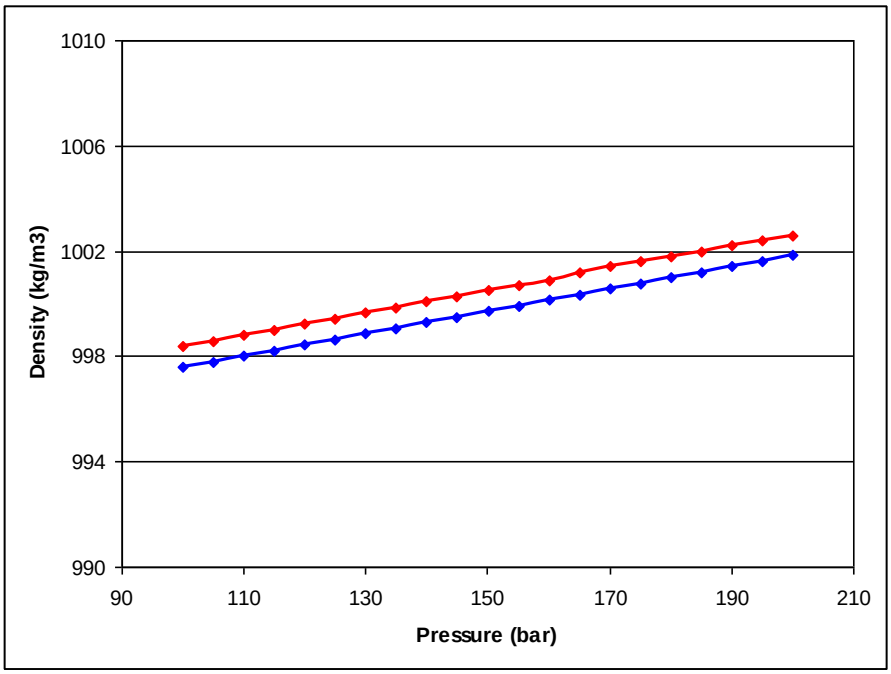

Figure 3.3: Density of H_2O calculated after Batzle and Wang (blue). A more recent study by Pruss and Wagner (red) propose a slightly higher density.

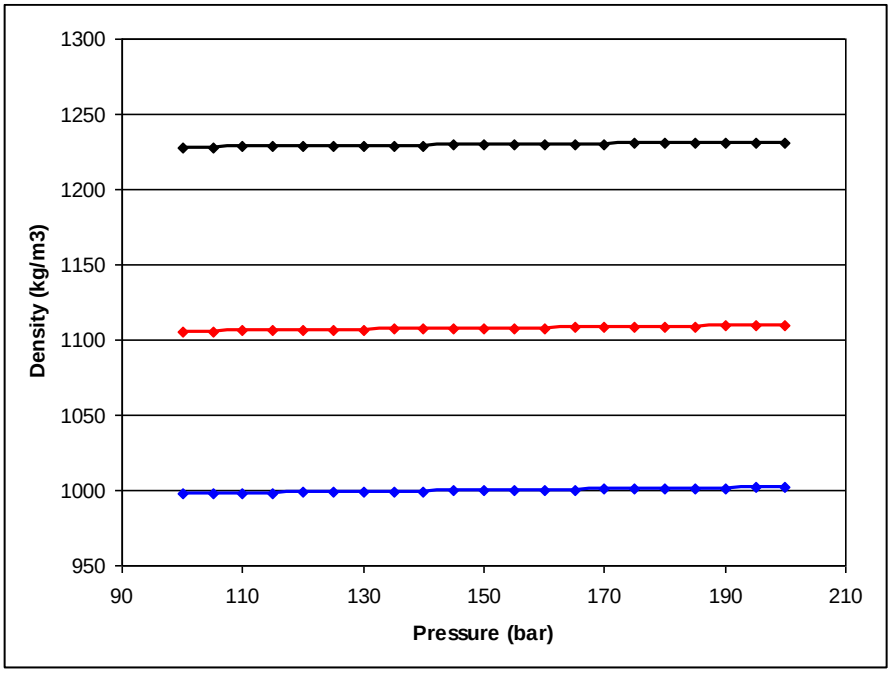

Figure 3.4: Density of H_2O and brine calculated after Batzle and Wang (1992) for salinities of 0 kg/l (blue), 0.15 kg/l (red) and 0.3 kg/l (black).

Viscosity of CO_2 and H_2O/brine

A simple and widely used viscosity correlation is that of Fenghour et al. (1998). The correlation implies that the viscosity of CO_2 is only dependent on density and temperature and that pressure influences viscosity only indirectly (as a parameter controlling the density). By applying linear regression, Mathias et al. (2009) found that for typical conditions used for geological storage of CO_2 (temperature range between 283 and 380˚K), the viscosity is relatively simple to calculate with:

$$\mu_{v-CO2} \approx 16.485 + (0.009487 \cdot \rho_{CO2})^2 - (0.0025939 \cdot \rho_{CO2})^4 + (0.0019815 \cdot \rho_{CO2})^6 \quad (1)$$

The density is in kg/m^3 and the viscosity in µPa·s. Figure 3.5 illustrates the CO_2 viscosity (1 cP = 0.001 µPa·s) calculated from the above equation and the CO_2 viscosity data taken from the NIST-website which were calculated with an original equation implemented by Fenghour et al. (1998). The NIST data predicts a slightly

higher viscosity (between 0.0022 and 0.004 cP) for the given temperature and pressure conditions. Also, the data calculated with the Mathias et al. (2009) approach shows a less convex pressure dependence.

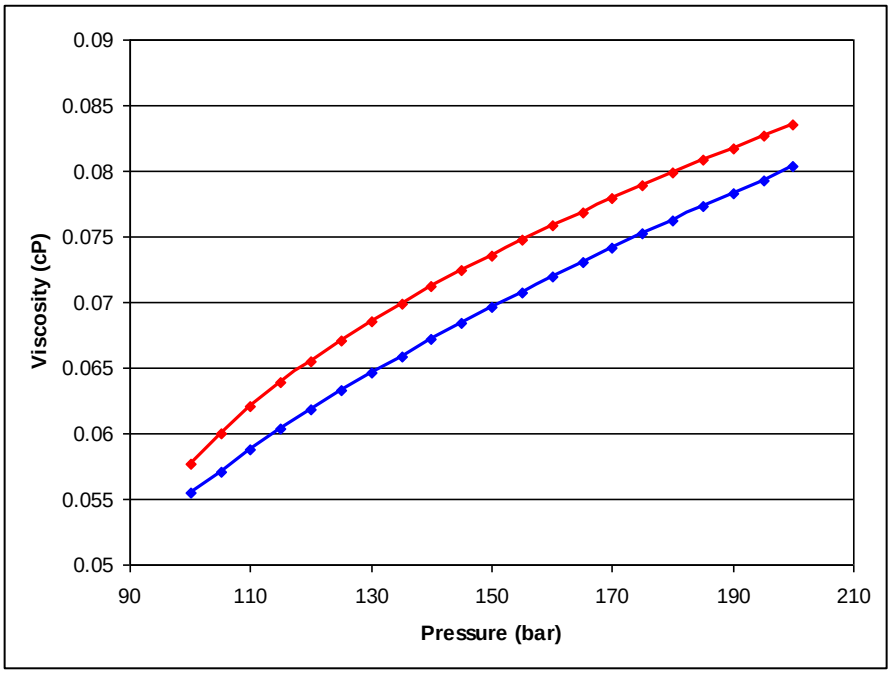

Figure 3.5: Viscosity of CO_2 calculated after Fenghour et al. (1998) (data taken from the NIST website, red). This study uses data calculated with an approximation to Fenghour's equation presented by Mathias et al. (2009) (blue).

To calculate the viscosity of H_2O and brine we used an approximation by Batzle and Wang (1992) of the viscosity relationship of Kestin et al. (1981). H_2O and brine viscosity calculated with their approach is not dependent on pressure. For temperatures below 250˚C the brine viscosity can be calculated by:

$$\mu_{v-brine} = 0.1 + 0.333 \cdot C_s + (1.65 + 91.9 \cdot C_s^{\,3}) \cdot \exp(-(0.42(T^{0.8} - 0.17)^2 + 0.045) \cdot T^{0.8} \quad (2)$$

The temperature is in Celsius, C_s is the salt content in kg/l and the viscosity μ is in cP. Figure 3.6 shows that an increase in salinity increases the viscosity significantly. The relative increase is not constant but increases with increasing salinity (0.32 cP for H_2O to brine (0.15 kg/l) and 0.54 cP for brine (0.15 kg/l) to brine (0.3 kg/l)).

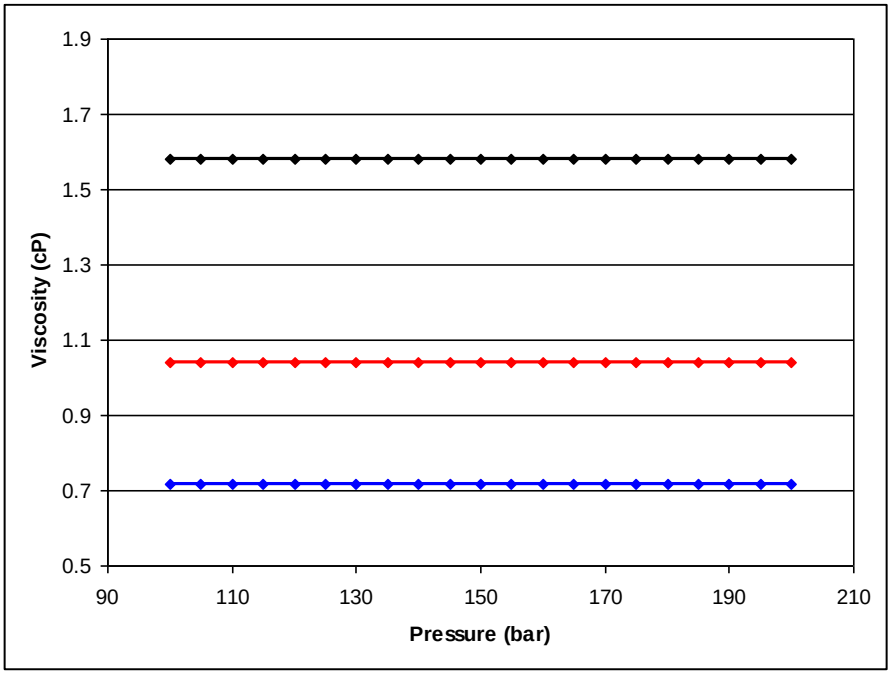

Figure 3.6: Viscosity of H_2O and brine with salinities of 0 kg/l (blue), 0.15 kg/l (red) and 0.3 kg/l (black). Data was calculated with Batzle and Wang's (1992) approximation of Kestin et al. (1981).

Compressibility of CO_2 and H_2O/brine

The black oil simulator E100 does not calculate the CO_2 compressibility. The compressibility is an input parameter and has to be provided as the formation volume factor (B), the volume ratio of CO_2 under reservoir conditions and standard conditions.

E100 defines 'standard condition' to have a temperature of 15.555˚C (60˚F) and a density of 1.0325 bar (1 atm). Figure 3.7 illustrates the B of CO_2 calculated with the Redlich-Kwong EoS with Spycher coefficients) and calculated with the Peng-Robinson EoS. The B of CO_2 is usually relatively small. This is common for all

fluids that are present as a gas phase under standard conditions and present as either a supercritical or a liquid phase under reservoir conditions. The B decreases with increasing pressure which reflects the decreasing volume of CO_2 under increasing pressure. For subsurface conditions (35˚C and 100 bar at a depth of 1000 m), the B calculated with the Redlich-Kwong approach is 0.00015 lower than the B calculated with the Peng-Robinson EoS. With increasing pressure, the Peng-Robinson B decreases relative to the Redlich-Kwong B until they are almost similar at ~ 145 bar. A further increase in pressure leads to a further decrease of the Peng-Robinson B relative to the Redlich-Kwong B.

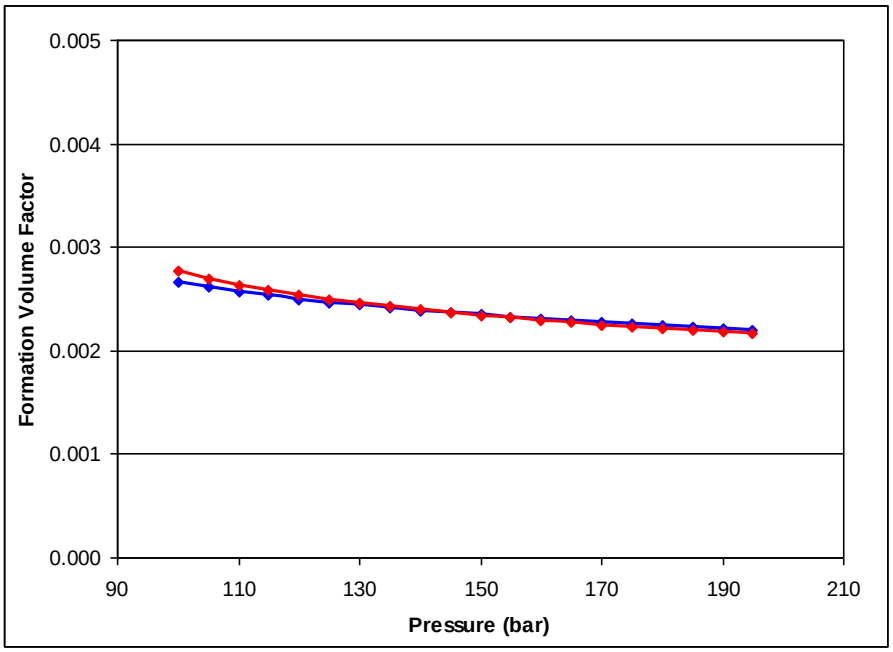

Figure 3.7: Formation volume factor of CO_2. The data derives from volumes calculated with the Redlich-Kwong EoS with Spycher coefficients (blue) and the Peng-Robinson EoS (red).

H_2O and brine compressibility also has to be converted to the B. Since H_2O is hardly compressible, even under extreme conditions, and H_2O is present as a liquid phase under both standard and reservoir conditions, the B of H_2O and brine barely changes. Figure 3.8 illustrates the B for water and brine. Because the B is the ratio of two densities, only parameters which have an impact on the relative ratio of those two

densities can change the B. As illustrated in Fig. 3.8, pressure only has a minor impact on H_2O density and the influence on the B is small. Therefore, the B has relatively constant values.

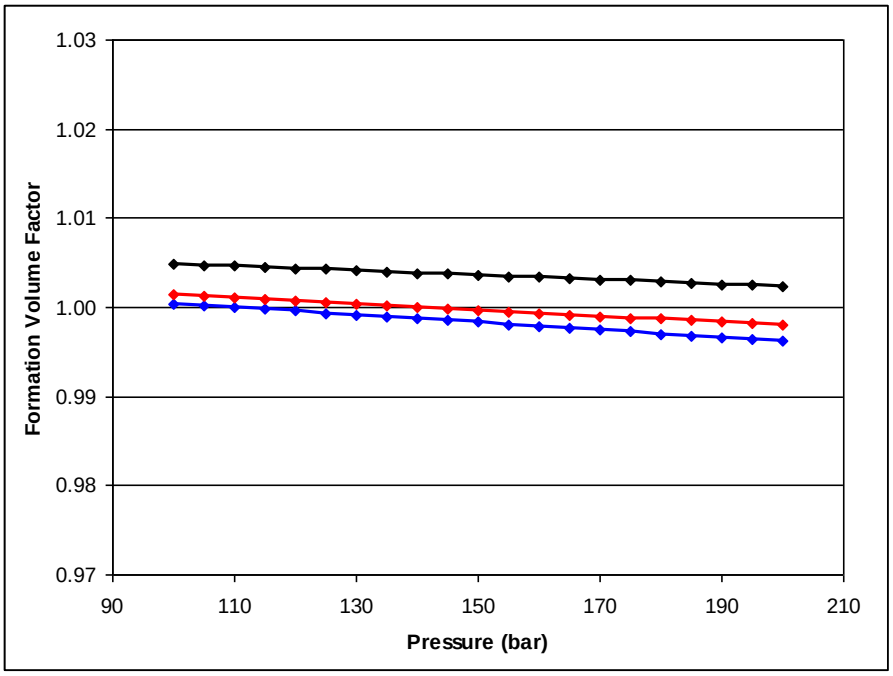

Figure 3.8: Formation volume factor of H_2O and brine with salinities of 0.0 kg/l (blue), 0.15 kg/l (red) and 0.3 kg/l (black) calculated with Batzle and Wang (1992).

For pure water, pressures above ~110 bar result in a relative compression whereas lower pressures lead to a volume increase of H_2O under reservoir conditions and constant temperature. Salinity alters the density of the liquid phase significantly but only has minor impact on the relative density ratio. Generally, salinity increases the B. With a fixed temperature of 35˚C, a salinity of 0.15 kg/l leads to a volume increase below 145 bar and a compression at pressures greater than 145 bar. Under the pressure and temperature ranges suggested for this study and a salinity of 0.3 kg/l, brine volume in the rock formation is always greater than the brine volume under standard conditions.

3.2.2 Mutual dissolution of CO_2 and H_2O/brine

The solubility model presented by Spycher et al. (2003) describes the mutual dissolution of CO_2 and H_2O (and a possible presence of salinity; see Spycher et al. (2005)) at equilibrium conditions. In order to represent the K values for the transitions of liquid H_2O to H_2O in the CO_2 rich phase and of gaseous/supercritical CO_2 in the H_2O rich phase more accurately, concentration is replaced by activities (a_a - for the aqueous phase) and fugacity (f - for the gaseous/supercritical phase). The constants (K) for the dynamic equilibrium of the reaction can be written as:

$$K_{H2O} = f_{H2O(g)} / a_{a-H2O(aq)}$$
$$K_{CO2} = f_{CO2(g)} / a_{a-CO2(aq)} \qquad (3)$$

where the fugacity, dependent on the partial pressure, is (Prausnitz et al. 1986)

$$f_{(i)} = f_{c-(i)} y_{(i)} P \qquad (4)$$

f_c is the fugacity coefficient, y is the mole fraction of the component, P the pressure in bar and the subscript, i, denotes the component. Values for K derive from K_0, the reference equilibrium constant and a temperature and pressure correction:

$$K = K_0 \exp\left(\frac{(P - P_0)V_{ap}}{RT}\right) \qquad (5)$$

P is the pressure in bar and P_0 is the reference pressure, here set to 1 bar. V_{ap} is the partial molar volume over the pressure gradient. K_0 is the equilibrium constant at reference pressure, calculated with regression coefficients for particular temperatures (see Spycher et al. 2003). Two K_0 values for CO_2 have to be distinguished: One for

liquid phase CO_2 at temperatures between 12 and 31˚C and a second value for gaseous/supercritical CO_2 at temperatures between 31 and 110˚C.

The target of these equations is to calculate the maximum mole fraction of the CO_2 in the H_2O rich phase and the mole fraction of H_2O in the CO_2 rich phase. The auxiliary parameter is the fugacity (Eq. 4) and its dependence on mole fraction and pressure. By substituting fugacity in equation (4), K_{H2O} in equation (3) may be expressed in terms of $y(H_2O)$, the mole fraction of H_2O in the CO_2 rich phase:

$$K_{H2O} = \frac{f_{c-H2O} y_{H2O} P}{a_{a-H2O}} \qquad (6)$$

and for $y(CO_2)$, the mole fraction of CO_2 in the CO_2 rich phase:

$$K_{CO2} = \frac{f_{c-CO2} y_{CO2} P}{a_{a-CO2}} \qquad (7)$$

For a system with CO_2 and H_2O as the only two components the following relationship is obvious:

$$y_{H2O} + y_{CO2} = 1 \qquad (8)$$

To bring the mole fraction to the K value calculation in one equation, (6) is substituted into (5).

$$y_{H2O} = \frac{K_{0(H2O)} a_{a-H2O}}{f_{c-H2O} P} \exp\left(\frac{(P - P_0) V_{ap(H2O)}}{RT}\right) \qquad (9)$$

The solubility of H_2O in CO_2 is relatively low at temperature and pressure conditions considered for carbon sequestration operations with temperatures below 100°C and pressures which may reach several hundred bar (Spycher et al. 2003). Therefore, Raoult's law can be applied for the activity of H_2O in the aqueous phase $\alpha_a(H_2O)$ which becomes equal to its mole fraction in the aqueous phase $x(H_2O)$. The H_2O activity vanishes in equation (9) and can be written as:

$$a_{a-H2O} = x_{H2O} = 1 - x_{CO2} \qquad (10)$$

To calculate the CO_2 fraction in the H_2O rich phase, equation (7) needs to be substituted into equation (5):

$$y_{CO2} = \frac{K_{0(CO2)} a_{aCO2}}{f_{c-CO2} P} \exp\left(\frac{(P - P_0) V_{ap(CO2)}}{RT} \right) \qquad (11)$$

In order to calculate CO_2 mole fraction in the aqueous phase $x(CO_2)$ and according to the fact that CO_2 activity equals an activity coefficient multiplied by its molality, a_{CO2} can be written as (Spycher et al. 2003):

$$a_{a-CO2} = 55.508 \cdot x_{CO2} \qquad (12)$$

As a second adjustment, equations (11) and (12) need to be connected. This can be achieved by:

$$y_{CO2} = 1 - y_{H2O} \qquad (13)$$

The new equation is:

$$x_{CO2} = \frac{f_{c-CO2}(1-y_{H2O})P}{55.508K_{0(CO2)}} \exp\left(-\frac{(P-P_0)V_{ap(CO2)}}{RT}\right) \quad (14)$$

The fugacity coefficient can be calculated as (e.g. Prausnitz et al. 1986):

$$\ln(f_c) = \ln\left(\frac{V}{V-b_{mix}}\right) + \left(\frac{b_k}{V-b_{mix}}\right) - \left(\frac{2\sum_{i=1}^{n} y_i a_{ik}}{RT^{1.5} b_{mix}}\right) \ln\left(\frac{V+b_{mix}}{V}\right) + \left(\frac{a_{mix} b_k}{RT^{1.5} b_{mix}^2}\right)\left[\ln\left(\frac{V+b}{V}\right) - \left(\frac{b_{mix}}{V+b_{mix}}\right)\right] - \ln\left(\frac{PV}{RT}\right) \quad (15)$$

The two mixing coefficients a_{mix} and b_{mix} can be calculated by the standard mixing rule (e.g. Prausnitz et al. 1986):

$$a_{mix} = \sum_{i=1}^{n}\sum_{y=1}^{n} y_i y_j a_{ij} \quad (16)$$

$$b_{mix} = \sum_{i=1}^{n} y_i b_i \quad (17)$$

For a binary H_2O-CO_2 system, equation (16) and (17) become:

$$a_{mix} = {y_{H2O}}^2 \cdot a_{H2O} + 2 \cdot y_{H2O} \cdot y_{CO2} \cdot a_{H2O-CO2} + {y_{CO2}}^2 \cdot a_{CO2}$$

$$b_{mix} = y_{H2O} \cdot b_{H2O} + y_{CO2} \cdot b_{CO2} \quad (18)$$

The input values $y(H_2O)$ and $x(CO_2)$, which are required to calculate the fugacity coefficient, are the output values of equation (11) and (14). Hence, the equations have to be solved simultaneously by an iterative scheme. In order to avoid that,

Spycher et al. (2003) proposed a simplification. Since the amount of dissolved H_2O in CO_2 ($y(H_2O)$) is relatively low it might be neglected for the fugacity calculation so that $y(H_2O)$ becomes 0 and $y(CO_2)$ becomes 1. Although this is a massive simplification, Spycher et al. (2003) claim that 'the strongly non-ideal mixing behaviour is still captured …' by the other coefficients which are used to calculate the fugacity coefficient and which are fitted to reference PVT data.

In order to calculate $y(H_2O)$ and $x(CO_2)$, equations (11) and (14) can be solved directly by replacing

$\frac{y_{H2O}}{(1-x_{CO2})}$ and $\frac{x_{CO2}}{(1-y_{H2O})}$ with A and B respectively. The mole fraction of H_2O in the CO_2 rich phase can now calculated with:

$$y_{H2O} = \frac{(1-B)}{(1/A-B)} \qquad (19)$$

The mole fraction of CO_2 in the H_2O rich phase is:

$$x_{CO2} = B(1-y_{H2O}) \qquad (20)$$

Influence of salt on the mutual dissolution of CO_2 and H_2O/brine

Salinity reduces the mutual dissolution of CO_2 and H_2O. Spycher and Pruess (2005) extended the dissolution model of Spycher et al (2003) by using a salinity correction. For further information the original paper should be consulted because only a brief summary of the correction is presented here.

The main adjustment of the model uses the parameter Ψ which determines the ratio of the molality of CO_2 in H_2O and the molality of CO_2 in brine. Duan and Sun (2003) introduced a method which simultaneously fitted a Pitzer ion-interaction model and a

thermodynamic equilibrium formulation to both H_2O and brine as a function of pressure and temperature. If halite is the only component in dissolution Ψ has the following form:

$$\ln(\Psi) = 2 \cdot \lambda \cdot m_{l-Na} + \xi \cdot m_{l-Cl} \cdot m_{l-Na} \quad (21)$$

with

$$\lambda = -0.411370585 + 6.07632013 \times 10^{-4} \cdot T + 97.5347708 / T - 0.0237622469 \cdot P / T + 0.0170656236 \cdot P /(630 - T) + 1.41335834 \times 10^{-5} \cdot T \cdot \ln(P) \quad (22)$$

and

$$\xi = 3.36389723 \times 10^{-4} - 1.9829898 \times 10^{-5} \cdot T + 2.1222083 \times 10^{-3} \cdot P / T - 5.24873303 \times 10^{-3} \cdot P /(630 - T) \quad (23)$$

Temperature is in $^{\circ}K$, pressure in bar and m_l is molality. The CO_2 molality in H_2O ($ml_{\text{-}CO2}$) can be calculated with the mole fractions:

$$m_{l-CO2} \frac{x_{CO2} \cdot 55.508}{x_{H2O}} \quad (24)$$

So that the molality of CO_2 in brine ($m°_{l\text{-}CO2}$) can be written as:

$$m°_{l-CO2} = m_{l-CO2} \cdot \Psi \quad (25)$$

By converting the molality of CO_2 and salt to mole fractions with:

$$x_{CO2} = \frac{m_{l-CO2}}{(d \cdot m_{salt} + 55.508 + m_{l-CO2})} \quad (26)$$

and

$$x_{salt} = \frac{d \cdot m_{salt}}{55.508 + d \cdot m_{l-salt} + m_{l-CO2}} \quad (27)$$

Where *d* is the stoichiometric number (2 for NaCl).The composition of the gas phase is then determined directly with:

$$y_{H2O} = A(1 - x_{CO2} - x_{salt}) \quad (28)$$

The mass of the three components can be calculated as follows:

$$m_{salt} = \frac{x_{salt} \cdot M_{salt}}{d} \quad (29)$$

$$m_{CO2} = x_{CO2} \cdot M_{CO2} \quad (30)$$

$$m_{H2O} = x_{H2O} \cdot M_{H2O} \quad (31)$$

M is the molar mass and m the mass in grams. Many equations which provide fluid properties require kg(salt) per volume as a unit for salinity. If the simplifying assumption is made that H_2O density is always 1 kg/l, the salinity in kg/l can be calculated as the salt molality multiplied by the molar mass.

3.2.3 PVT data predicting the properties of saturated CO_2 and H_2O/brine

The dissolution of CO_2 into brine and H_2O into CO_2 changes the properties of the phases. According to King et al. (1992) and Hebach et al. (2004), there is no measurable change of density due to the dissolution of H_2O into CO_2 within the experimental range. Data representing a possible change in CO_2 viscosity is not taken into account because it could not been found. Under the conditions considered here the dissolution of H_2O into CO_2 is relatively small and alterations of the CO_2 properties will be neglected in this study. Therefore, this chapter focuses on the properties of H_2O and brine and how they change if dissolved CO_2 is present.

Density of CO_2 saturated H_2O/brine

If CO_2 dissolves into H_2O or brine, the mixture becomes denser relative to the initial density of the solvent. Figure 3.9 shows the density of H_2O (calculated with Batzle and Wang (1992)) and two approaches to calculate the density of H_2O saturated with CO_2 (Bando et al. 2004; Hebach et al. 2004).

To measure the viscosity of CO_2 saturated H_2O and brine, Bando et al. (2004) proposed the following equation to account for the impact of CO_2 dissolved in:

$$\rho_{(H2O,CO2)} = \rho_{(H2O)} + 196 \cdot x_{mol(CO2)} + 15400 \cdot x_{mol(CO2)}^2 \qquad (32)$$

$\rho_{(H2O,\,CO2)}$ is the density of H_2O containing $x_{mol(CO2)}$, the mole fraction of CO_2. $\rho_{(H2O)}$ is the density of water calculated after Batzle and Wang (1992).

Hebach et al. (2004) determined the density of the H_2O + CO_2 system over an appropriate pressure and temperature range (10 to 300 bar; 284 to 332˚K). According to their publication, 'the water-rich phase density showed a pronounced dependence on pressure and temperature' (Hebach et al. 2004). Their regression function for CO_2 with a density higher than 468 kg/m^3 is:

$$\rho_{(H2O,CO2)} = 949.7109 + 0.559684 \cdot P + 0.883148 \cdot T - 0.00097 \cdot P^2 - 0.00228 \cdot T^2 \quad (33)$$

Temperature is in ˚K and pressure in MPa. Figure 3.9 shows that both approaches show almost similar results for the temperature and pressure conditions. The main difference of the two studies is that Bando et al. (2004) developed a correction for CO_2 in dissolution whereas the formula introduced by Hebach et al (2004) provides the density of saturated H_2O directly. This study uses the Bando's method for two reasons. Firstly, it deals with the mole fraction of CO_2 in H_2O which also allows for calculating the density of partially saturated H_2O. Secondly, it is able to handle the presence of salinity.

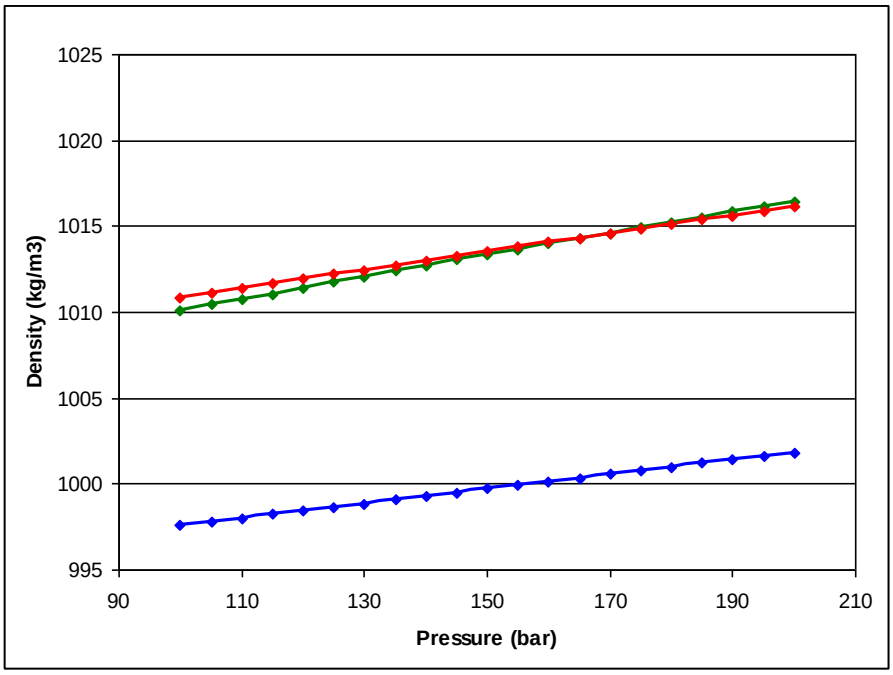

Figure 3.9: Density of H_2O calculated after (Batzle and Wang 1992, blue) and two different approaches to calculate the density of H_2O saturated with CO_2 (Bando et al. 2004, green; Hebach et al. 2004, red).

The formula presented by Bando et al. (2004) is also applicable to brine. In equation (32), the density of H_2O has to be replaced by brine density and the mole fraction of CO_2 in H_2O needs to be calculated taking the dissolution reducing effect of salinity into account. Figure 3.10 shows the density of brine and the corresponding density of brine saturated with CO_2. The average density difference of saturated H_2O, brine (0.15 kg/l) and brine (0.3 kg/l) calculated with Bando et al. (2004) for a pressure between 100-200 bar and a temperature of 35˚C is 13.6, 5.3 and 2.6 kg/m^3 respectively. The main reason for the decrease in density difference is probably due to the decreasing amount of CO_2 which is allowed to dissolve into a volume of brine. This effect, which leads to a lower density gradient, might also postpone the onset of gravity driven convection of CO_2 saturated and fresh brine.

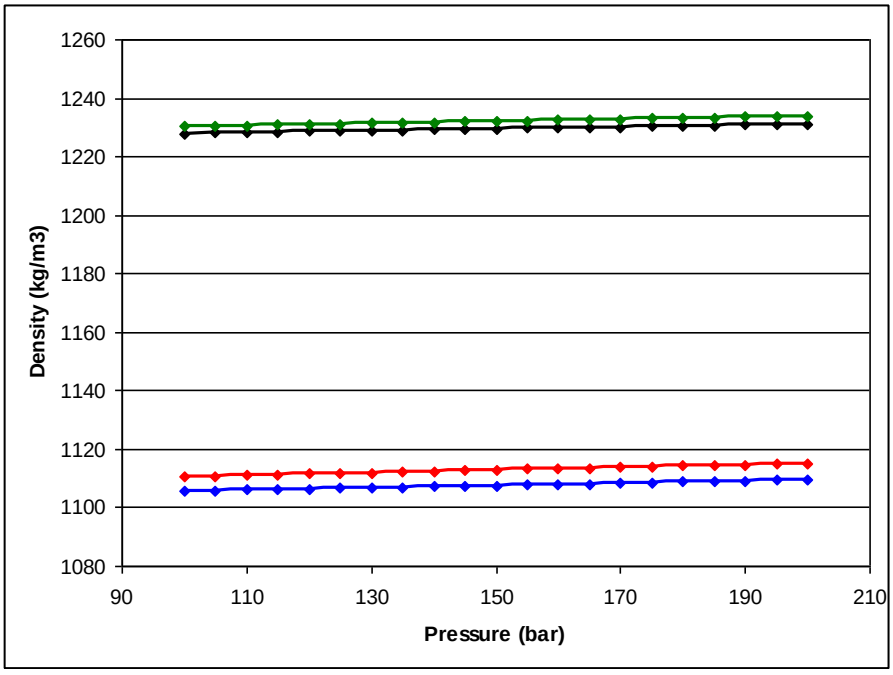

Figure 3.10: Density of brine (0.15 kg/m^3; blue) and brine (0.3 kg/m^3, black) and the corresponding density of the CO_2 saturated phase (red and green, respectively). An increase in salinity decreases the density difference between fresh and saturated brine.

Volume change of H_2O/brine due to dissolved CO_2

The pressure reducing effect of mutual H_2O and CO_2 dissolution has been discussed earlier. Even if all the CO_2 dissolves into the pore-water, the pressure will not reach its initial level because during the reaction of CO_2 dissolving into H_2O, the aqueous phase increases its volume. If CO_2 dissolves into the aqueous phase, the density increases but because CO_2 is added to the aqueous phase, its overall volume also increases. This has to be coded into the input file of the black-oil simulator separately in order to prevent the volume being calculated via the density (which would lead to a volume decrease).

Tegetmeier et al. (2000) presented a study where they measured the volume increase of H_2O in contact with CO_2. They found that the relative volume change of H_2O is 'linearly dependent on the mass fraction of the dissolved CO_2 in the liquid phase' (Tegetmeier et al. 2000). Their observed volume change of the liquid phase can be calculated with:

$$\Delta V = \frac{V_{(H2O,CO2)} - V_{H2O}}{V_{H2O}} = D \cdot w \qquad (34)$$

ΔV is the volume change, $V(H_2O)$ the volume of H_2O before the dissolution and $V(H_2O, CO_2)$ the volume of H_2O with dissolved CO_2. D is the material dependent coefficient (0.56 for H_2O) and w is the mass ratio of CO_2 (mCO_2) and H_2O (mH_2O) in the liquid phase.

$$w = \frac{m_{CO2}}{m_{H2O}} \qquad (35)$$

Figure 3.11 shows the volume change of H_2O and brine saturated with CO_2 for a pressure between 100-200 bar and a temperature of 35˚C. Again, the decrease in volume change with increasing salinity is probably due to the decreasing amount of

CO_2 which is allowed to dissolve into a volume of brine. Also, the volume increase of H_2O is greater with increasing pressure because the dissolution enhancing effect of increasing pressure decreases with increasing salinity.

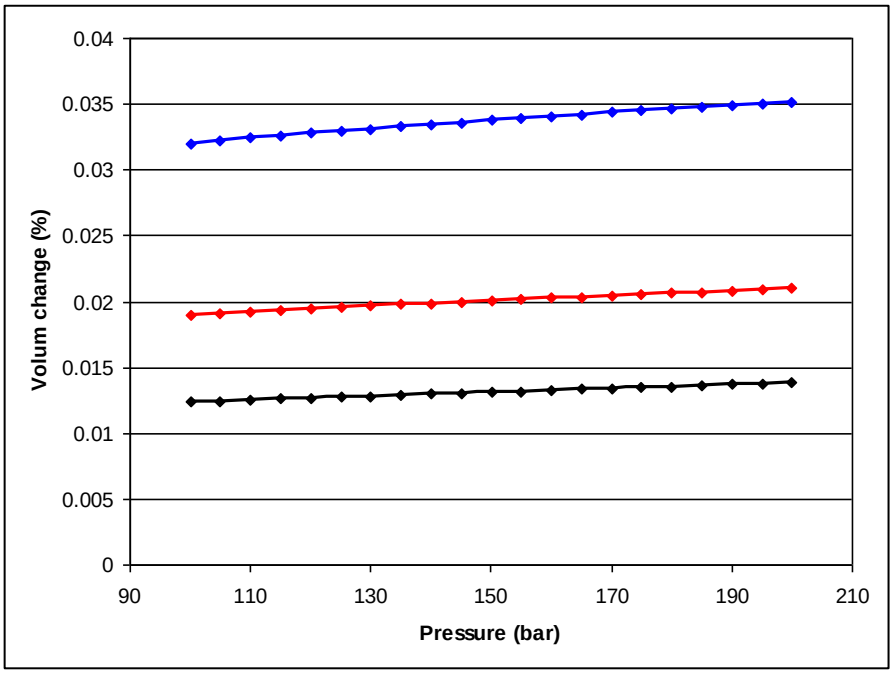

Figure 3.11: Volume change of H_2O (blue), brine (0.15 kg/m^3, red) and brine (0.3 kg/m^3, black) if saturated with CO_2. An increase in salinity leads to a decrease in pressure dependence and a generally lower volume increase.

Viscosity change of H_2O/brine with dissolved CO_2

The viscosity of H_2O and brine increases with an increasing amount of dissolved CO_2. Bando et al. (2004) measured the viscosity of H_2O and brine with and without dissolved CO_2 at conditions representing a typical aquifer CO_2 storage site (30-60˚C; 100-200 bar). Their empirical equation based on their experimental data for the viscosity change of dissolved CO_2 is:

$$\mu_{v-l,CO2} = \mu_{v-l}\left(1+\left(-0.004069\cdot T+0.2531\right)\cdot\frac{x_{molCO2}}{x_{molCO2(s)}}\right) \qquad (36)$$

$\mu_{v\text{-}l}$ is the viscosity of the aqueous phase (H_2O or brine), $\mu_{v\text{-}l,CO_2}$ is the viscosity of the aqueous phase with dissolved CO_2 (in cP). Temperature is in ˚C and x is the mole fraction of CO_2 in the aqueous phase (with 's' for saturated).

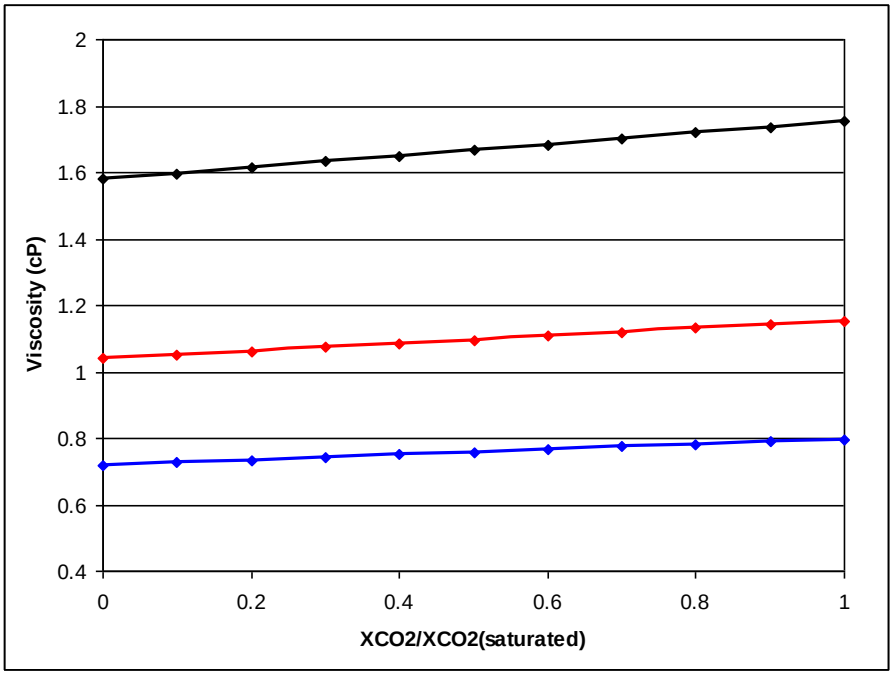

Figure 3.12: Viscosity change of H_2O (blue), brine (0.15 kg/m^3, red) and brine (0.3 kg/m^3, black) due to dissolved CO_2. The x-axis shows the ratio of the mole fraction of CO_2 and the CO_2 mole fraction if the aqueous phase is saturated with CO_2. The viscosity change is greater if salinity is higher.

This study does not use the viscosity data from the Bando et al. (2004) experiments but uses the proposed empirical equation derived from Batzle and Wang (1992) based on Kestin et al. (1981) for H_2O and brine viscosities. The methodology of Bando et al. (2004) is used to calculate the change in viscosity if CO_2 is dissolved. The observed pressure dependence on viscosity in the survey of Bando et al. (2004)

is insignificant and their viscosity of H_2O and brine matches the viscosity used for this study (Batzle & Wang 1992). Additionally, the Batzle and Wang (1992) method has been used in recent comparable studies such as Mathias et al. (2009) or Kopp et al. (2008). This gives high confidence in the accuracy of the equation. Figure 3.12 shows a linear increase in viscosity calculated with Batzle and Wang (1992) and the Bando et al. (2004) correction for dissolved CO_2. CO_2 saturated brine with a high salinity shows a greater viscosity increase than brine with lower salinity or H_2O, although the amount of dissolved CO_2 is lower. This is because only the ratio of the CO_2 mole fraction and the CO_2 mole fraction if the aqueous phase is saturated determines the impact on viscosity.

3.3 Hydro fracturing

3.3.1 Introduction

Pore pressure is a key parameter affecting the stability of rocks in the earth's crust. A geological formation in the subsurface with a high pore pressure is less stable than the same formation at the same depth with a low pore pressure. There are several reasons for an unusually high local pore pressure, such as metamorphic dehydration or the rapid subsidence and burial of fluid saturated sediments (Etheridge et al. 1983; Fertl et al. 1976). An example of how pore pressures affect rock stability was discovered by Raleigh (1976). He showed that an increase in pore pressure by injecting fluids into the subsurface can trigger earthquakes.

Under normal circumstances and a given depth, the pore pressure (P_p) is defined in terms of the pore fluid factor (λ) (Sibson 1990):

$$\lambda = \frac{P_p}{P_l} = \frac{P_p}{\rho \cdot g \cdot z} \qquad (37)$$

where P_l is the lithostatic pressure, ρ is the density of the overburden rocks, g the gravity constant and z the depth in meters. If pores are interconnected to the surface, pore pressure may be approximately 2.5 times smaller than the lithostatic pressure at the same depth (λ = 0.4-0.45). This is because the most widespread fluid, brine, has a density of slightly more than 1 g/cm^3 whereas common sedimentary rocks have an assumed density of 2.5 g/cm^3. If pores are partly closed, λ may increase to higher values. Development of unusually high pore pressure gradients in the subsurface requires the existence of localized or regionally extensive low permeability barriers. High pore pressure can significantly reduce rock strength typically expressed as differential stress (σ_1- σ_3). This strength reduction is described by the change of normal stress (σ) to the typically lower effective normal stress (σ'):

$$\sigma_n' = \sigma_n(1-\lambda) \qquad (38)$$

The stability of rocks in the fractional strength dominated zones of the subsurface (i. e. 'brittle crust') can be described by the empirical relationship of Coulomb:

$$\tau = C_c + \mu_f \cdot \sigma_n(1-\lambda) \qquad (39)$$

where τ is the frictional shear resistance, C_c is the cohesive or cementation strength (which can be neglected in deeper regions) and μ_f is the coefficient of friction. Typical values for the coefficient of friction are between 0.6 and 0.85 (Byerlee 1978), a representative value for rocks over a broad range of common stress situations is μ_f = 0.75.

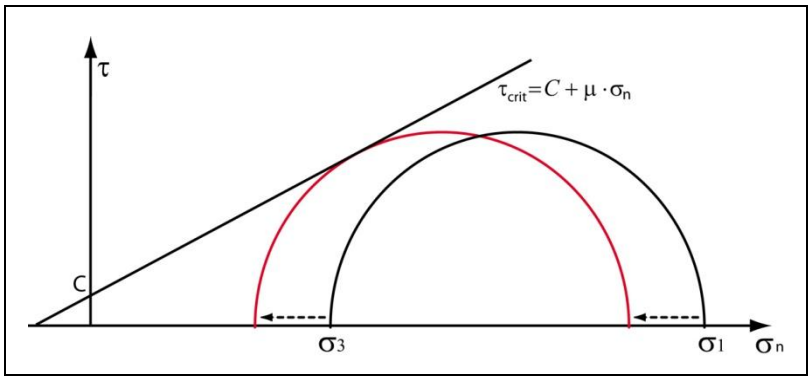

Figure 3.13: Schematic failure envelope on the Mohr diagram for stress, illustrating weakening of a rock due to increasing pore pressure. The black Mohr-circle represents the situation without pore pressure. With increasing pore pressure, the Mohr-circle is shifted to the left (red circle). The situation becomes unstable after touching the failure envelope.

Equation (39) gives the shear stress that a rock can endure under a particular normal stress. The resistance of a rock to brittle deformation can be illustrated with the failure envelope (Fig. 3.13). An increase of the pore pressure can lead to a) failure of unfractured rocks (expressed by the Coulomb criteria, Coulomb (1773)) or b)

frictional sliding along pre-existing fractures on fault planes (expressed by the criteria in Byerlee (1967)); and thereby destabilize a rock formation.

Prediction of the 'maximum sustainable pore pressure'

A common method to predict a 'maximum sustainable pore pressure' is the interpretation of leak-off pressure data. Leak-off pressure data are important because they predict the pore pressure which is necessary to open tensile fractures and therefore predict σ_3, the minimum horizontal stress, relatively accurately. Opening of tensile fractures, together with fracturing/shearing of intact rocks and fracturing/shearing of already fractured rocks, represents the three modes of rock failure in the subsurface (Mathias et al. 2009). Failure of intact rocks is difficult and is more likely to take place in deeper parts of the crust where temperature and confining pressure are higher.

The next section introduces the basic theory behind hydro fracturing. Subsequently, in section 3.3, the poroelastic behaviour of rocks will be introduced because it could have a significant impact on CO_2 injection scenarios. Section 3.4 describes different approaches to predict the critical pore pressure that triggers slip displacement of already fractured rocks. Finally, in section 3.5, the 'maximum sustainable pore pressure' which was used for this study is introduced.

3.3.2 Basic theory behind hydro fracturing

The critical wellbore pressure for tensile failure or hydrostatic fracturing is described in Jaeger (2007). During hydraulic fracturing of a particular formation, water or other liquids are pumped into the wellbore, until the induced stresses are large enough to open fractures which than propagate into the formation. The orientation of fractures is determined by the orientation of the stress field and is perpendicular to the minimum horizontal stress. There are several ways to use the equations which describe the relationship between tensile strength, pore pressure and stress field. The prediction of the wellbore fluid pressure that would be needed to fracture the rock in

the vicinity of the well is important. Scheidegger (1960) and Fairhurst (1964) pointed out that with the critical pore pressure the in situ horizontal stress field can also be calculated.

The critical environment for hydraulic fracturing is connected by the minimum stress which can be calculated with (Jaeger et al. 2007):

$$\sigma_w = \sigma_H + \sigma_h - 2(\sigma_H - \sigma_h)\cos 2\theta - P_w \qquad (40)$$

σ_w is the principal stress away from the well in the direction θ (the angle of clockwise rotation from the direction of the maximum horizontal stress). σ_h is the minimum horizontal stress, σ_H the maximum horizontal stress and P_w is the fluid pressure in the borehole.

Normally, when at least one of the in situ principle stresses is less than the vertical in situ stress, the minimum stress value after the borehole is drilled will be the tangential normal stress at $\theta = 0$ and $\theta = \pi$. By setting:

$$-T_s = \tau \qquad (41)$$

T_s is the tensile strength. For the case that the surrounding rock mass does not have porosity and is impermeable, the critical pore pressure (P_c) in the borehole which creates new fractures in the rock can be calculated with the Hubbert and Willis breakdown equation (Hubbert & Willis 1957):

$$P_c = 3\sigma_h - \sigma_H + T_s \qquad (42)$$

For the opening of pre-existing fractures which do not have tensile strength, T becomes zero and vanishes. If the surrounding rock mass has a fluid filled porosity (which it usually does) but no permeability (i. e. no connection between injection pressure and pore pressure), the pore pressure reduces the strength and *'–P_P'* has to be added to the right hand side of the equation. Schmitt and Zoback (1989) proposed that only a fraction of the pore pressure should account for the stability of the rock and introduced the parameter 'β', which lies in the range between 0.2-0.6. Although only a limited number of laboratory fracture experiments on one particular limestone were conducted, the results show at least that 'β' has to be below 1.

For the likely case that drilling fluid enters the permeable surrounding rock mass, an additional expression must account for poroelastic properties of the formation. The final equation is (Haimson & Fairhurst 1967):

$$P_c = \frac{3\sigma_h - \sigma_H + T - 2\eta P_P}{1 + \beta - 2\eta} \qquad (43)$$

where:

$$\eta = \frac{\alpha_b}{2}\frac{(1-2\upsilon)}{(1-\upsilon)} \qquad (44)$$

α_b is the Biot coefficient and v the Poisson's ratio.

The Poisson's ratio is defined as the 'ratio of the shortening in the transverse direction to the elongation in the direction of applied force in a body under tension below the proportional limit' (ISRM. Terminology (English, French, German). Lizbon: ISRM; 1975.). A more recent and more complete definition by Gercek (2006) for the ratio is: '(Poisson's ratio), simply, is the negative of the ratio of transverse strain to the axial strain in an elastic material subjected to a uniaxial stress. In mechanics of deformable bodies, the tendency of a material to expand or shrink in

a direction perpendicular to a loading direction is known as the "Poisson effect"'. It can be measured or calculated via several coefficients. For example, constants λ_l and G, which are known as the Lame's parameters, lead to:

$$\nu = \frac{\lambda_l}{2(\lambda_l + G)} \qquad (45)$$

Domenico (1983) used S- and P-wave velocities in order to determine Poisson's ratio from the equation:

$$\nu = \frac{0.5(V_p/V_s)^2 - 1}{(V_p/V_s)^2 - 1} \qquad (46)$$

where V_s are s-wave velocities and V_p p-wave velocities. His survey found that sandstones have a ratio of 0.17-0.26, dolomite of 0.27-0.29 and limestone of 0.29-0.33. Sandstones show a relatively large range of values which is likely because the number of sandstone samples is nearly three times higher than the number of dolomite and limestone samples. Gercek (2007) states in his review paper 'typical ranges of values (are presented) for Poisson's ratio of some rock types' and determines the ratio of sandstone to be in a range of 0.05-0.4, where values of un-drained rocks are larger than the drained values. For further references, see Gercek (2007).

The Biot coefficient is defined to be:

$$\alpha_b = \frac{K_m}{H'} \qquad (47)$$

where K_m is the macroscopic bulk modulus and *H'* is an 'inverse of the coefficient *1/H* which is a measure of the compressibility of the soil for a change in water pressure' (Detournay & Cheng 1993).

This equation gives a meaning to the Biot coefficient as the ratio of the fluid volume gained (or lost) in a material element to the volume change of that element, when the pore pressure is allowed to return to its initial state.

The coefficient α_b cannot exceed 1, since the volume of fluid gained (or lost) by an element cannot be greater than the total volume change of that element (under the linearised approximation). The range of variation of α_b is [0, 1]; if α_b is 0, no volume change of the fluid has occurred, if α_b is 1, the entire volume change of the sample has occurred only by the volume change of the fluid. Both K_m and *H'* can be measured directly in the lab. In their textbook, Paterson and Wong (2005) present a selection of eight values of α_b for six different sandstones published by five research teams and obtained a variation for α_b of between 0.12 and 0.91, whereas six out of seven values are between 0.64 and 0.91.

The value of the Biot' coefficient used in Mathias et al. (2009) is taken from Rutquist et al. (2007). They set the coefficient to 1 because together with their chosen Poisson's ratio in the equation:

$$\Delta\sigma_x = \Delta P \alpha_b \frac{1-2\nu}{1-\nu} \qquad (48)$$

where ν is the Poisson's ratio, $\Delta\sigma_x$ is the injection induced horizontal stress, ΔP the pore pressure change and α_b the Biot coefficient. This produces a 'theoretical value that compares reasonably well with analyses of horizontal stress measurements in depleted hydrocarbon reservoirs' (Rutquist et al. 2007).

Equation (43) predicts the pore pressure that opens pre-existing fractures. Mathias et al. (2009) propose three assumptions to simplify the equation. Firstly, the fractures are cohesionless. Secondly, they assume perfect connection between the pores and

the injected fluid. Hence, the presence of a 'mud cake' is neglected. 'Mud cakes' are accumulations of small particles in the vicinity of a well which can reduce the permeability. They are likely to develop around production wells but also occur around injection wells where mud filtrate from drilling accumulates. Additionally, the parameter β is set to 1. This assumption does not follow Schmidt and Zoback's (1989) recommendation who proposed a value between 0.2-0.6. A justification for the assumption is that the experiments conducted by Schmidt and Zoback were performed on limestones which might have a lower permeability than the North Sea sandstones and the fact that an overestimation of the parameter β represents a 'worst case' scenario. The third assumption is not to account for regional stress field. Mathematically, the assumptions are:

$$T_l = 0 \;\; ; \;\; \beta = 1 \;\; ; \;\; \sigma_H = \sigma_h \quad (49)$$

Equation (43) than becomes:

$$P_c = \frac{3\sigma_{h/H} - \sigma_{h/H} - 2\eta P_P}{2 - 2\eta} \quad (50)$$

P_c is the pressure at which a cohesionless tensile fracture opens and $\sigma_{h/H}$ is the stress in all horizontal directions. Furthermore, Mathias et al. (2009) proposed setting the critical fracture pressure equal to the pore pressure and concluded that:

$$P_c = \sigma_{h/H} \quad (51)$$

3.3.3 Introduction to poroelastic behavior

Poroelastic behaviour and its impact on rock stability during CO_2 sequestration has infrequently been taken into account. Many sedimentary basins have zones of abnormally high pore pressure. In these basins, an unusually high minimum horizontal stress is also recognized. The usual explanation for the correlation of high pore pressure and high minimum horizontal stress is that the pore pressures trigger slip along fault planes at relatively low differential stresses. The mathematical equation, which describes the value of the differential stress (σ_d) at which frictional sliding occurs, is:

$$\sigma_d = 2\mu_f(\sigma_n - P_p) \qquad (52)$$

where σ_n is the normal stress across the fault zone. If the pore pressure is high, small differential stresses are necessary to cause slip. Since σ_1 is vertical in many sedimentary basins and is only controlled by the weight of the overlying sediments, σ_3 or σ_h (the minimum horizontal stress) has to be high in overpressured areas.

An appropriately selected coefficient of internal friction provides reasonable lower bounds for σ_h in sedimentary basins with hydrostatic pressure. For a deeper region with a higher pore pressure / vertical stress ratios, the coefficients sometimes underestimate σ_h. With the measured pore pressure and vertical stress, the horizontal stress calculated with leak-off pressure data would require a lower coefficient of friction than 0.6 – a requirement which is not indicated by laboratory data (see Byerlee 1967). Therefore, an alternative theory has to be found which accounts for the high horizontal stresses combined with overpressure.

Poroelastic behaviour describes how porous rocks deform when pore space is filled with fluid and pressurized (Biot 1941, Kuempel 1991). The dilatation of a rock

volume with respect to the initial volume is induced by an increase in pore pressure according to the equation:

$$\frac{\Delta V}{V} = a_b \beta \Delta P_p \qquad (53)$$

The volume change (ΔV) is dependent on the Biot coefficient (α_b) and the rock compressibility (c) (Detournay et al. 1989). Compressibility is dependent on the confining pressure (P_{co}) and can be derived from:

$$c = \frac{1}{V}\frac{\Delta V}{\Delta P_{co}} \qquad (54)$$

Assuming that the volume strain is zero, equation (53) may be rewritten as:

$$\Delta P_{co} = a_b \Delta P_p \qquad (55)$$

If the Biot coefficient is less than 1 (as it typically is), a change in the confining pressure causes a bigger change in pore pressure. To determine the horizontal stress, Engelder and Fischer (1994) proposed a more elaborate equation for stress under uniaxial strain conditions:

$$\sigma_h = \sigma_v \left(\frac{\nu}{1-\nu}\right) + a_b \frac{1-2\nu}{1-\nu} P_p \qquad (56)$$

According to Engelder and Fischer (1994), rewriting equation (56) leads to:

$$\frac{\Delta\sigma_h}{\Delta P_p} = a_b \frac{1-2\nu}{1-\nu} \qquad (57)$$

If the Biot coefficient is set to 0.9 and Poisson's ratio is set to 0.25, the predicted ratio of horizontal stress to pore pressure changes is 0.6. Data taken from North Sea basins suggest that the ratio of $\Delta\sigma_h$ to ΔP_p is ~0.7 (Engelder & Fischer 1994). Recent studies performed by Swarbrick et al. (2011) determine coupling values much lower than previous studies. For the North Sea Central Graben, mid-Norway and North Viking Graben basin areas their coupling values are 0.35, 0.28 and 0.3 respectively.

3.3.4. Basic theory behind failure of fractured rocks

The critical pore pressure that may cause slip on pre-existing faults can be estimated from the ratio of the principle stresses that would allow frictional sliding on cohesionless, optimally oriented faults. According to the French scientist Amonton (1663-1705), the force of friction is directly proportional to the applied load and the force of friction is independent of the apparent area of contact (although fundamental ideas of friction had presumably been introduced by Leonardo da Vinci about 150 years before). Hence if the shear stress (τ) applied to cohesionless fault surface reaches a value:

$$\tau = (\sigma_n - P_P)\mu_f \qquad (58)$$

where μ_f is the coefficient of internal friction, slip on a pre-existing fault will occur. The angle of the fault plane θ, measured from σ_1, would be:

$$2\theta = (\tan^{-1}\mu_f + 90) \quad (59)$$

Tan^{-1}(μ_f) equals the 'angle of internal friction', Typical values for μ_f lie between 0.6 and 0.85 (Bayerlee 1978). If a fault has a favourable orientation, the situation can be described with (Jaeger & Cook 1969):

$$\frac{(\sigma_3 - P_P)}{(\sigma_1 - P_P)} = [\mu_f + (\mu_f{}^2 + 1)^{1/2}]^{-2} \qquad (60)$$

This is a very useful relationship to estimate the minimum horizontal stress in a normal fault region. This equation derives from the Mohr-Coulomb diagram and is described in Jaeger et al. (2007). The failure criterion can be written to describe mathematically the opposite side of the triangle (*TPM*, Fig. 3.14):

$$MP = (TA + AM)\sin\phi \qquad (61)$$

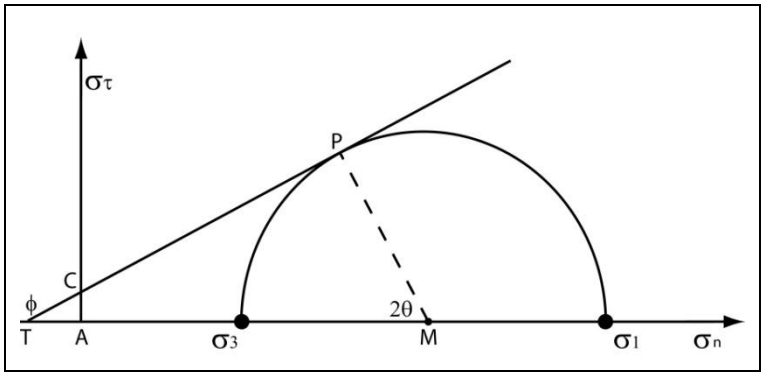

Figure 3.14: Mohr diagram with failure curve. The angle θ is the angle of the fault plane relative to the maximum principle stress.

TA and *AM* are known but *PM* has to be expressed as:

$$TA = C_c \cdot \cot\phi \quad \text{or} \quad TA = C_c \cdot \frac{\cos\phi}{\sin\phi} \qquad (62)$$

Equation (61) then becomes:

$$(\sigma_1 - \sigma_3) = \left(2C_c \cdot \frac{\cos\phi}{\sin\phi} + (\sigma_1 + \sigma_3)\right)\sin\phi \qquad (63)$$

By multiplying the brackets on the RHS with (sin ϕ):

$$(\sigma_1 - \sigma_3) = 2C_c \cdot \cos\phi + (\sigma_1 + \sigma_3)\sin\phi \qquad (64)$$

By rearranging equation (64) and by isolating the maximum principle stress (σ_1):

$$\sigma_1 = 2C_c \frac{\cos\phi}{1-\sin\phi} + \sigma_3 \frac{1+\sin\phi}{1-\sin\phi} \qquad (65)$$

The failure criterion can be written in terms of the coefficient of friction by replacing:

$$\cos\phi = \frac{1}{\sqrt{1+\mu_f{}^2}} \qquad (68) \qquad \text{and} \qquad \sin\phi = \frac{\mu_f}{\sqrt{1+\mu_f{}^2}} \qquad (66)$$

The equation becomes:

$$\left(\sqrt{1+\mu_f{}^2} - \mu_f\right)\cdot\sigma_1 = 2C_c + \left(\sqrt{1+\mu_f{}^2} + \mu_f\right)\cdot\sigma_3 \qquad (67)$$

This is an equivalent expression to equation (60) if pore pressure is not accounted for and cohesionless faults are assumed. The maximum stress is vertical and can be calculated by the density of the overburden and the pore pressure should be well known for non over- or underpressured areas. Alternatively, with a simple conversion of equation (60) the critical pore pressure can be calculated:

$$\frac{\{\sigma_3 - [\mu_f + (\mu_f{}^2 + 1)^{1/2}]^{-2}\sigma_1\}}{\{1 - [\mu_f + (\mu_f{}^2 + 1)^{1/2}]^{-2}\}} = P_C \quad (68)$$

It is important here to consider that the equation describes the conditions when they are critical. P_p becomes P_c because the left hand side of the equation now equals the critical pore pressure.

The main problem is that usually the minimum horizontal stress is unknown. One simple method for estimating horizontal stress (which may be the minimum or maximum horizontal stress) is to assume a linear rule such as:

$$\sigma_{h/H} = \kappa\sigma_v \quad (69)$$

Brown and Hoek (1978) obtained the following empirical bounds for κ:

$$0.3 + \frac{100}{z} \leq \kappa \leq 0.5 + \frac{1500}{z} \quad (70)$$

Unfortunately, the upper boundaries are very high and the lower boundaries are very low. Mathias et al. (2009) assumes that the samples used for the experiments conducted by Brown and Hoek (1978) were not pre-faulted and therefore too cohesive.

A second approach to calculate σ_3 is to assume uniaxial strain based on Hooke's law. Uniaxial strain is assumed to occur when fluid is withdrawn from a reservoir. If the lateral strain is inhibited by the surrounding rock mass and the vertical stress contractile (Jaeger et al. 2007), the principle stresses can be expressed as:

$$\frac{(\sigma_3 - a_b P_P)}{(\sigma_1 - a_b P_P)} = \frac{\nu}{1-\nu} \quad (71)$$

If fluid was injected into a reservoir (i.e. the reverse case), (71) should also be applicable.

Uniaxial strain is defined as the strain of a sample during a compression experiment with confining pressure and no horizontal strain. The right hand side of the equation is a well known relationship and equals σ_3/σ_1. The addition of pore pressure and the Biot coefficient is not mentioned in Jaeger et al. (2007) and was probably first introduced in Zimmerman (2000). Mathias et al. (2009), who use the equation, consider the Biot coefficient to be 1 so it does not have any impact on their results.

The relationship (71) describes the effect of the vertical stress on a linear elastic rock body with no confining pressure but fixed horizontal boundaries. If σ_1 increases, the rock deforms, controlled by Poisson's ratio and, with increasing horizontal dilatation, the horizontal stress increases too. In practice, the equation provides one σ_h for each σ_v, only dependent on Poisson's ratio. This assumption clearly contradicts Heim's rule which states that stresses in rock are hydrostatic because of the ability to creep. Although upper crustal sandstones do not tend to creep, the equation and its stress relationship which are only dependent on the Poisson's ratio has to be seen as a simplification. As Engelder and Fischer (1994) pointed out, poroelastic responses make only physical sense for short time scales during which uniaxial strain behaviour applies. Temperature is not accounted for but in relatively shallow depths of the upper crust, the temperature gradient will not influence the rheology of relatively pure sandstone. The main uncertainty is that the equation defines the

subsurface as a homogenous rock formation. Tilted formations of variable thickness and rock strength (especially softer materials (such as anhydrite or carbonates)) and the presence of geological structures make the stress field more complicated. Additionally, the presence of a nearly infinite amount of fractures, folds, dikes and other geological structures as well as plate tectonic forces that persist 100's – 1000's km inland from plate boundaries, makes the absence of a regional stress field very unlikely in the upper crust.

The equation is presented by Daines (1982) and is written as:

$$\sigma_{H/h} = \sigma_1^{'}(\frac{\nu}{1-\nu}) \qquad (72)$$

σ'_1 is the effective maximum stress. The idea which derives from this assumption is that in actively subsiding basins the vertical stress increases more than the horizontal stress until the differential stress becomes high enough and listric faults develop. However, an external force should be taken into account which Daines calls the tectonic stress (Daines 1982).

Mathias et al. (2009) proposes to set equation (60) and (71) to σ_3 and combine the two equations. In order to get the pore pressure on the left site we recalculate to:

$$P_C = \{\frac{[\mu_f + (\mu_f{}^2 + 1)^{1/2}]^{-2} - \nu(1-\nu)^{-1}}{[\mu_f + (\mu_f{}^2 + 1)^{1/2}]^{-2} - [\nu(1-\nu)^{-1} - 1]a_b - 1}\}\sigma_1 \qquad (73)$$

The simple advantage of this equation is that if the Biot coefficient is 1 (as Mathias et al. 2009 propose) the critical pore pressure is equal to the vertical pressure (σ_1).

$$P_C = \sigma_v \qquad (74)$$

If the Biot coefficient is assigned a more realistic value (a_b<1), the critical pore pressure will be lower.

$$P_C \langle \sigma_v \qquad (75)$$

3.3.4 Estimation of the 'maximum sustainable pore pressure' used for this study

Two different critical pore pressures for tensile fractures and three different pressures for shear fractures can be interpreted from the theory previously introduced in section 3.3.2. A coefficient of friction of 0.75 was selected which lies within the range suggested by Byerlee (1973). If the Biot coefficient is taken into account, a value of 0.9 can be selected which is within the range suggested by Paterson and Wong (2005). The Poisson's ratio is derived from Domenico (1983) and is set to 0.25 for sandstone. The parameter β is set to 1 and vanishes because the permeabilities of rock formations generally suitable for CO_2 storage tend to be relatively high.

For tensile fractures and no horizontal differential stress field the critical pore pressure can be predicted with:

$$P_C = \frac{3\sigma_{h/H} - \sigma_{h/H} - 2\eta P_P}{2 - 2\eta} \qquad (50)$$

If the pore pressure and fracture pressure are similar, the equation becomes:

$$P_C = \sigma_{h/H} \qquad (51)$$

If horizontal differential stress is present, the critical pore pressure is:

$$P_C = \frac{3\sigma_h - \sigma_H - 2\eta P_P}{2 - 2\eta} \qquad (76)$$

To estimate the critical pore pressure for shearing along existing planes assuming uniaxial strain Mathias et al. (2009) proposed the following equation:

$$P_C = \{\frac{[\mu_f + (\mu_f{}^2 + 1)^{1/2}]^{-2} - \nu(1-\nu)^{-1}}{[\mu_f + (\mu_f{}^2 + 1)^{1/2}]^{-2} - [\nu(1-\nu)^{-1} - 1]a_b - 1}\}\sigma_1 \qquad (73)$$

If the Biot coefficient is 1 (Mathias et al. 2009) or not a part of the equation (Daines 1982) the critical pore pressure will be:

$$P_C = \{\frac{[\mu_f + (\mu_f{}^2 + 1)^{1/2}]^{-2} - \nu(1-\nu)^{-1}}{[\mu_f + (\mu_f{}^2 + 1)^{1/2}]^{-2} - [\nu(1-\nu)^{-1} - 1] - 1}\}\sigma_1 \qquad (77)$$

For this particular case the critical pore pressure is always equal to vertical stress:

$$P_C = \sigma_v \qquad (74)$$

If the vertical and the minimum horizontal pressure are known the critical pore pressure can be calculated with:

$$P_C = \frac{\sigma_3 - [\mu_f + (\mu_f{}^2 + 1)^{1/2}]^{-2}\sigma_1}{1 - [\mu_f + (\mu_f{}^2 + 1)^{1/2}]^{-2}} \qquad (68)$$

According to Swarbrick et al. (2011), the factor that determines $\Delta\sigma_h$ with increasing ΔP_p if poroelastic behaviour is taken into account is:

$$\frac{\Delta\sigma_h}{\Delta P_p} = 0.3 \qquad (78)$$

The minimum horizontal stress is derived from leak-off pressure data (Moss et al. 2003). Three values for σ_h were chosen, a conservative, an intermediate and an optimistic value (Fig. 3.15).

The maximum horizontal stress is unknown. Schmitt and Zoback (1989) used equation (76) to determine σ_H with hydraulic fracturing tests. The necessary additional parameter is the re-opening pressure which can be seen as P_c for cohesionless fractures. Schmitt and Zoback (1989) present re-opening pressures depth at depth of 890 m, 1076 m, and 1284 m of crystalline rocks at Moodus (Connecticut, US). The re-opening pressures are approximately 10 % lower than the measured shut-in pressures (minimum horizontal stress). Although the data are dependent on the regional geology and it would be very unlikely if the re-opening pressures were similar, this assumption will provide 'synthetic data' which allow studying the impact of a 'realistic' stress field.

The parameters for calculating the fracture pressure in the vicinity of the injection well (in this study 1095 m) are:

- average vertical pressure is 273.8 bar (250 bar per km)
- average minimum horizontal pressure is 158/180/202 bar (Fig. 3.13)
- Biot coefficient: 0.9 (alternatively 1)
- Poisson's ratio: 0.25
- Coefficient of internal friction 0.75
- Average pore pressure: 109 bar (40 % of the vertical pressure)

- Assumed maximum horizontal stress: 175/222/269 bar

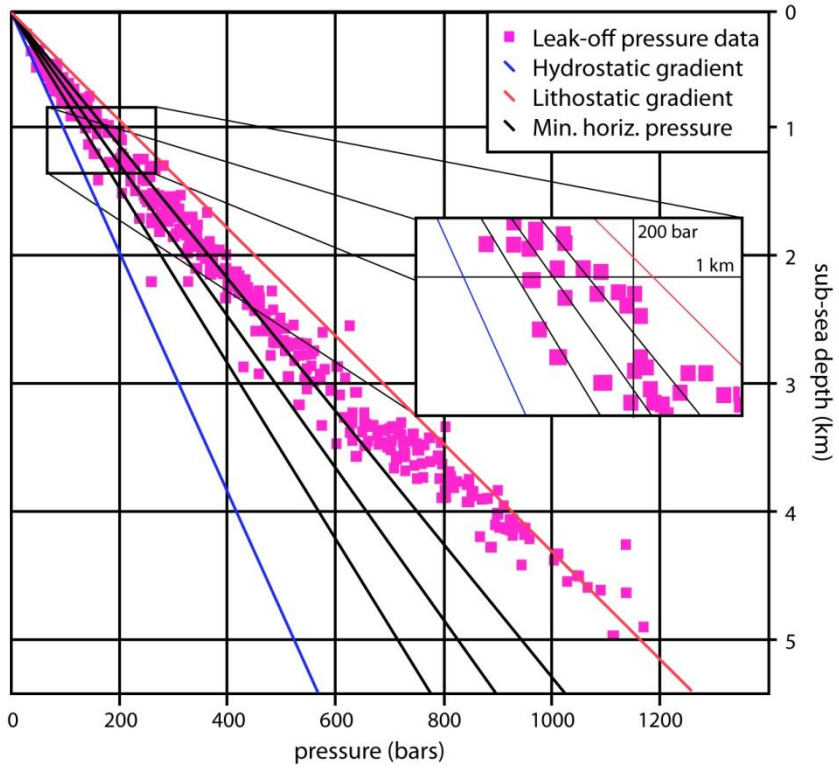

Figure 3.15: Leak-off pressure data from drilling operations in the central North Sea. The Data was used to estimate the fracture pressure of at a depth just below 1000 m (see magnification). Three fracture pressure cases were interpreted: A high, low and mid case (black lines). Due to overpressure in the Mesozoic formations of the central North Sea the fracture pressure increases relative to the lithostatic pressure. Therefore the values of the three cases cannot be interpolated to great depth. Redrawn from Moss et al. 2003.

Figure 3.16 summarizes the critical pore pressure for the proposed scenario calculated with different methods. The uncertainties to determine a 'maximum sustainable pore pressure' are huge and even with small changes of the Biot coefficient, the coefficient of friction or the principle stresses can alter the maximum sustainable pore pressure significantly. With the chosen coefficients and values, the critical pore pressures for tensile fractures are generally slightly higher than the pressures for shearing along pre-existing fractures. All values are crucially dependent on the interpretation of the stress field and on the accuracy of the leak-off pressure

data. The ‘maximum sustainable pore pressure’ of 150 bar is seen to be a fair estimation considering the fact that the data are scattered due to the application of different equations and assumptions.

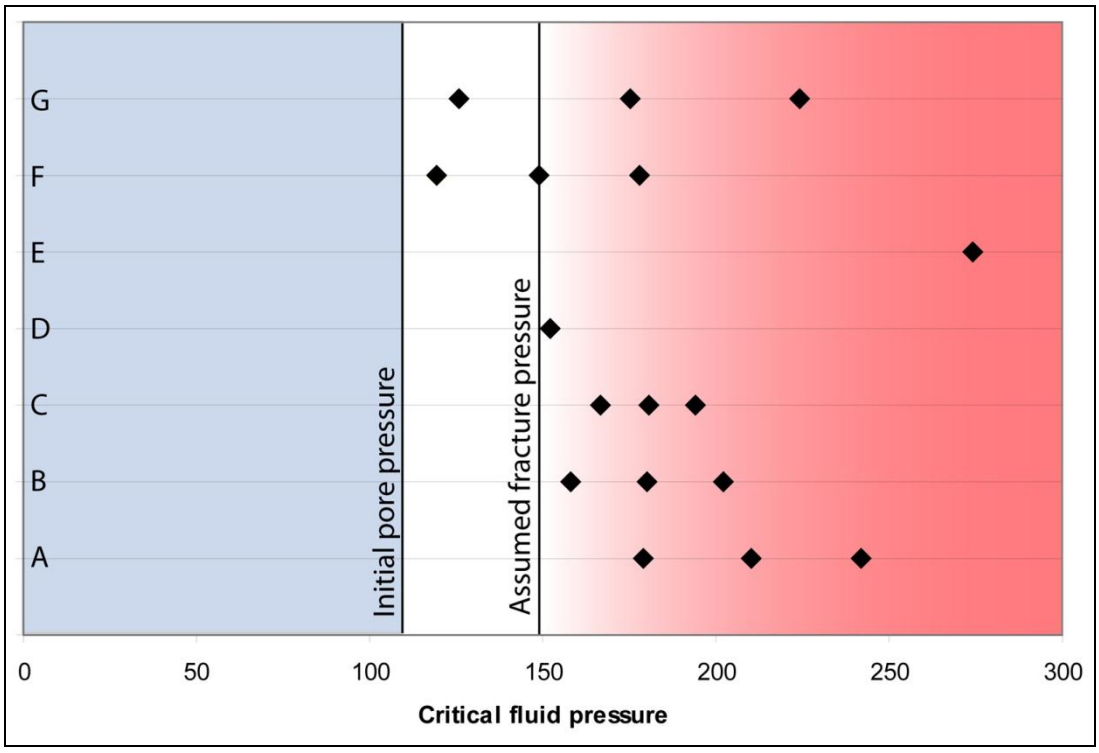

Figure 3.16: Critical pore pressure calculated with different equations based on different theories. Three values for the fracture pressure derive from three estimations for the minimum horizontal stress (see Fig. 3.15). A, B and C are calculated critical pore pressures for tensile fractures according to equations (Eq. 50), (Eq. 51) and (Eq. 76), respectively. D, E and F are critical pressures which allow shearing along existing, appropriately oriented fault planes calculated with equations (Eq. 73), (Eq. 74) and (Eq. 68), respectively. G uses equation (Eq. 68) but takes poroelastic behaviour into account (Eq. 78). As a value for the fracture pressure, 150 bar was chosen. The conservatively calculated fracture pressures of G and F are very low, nearly as low as the calculated hydrostatic pressure. The selected value takes shearing along existing fractures (F) into account and is only slightly lower than the fracture pressure calculated for uniaxial strain (D).

3.4 Model set-up

The simulation of the injection of CO_2 into a saline aquifer was conducted with the Eclipse black oil simulator (E100). To investigate the two-phase fluid flow and its impact on pressure, a two dimensional radial model was developed. A radial grid is capable of simulating fluid flow more accurately than a cartesian grid because fluid flow propagates radially outwards from the injection well. The rock formation in which the CO_2 is injected has a thickness of 100 m and the top of the aquifer is at 1000 m. The top and the bottom of the storage formation were defined as impermeable.

The inner boundary of the model, in other words the injection well, has a radius of 0.15 m. The horizontal radius, measured from the margin of the injection well to the outer boundary of the model, is 740.32 m with a corresponding footprint area of nearly 1.723 km^2. The first ten cells have a length 0.25 m in the radial direction in order to minimize numerical dispersion effects. Cell 11 has a length of 0.56 m in the radial direction and the following cells have a radial length which is defined by the equation:

$$R_X = R_{X-1} + \left(\frac{R_{X-1}}{2} \right) \qquad (79)$$

R_x is the radial length of the cell and R_x*-1* is the radial length of the previous cell. According to the equation, cell diameter and volume increase rapidly with increasing distance from the injection well so that cell 26, the outermost cell, has a radial length of 246.32 m. The grid is relatively large for an injection pressure study but the size guarantees that the impermeable horizontal boundary has no effect on the results. The increase in cell length is necessary in order to reduce the number of cells. The vertical size of the model is distributed into 20 layers of 5 meters thickness. The

modeled well injects CO_2 into the bottom cell. That corresponds to a perforation of 5 meters.

The initial fluid pressure at 1000 m is 100 bar and the isothermal temperature is 35°C. An isothermal system was chosen in order to avoid a complicated model with too many variables. Gas with CO_2 properties is injected with a rate of 200,000 m^3 per day (defined as standard conditions; 60°F, 1 atm., Eclipse Technical Description (2008), pp. 1039). Converted with the Redlich-Kwong EoS and Spycher coefficients the corresponding injection rate is 0.13635 Mt per year. The relatively low injection rate was chosen to illustrate a comparable pressure increase. Industrial-scale CO_2 storage operations will generally use injection rates of 1 million tons per year of CO_2 and above although they will initiate the injection process at a lower rate.

The models that are supposed to represent the most realistic approach are named 'full model' in this study. Two different versions are available, one with the mutual dissolution of CO_2 and H_2O and one without. Sensitivity models have the same setup but either temperature or salinity varies.

Table 1. Details of the base case

Thickness	100 m
cell size (x)	variable
cell size (z)	5 m
Horizontal permeability	100 mD
Vertical permeability	10 mD
Porosity	0.18
Rel. Permeability (aqueous phase)	van Genuchten (1980)
Rel. Permeability (gas phase)	Corey (1954)
Capillary pressure	van Genuchten (1980)
Aquifer depth	1000 m
Initial water saturation	100%
Brine salinity	0.15 kg/kg
Injection depth	1097.5
Rock compressibility (at 1000 m)	0.000045 bar-1
Perrforation	10 m
Well diameter	0.3 m
Injection rate	0.13635 Mt per year
Temperature	35 C

The porosity of the whole model is 18 %. Horizontal permeability is 100 mD and the vertical permeability is ten times lower (10 mD). The top surface has a depth of 1000 m. Three components are allowed in the model: H_2O, CO_2 and NaCl. The salinity of the brine is 0.15 kg salt per 1 kg water. The rock compressibility at 100 bar (1000 m depth) is 0.000045 /bar.

The relative permeability of the aqueous phase was calculated after van Genuchten (1980):

$$K_{rl} = (S^*)^{\alpha p}[1-(1-(S^*)^{1/m})^m]^2 \qquad (80)$$

with

$$S^* = (S_1 - S_{lr})/(1 - S_{lr}) \qquad (81)$$

The relative permeability of the gas phase was calculated after Corey (1954):

$$K_{rg} = (1-S')^2(1-S'^2) \qquad (82)$$

with

$$S' = (S_1 - S_{lr})/(1 - S_{lr} - S_{gr}) \qquad (83)$$

The capillary pressure was calculated after van Genuchten (1980):

$$P_{ca} = P_{c0}\left(\left(\frac{S_w - S_{rw}}{1 - S_{rw}}\right)^{-1/mp} - 1\right)^{1-mp} \qquad (84)$$

The parameter '*ap'* has a value of 0.5 (Mualem 1976) and '*mp*', the pore size distribution index, is set to 0.5614 for loamy sand (Pruess et al. 2003). The residual water saturation is 0.139 and the residual gas saturation is 0.05 (Pruess et al. 2003). The 'strength coefficient', P_{c0}, was set to 0.04 bar for a sandy aquifer (Chadwick et al. 2009). Relative permeability and capillary pressure curves are shown in Fig. 3.17.

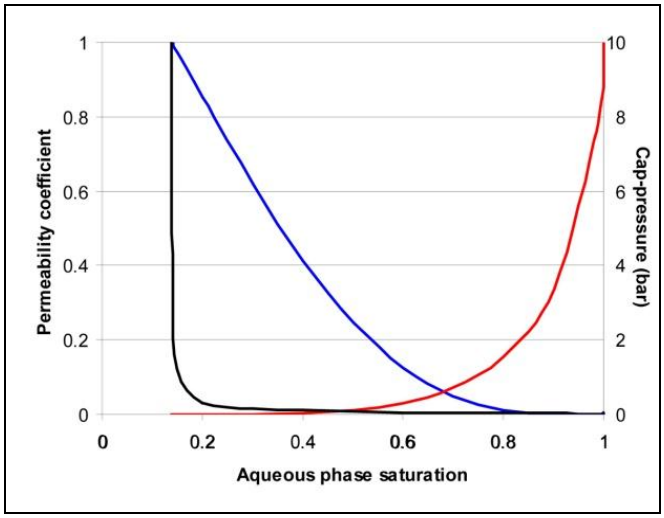

Figure 3.17: Capillary pressure (black), aqueous phase (red) and gas phase (blue) relative permeability curves used in this study. See text for more information.

3.5 Results

This chapter starts with the results of a study which investigates the increase of the fluid pressure and the gas phase/liquid phase saturation in the vicinity of the injection well. Subsequently, the effect of mutual dissolution of the gas and the liquid phase are accounted for and the change of pressure, phase saturation and the amount of dissolved gas and water are illustrated. If not otherwise annotated, the pressure of three cells is presented: Cell 1, the cell closest to the injection point, cell 4 and cell 7. All pressures and saturations are measured in cells in the bottom layer. The pressure value presented is the aqueous phase pressure.

3.5.1 Simulated CO_2 injection without mutual dissolution of CO_2/H_2O

Pressure increase in the vicinity of the injection well

Figure 3.18 illustrates the pressure increase in the vicinity of a CO_2 injection well of the cells 1, 2, 4, 7 and 10 in the bottom layer of the 'base case model'. All curves start at an initial pressure of 110.6 bar before injection started: the average fluid pressure at the bottom cells of the model. As injection starts, fluid pressure increases almost instantaneously until it reaches a certain value. The pressure adjacent to the well is highest. With increasing horizontal distance away from the injection point, the pressure maximum decreases and the time it takes to reach the maximum pressure increases. The maximum pressure of cell 1 reaches 185 bar after approximately 2.1 minutes and then decreases steadily. After 90 minutes, pressure is still decreasing and has not reached equilibrium. Pressure maximums are lower with increasing distance but also become less distinct. For example, the maximum pressure in cell 4 is already difficult to detect due a relatively broad pressure peak.

In addition, the bottom-hole pressure (BHP) is illustrated. The BHP is the pressure at the bottom of the well (in the centre of the perforation at 1097.5 m) and, for the injection simulations, the region of highest pressure. The BHP reaches 206 bar after 17 seconds and drops immediately afterwards.

Figure 3.18 also illustrates the time at which the fluid pressure increase has almost stopped. This time represents the instant when the pressure pulse penetrates the cell with maximum strength. The shape of the curve shows that not only the intensity but also the velocity of the pressure maximum decreases rapidly with increasing distance from the injection well.

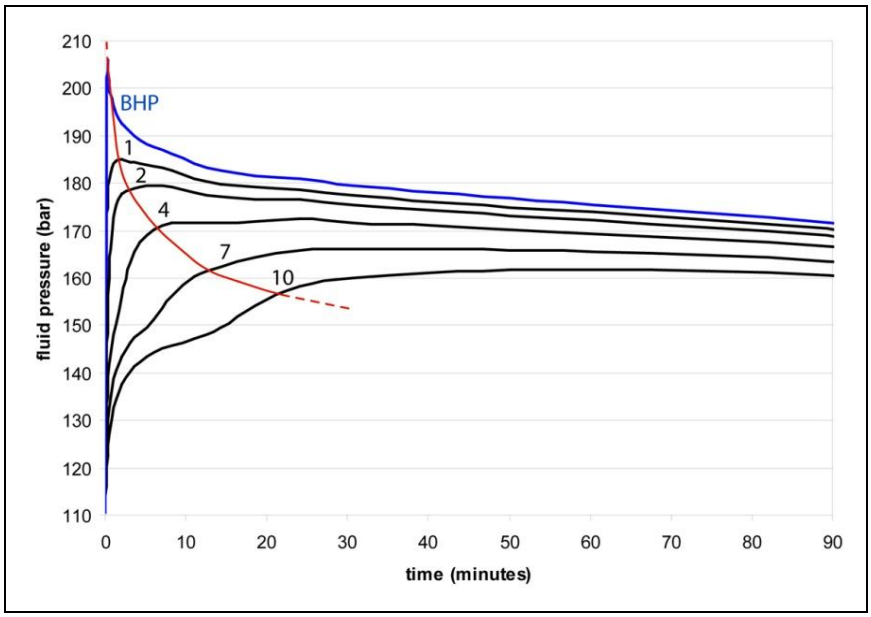

Figure 3.18: The graph shows the pressure development of the 'base case model' in 5 cells (1, 2, 4, 7, and 10; black) in the vicinity of the injection well. Also shown is the bottom whole pressure (BHP, blue). The red line highlights the time when pressure is about to reach its maximum.

The 'base case model' takes all parameters presented in this study into account. Only mutual dissolution of CO_2 and H_2O is not included in this simulation. All the results of the pressure sensitivity test are presented with respect to the 'base case model'.

Phase saturation in the vicinity of the injection well

Pressure increase is directly connected with the capability of the invading fluid to displace the host fluid. Figure 3.19 illustrates the saturation of brine and CO_2 in the vicinity of the injection well. Because CO_2 and brine are the only phases, their sum is always unity. Adjacent to the injection well, brine is being displaced almost instantaneously during the beginning of injection which occurs in compliance with the Buckley-Leverett theory (see 3.6.5 for additional information). With time the displacement rate decreases but after 90 min the CO_2 saturation is still increasing. The brine displacement of cells 4 and 7 starts when CO_2 reaches the cell and starts displacing brine. With increasing distance from the injection well the amount of displaced brine decreases. After 90 minutes, cell 7 still contains 58 % brine. At the same time, cell 1 contains 33 % brine, a value much higher than the defined minimum liquid phase saturation of ~13.9 %.

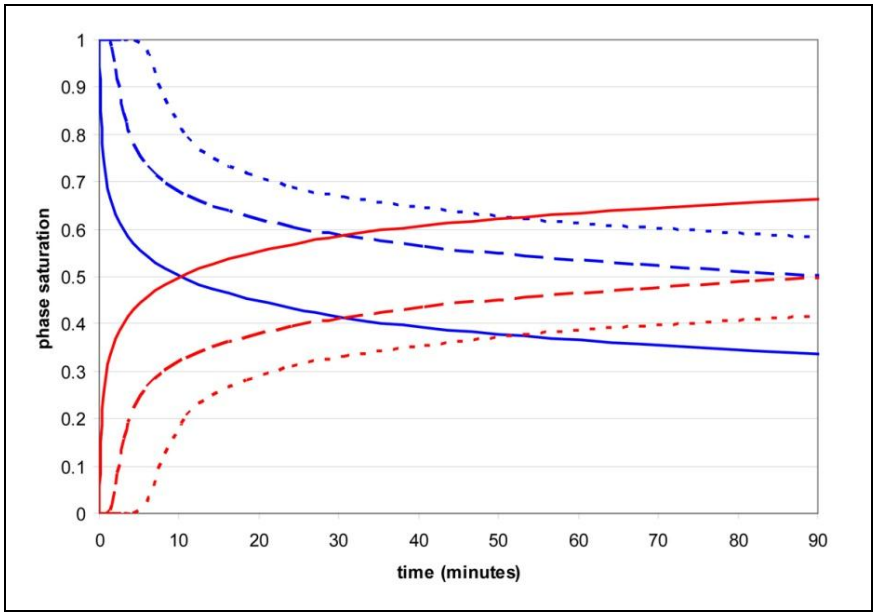

Figure 3.19: Graph showing the aqueous phase saturation (blue) and the gas phase saturation (red) of cell 1 (solid line), cell 4 (dashed line) and cell 7 (dotted line).

Temperature and salinity effects on the injection pressure

Figure 3.20 shows the change in pressure if the temperature changes. Generally, cooler temperatures lead to higher pressure accumulations and warmer temperatures lead to lower pressure accumulations. The maximum pressure of the ’30 C model’ is 1.6 bar higher than the reference model and that of the ‘40 C model’ is 2.1 bar lower (102 % and 97 % of the ‘base case model’ pressure increase, respectively).

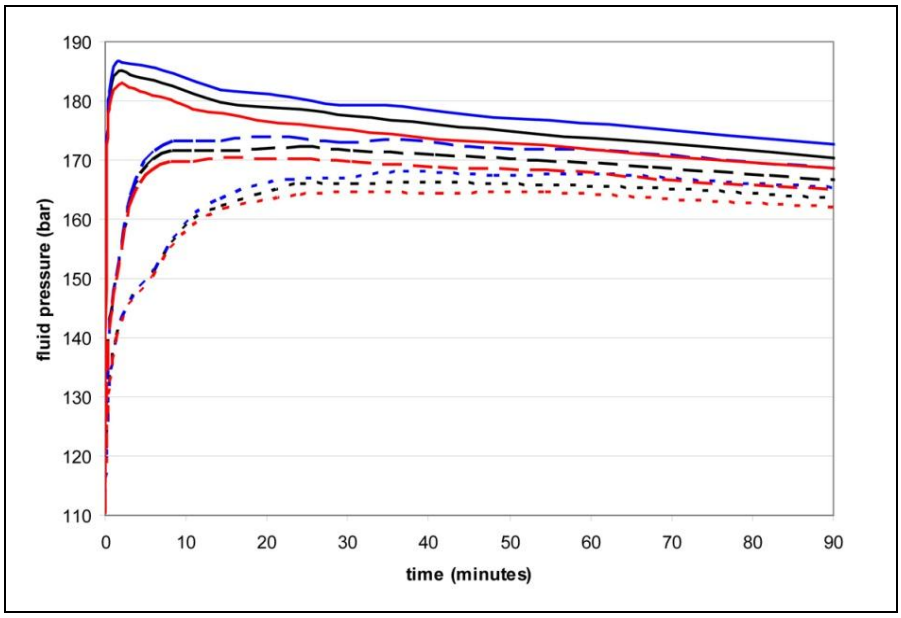

Figure 3.20: The graph shows the impact of temperature on the modelled pressure development. Illustrated are the ‘base case model’ (black), the ‘30 C model’ (blue) and the ‘40 C model’ (red). All temperatures are isothermal. Pressures are shown for cell 1 (solid lines), cell 4 (dashed lines) and cell 7 (dotted lines).

Figure 3.21 illustrates the impact of salinity on the pressure increase in the vicinity of the injection well. A lower salinity reduces pressure and higher salinities lead to greater pressure accumulations. If CO_2 is injected in pure water, the maximum pressure is 18.8 bar lower than the pressure of the ‘full model’ (76 % of the ‘base case model’ pressure increase). If the salinity is 0.3 kg/l, therefore twice as high as in the ‘base case model’, the maximum pressure is 28.9 bar higher than the pressure of the ‘base case model’ (137 % of the ‘base case model’ pressure increase).

Additionally, with increasing salinity, the pressure gradient between cell 1 and cell 7 increases slightly. The maximum pressure relative to the pressure after 90 minutes in cell 1 increases drastically from 18.3 bar for an injection into water to 36.1 bar for an injection into high salinity brine.

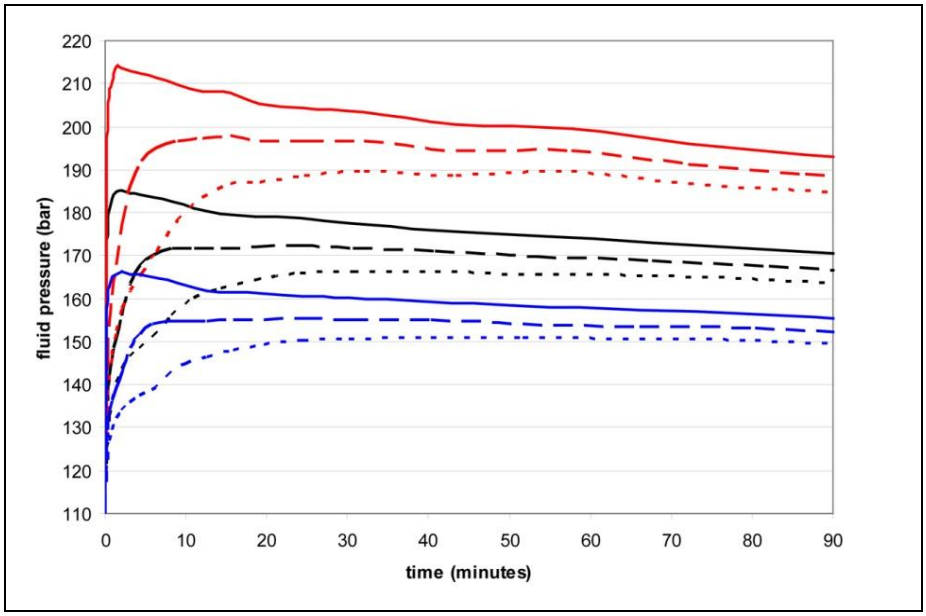

Figure 3.21: The graph shows the impact of different salinities on the modelled pressure development. Illustrated are the 'base case model' (black), the '0.3 kg/l model' (red) and the 'pure H_2O model' (blue). Salinity is modelled as pure NaCl. Pressures are shown for cell 1 (solid lines), cell 4 (dashed lines) and cell 7 (dotted lines).

3.5.2 Simulated CO_2 injection with mutual dissolution of CO_2/H_2O

Pressure increase in the vicinity of the injection well

Figure 3.22 illustrates the pressure increase of a 'base case model' injection pressure simulation without mutual dissolution in comparison to the 'base case model' pressure which accounts for the mutual dissolution of the H_2O and CO_2. The injection pressure of the latter should be always lower than the corresponding model without dissolution. Measuring the pressure reduction is difficult because the pressure is not shown as a curve anymore but as a wiggly line. The wavelength of the

undulations is relatively short at the beginning and increases with time (the undulations will be discussed later). The liquid phase saturation in the vicinity of the injection well is shown in Fig. 3.23. For the cells next to the injection well, the saturation is similar in both models.

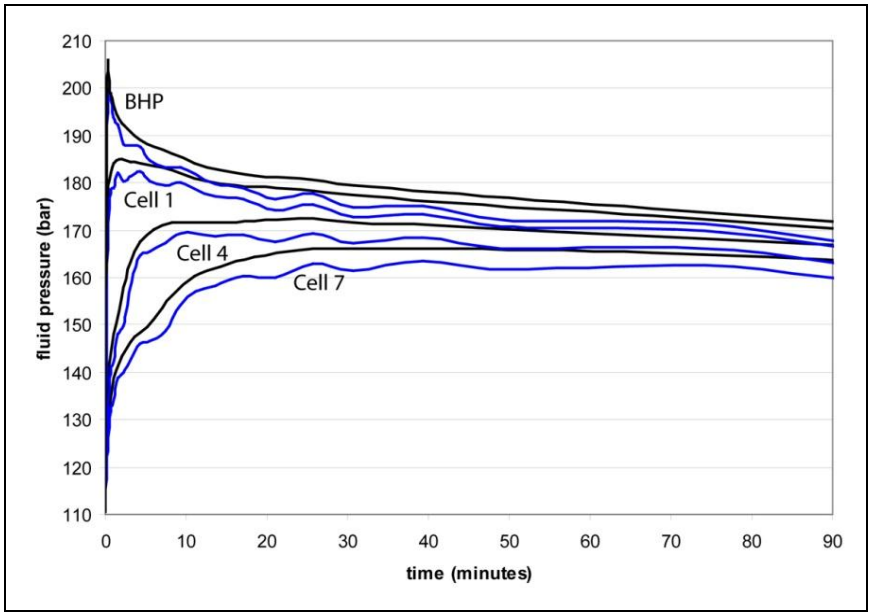

Figure 3.22: The graph shows the BHP (top curve) and the injection pressure of cells 1, 4 and 7 of the 'base case model' simulated with mutual dissolution of CO_2 and H_2O (blue) and without (black). Note the 'undulations' which appear when dissolution is included.

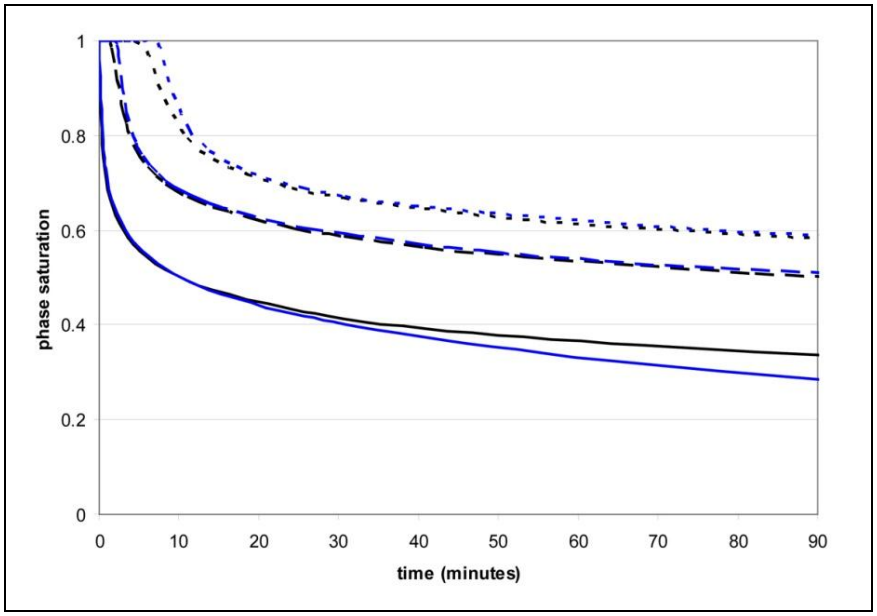

Figure 3.23: Graph shows the aqueous phase saturation of the 'base case model' with (blue) and without mutual dissolution of H_2O and CO_2 (black) of cell 1 (solid line), cell 4 (dashed line) and cell 7 (dotted line). Saturations are shown for cell 1 (solid lines), cell 4 (dashed lines) and cell 7 (dotted lines).

After approximately 20 minutes, the brine saturation decreases with a greater rate in the model with dissolution. After 90 minutes, the brine saturation is approximately 5 % higher for the model without dissolution. The brine displacement with increasing distance from the injection well starts slightly later if the model allows mutual dissolution. After 90 minutes, the aqueous phase saturation of cell 1 is 5 % higher in the model without dissolution. The saturation of cell 4 and cell 7 is lower by less than 1 % in the model without dissolution.

Temperature influencing the fluid pressure increase

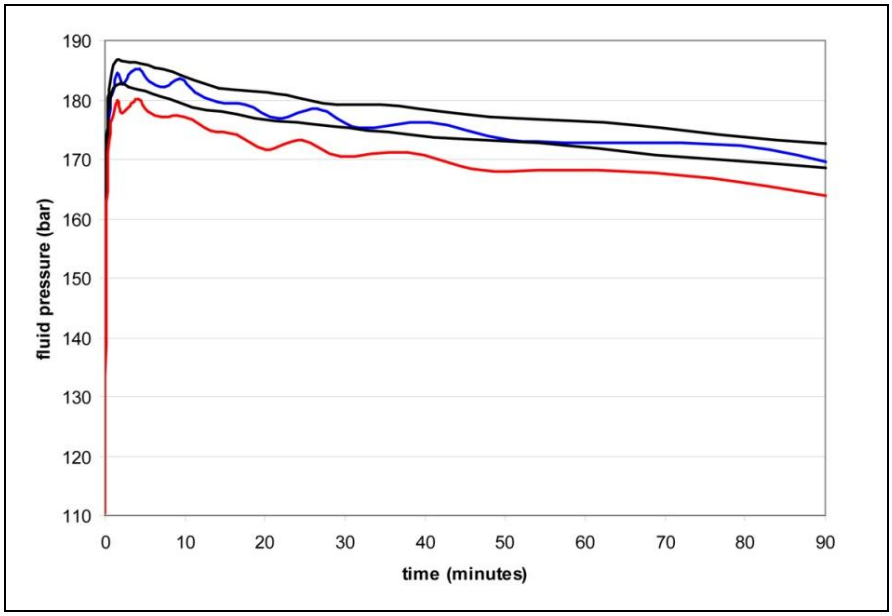

Figure 3.24: The graph shows the pressure increase in cell 1 of simulations which account for mutual dissolution with 30°C (blue) and 40°C (red). The corresponding injection pressure modelled without mutual dissolution is also shown for comparison (black).

Figure 3.24 shows the pressure development of the ’40 C model’ and the ’30 C model’ with dissolution in the cell next to the injection well and the pressure simulated without dissolution. The pressure decrease due to dissolution is greater in the ‘40 C model’ than in the ’30 C model’. After 90 minutes, the pressure difference between the two models with 40°C is ~5 bar and the pressure difference between the two models with 30°C is ~3 bar. Both models with dissolution show the same undulations except the undulation at minute 10 which is more defined in the ‘30 C model’. Additionally, the undulations of the warm model occur slightly earlier.

Salinity influencing the fluid pressure increase

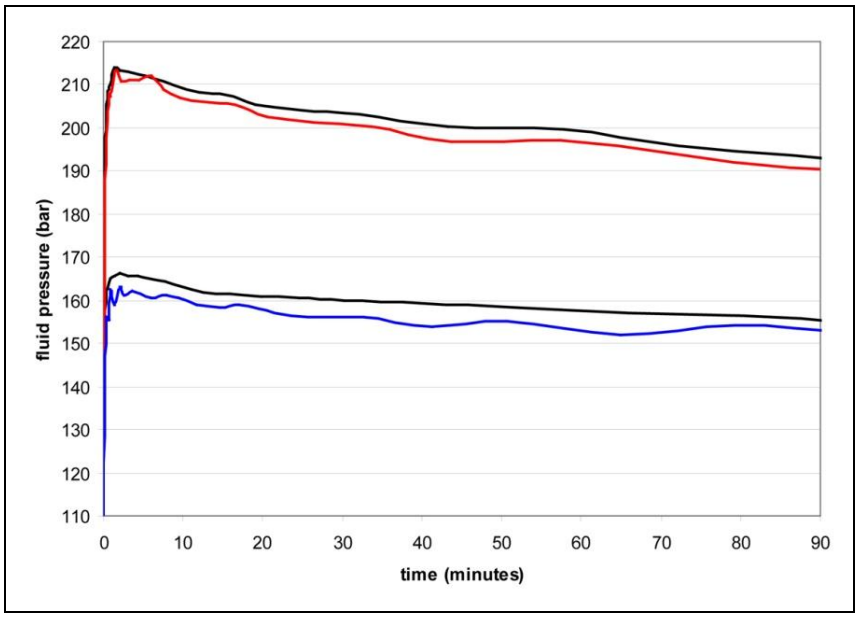

Figure 3.25: The graph shows the pressure increase in cell 1 of simulations which accounts for mutual dissolution with an aqueous phase and a salinity of 0.3 kg/l (red) and pure H_2O (blue). The corresponding injection pressure modelled without mutual dissolution is also shown for comparison (black). Note that modelled pressure with dissolution in the '0.3 kg/l model' exceeds the corresponding pressure modelled without dissolution at minute 7.

Figure 3.25 shows the pressure differences of models with high salinity and pure water with and without mutual dissolution. In the '0.3 kg/l model', the pressure difference is almost identical and the pressure reducing effect becomes recognizable after ~8 minutes compared to the model with no dissolution. After ~7 minutes, the modelled pressure is actually higher in the model that accounts for dissolution. The difference in pressure of the 'pure H_2O model' is greater. For the 'high 0.3 kg/l model' the maximum pressure difference between the dissolution and the no-dissolution model is ~0.5 bar and for the 'pure water model' the difference is ~3 bar. The undulations of the '0.3 kg/l model' have a lower amplitude and a greater wavelength compared to all previously described dissolution models. The most distinctive feature of the pure water model with dissolution is the very short wavelength, well-illustrated during the first 4 minutes of the simulation.

Mutual dissolution of CO_2 and H_2O

The amount of dissolved CO_2 and H_2O in the simulations is shown in Fig. 3.26. Results of the model with capillary pressure set to zero are not shown because only minor differences in the amount of dissolved CO_2/H_2O occur compared to the 'base case model'. Simulations with no rock compressibility also hardly change the dissolution compared to the 'base case model'. Temperature variation changes the amount of dissolved CO_2 slightly. The '40 C model' generally shows most of the time a slightly higher dissolution and the curve is shifted slightly to the left relative to the '30 C model' curve. After 90 minutes, the differences in dissolved CO_2 in the '40 C model' and the '30 C model' model with respect to the 'base case model' are relatively small (< 2.5 %). The impact of temperature on H_2O dissolution is more significant. After 90 minutes, the differences in dissolved H_2O in the '40 C model' and the '30 C model' model in relation to the 'base case model' are approximately -8.9 % and +9.7 %, respectively.

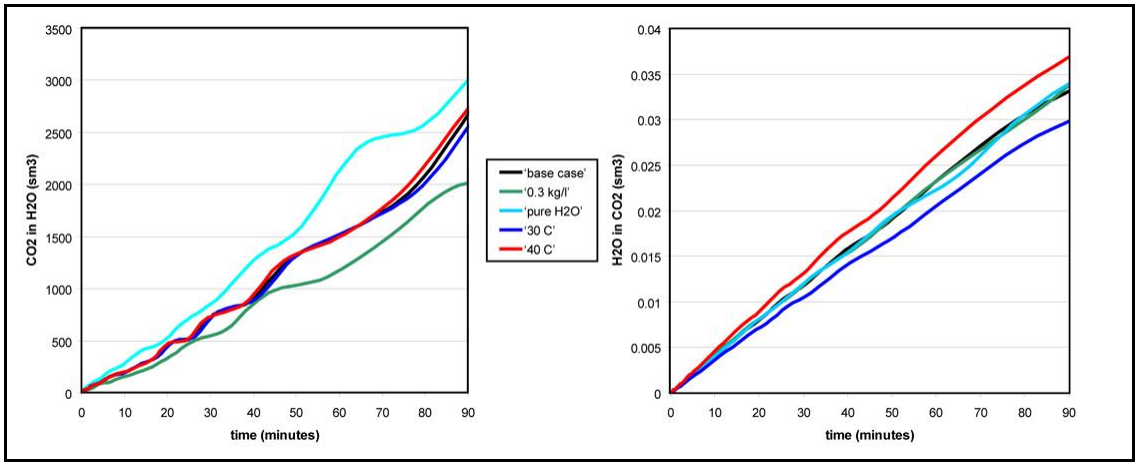

Figure 3.26: The left graph shows the amount of dissolved CO_2 in H_2O for different models. The right graph shows the amount of dissolved H_2O in CO_2. Unit is cubic meters under standard conditions (1 atm and 60°F).

If CO_2 injection into pure water or high saline brine is simulated, the variations in CO_2 dissolved into water are significant. The amount of dissolved CO_2 is higher in pure water (+13 % after 90 minutes) and lower in highly saline water (-27 % after 90

minutes). The dissolution of H_2O in CO_2 does not seem to be significantly affected by salinity variations. All dissolution variations in percent are strongly affected by the undulations of the graphs and have to be used carefully. The amplitude of the undulations is highest if the amount of dissolved CO_2 is highest.

The impact of mutual dissolution on the simulated maximum injection pressure in cell 1 is difficult to assess because of the undulations of the pressure graphs. If it is assumed that the average of the undulations represents the simulated pressure (Fig. 3.22; 3.24; 3.25; 3.26), then the pressure declining effect of the mutual dissolution lies between ~0.5 bar for the '0.3 kg/l model'. For the '30 C model' and the 'pure H_2O model', the pressure declining effect is ~4 bar and for the 'base case model' it is 3.5 bar. This corresponds to a reduction of the increase in injection pressure of between 0.5 % for the '0.3 kg/l model' and 7 % for the 'pure H_2O model'; the relative pressure reduction of the 'pure H_2O model' is 4.7 %.

3.5.3 Hydro fracturing in the vicinity of the injection well

If a fracture pressure of 150 bar is selected, the rock around the injection well will be fractured. All modelled pressure increases exceed the fracture pressure, often in several cells with increasing distance from the injection point. Figure 3.27 shows the pressure development in the vicinity of the injection well for simulations with and without mutual dissolution of CO_2 and H_2O. Even the pressure in cell 7 exceeds the fracture pressure by ~16 bar without mutual dissolution and by ~13 bar if dissolution is accounted for.

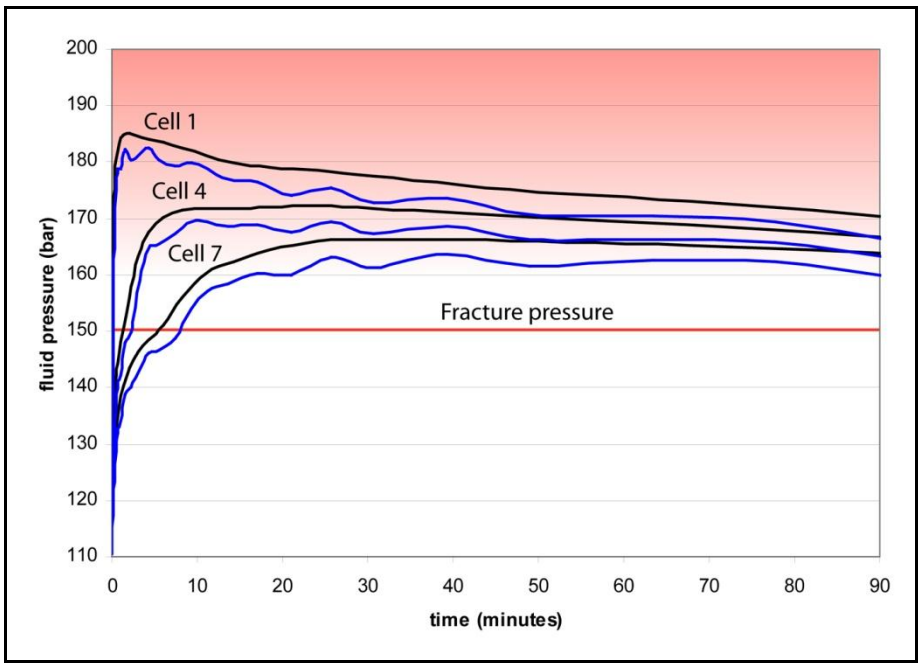

Figure 3.27: The graph shows the injection pressure of cells 1, 4 and 7 of the 'base case model' simulated with mutual dissolution of CO_2 and H_2O (blue) and without (black). The previously determined fracture pressure is illustrated by a red line. If the pore pressure exceeds the fracture pressure (red area) the rock stability will be compromised. The pressure of all cells of both simulations exceeds the fracture pressure.

3.6 Discussion

3.6.1 Pressure increase in the vicinity of the injection well

The main difference in pressure between the simulation of the injection of a gas phase into an aqueous phase and the simulation of an aqueous phase into another aqueous phase is the absence of a pressure pulse in the latter case. If two phases are present, phase saturation dependent parameters and phase dependent fluid properties become important. If one phase (e.g. supercritical CO_2), is injected into a different phase (e.g. liquid brine), the pressure increases almost instantaneously in the vicinity of the injection point. The pressure rise is due to the displacement of the in-situ phase by the invading phase. Two main factors are responsible for the pressure peak:

Firstly, differences in fluid properties such as viscosity have an important impact. If a low viscosity phase is injected into a relatively high viscous phase, a certain momentum has to be applied to shift the interface, which separates the two phases, away from the injection point. The higher the necessary momentum is, the higher the pressure accumulation will be. The subsequent decrease in pressure is also dependent on the decrease in velocity of the migrating phase interface. Because the surface of the front increases dramatically with increasing distance, the velocity of the phase front decreases and less power is available to move it further.

Secondly, relative permeability constrains fluid flow by making it dependent on phase saturation. Additionally, the presence of residual water saturation restricts parts of the pore network available for CO_2 migration. If one phase is injected into the same phase, the concepts described previously do not apply: neither a phase interface is present, nor a phase saturation. The pressure simply increases due to the injection process and prevails if the injection rate is kept constant. If injected into a closed system, both the two-phase and single-phase injection pressure will increase after a certain time as the overall system pressure increases due to mass-addition.

The pressure pulse, which occurs in the two-phase injection scenario, can be tracked over a given distance. The time when pressure is about to reach its maximum

(highlighted in Fig. 3.18) moves relatively slowly through the reservoir, and does not represent the diffusive front of the pressure wave. According to Mathias et al. (2009), the diffusive front can be calculated for cylindrical diffusion analytically from the following equation:

$$r^2 = \frac{2 \cdot t \cdot k}{\phi \cdot \mu_{v-CO_2} \cdot (c_w + c_r)} \qquad (85)$$

The radius (r) is given in meters, time (t) in seconds, k (permeability) in m^2, $\mu_{v\text{-}CO2}$ is the CO_2 viscosity in Pa*s and formation (c_r) and brine (c_w) compressibility is in $m*sec^2/kg$. By considering that the compressibilities, permeability and viscosity are constant, hydraulic diffusivity (D_h; see chapter 2.1.2 for more information) can be used to simplify the equation to:

$$r^2 = 2 \cdot t \cdot D_h \qquad (86)$$

According to equation (86), the diffusive pressure front migrates with a velocity of ~447 m per minute through the aquifer. The velocity of the diffusive front decreases in addition to the velocity of the brine/CO_2 phase front with time (Mathias et al. 2009). This analytical solution is based on a relatively simple model and these results cannot be applied on a more complicated model setup but it can be observed that the maximum pressure and diffusive pressure front are dissimilar.

All simulations of CO_2 injection into an aqueous phase show that a decrease in velocity of one (e.g. a decrease in salinity), or in both fluids (e.g. due to a temperature increase), will lead to smaller pressure accumulations. In particular, variations in salinity can alter the viscosity of the aqueous phase dramatically. The low injection pressure of models with linear relative permeability is related to the absence of a steep phase front and the absence of residual water saturation. In the

model, CO_2 can now occupy the entire cell whereas previously, residual water saturation restricted access to part of the cell. A more detailed discussion on the fluid flow and the impact of certain parameters is presented in the following paragraphs.

An analytical methodology for estimating pressure build-up due to the injection of CO_2 into a brine filled formation was presented in 2009 (Mathias et al. 2009; Mathias et al. 2009). Their solution assumes the Buckley-Leverett equation which describes one-dimensional two-phase immiscible flow. They improved the equation by incorporating formation and fluid compressibility and Forchheimer flow effects. By using their large-time approximation the estimated maximum pressure will be 138 bar. The analytical result is much lower than the maximum pressures modelled in this study. The comparison of the results remains difficult because analytical and numerical solutions use different assumptions and have different limitations. For example, the analytical approach presented by Mathias et al. (2009) assumes injection along the entire thickness of the reservoir whereas realistic injection scenarios would instead inject into the bottom of the reservoir.

3.6.2 The impact of temperature on pressure increase

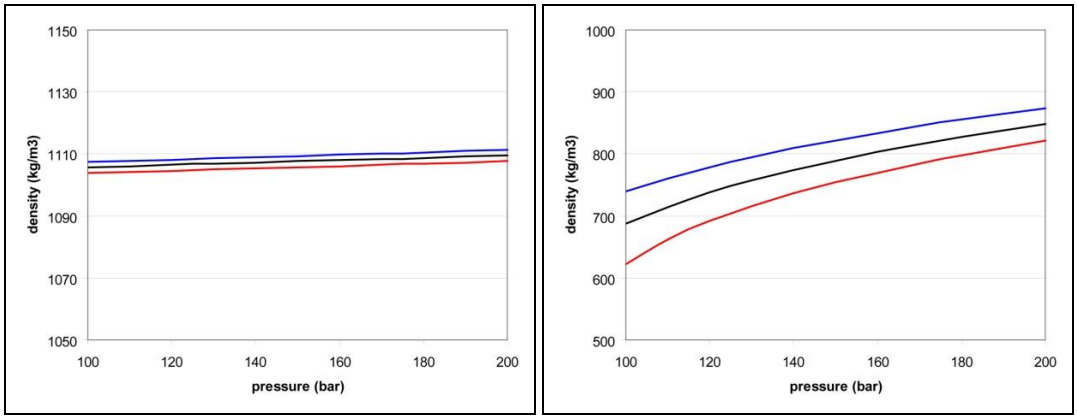

Figure 3.28: Density changes of brine (left) and CO_2 (right) with varying pressures for three different temperatures. The isothermal temperatures are 35°C ('base case model'; black), 30°C (blue) and 40°C (red).

The simulations with different temperatures provide a good example for investigating the impact of varying parameters on pressure. A change in temperature changes the properties of both CO_2 and brine; some of the variations reduce and others increase the injection pressure. First, the density of H_2O and CO_2 is temperature dependent (Fig. 3.28). The change in density of H_2O can be neglected because it is relatively small and the top pressure of the model is set to 100 bar by default. Therefore, the temperature variation only changes the initial pressure at the bottom of the reservoir slightly (initial pressure at the bottom cell of the reservoir for models with 30°C, 35°C and 40°C is 110.59, bar, 110.58 bar and 110.56 bar, respectively). The injection of warmer CO_2 into a reservoir has a pressure increasing effect because the volume of CO_2 under constant pressure increases with increasing temperature. A higher temperature also amplifies buoyancy forces, because of the decrease in CO_2 density with increasing temperature. Hence, the density difference between CO_2 and water increases, which results in an increased buoyancy force. The effect of amplified vertical migration due to buoyancy is not discussed further in this study.

Both H_2O and CO_2 viscosity decrease with increasing temperature (Fig. 3.29). Viscosity is one of the major drivers of fluid mobility. A low viscosity and corresponding high mobility will lead to an increase in fluid flow away from the injection well, both vertically and horizontally. Due to the enhanced fluid flow, the phase front will migrate faster and lower pressure accumulations in the vicinity of the injection well can be expected.

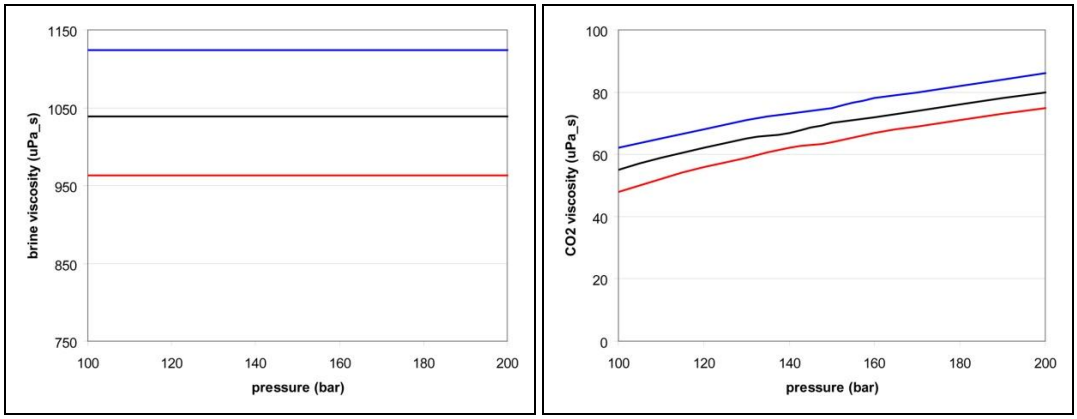

Figure 3.29: Viscosity change of brine and CO_2 at 30°C (blue), 35°C (black) and 40°C (red) and varying pressure.

3.6.3 The impact of salinity on pressure increase

Changes in salinity will alter the properties of brine but will not have an impact on the properties of CO_2. Increases in salinity will also increase the viscosity of the brine (Fig. 3.6) and the larger pressure accumulation for the high salinity model is mostly due to this increase. The viscosity change increase is not linear but rises significantly with increasing salinity (Fig. 3.6). As a consequence, the increase in injection pressure is also not linear.

By comparing the results of the different temperature and salinity models it may seem apparent that the impact of salinity has a greater effect on pressure. The impact of different parameters is not only dependent on the parameter itself, but also on the degree of its variation. Whereas the temperature variation was 5°C, the variations in salinity were, with respect to the salinity variation in saline aquifers, much more drastic.

3.6.4 Mutual dissolution of CO_2 and H_2O and the impact on pressure

What controls mutual dissolution?

Two parameters determine the rate of dissolution in the simulation:

1) By calculating the dissolution coefficients and adding them to the input file, the amount of one phase that can dissolve in another is defined. The coefficients are dependent on temperature and pressure and on the salinity of the brine. Figure 3.30 illustrates the dissolution coefficients for mutual dissolution as a function of temperature and pressure. Dissolution generally increases with increasing pressure. Temperature has a significant effect on the dissolution constants such that increasing temperature reduces the dissolution of CO_2 in brine and increases the dissolution of H_2O into CO_2. High salinity reduces the mutual dissolution of CO_2 and brine. Figure 3.30 shows that for the dissolution of CO_2 the dissolution coefficients of pure water are three times higher than those for high salinity brine.

2) The dissolution coefficients control how much fluid is allowed to dissolve within a cell. The second parameter that determines the degree of dissolution is the position of the CO_2 shock front. If the CO_2 reaches most of the grid cells where it can dissolve, the amount of dissolved CO_2 will be high. If the CO_2 migration is fast and a large number of grid cells are entered quickly, the dissolution rate will be high. Although this effect is mainly due to the model set-up, it is usually important for modelling mutual dissolution. This is illustrated in Fig. 3.31, where the dissolution is shown as a function of time for different temperatures. Although the dissolution coefficients are significantly lower at lower temperatures, for most of the time the amount of dissolved CO_2 is higher with elevated temperatures which tend to decrease the viscosity and enhance fluid flow.

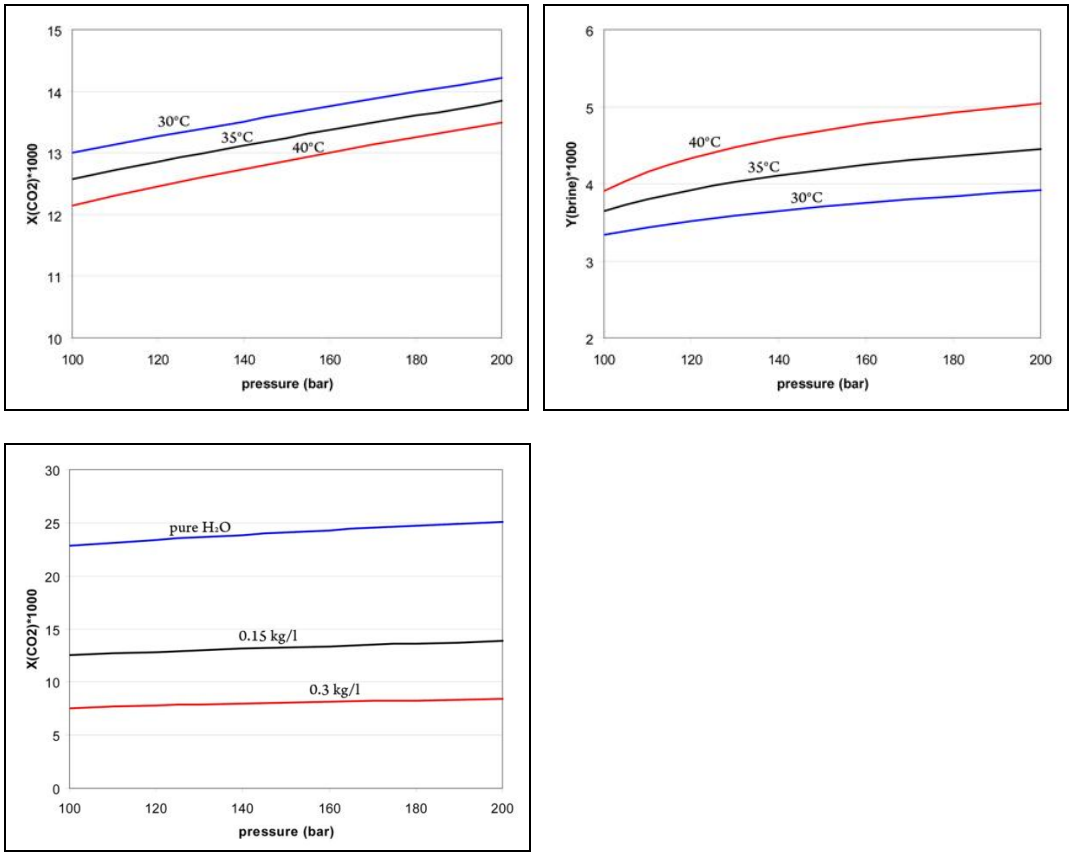

Figure 3.30: (Top figures): Mutual solubility of brine and CO_2 at 30°C (blue), 35°C (black) and 40°C (red) and varying pressures. x(CO_2) is the mole fraction of CO_2 in brine; y(brine) is the mole fraction of H_2O in CO_2. (Bottom figure): Solubility of CO_2 in pure water ('pure H_2O model', blue), intermediate salinity ('base case model', black) and highly saline brine (0.3 kg/l, red) and varying pressures.

The incorporation of mutual dissolution into the model will lead to a reduction in injection pressure if the dissolution constants have realistic values. Although brine swells if it is saturated with CO_2, the volume loss of supercritical CO_2 dissolving in H_2O should lead to a noticeable pressure decrease. Additionally, the viscosity increase of brine saturated with CO_2 is relatively small and will not alter the pressure significantly.

In theory, dissolution of CO_2 into H_2O occurs at two locations within the reservoir. Along the CO_2/H_2O interface and with ongoing migration of the phase front, this

interface grows. Additionally, CO_2 dissolves into trapped residual water, which is defined by the relative permeability curves. A reservoir simulator cannot model the CO_2/H_2O shock front but simulates cells with different phase saturations depending on pressure differences. Whenever CO_2 migrates in a H_2O filled cell, CO_2 and H2O dissolve instantaneously until the H_2O in the entire cell is saturated. Instantaneous dissolution is impossible in nature and is a simplification used in reservoir engineering software due to the absence of kinetic data for the chemical reactions involved. The consequence of the dissolution reaction is that a certain amount of CO_2 and H_2O is being removed which has a pressure reducing effect. Because the reaction is instantaneous, the system undergoes an immediate saturation change and the modelled pressure reducing effect is always highest. Since instantaneous dissolution does not occur in nature and the phase front and residual saturations are difficult to model, the 'real' injection pressure should lie somewhere between the results modelled without and those modelled with mutual dissolution.

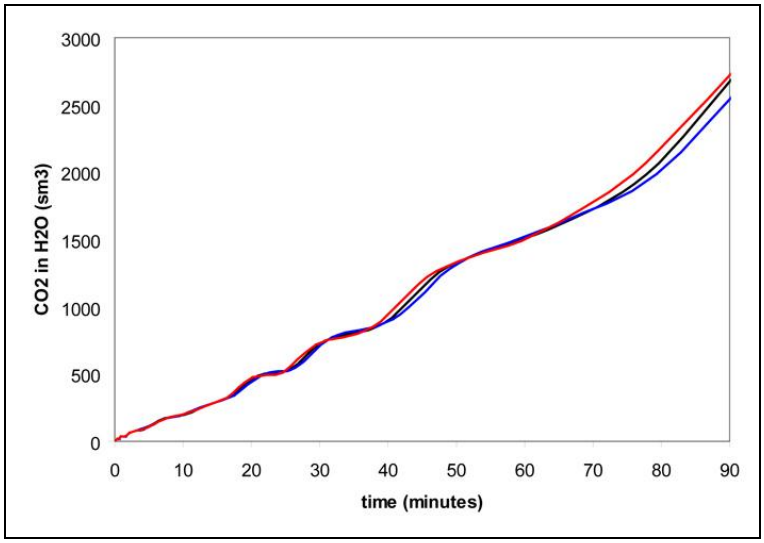

Figure 3.31: Amount of dissolved CO_2 of different simulations. '30 C model' (blue), 'base case model' (black) and '40 C model' (red).

The capability for H_2O to dissolve into CO_2 is much lower than the reverse case (see Fig. 3.26, 3.30) and additionally the amount of CO_2 into which H_2O can dissolve is much smaller than the amount of H_2O into which CO_2 can dissolve. Therefore the

pressure reducing effect of this reaction is minor and will not be discussed further within this study. However, the dissolution of H_2O into CO_2 can have an impact on the injectivity. In fluid flow simulations, residual brine saturation is modelled as being in contact with the invading phase. The residual water cannot be removed but it can dissolve into the dry CO_2 stream. With time the residual saturation decreases and will disappear eventually. This so called 'drying-out' effect leads to enhanced injectivity because it increases the relative permeability (Hurter et al. 2007). If the aqueous phase has a high salinity, the residual brine will be supersaturated relatively quickly and salt will precipitate and may eventually reduce the permeability (Pruess & Mueller 2009). The beginning of a dry-out effect is illustrated in Fig. 3.23. The aqueous phase saturation in cell 1 starts to decrease after ~ 25 min if mutual dissolution is activated compared to the saturation of a simulation with no dissolution. With time, the saturation will decrease further until no brine is left in the vicinity of the injection well. Salt is only present as dissolved in H_2O and its precipitation due to super-saturation is not allowed. Therefore permeability changes due to saturation changes are possible, but the permeability will not change due to theoretical salt precipitation. An additional reason for the change of the saturation profiles (Fig. 3.23) for the simulations with and without mutual dissolution is a change from the classic Buckley-Leverett shock front which separates two phases. If dissolution is activated, the near wellbore region of the injection well is occupied by CO_2 (and residual brine) surrounded by a zone of brine saturated with CO_2 and finally a pure brine region. Therefore two shock fronts have to be considered.

The reduction of the injection pressure increase simulated with the parameters used for the 'base case model' and model set-up used for this study is expected to be approximately 4-5 %. It will vary if the model set-up and the parameters (such as temperature, salinity or relative permeability) are changed and will be significantly lower if the salinity is high.

3.6.5 The origin of the 'undulations'

Simulations, which run with mutual dissolution of CO_2 in H_2O, show undulations of the pressure and of the amount of dissolved CO_2 (e.g. Fig. 3.22, 3.26). There is no chemical or physical explanation that could explain those undulations in nature. Therefore, they are seen as artefacts of the simulation and will not occur in engineered CO_2 injection scenarios. They lead to uncertainties in the injection pressure and injectivity simulations, thus they should be understood and if possible avoided. An interpretation of the undulations is proposed here which is based on the interrelation of the pressure, CO_2 dissolution, model cell size and the software used to perform these simulations. Model instabilities due to convergence problems can be excluded as a reason for the undulations. The simulations run with up to four convergence failures which is a relatively low number and this proves the stability of the model. To gain a better understanding of the problem, a new grid was designed. The difference of this 'special grid' is that cell 7 has a length of 3 m in the radial direction. In the simulation, migrating CO_2 will therefore flow out of a relatively small cell 6 (12 m^3) into a much larger cell 7 (296.9 m^3) rather than into a small cell 7 with a volume of 13.9 m^3.

Before their origin is discussed, several observations concerning the undulations shall be presented:

1. Undulations do not occur if mutual dissolution is deactivated (e.g. Fig. 3.18).
2. If linear relative permeability and mutual dissolution is used, no undulations can be observed (Fig. 3.32).
3. There is a correlation between pressure lows and an increase of dissolution in addition to a decrease of the dissolution rate and pressure highs (Fig. 3.33).
4. If the fluid mobility is increased, undulations of both pressure and dissolution appear earlier relative to models with lower fluid mobility (Fig. 3.33)
5. The wavelength of the undulations increases with time (e.g. Fig. 3.22, 3.33).
6. The amplitude of the undulations increases with increasing dissolution

coefficients (Fig. 3.25).

7. Both amplitude and wavelength increase with increasing cell size (Fig. 3.34).
8. If the cell size increases, the CO_2 dissolution rate increases while the pressure increases rapidly and subsequently drops. The dissolution rate then decreases simultaneously with a pressure increase (Fig. 3.34).
9. An increased cell size leads to undulations in a model with linear relative permeability (Fig. 3.32). These undulations are better described as pressure lows and dissolution highs followed by a normalization of both pressure and dissolution rate relative to the 'base case model'. Those undulations are different from undulations observed in models with mutual dissolution and relative permeability curves (Fig. 3.34).

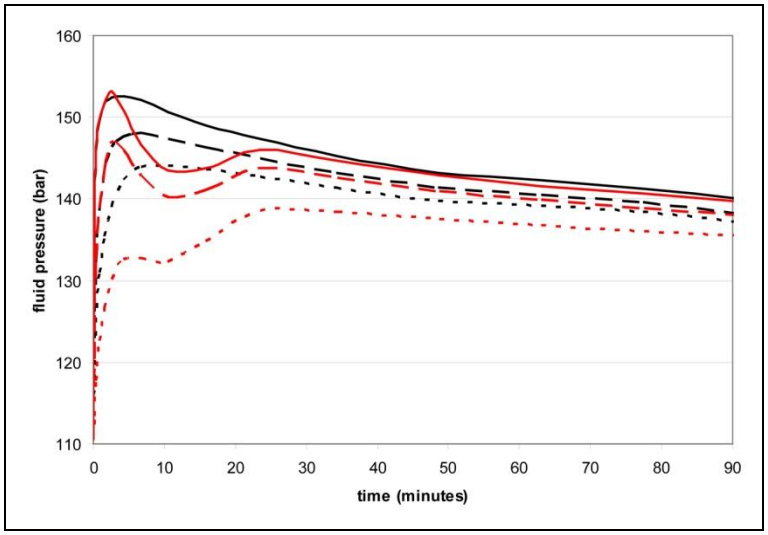

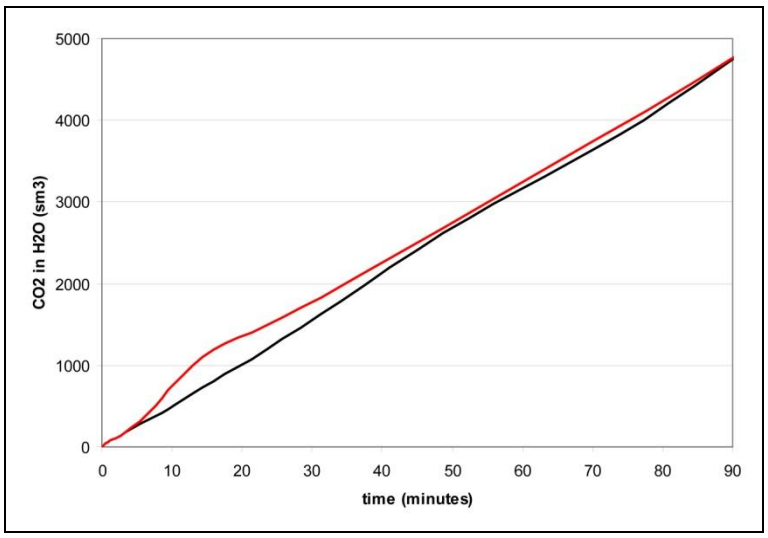

Figure 3.32: (Top figure) Simulation of the pressure in the vicinity of the injection well with linear relative permeability and no capillary pressure. The black graphs represent pressure simulations results modelled with the normal grid. The red graphs are results of models with the 'special grid' (see text). Pressure data are presented for cell 1 (solid line), cell 4 (dashed line) and cell 7 (dotted line). (Bottom figure) Amount of dissolved CO_2 for the simulations.

Accounting for all these observations, it becomes apparent that an undulation of the pressure and the dissolution occurs when CO_2 migrates into a fresh cell. Thus, two plausible explanations for undulations are possible:

1. When CO_2 migrates into a cell occupied by brine, instantaneous mutual dissolution takes place and a certain amount of CO_2 dissolves into the brine. Depending on the cell size, the volume decrease due to CO_2 dissolution may be high enough to pull the pressure down. Theoretically, this effect always takes place but becomes more dominant with increasing distance from the injection well (because the cell volume increases although the radial size remains similar). But if the grid is sufficiently fine, it is hardly recognizable. The pressure decrease and the increase in dissolution rate are apparent in Fig. 3.32, where CO_2 migrates out of a relatively small cell 6 into a significantly larger cell 7.

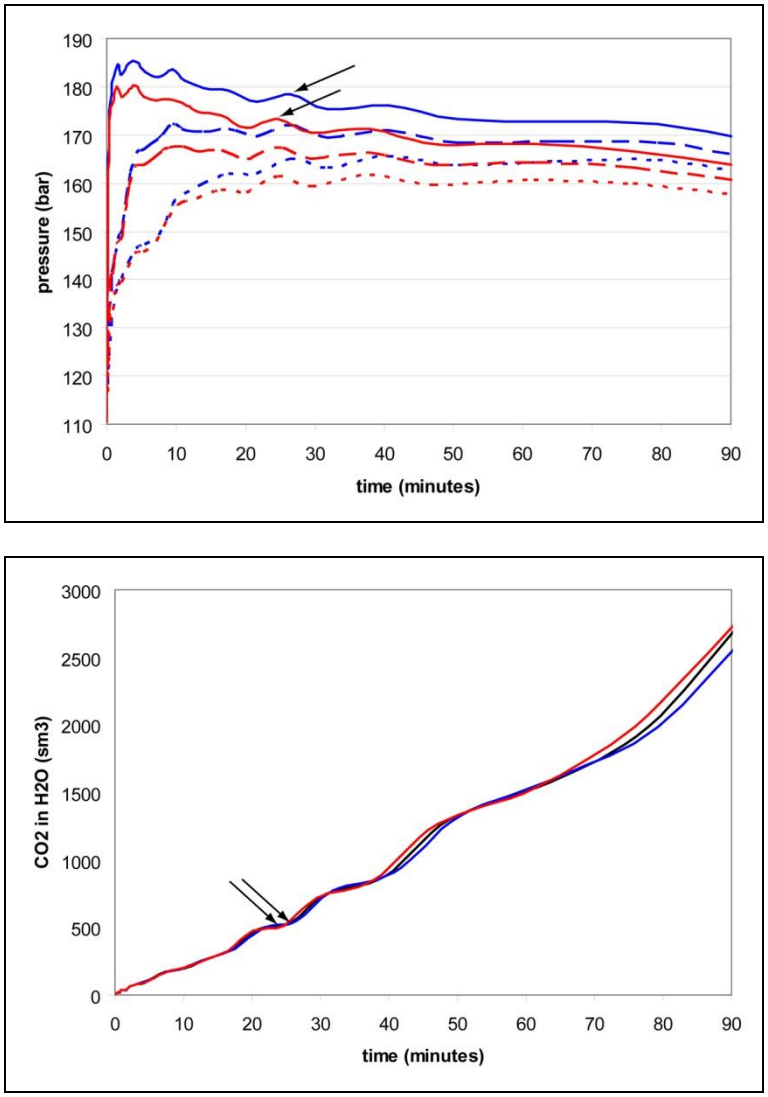

Figure 3.33: (Top figure): Pressure development in the vicinity of the injection well at 30°C (blue) and 40°C (red). Pressure data are presented for cell 1 (solid line), cell 4 (dashed line) and cell 7 (dotted line). The two arrows show pressure highs that occur simultaneously with the dissolution-lows in the bottom figure. (Bottom figure): Amount of dissolved CO_2 for the same simulations. The two arrows show dissolution-lows that occur simultaneously with the pressure highs as observed above.

The dissolution rate of the 'base case model' (Fig. 3.34), is lower than in the model with linear relative permeability (Fig. 3.32). The application of relative permeability curves changes the flow of the fluid significantly. According to the Buckley-Leverett theory, the application of relative permeability results in a steep fluid front that sweeps through the reservoir in a piston-like manner. For horizontal flow, with

negligible capillary pressure, the fractional flow (f_{CO2}) curve can be calculated with the following equation:

$$f_{CO2} = \left(1 + \left(\frac{k_{raq} \cdot \mu_{v-CO2}}{k_{rCO2} \cdot \mu_{v-aq}}\right)\right)^{-1} \quad (87)$$

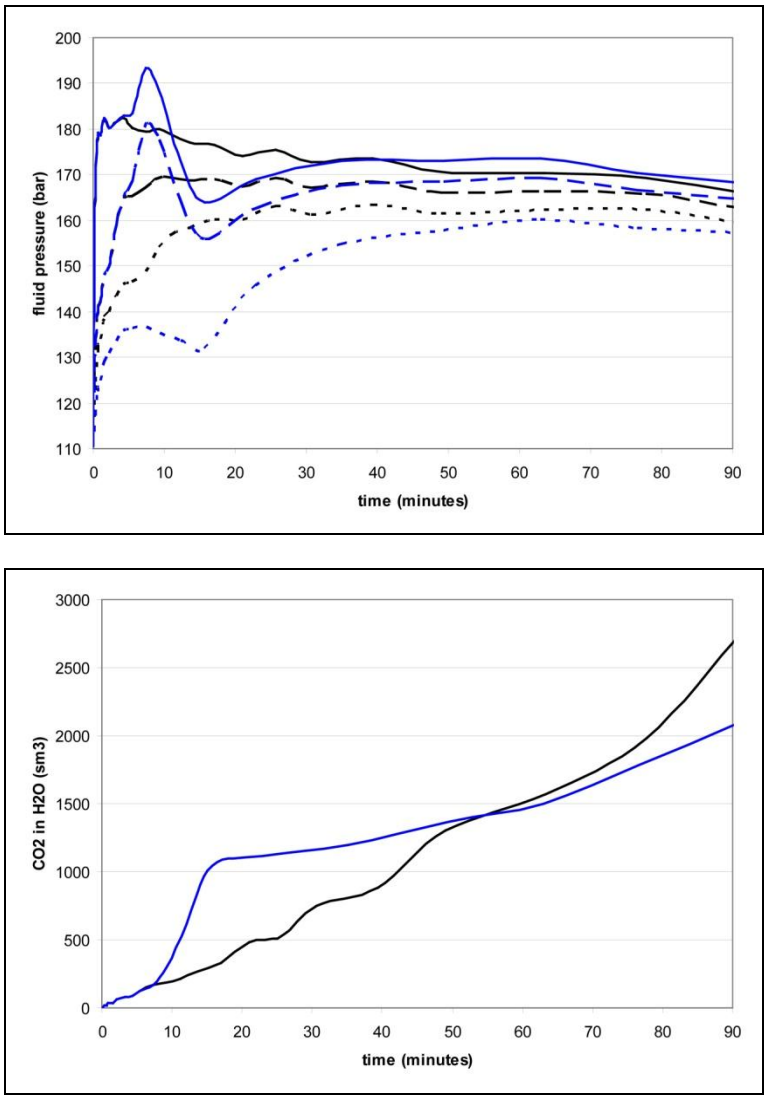

Figure 3.34: (Top figure) 'Base case model' simulation of the pressure in the vicinity of the injection well. The black graphs represent pressure simulation results modelled with the normal grid. The blue graphs are results of models with the 'special grid' (see text). Pressure data are presented for cell 1 (solid line), cell 4 (dashed line) and cell 7 (dotted line). (Bottom figure) Amount of dissolved CO_2 for the two simulations.

Figure 3.35 shows the solution for the relative permeability used in this study and for linear permeability. The determination of the CO_2 saturation at the phase front is shown graphically with the tangent of the fractional flow curve that has its origin at the residual CO_2 saturation. The same tangent for the fractional flow curve with linear permeability would be a vertical line. No piston-like sweep of the CO_2 front but a gradual increase of the CO_2 saturation would be expected.

A distinct CO_2 front would support a pressure pull-down because a maximum amount of CO_2 can dissolve if the front enters a new cell. A gradual increase in fluid saturation in numerous cells would lead to a more homogenous removal of CO_2 and therefore smaller dissolution driven pressure pull-downs.

However, the pressure decrease and the increase of dissolution rate due to this effect are not recognizable in the model with linear relative permeability and activated dissolution (Fig. 3.32, black lines). Although it can be speculated that it might appear if relative permeability curves are used, it is very unlikely that the undulations shown in Fig. 3.22 are related to this kind of dissolution effect. Additionally, the pressure pull-down due to enhanced dissolution cannot explain the increase in pressure before the pressure drop that is illustrated in Fig. 3.34.

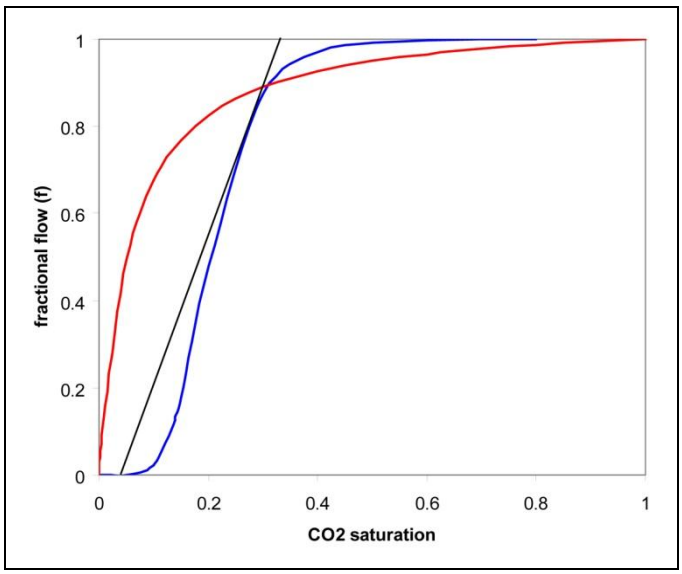

Figure 3.35: Fractional flow function of simulations with relative permeability (blue) and linear permeability (red). The point where the 'welge tangent' (Dake 1984; black) touches the fractional flow curve gives the Buckley-Leverett front height. The tangent for the linear permeability model would be a vertical line and no Buckley-Leverett shock front would appear.

2. Undulations are caused by a combination of mutual dissolution and relative permeability effects and usually show an increase in pressure and a decrease of the dissolution rate followed by a subsequent decrease in pressure and increase of the dissolution rate. If the dissolution constants are low, this artificial increase in pressure may even lead to pressures which exceed the pressure curves of simulations with no dissolution (e. g. '0.3 kg/l model', Fig. 3.25). The most logical conclusion is that the software over- and underestimates pressure and dissolution when invading a new cell. The average of the pressure and dissolution curves is therefore considered as being a good representation of the simulated injection pressure with activated mutual dissolution.

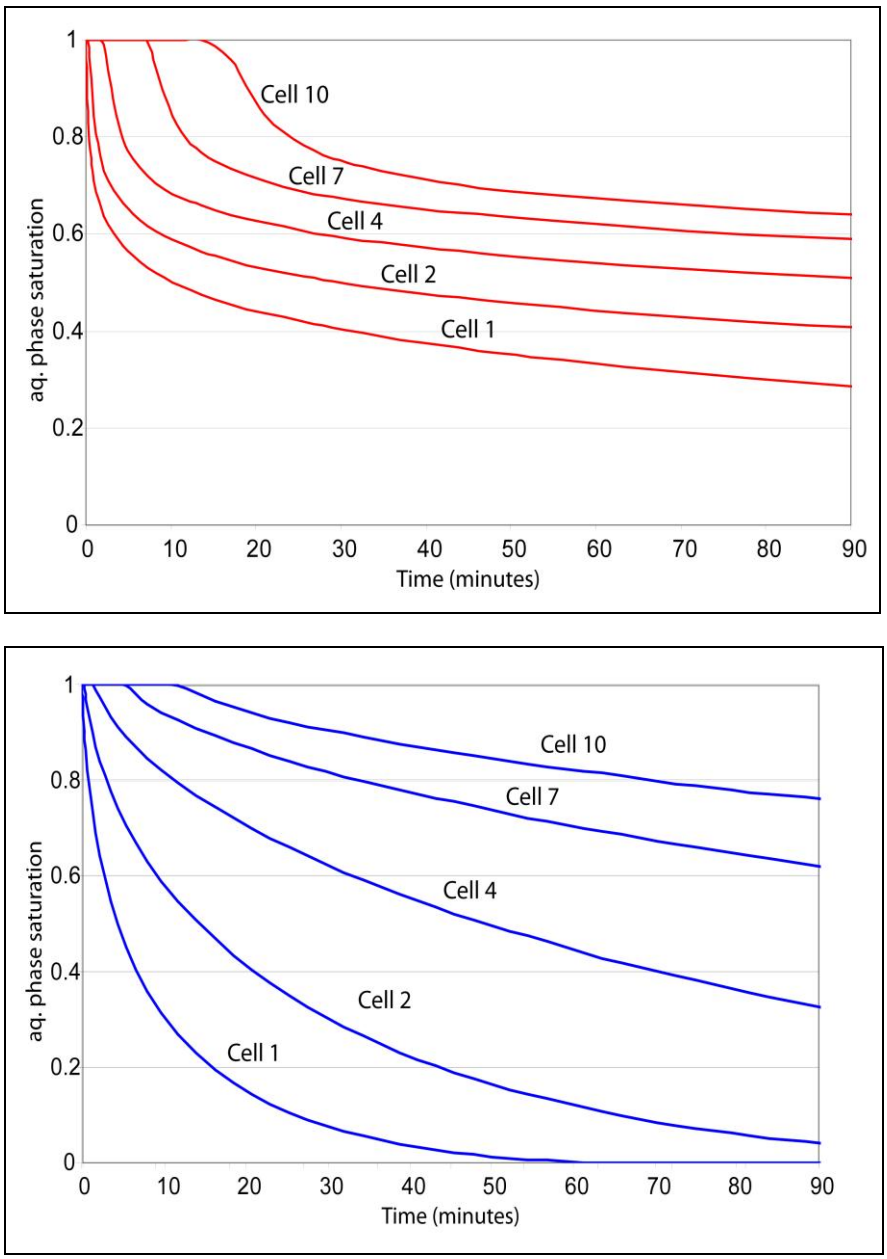

Figure 3.36: Aqueous saturation of simulations with curved relative permeability (above, red) and linear relative permeability (below, blue).

Final remarks on the undulations

As described previously, it is important for the accuracy of the injection pressure prediction to distinguish between the two possible origins of the undulations. Especially when the grid cells have a large volume adjacent to the injection well, the first explanation will lead to a significant pressure underestimation whereas the

second explanation will lead to an overestimation. The simulated injection pressures presented in Chadwick et al. (2009) are therefore impossible to interpret and do not provide an accurate representation of the real or simulated injection pressure.

3.6.6 Hydro fracturing in the vicinity of the injection well

The pressure increase in the vicinity of the injection well simulated in this study would be high enough to fracture the surrounding rock. However, the injection rate cannot to be seen as an independent parameter when it comes to pressure simulations in the vicinity of the injection well. An increase of the injection rate will only lead to an increase in pressure if the perforation length remains constant. If the perforation length is increased and the injection rate remains constant, the injection pressure decreases. The perforation length for the modelled scenario is 5 meters and the entire volume/mass of CO_2 will be injected through this relatively small interval. Many EOR injection scenarios use significantly longer perforations and/or horizontal injection wells that do not compromise the rock stability.

Although the pressure increase is relatively high, the applied injection rate of ~0.136 Mt per year is a relatively low injection rate for an industrial-scale injection project. However, in practice higher injection rates are usually accomplished by an incremental increase in the injection rate. This leads to a pressure increase that can be controlled by the operations staff and extensive formation damage can thus be prevented.

The intensity of the pressure peak crucially depends on the cell size and the location of the pressure measurement point. If the cell size is small and its position is close to the injection point, the pressure may almost be as high as the bottom hole pressure. If, as in the study performed by Chadwick et al. (2009), the ‘mesh element at the injection point is 2 m high and 5 m in radius’ (Chadwick et al. 2009), the modelled

pressure increase will be relatively small although the injection rate is much higher and the their results do not have much value for CO_2 injection scenarios.

3.7 Conclusions

The injection of CO_2 at a rate of ~0.136 Mt per year into a saline aquifer has been simulated with a black oil simulator. The aquifer has a top formation depth of 1 km and a thickness of 100 m. Injection took place in the lowest 10 m of the aquifer. The rock properties were taken from North Sea Bunter Sandstone aquifer studies and had a porosity of 18 % and a horizontal and vertical permeability of 100 and 10 mD respectively. The in-situ brine salinity was 0.15 kg salt in 1 kg water.

The results of this study show that if CO_2 is injected into a reservoir, the pressure in the vicinity of the injection well will increase to very high values and is likely to damage the rock formation. Because rock stability is crucial for successful CO_2 storage operations, accurate simulations concerning the fluid pressure increase are required to achieve an optimum injection scenario that will not compromise the formation or be unviable in economic terms.

Subsurface formations have a sensitivity to high pore pressure. The most likely reaction for reducing an increase in pore pressure is shearing along existing fractures. Considering the simulation conditions used for this study, a pore pressure increase of ~37.5 % relative to hydrostatic will compromise formation stability.

Temperature and salinity variations will change the properties of the fluids involved in a CO_2 storage operation and can reduce or increase the injection pressure. Salinity in particular, can have a distinct impact because it changes the viscosity of the aqueous phase significantly. An accurate determination of these two parameters is crucial to ensure a realistic injection pressure simulation.

Simulated mutual dissolution of H_2O is always an overestimation because it occurs instantaneously. However, the degree of overestimation can be reduced if the grid is sufficiently small. Generally, the injection pressure reduction effect of mutual dissolution varies and should be accounted for. To model it realistically, both dissolution coefficients and fluid properties need to be determined as accurately as possible because dissolution is determined by a combination of fluid flow and the dissolution itself.

If mutual dissolution and relative permeability curves are accounted for, the simulation of a CO_2 injection scenario leads to the development of undulations for the pressure and dissolution profile. These undulations can either be related to:

1) Enhanced mutual dissolution due to grid effects, or
2) Over- and underestimation of pressure/dissolution. A detailed interpretation of the undulations is necessary to determine whether they underestimate the pressure.

The undulations observed in model results presented in this chapter are presumably due to the latter and the average of the undulations is believed to provide an appropriate result – with respect to the impact of mutual dissolution.

4 CO_2 storage capacity calculation of the Bunter Sandstone Formation, UK southern North Sea, based of fluid pressure

4.1 Introduction

4.1.1 Introduction to the problem

This study proposes a new method to calculate CO_2 storage capacity based on fluid pressure, taking advantage of independent pressure compartments (compartments with impermeable boundaries) during a multi-well injection scenario. The method could be useful for estimating the capacity of poorly known large scale aquifers because only basic data on the aquifer information are needed.

Fluid pressure is not a static value; it changes with time due to injection processes and the mutual dissolution of CO_2 and H_2O and varies not only vertically but also horizontally. Therefore, a numerical simulator is needed to take all the parameters into account. We compare our method using a numerical simulator with a simple analytical approach to calculate the pore pressure increase. The study shall show how important the impact of parameters and effects are, which can only be taken into account by a numerical simulator, and therefore will answer the question whether a numerical simulator is necessary or not. To calculate a theoretical maximum sustainable pore pressure we use real data from leak-off pressure tests from the North Sea. As a case study, we take a closer look at the Bunter Sandstone aquifer (southern North Sea). Finally, we compare our results with a CO_2 storage capacity estimation performed by Holloway et al. (2006).

4.1.2 Fluid pressure as storage capacity estimation

Fluid pressure is one of the key parameters affecting the physical strength of rock within the Earth's crust and it has long been known that an unusually high fluid pressure triggers hydro fracturing or fault reactivation (Raleigh 1976; Sibson 1981;

Rutqvist & Tsang 2002). The injection of CO_2 into a geological formation leads to an artificial and rapid increase of fluid pressure. During the injection process the reservoir fluid pressure will remain relatively high and therefore compromises the stability of the potential CO_2 storage formation and overlying cap rock. Therefore, fluid pressure is one of the limiting factors for estimating the CO_2 storage capacity and a pressure which guarantees a safe injection process has to be determined.

The maximum sustainable pore pressure depends on several parameters such as rock mechanical properties, the orientation and type of the stress regime, the magnitude of the regional stress field and the increase of fluid pressure during injection. These factors are commonly unknown. Therefore we used a different approach in order to avoid the uncertainties of a calculated maximum fluid pressure. Moos et al. (2003) presented a fracture-pressure gradient from several wells in the central North Sea. The fracture-pressure gradient was determined from leak-off pressure data designed to test the strength of the formation around the well.

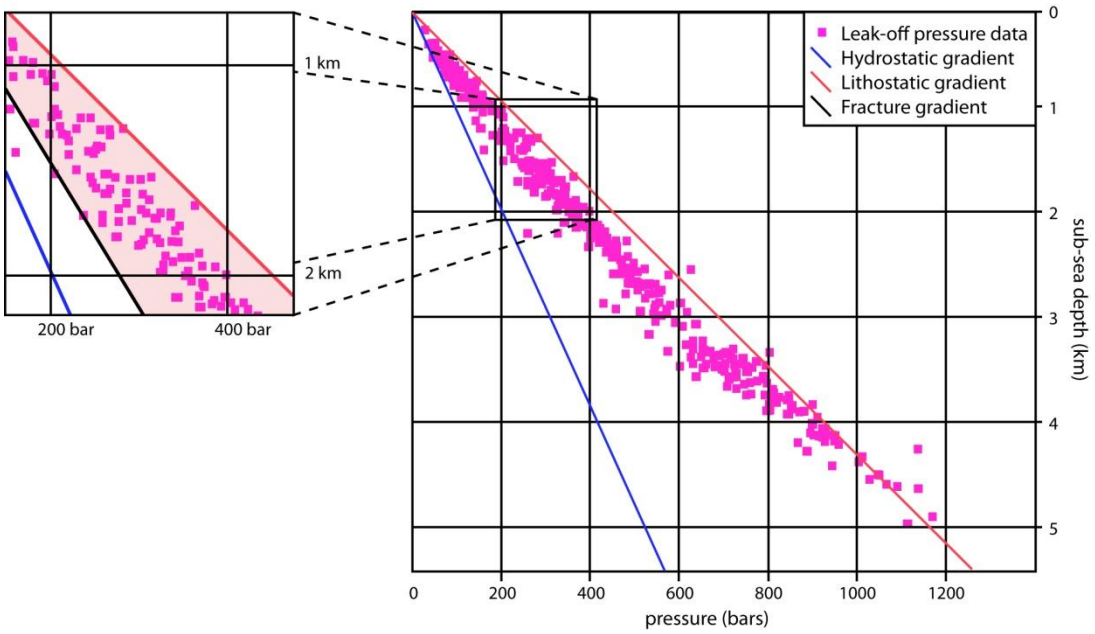

Figure 4.1: Estimated fracture-pressure gradient of a depth around 1500 m, a typical depth range of potential CO_2 storage sites in the southern North Sea. Due to overpressure in the Mesozoic formations of the central North Sea the fracture pressure increases relative to the

lithostatic pressure at greater depth. Therefore the overall fracture gradient cannot be drawn as a single gradient. Redrawn from Moss et al., 2003.

Leak-off pressure data should not be mixed up with shut-in pressure which is seen as a representation of the minimum horizontal stress. According to Jaeger (2007), the shut in pressure represents the minimum horizontal stress but Bell (1990) suggested that leak-off pressure overestimates the minimum horizontal stress by <5%. This is mainly due to a disturbed stress field at the wellbore wall and the tensile strength of the surroundings (Hillis 2001) but the lower bound to leak-off pressures is accepted as an estimate of the minimum horizontal stress (Breckels & van Eckelen 1982; Gaarenstroom et al. 1993). Leak-off is defined to occur when a crack opens in a sealed well and drilling fluid is able to penetrate the surrounding rock mass. Leak-off pressure data are routinely collected during drilling scenarios. Figure 4.1 illustrates that the fracture gradient is not a straight line but changes with increasing depth. For example, at a depth of 1500 m a reasonable assumption for the maximum fluid pressure is 60 % of the lithostatic pressure. Fracture pressure data only measure the response of a rock to a relatively rapid pressure increase in the vicinity of the test well. Natural faults, which could act as potential leakage pathways for stored CO_2, are not accounted for in the tests, neither are the potential effects of long-term high fluid pressure. Increased fluid pressure may open fractures, or shear movement may occur on fault planes (Rutqvist et al. 2007). Faults are especially sensitive to fluid pressure changes, which has particular relevance to CO_2 storage in the subsurface. When over-pressured, fault rupture may compromise permeability barriers causing an episode of fluid discharge until the pressure in the aquifer is reduced. CO_2 leakage along activated fault surfaces, so-called 'fluid activated valves' (Sibson 1990) could cause an effective thinning of the sealing rock formation.

4.1.3 The Bunter Sandstone aquifer as a CO_2 storage site

Within the southern North Sea, there are two large saline formations in which UK and other European CO_2 emissions could potentially be stored. These are the Triassic

Bunter Sandstone and the Permian Rotliegend Sandstone. The Bunter Sandstone (Fig. 4.2) is the subject of this study as the formation is hardly compartmentalised by sealing faults, and is less deeply buried than the Rotliegend Sandstone (Vandeweijer et al. 2009). The Bunter Sandstone consists of red, orange and white sandstones which are mostly fine grained, but contains some localised regions which are medium or coarse grained (Rhys 1974). It is underlain by the Bunter Shale, a 300 m thick formation which consists of mudstone, and overlain with a thick layer of partially anhydritic mudstone. The seal is commonly in excess of 500 m thick so that thinning by fault movement should not be significant. The Bunter Sandstone forms several dome structures which were created mainly by movement of the deeper Zechstein salt (Bentham 2006). Most of these domes are filled with brine and only a few Triassic structures in the southern North Sea hold natural gas (Cameron et al. 1992).

To ensure safe CO_2 storage, both the injection period and long-term fate of the CO_2 plume have to be considered. Since there are few gas fields in this area, mainly due to a lack of hydrocarbon supply constrained by the underlying mudstones, one of the major risks is the seal quality. Fortunately, there are a small number of gas fields with a Bunter Sandstone reservoir, where the seal has proven to be effective – the Hewitt Field group in the SW of the area, and the Esmond, Forbes and Gordon fields in the north of the area (Fig. 4.2). By comparing the seal above the gas fields with that in the remainder of the area, it can be deduced that the Bunter Sandstone is likely to be effectively sealed (Heinemann et al. 2012).

Holloway et al. (2006) calculated the average thickness of the southern North Sea Triassic aquifer to be 140 m in the British territory of the North Sea. The depth to the top of the Bunter Sandstone is variable because the formation is gently folded and dips on average to the east away from the outcrops of onshore England. We set the depth of the formation top to be at 1500 m, which is the average depth of the Bunter Sandstone Formation in the target area. As a 'maximum sustainable injection pressure' we extrapolated the leak-off pressure data presented by Moos et al. (2003)

to the southern North Sea. We assume that the lithostatic pressure gradient of the southern North Sea increases by 250 bar per km depth which is within the generally accepted range for sedimentary basins (Allan & Allan 2005). Since the confining pressure increases the rock strength we used the calculated lithostatic pressure as a reference.

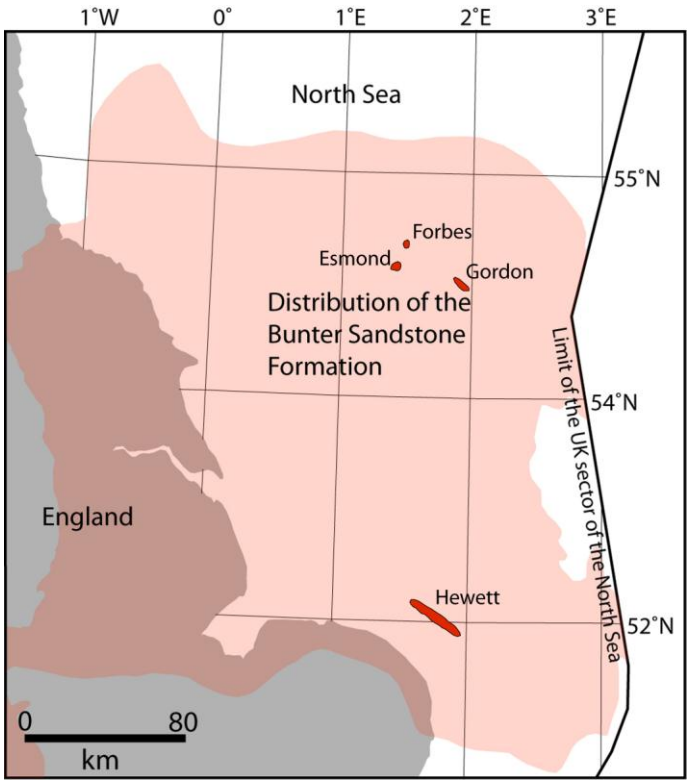

Figure 4.2: Distribution of the Bunter Sandstone Formation (red shaded area) of the southern North Sea. Also shown are the Triassic gas fields which are mentioned in the text. Modified after Holloway et al. 2006.

4.2 Method

4.2.1 A new method to assess CO_2 storage capacity

We propose a method to calculate CO_2 storage capacity of saline aquifers based on fluid pressure. The basic idea is to divide a saline aquifer into many homogenous pressure compartments. By implementing a symmetric grid of injection wells over the entire dimension of the aquifer, every compartment consists of one injection well and its adjacent area. By simulating the injection into one of the compartments with reservoir engineering software the CO_2 storage capacity can be calculated. Each well injects a fixed quantity (1 Mt per year) of CO_2 at a constant rate over a fixed period of time (30 years). The injection period was taken from other CO_2 injection studies (e. g. Birkholzer et al. 2009; Ghanbari et al. 2006) and is regarded as the average lifetime of a coal combustion power plant. The increasing fluid pressure in the vicinity of the injection well cannot dissipate because it is surrounded by other injection wells, each with its own pressure zone. Because of the high degree of symmetry of this idealised scenario, only a quarter of a cell needs to be analysed. Since all boundaries of this unit have pressure gradients perpendicular to the boundaries (i.e. the pressure is symmetrical across them), all boundaries are effectively no-flow boundaries (Fig. 4.3).

Each pressure compartment contains one quarter of an injection well into which one quarter of the total CO_2 per year is injected. In such a regular system, pressure build-up and hence the amount of CO_2 that can be stored will be determined by the size of the pressure cell. If the well spacing, that allows the safe injection of 30 Mt of CO_2, is known, the overall CO_2 capacity of the aquifer can be calculated. The assumed model set-up is relatively simple but could be adjusted to a certain extent. For example, the simple addition of permeable upper and lower model boundaries would take pressure dissipation into account. A disadvantage is that horizontal injection wells are difficult to include in the model because their geometry would interfere with the highly symmetric basic assumption of the method.

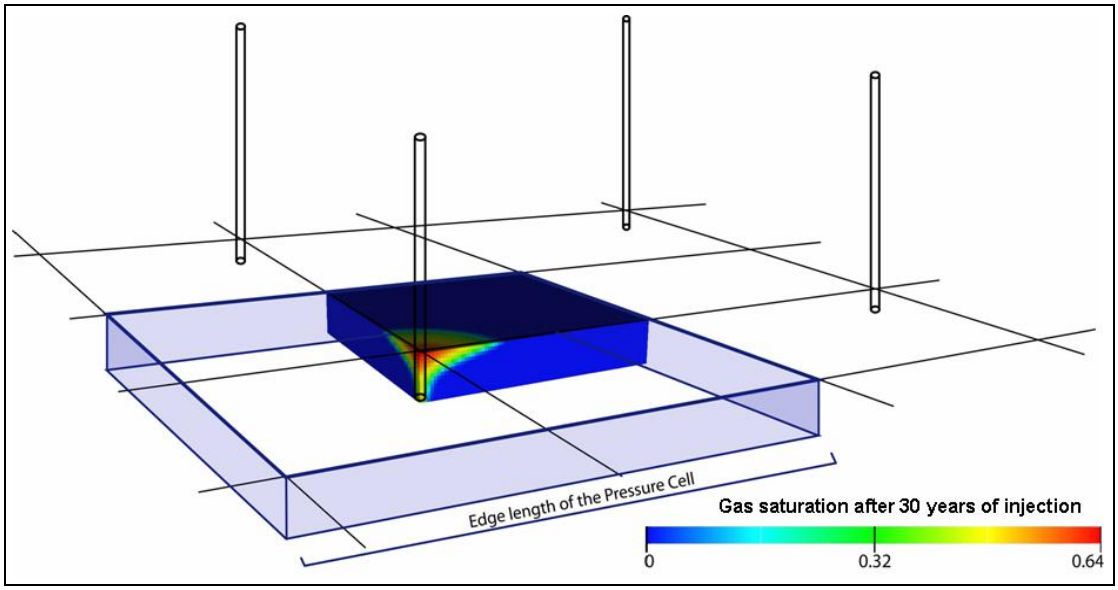

Figure 4.3: Simplified view of an isolated pressure cell. Each cell has a single CO_2 injection well in its centre. Cell boundaries follow the area between the injection wells where the pressure cannot dissipate. Due to the symmetry only one quarter of the elementary cell and one quarter of the actual injection has to be simulated. The model shows the gas saturation of a developing CO_2 plume after 30 years of injection into a pressure cell with an edge length of 15.4 km.

The average thickness of the Bunter Sandstone is set to 140 m; a top depth of 1500 m was used as an average. Although the burial depth of the aquifer is variable, the density of CO_2 over the likely range of injection depth will not vary significantly (Chadwick et al. 2008). Assuming a temperature gradient of around 33˚C per km and a surface temperature of ~5˚C, a temperature of 55˚C was chosen for the top of the formation. The temperature at the bottom of the formation was 60˚C. The initial fluid pressure is 150 bar at the top and has an average value of 157 bar. If, as a result of CO_2 injection, the pore pressure within the formation exceeded the strength of the rock, then fracturing would occur and endanger the integrity of the seal.

Chemical reaction between the rock and the acidified pore water is neglected in the proposed CO_2 storage calculation method. This is justified for the Bunter Sandstone aquifer by the absence of significant reaction products in natural Rotliegend Group

reservoirs in the southern North Sea which have been exposed to high concentrations of CO_2 for geological time (Wilkinson et al. 2009). However, the Rotliegend Group sandstones have only c. 5 % feldspar (Ziegler 2006) where as the Bunter Sandstone can be substantially more feldspathic; e.g. an average of 30% feldspar in the Middle Bunter of the Thuringian basin (Götze 1998). Therefore reaction products could potentially be more abundant than reported by Wilkinson et al. (2009).

The conceptual model is relatively simple but could be refined. For example, the addition of permeable upper and lower model boundaries would take pressure dissipation into account. Horizontal injection wells cannot be included because their geometry would interfere with the symmetry of the model. Pore fluid pressure is reported from the cell located at the top of the reservoir, directly above the injection well, where the pore fluid pressure is maximal. In a homogeneous system, this is the location where mechanical failure of the seal is most likely. The initial fluid pressure at the top of the reservoir is 150 bar and the maximum permissible fluid pressure is 225 bar. The model cannot include heterogeneities in either reservoir or seal unit, e.g. due to pre-existing fractures. However, the reservoir could be layered, i.e. have multiple horizontal layers, each with uniform rock properties. The use of a single, non-layered, model was justified by examination of gamma ray logs from wells penetrating the formation, which show overall uniform values, lacking in either significant vertical variation, or intra-reservoir shale layers that could partition a significant portion of the reservoir (Heinemann et al. 2012).

Rock properties are uniform throughout the model: horizontal permeability is 250 mD, which is a conservative estimate compared to the Bunter gas accumulations (e.g. Hewett gas field: 500 mD; Cooke-Yarborough 1991); vertical permeability is 25 mD based on a generic vertical to horizontal permeability ratio of 1:10; and porosity is 18 % (Holloway et al., 2006).

Carbon dioxide is injected through the lowest 10 meters of the well. All outer boundaries have no-flow conditions. The vertical thickness of the model is 140 m, according to the average thickness of the Bunter Sandstone; the horizontal extent

varies with every model run. Pore water salinity is 0.15 kg/kg, which lies in the salinity range of the Triassic Bunter Sandstone reservoirs in the southern North Sea (Ketter 1991). In the absence of measured data from the Bunter Sandstone, experimental relative permeability data are taken from Bennion and Bachu (2006). The data were measured from sandstones and conglomerates of the Cardium Formation in the Pembina area, Canada, conducted under the conditions of 200 bar, 43˚C and a salinity of 27.096 g/l. Capillary pressure was modelled after van Genuchten (1980):

$$P_c = P_0\left(\left[S*\right]^{-1/m} - 1\right)^{1-m} \qquad (1)$$

The effective saturation is:

$$S* = (S_w - S_{rw})/(1 - S_{rw}) \qquad (2)$$

The chosen parameter values are mp=0.5614 (for 'loamy sand', Pruess et al. 2003) and for the strength coefficient (P_{c0}) 0.0358 bar (for 'sand', Pruess et al. 2002). The residual water saturation was set to 0.197, according to the experimental data (Bennion & Bachu 2006). For further information see chapter 2.1. The van Genuchten formula does not allow the calculation of the capillary pressure for the actual residual saturation. This makes sense because theoretically, the pressure should be infinite. A reservoir simulator requires a capillary pressure value for the residual saturation and this value has to be chosen carefully and has to be listed. For the calculation of the capillary pressure at the residual water saturation of 0.197, models conducted for this study use a theoretical residual water saturation of 0.1971.

The simulations were performed using ECLIPSE300 CO_2STORE **(**Schlumberger 2008), a reservoir simulator used extensively by the oil and gas industry. The

CO_2STORE option is a 'black box' simulator. This means that the option is inflexible and uses default values and parameters. Additionally, the physics behind the CO_2STORE option is difficult to check, mainly because the descriptions are poor and badly explained. It is rather an add-on for engineers who do not know a lot about the physics of the brine/CO_2 system and are not interested in more details. It will be discussed in the next chapter that such a 'black box' option is not necessarily needed if the physics and chemistry of the brine/CO_2 system is known. Another disadvantage of these 'black box' simulators is that general research progress can often not be implemented.

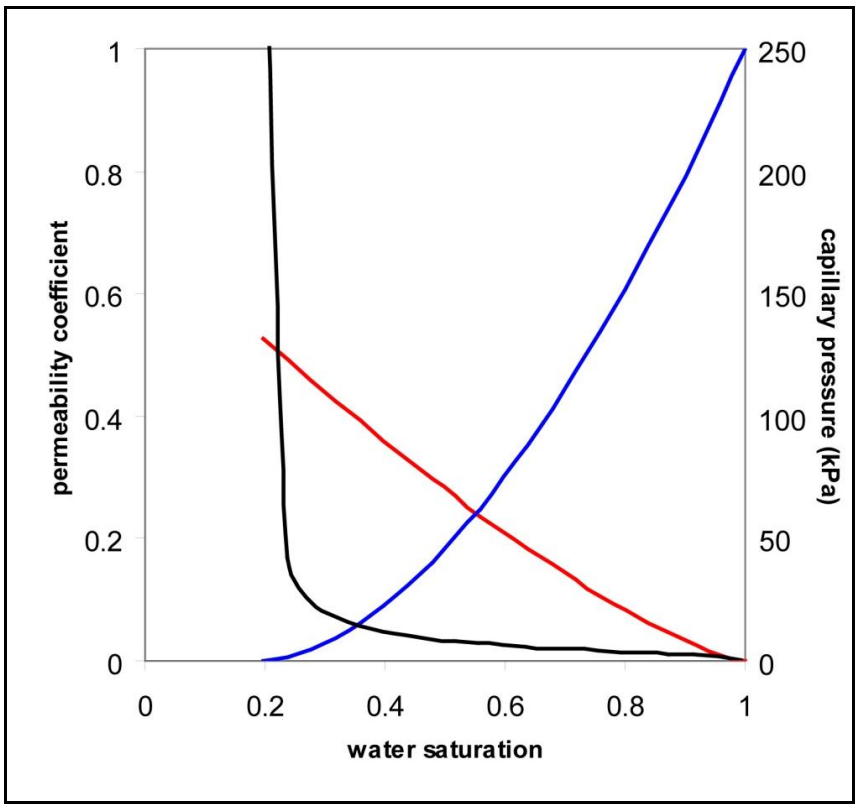

Figure 4.4: Liquid relative permeability data (blue) for brine and relative permeability data for CO_2 (red) taken from Bennion and Bachu (2006). Capillary pressure data (black) were modelled after van Genuchten (1980).

Table 1. *Details of the base case model*

Thickness	140 m
Cell size, horizontal	100 m
Cell size, vertical	10 m
Horizontal permeability	250 mD
Vertical permeability	25 mD
Porosity	18%
Rel. Permeability	Bennion and Bachu (2006)
Aquifer depth	1500 m
Initial pressure (at datum 1500 m)	150 bar
Initial water saturation	100%
Brine salinity	0.15 kg/kg
Rock compressibility	0.000045 bar-1
Injection depth	1635 m
Perforation	10 m
Well diameter	0.4 m
Injection rate	0.25 Mt CO_2 per year

ECLIPSE300 CO_2STORE uses the Peng-Robinson EoS to calculate density and volume of CO_2 by default. A simpler EoS is the Redlich-Kwong EoS (Redlich & Kwong 1949) with the approximation presented by Spycher et al. (2003) who fitted the coefficients a and b to the Span & Wagner EoS (Span & Wagner 1996), would provide better results but the EoS cannot be changed. The formula of the Peng-Robinson EoS is:

$$P = \frac{RT}{(V-b)} - \left(\frac{a \cdot \alpha}{V^2 + 2Vb + b^2)} \right) \qquad (3)$$

The cubic version is written as:

$$0 = V^3 - V^2\left(\frac{RT}{P} - 2b + b\right) - V\left(\frac{2RTb}{P} - \frac{a \cdot \alpha}{P} + b^2 + 2b^2\right) - \left(\frac{-RTb^2}{P} + \frac{a \cdot \alpha \cdot b}{P} - b^3\right) \qquad (4)$$

With the two coefficients:

$$a = 0.457235 \cdot \frac{R^2 T_c^2}{P_c} \quad ; \quad b = 0.0.77796 \cdot \frac{R\ T_c}{P_c} \qquad (5)$$

The temperature dependent term is:

$$\alpha = (1 + (0.37464 + 1.54226 \cdot \omega - 0.26992 \cdot \omega^2)(1 - T_r^{0.5}))^2 \qquad (6)$$

T_r is the reduced temperature and ω is the acentric factor. The CO_2 viscosity is calculated with Fenghour et al. (1998) and Vesovic et al. (1990). The CO_2 compressibility is directly calculated with the Peng-Robinson EoS. The mutual solubility of CO_2 and brine is calculated in a way proposed by Spycher et al. (2003).

The simulated brine consists only of water and NaCl. CO_2STORE calculates with mole fraction as salinity unit. Using the density calculation of Batzle and Wang (1992), the density of brine (57.5 C and 157.5 bar) with a salinity of 0.150 kg/kg is 1098 kg/m^3. 1 Litre of brine contains 53.4592 mole of H_2O and 2.5666 mole of NaCl. The mole fraction is 0.953 and 0.047 for H_2O and NaCl respectively.

Eclipse usually calculates water density as the inverse of the volume. The molar volume is calculated as follows:

$$V_M = \frac{M}{\rho_{ref}(1 + (\beta_w (P - P_{ref})) + 0.5(\beta_w (P - P_{ref})^2} \qquad (7)$$

The parameters are molecular weight (M), reference density (ρ_{ref}), water compressibility (β_w) and reference pressure (P_{ref}). However, CO_2STORE calculates the brine density in a way proposed by Kell and Whalley (1975), which used the idea that the speed of sound is related to the isotropic change of density with varying pressure. The equation that describes the density is:

$$\rho(P) = \rho(P_0) + \int_{P_0}^{P} \upsilon^{-2} dP + T \int_{P_0}^{P} (\alpha^2 / C_P) dP \qquad (8)$$

$\rho(P)$ is the water density (kg/m^3) at pressure P, P_0 equals 1 atm (the reference pressure), v is the speed of sound, α is the thermal expansivity and C_p is the isobaric heat capacity (J/K). The solution of the integral is:

$$\rho(P) = \rho(P_0) + [\upsilon^{-2}(P_0 - P)] + T\left[\frac{\alpha^2}{C_P}(P_0 - P)\right] \qquad (9)$$

The impact of salinity and CO_2 in solution on the density is calculated using Ezrokhi's method (Zaytsev & Aseyev 1993) so that the brine density is calculated as follows:

$$\lg(\rho_b) = \lg(\rho) + \sum(A_i c_i) \qquad (10)$$

C_i is the mass fraction of each component and A_i is the activity coefficient of each component (which is temperature dependent). The advantage of this method is that it calculates density differences due to salinity changes and CO_2 dissolved into the pore water with only one equation. Furthermore, it takes temperature into account.

The viscosity (μ) of water is calculated as follows:

$$\mu = \frac{\mu_{ref}}{(1 + (-c_V (P - P_{ref})) + 0.5(-c_V (P - P_{ref}))^2} \quad (11)$$

Where μ_{ref} (set to 0.3 cP) is the reference viscosity and c_V is the viscosibility (set to 0). Therefore, the viscosity of water is constant (0.3 cP) and does not take pressure, temperature or other components into account.

Pore compressibility is set to 0.000045 bar^{-1} at a reference pressure of 150 bar (Birkholzer et al. 2009). The pore volume change in percent is calculated to be:

$$C_P \cdot \Delta P \cdot 100 = \Delta V \quad (12)$$

The normalised change in pore volume over the pressure range of interest is illustrated in Fig. 4.5.

Several model-runs were performed with the same parameters but different well spacing. The cell size in the models remained constant hence the number of cells increased with increasing horizontal edge length. Two sets of sensitivity tests were designed to assess uncertainties in pressure build-up within the pressure cell due to two parameters. The first sensitivity test investigated the effects of varying horizontal and vertical permeabilities. The second sensitivity test involved variable injection rates.

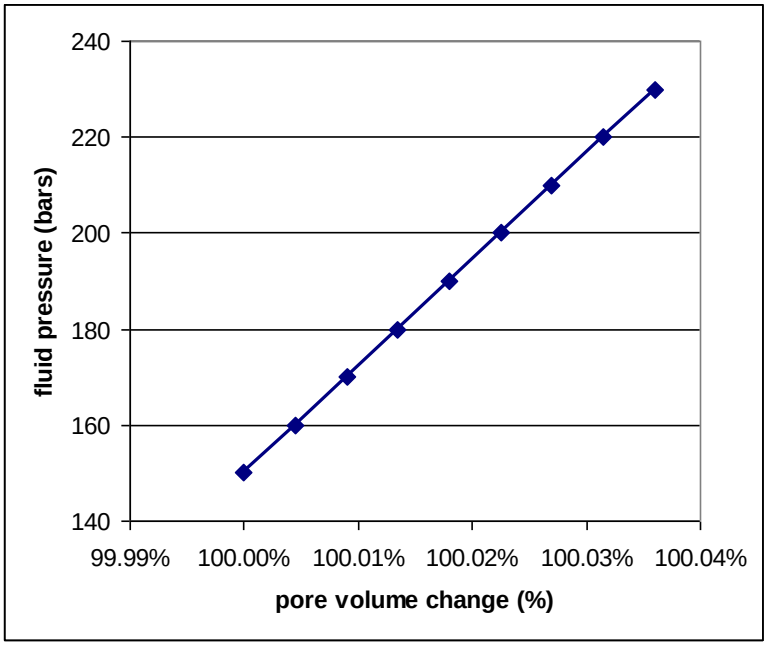

Figure 4.5: Normalised change in pore volume over the pressure range of interest.

4.2.2 Analytical method to assess CO_2 storage capacity of a saline aquifer

Analytical methods to estimate CO_2 storage capacity of saline aquifers are usually based on the effective pore space and a storage efficiency factor. Zhou et al. (2008) presented a way to calculate the pressure build of a formation analytically for closed, semi-closed and open systems. As described above, we regard the pressure compartments of the Bunter Sandstone as closed systems, which simplifies the calculation.

If the pore pressure of the aquifer is disconnected from the surrounding regions and cannot equilibrate, the injection of CO_2 into brine filled formation will cause three effects: (i) The rock will be compressed; (ii) the brine will be compressed; (iii) the pressure will rise. The available volume for stored CO_2 is provided by density increase of brine and an increase in pore space. The available volume for CO_2 can be calculated by:

$$V_{CO2} = (\beta_r + \beta_b)\Delta P \cdot V_P \qquad (13)$$

where V_{CO2} is the total CO_2 volume, β_r and β_b are the pore and brine compressibility, ΔP is the pressure increase and V_P is the total available pore space (total rock volume multiplied by the porosity). It is common to use a mass unit for CO_2 instead of a volume. To convert CO_2 volume into mass we chose the Peng Robinson Equation of State (EoS, Peng & Robinson 1976). This equation can simply be attached to the storage capacity equation. We chose the Peng-Robinson EoS not because it provides the most realistic density/volume curves for CO_2 but rather because one aim of this study was to compare a numerical storage capacity estimation with a simple analytical capacity estimation. The simulator we used for the numerical approach calculates CO_2 properties with the Peng-Robinson EoS by default. For the sake of a consistent study, Peng-Robinson is used for the analytical approach as well. For additional information on the Peng-Robinson and comparable EoS's see chapter 2.2.

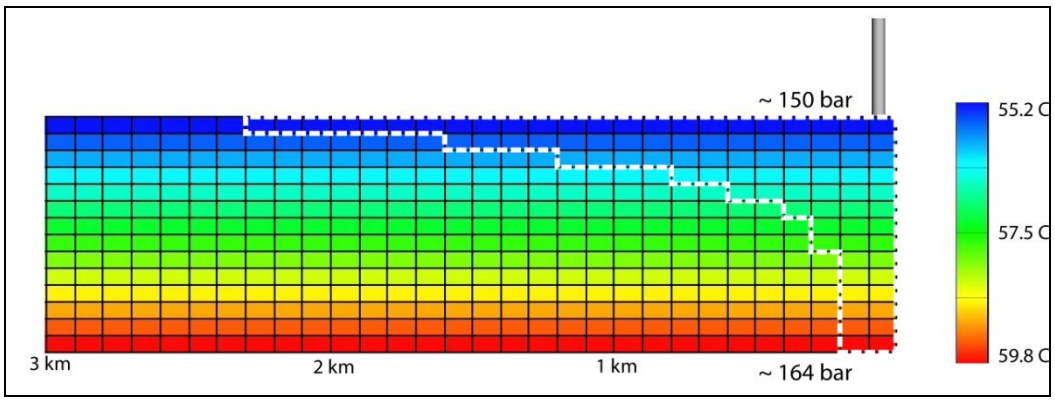

Figure 4.6: Side view of an injection model conducted with ECLIPSE300/CO_2STORE. Vertical cell size is exaggerated by the factor 6. The entire edge length of the model is 7.7 km. 7.5 Mt of CO_2 over 30 years has been injected into the two lowest cells of the right hand site (under the illustrated injection well). The white dashed line shows the spread of the CO_2 plume after 30 years of injection. At this time, most of the CO_2 has accumulated in the top third of the model.

An appropriate choice of the temperature usually depends on the depth at which most of the CO_2 is present. Figure 4.6 shows that after the injection period of 30 years,

most of the CO_2 has accumulated in the upper part of the reservoir and average values would require a majority of the CO_2 in the middle of the reservoir. Figure 4.7 shows the density of a rising CO_2 plume under the conditions chosen for this study and a pressure gradient at the beginning of injection. It can be seen that only minor changes in density occur. Under higher pressure but at the same temperature (after the CO_2 has been injected into the reservoir), the density change is greater but still not significant. Therefore, the density gradient within the reservoir can be neglected and the choice of the average temperature and pressure is sufficient. A variation of the temperature gradient does not change this conclusion. For the calculation an average temperature of 57.5˚C was used. The main reason for that is the relatively small thickness of the reservoir.

Equation (13) is independent of the depth of the aquifer because only pressure increase is taken as a parameter and not the total pressure. Hence, the volume of stored CO_2 can be calculated for every hypothetical 'maximum sustainable pore pressure'. Since this pressure is not constant but increases with depth, the capacity of the Bunter Sandstone aquifer changes too. If the top of the reservoir is considered, the 'maximum sustainable pore pressure' is 75 bar; the 'maximum sustainable pore pressure' at the bottom is 82 bar. The equation shall give the average pressure and therefore, the average depth of the aquifer is taken. The average pore pressure of the Bunter Sandstone aquifer is set to 157 bar (according to the average depth of 1570 m). ΔP, the allowed pressure increase, is 78.5 bar and the maximum average reservoir pressure is 235.5 bar. The porosity is set to 18 % (Holloway et al. 2006).

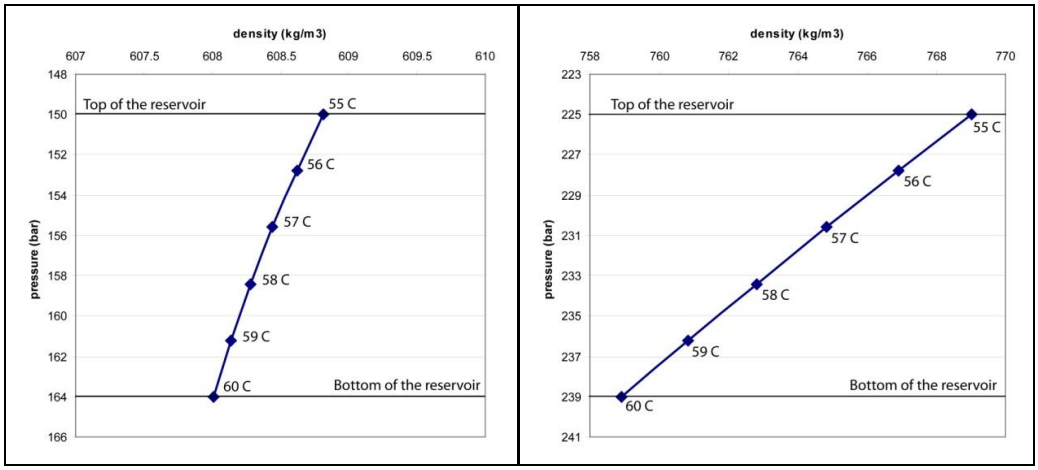

Figure 4.7: Density of CO_2 rising from the bottom to the top of the reservoir. The graph on the left hand site uses pre-injection pressure. The density and the volume of rising CO_2 hardly changes at all. The graph on the right hand site uses post-injection pressure when the pressure at the top has reached its limit (225 bar). Density and volume changes are greater but still not significant. Hydrostatic pressure gradient within the reservoir is assumed.

The pore compressibility is taken from saline aquifer studies conducted by Birkholzer et al. (2009) and set to 0.000045 bar^{-1}. Brine compressibility is defined to be the brine density change with pressure and brine density is also dependent on the salinity. Although the idea of this analytical model is to provide relatively quick answers, the impact of brine compressibility is too important and therefore should be calculated accurately. An expression for brine compressibility can be obtained from Bear (1979):

$$\beta_b = \frac{1}{\rho_b}\frac{d\rho_b}{dP} \qquad (14)$$

where β_b is the brine compressibility and ρ_b the brine density. The density of pure water can be calculated with (Batzle & Wang 1992):

$$\rho_w = 1 + 10^{-6}(-80T - 3.3T^2 + 0.00175T^3 + 489P - 2TP + 0.016T^2P - 0.000013T^3P - 0.333P^2 - 0.002TP^2 \quad (15)$$

where T is the temperature in ˚C and P the pressure in MPa. The salinity correction is:

$$\rho_b = \rho_w + S\left[0.668 + 0.44S + 10^{-6}\left(300P - 2400PS + T\left(80 + 3T - 3300S - 13P + 47PS\right)\right)\right] \quad (16)$$

Differentiating the two equations with respect to P leads to (Mathias et al. 2009):

$$\frac{d\rho_w}{dP} = 10^{-6}\left(489 - 2T + 0.016T^2 - 0.000013T^3 - 0.666P - 0.004TP\right) \quad (17)$$

and as a correction for the salinity:

$$\frac{d\rho_w}{dP} = \frac{d\rho_w}{dP} + S\left[10^{-6}\left(300 - 2400S + T\left(-13 + 47S\right)\right)\right] \quad (18)$$

Figure 4.8 shows the density and compressibility of water and brine with the salinity and temperature chosen for this study (0.15 kg/kg; 55˚C) over a pressure range of interest. It can be seen that neither density nor compressibility are affected significantly by pressure. It can also be seen that salinity has an important effect. The chosen salinity of the brine reduces the compressibility of the pore fluid by approximately 25 % with respect to pure water. For the storage capacity calculation, a brine compressibility of 0.000031 bar^{-1} is chosen.

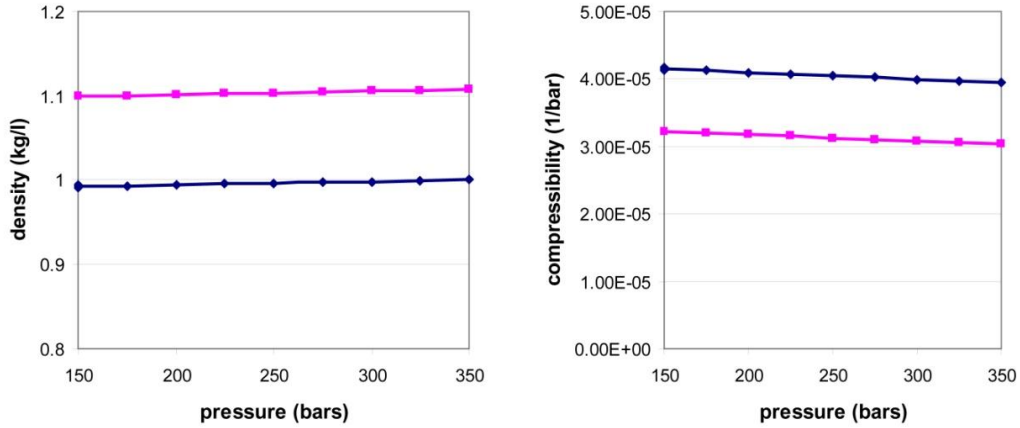

Figure 4.8: The graph on the left side shows the density of pure water and brine (0.15 kg/kg) over a pressure range of interest. The right graph illustrates their compressibility dependent on pressure. Pressure has only minor impact on the density and on the density related compressibility. A much more important influence has salinity. Hence, brine salinity has to be taken into account if liquid compressibility is being used.

To obtain the theoretical minimum well spacing that allows a secure injection, equation (13) can quickly be rearranged to:

$$V_P = \frac{V_{CO2}}{(\beta_r + \beta_b)\Delta P} \qquad (19)$$

The pore volume (V_p) can be written as:

$$V_P = \phi \cdot l^2 \cdot t \qquad (20)$$

where l is the well spacing and t the thickness of the formation. The compressibility (β_r and β_b), the volume of the injected CO_2 (V_P; 30 Mt for an injection period of 30 years) and the maximum pressure increase (ΔP) is known, the well spacing can be calculated.

4.3 Results

4.3.1 Results of the numerical method

Figure 4.9 illustrates the fluid pressure after 30 years of injection as a function of the pressure cell edge length. The minimum edge length which would support an injection process without exceeding the maximum permissible fluid pressure is approximately 15.4 km. According to this result, the Bunter Sandstone Formation would be separated into 239 pressure cells since the formation covers an area of 56,660 km^2 in the UK southern North Sea (Holloway et al. 2006).

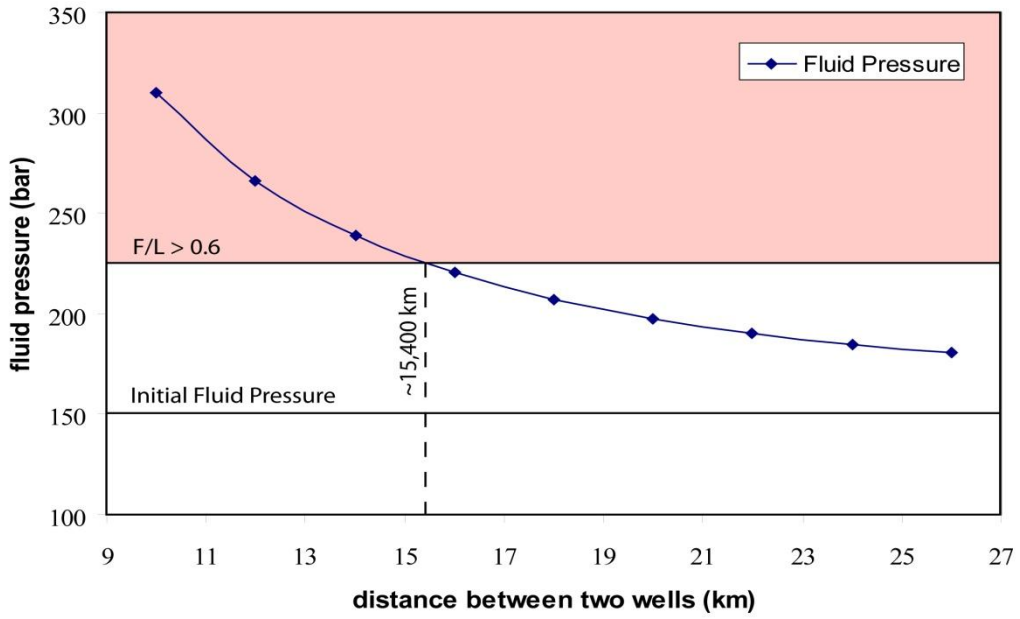

Figure 4.9: Fluid pressure of a CO_2 injection scenario after 30 years injection, measured at the top of the reservoir adjacent to an injection well. The pressure decreases as the distance between wells increases. A well spacing of at least 15.4 km ensures that the pressure stays within the safety limit.

After 30 years, a total amount of approximately 7.17 Gt of CO_2 would have been injected. Simulation results show that ~389.1 Mt of the CO_2 would dissolved into the

pore water. This corresponds to 5.45 % of the entire injected CO_2. The majority of the CO_2 would still be present as a supercritical fluid and would occupy ~0.613 % of the total estimated pore space.

The pressure increase due to CO_2 injection, directly below the seal and adjacent to the injection well is illustrated in Fig. 4.10 for a simulation run with a well spacing of 15,400 m. The pressure increases uniformly up to 225 bar after 30 years. When injection ceases, the pressure drops by approximately 2 bar (from 225.17 bar after 30 years to 223.02 bar after approximately 32 years). During the 10 years of recovery (the post-injection phase) it continues to rise with a low rate (from 223.02 bar to 223.38 after 40 years). The dissolution of CO_2 into brine (Fig. 4.10) is relatively high during the first 1.5 years and continues thereafter at a lower rate. The rapid dissolution at the beginning of injection is due to the fast vertical penetration of the CO_2 to the top of the reservoir. The CO_2 enters many cells in a relatively short time and dissolves instantaneously. This is largely an artefact of the model; however this instantaneous dissolution combined with numerical dispersion effects exhibits a very small general pressure decline. Once the CO_2 has reached the top of the reservoir it slowly spreads out laterally and the rate of dissolution stabilises on a lower level.

When injection ends the CO_2 stream ceases and the spreading of the plume is reduced. The relatively low dissolution rate is due to the relatively immobile CO_2 plume which is isolated from the fresh brine by a layer of CO_2 saturated brine. The dissolution rate will increase if the boundary between fresh and saturated brine will become gravitationally unstable and convection begins. This convection brings CO_2 in contact with fresh brine and the dissolution rate increases again. Riaz et al. (2006) proposed the ‘critical time’, the time when convection starts, to be calculated as:

$$t_c = 146 \cdot \frac{\phi \cdot \mu^2 \cdot D}{\left(k \cdot \Delta\rho \cdot g\right)^2} \qquad (21)$$

where t_c is time in seconds, ϕ is porosity, μ is viscosity, D is the diffusion coefficient, k is permeability, $\Delta\rho$ is the density difference of brine and CO_2 saturated brine and g is gravitation. If the parameters are fitted to the Bunter Sandstone top layer (ϕ =0.18, η =0.00078 Pa*s (viscosity of brine calculated with the viscosity relationship of Kestin et al. (1981) and modified Batzle and Wang (1992), should be slightly higher because the dissolved CO_2 increases the viscosity of the brine), D=10^{-9} m^2/s, K=2.5^{-14}, $\Delta\rho$ =5 kg/m^3 and g=9.81 m/s^2) the circulation starts after 337 years, far later than the injection phase.

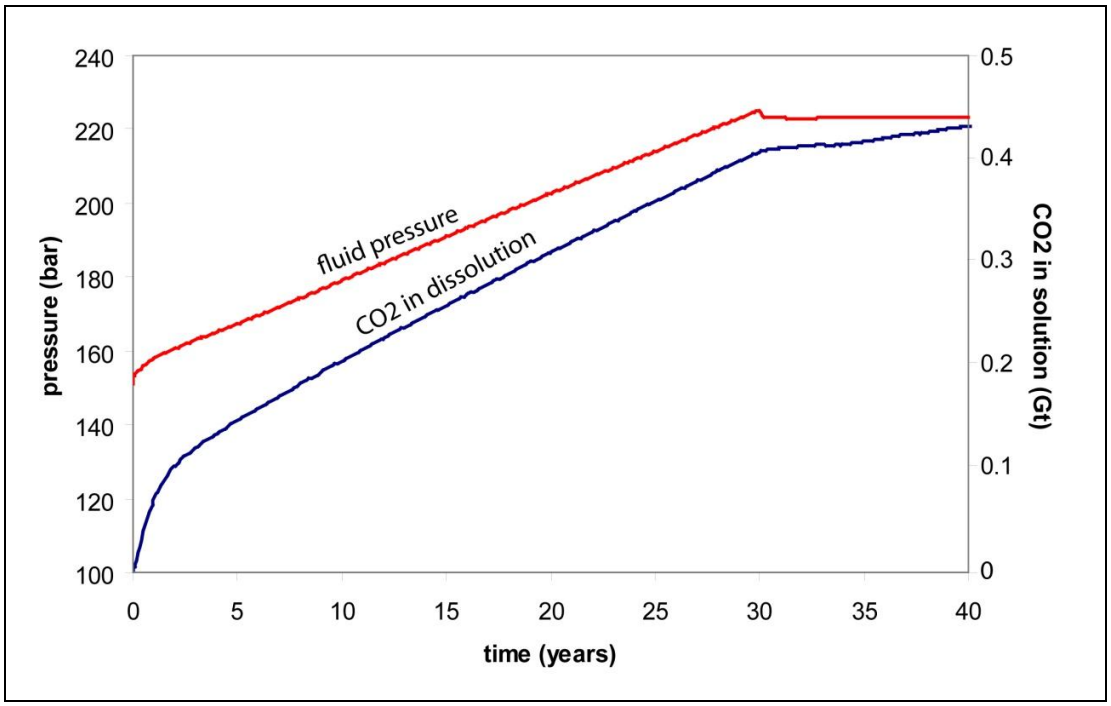

Figure 4.10: (Red graph) Pressure development during 30 years of injection and 10 years of recovery. After injection ceased the pressure slightly drops due to a collapse of the CO_2 stream. (blue graph) CO_2 dissolved in the brine. There is no significant pressure decline after injection due to further CO_2 dissolution.

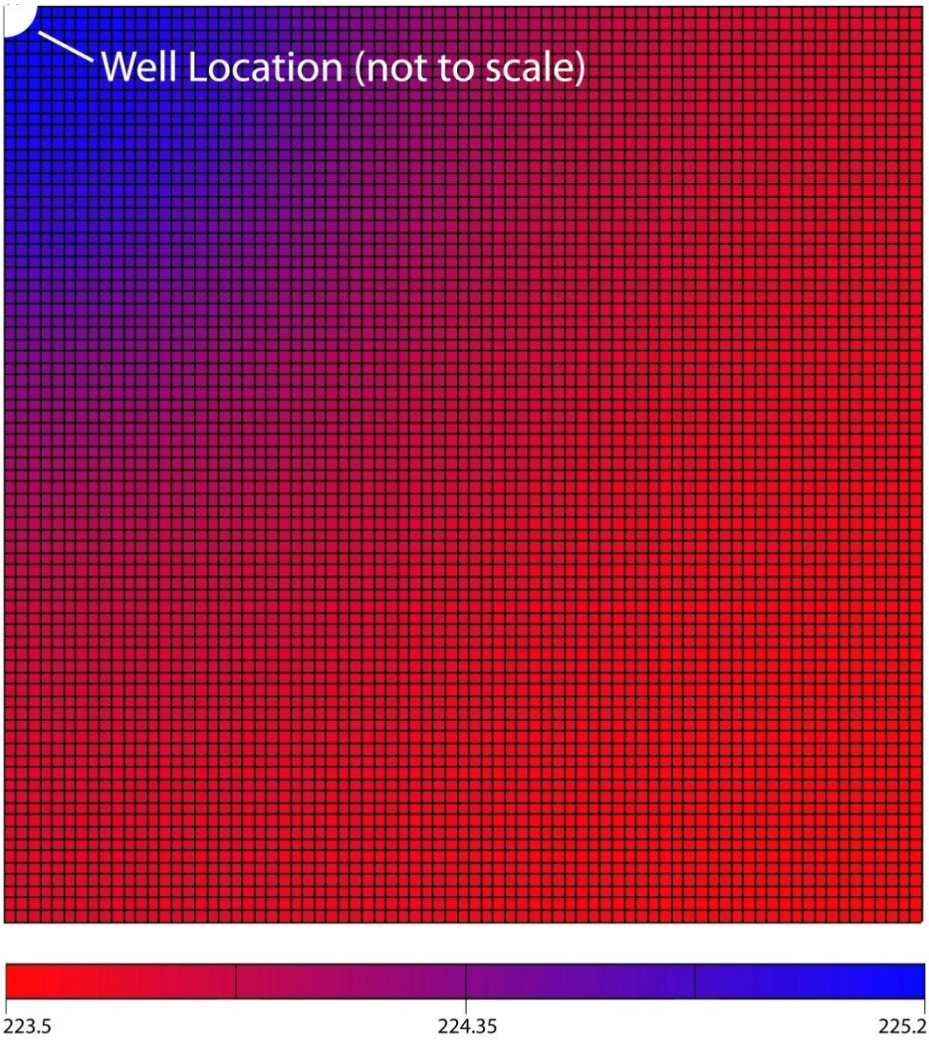

Figure 4.11: Pressure distribution of the top layer of a model with UK North Sea Bunter Sandstone properties after 30 years of injection and a maximum permissible fluid pressure of 225 bar. Pressure is highest above the injection point. Note the low horizontal pressure gradient across the simulated reservoir compartment.

As mentioned before, the pressure is measured at the top layer above the injection well where pressure is highest. Figure 4.11 is a pressure map of the top layer of a model with an edge length of 7.7 km. A pressure gradient with decreasing pressure away from the injection well is obvious, although the gradient is very weak (~1.5 bar).

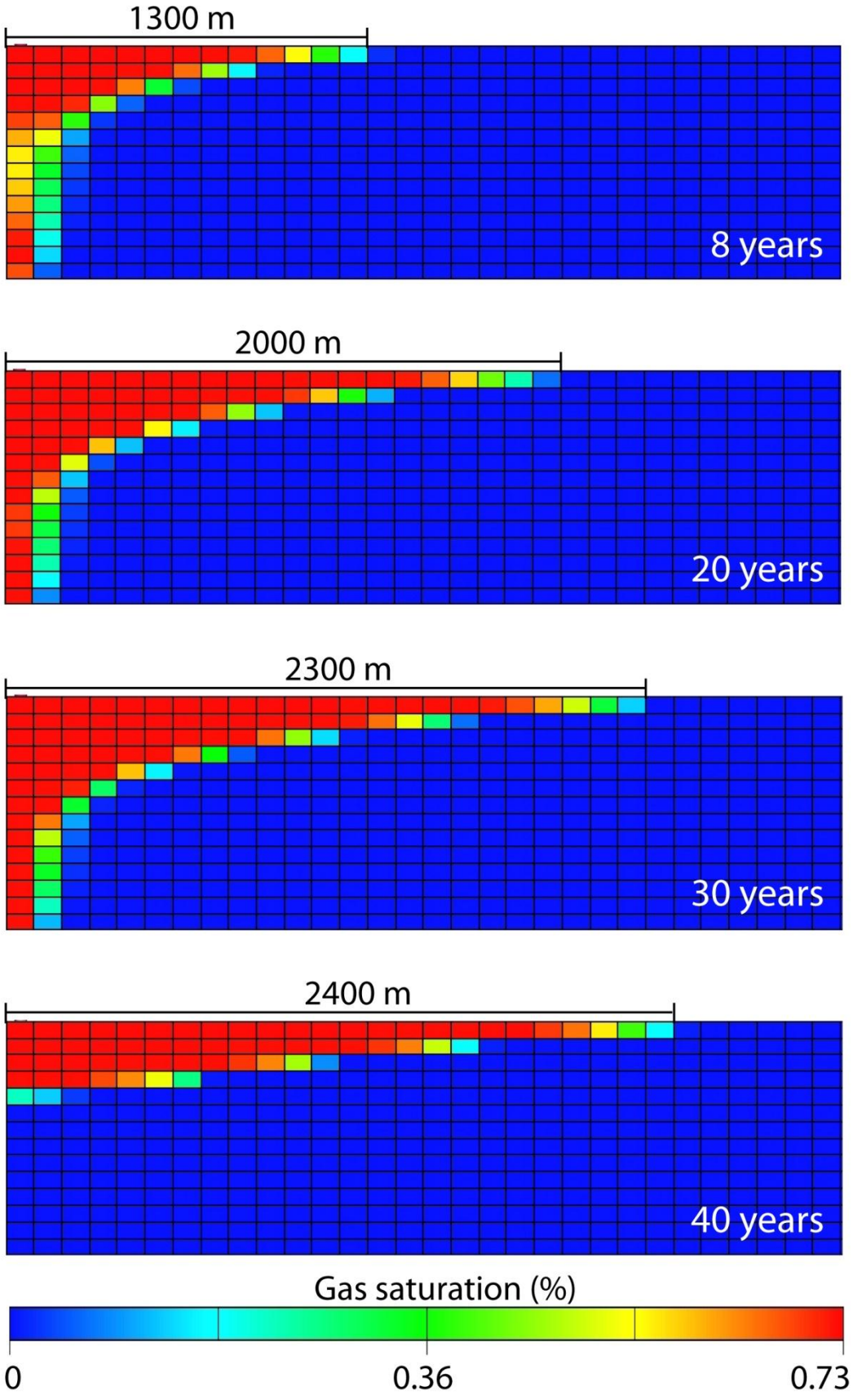
1300 m
8 years
2000 m
20 years
2300 m
30 years
2400 m
40 years
Gas saturation (%)
0
0.36
0.73

1

Figure 4.12: Plume radius for four different time-steps. Injection ceases after 30 years. The entire edge-length of the model is 7.7 km. Only a part of the side view of the every model is shown. Vertical exaggeration is 6. The figures document how rapidly the plume slows down spreading.

Figure 4.12 illustrates the CO_2 saturation and the corresponding plume size at different time-steps. The chosen well spacing of the model is 15.4 km (edge-length of 7.7 km). This is the model edge length that was formerly identified as the one in which the pressure reaches the sustainable fluid pressure. When injection ceases, the CO_2 plume is approximately 4,600 m wide and is located in the top part of the aquifer. The strong buoyant forces of CO_2 lead to a rapid outspread of the plume at the beginning of the injection. With the given model results it is difficult to predict the development of the plume over a longer time period but it can be seen that the spreading slows down significantly with proceeding time (Fig. 4.13). The plume will stop spreading eventually when buoyancy forces become lower than the forces constraining the two-phase fluid flow. Additionally, enhanced dissolution due to gravitational instability driven convection will decrease the size of the plume.

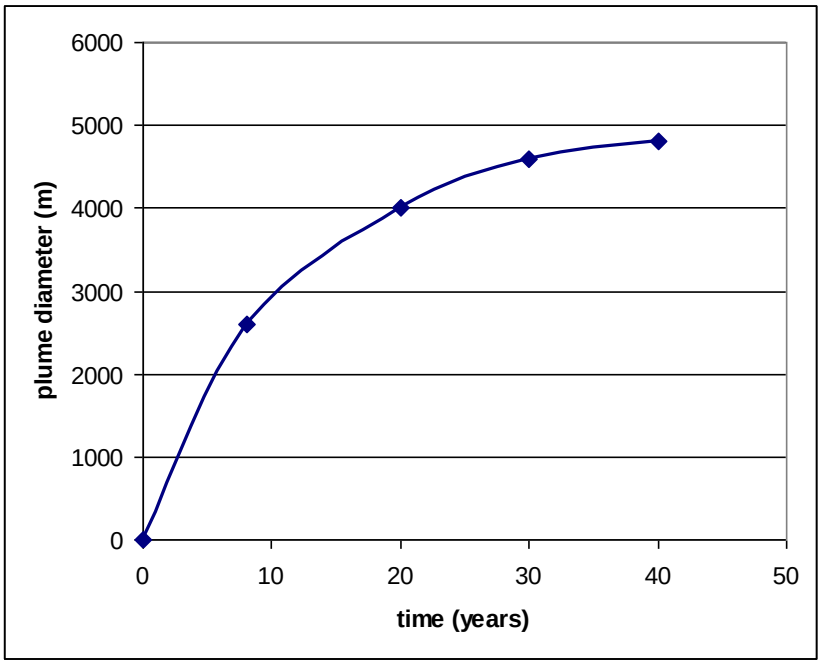

Figure 4.13: Graph shows the increase of the plume diameter during 30 years of injection and 10 years of post-injection.

Sensitivity test 1 presents the impact of a bulk permeability variation on the model result. Figure 4.14 shows the fluid pressure after 30 years of injection for different horizontal permeabilities from 1000-50 mD, which corresponds to 400-20 % of the base case scenarios. A permeability increase does not have a great impact and the fluid pressure decreases only slightly. A horizontal permeability of 1000 mD (400 % of the base case permeability) reduces the pressure by less than 1 % compared to the base case simulation. A permeability reduction can have some impact on the pressure. A reduction to 50 % of the base case horizontal permeability can increase the fluid pressure by ~1 %. The percentile increase in the post-injection pressure is a function of the cell dimensions, so that a reduction down to 20 % of the initial permeability leads to an increase of the fluid pressure by ~1.5 % for pressure cells with an edge length of 10 km, and to a more significant increase in fluid pressure of 4.5 % of cells with 22 km. In all cases, the change in fluid pressure is small (< 5 %).

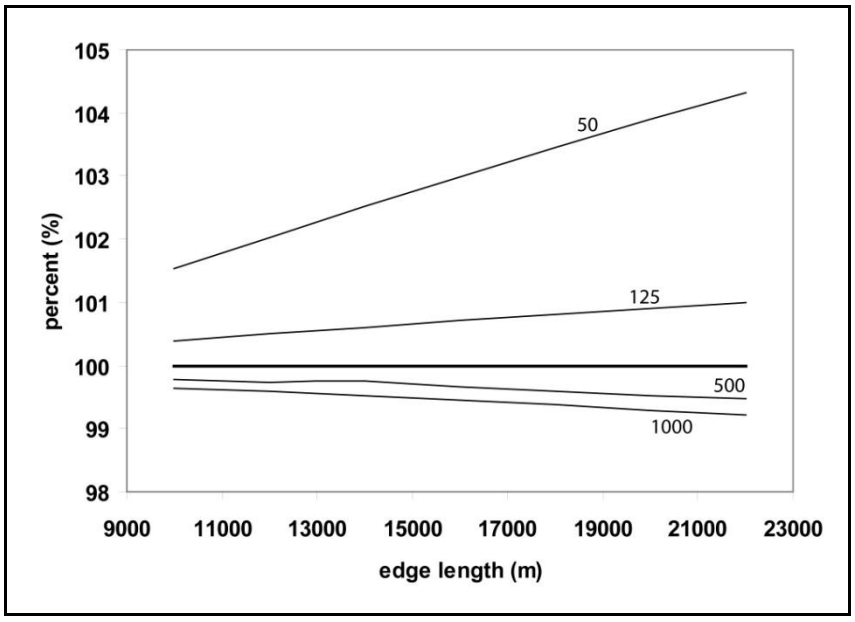

Figure 4.14: Fluid pressure after 30 years of injection and for pressure cell edge lengths between 10-22 km with different horizontal permeabilities, measured at the top of the reservoir adjacent to an injection well. The bold line at 100 % represents the base case with a horizontal permeability of 250 mD; all other fluid pressure measurements are displayed with respect to the base case scenario. Even a reduction of horizontal permeability to 50 mD has only a moderate affect on the pressure.

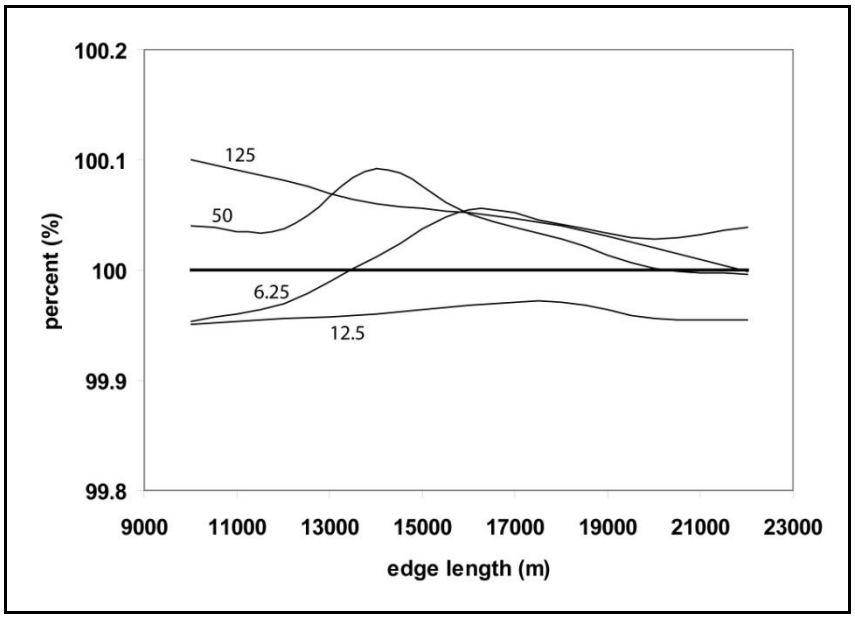

Figure 4.15: Fluid pressure after 30 years of injection and for pressure cell edge lengths between 10-22 km with different vertical permeabilities, measured at the top of the reservoir adjacent to an injection well. The bold line at 100 % represents the base case with a vertical permeability of 25 mD; all other fluid pressure measurements are displayed with respect to the base case scenario. The pressure measurements do not show the expected clear trend but it can be seen that even the reduction of vertical permeability down to 6.25 mD does not change the pressure significantly. The apparent irregularities of the 6.25 mD and 50 mD are probably the result of numerical errors.

Sensitivity tests assessing the impact of vertical permeability in a realistic range for a CO_2 storage site of 25-500 % of the base case were also conducted (Fig. 4.15). A variation in vertical permeability has only a minor impact on the pressure distribution (<0.5 %). This is most likely due to the pressure cells always having a very low ratio of vertical to horizontal scale.

Sensitivity test 2 shows the effect of different injection rates on the CO_2 storage capacity for the offshore southern North Sea Bunter Sandstone. When the injection rate is increased the size of the pressure cells increase so that the number of cells within the entire Bunter Sandstone decreases. Figure 4.16 demonstrates that an injection rate which is twice as high as the base case scenario decreases the number

of pressure cells to 126. A reduction of the injection rate to 50 % of the base case scenario increases the number of pressure cells to 484. The impact of different injection rates on the calculated storage capacity is relatively small (Fig. 4.16). It can be seen that with twice the injection rate (2 Mt per year per well) the storage capacity of the offshore North Sea Bunter Sandstone aquifer will be reduced by less than 3 %.

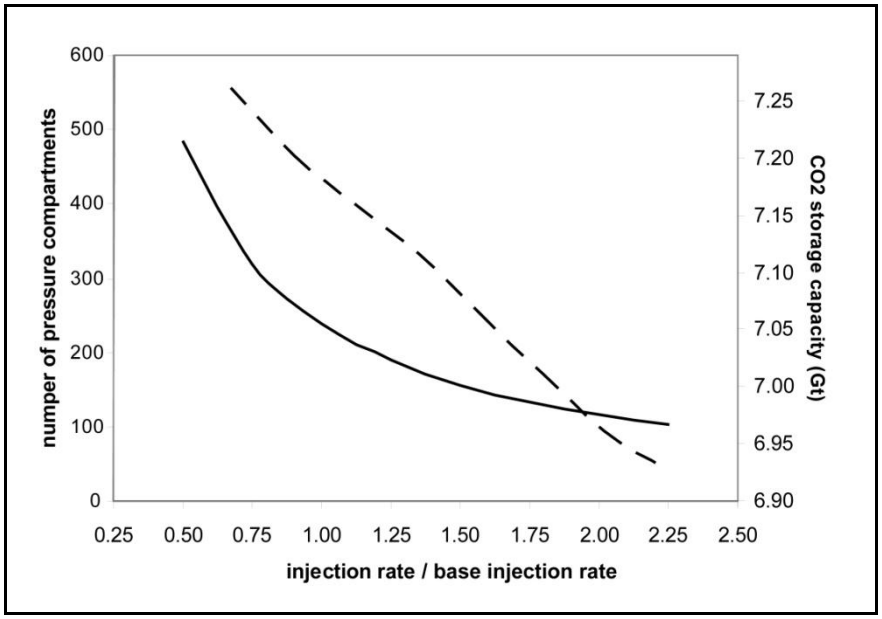

Figure 4.16: Number of pressure compartments as a function of the injection rate per year applied on the UK southern North Sea. A higher injection rate leads to fewer (and larger) pressure cells (solid line) but the storage capacity (dashed line) does not change significantly compared to the base case scenario. Base injection rate is 1 Mt of CO_2 per year.

4.3.2 Results of the analytical method

If the 'maximum sustainable pore pressure' of the Bunter Sandstone is calculated (60 % of the fluid pressure; hence the pore pressure is allowed to increase by 78.5 bar), after 30 years a total amount of approximately 6.55 Gt of CO_2 would be injected. Dissolution is not taken into account. The stored CO_2 would occupy ~0.6 % of the total estimated pore space.

The minimum well spacing which could support an injection process without a fluid pressure increase that would compromise the rock formation is approximately 16.1 km. According to this result, the UK southern North Sea Bunter Sandstone Formation would be separated into 218 pressure cells.

4.4 Discussion

4.4.1 Discussion of the numerically derived results

With the reservoir engineering software, the pressure at any cell can be calculated. The buoyancy difference between CO_2 and brine establishes a steady CO_2 flow from the injection point to the top of the reservoir. This CO_2 flow leads to a slight pressure increase above the injection point and enhances the pressure gradient of the top layer. After injection ceases the CO_2 stream breaks down and the pressure decreases (illustrated by the pressure drop after injection ceases; Fig. 4.10).

The calculated CO_2 storage capacity of 7.77 Gt for the offshore UK North Sea Bunter Sandstone Formation is the result of a multi-well injection scenario with constant injection rates of 1 Mt per year and an injection period of 30 years. Unlike estimation based on CO_2 solubility in brine, the capacity estimate by the proposed method is time dependent. In other words, the injection period and injection rate are suppose to determine CO_2 capacity. A longer injection period should lead to more CO_2 in solution and should decrease the pressure and increase the storage capacity. However, it is evident from Fig. 4.10 that the dissolution of CO_2 into brine has a relatively small impact on pressure. A moderate change in the injection period will therefore not alter the overall capacity significantly.

Permeability is one of the main parameters affecting rock heterogeneity, because it affects pressure diffusion through the formation. Permeability variations due to facies changes or zones of fractures can only be included in a regional model based on the accuracy of the characterisation of the aquifer. As mentioned previously, rock heterogeneities cannot be included into the proposed method and therefore have to be neglected. This is a reasonable compromise as for most saline aquifers the geology is only known on a regional scale, and heterogeneities are not well characterised.

A change of the vertical permeability in the range of 6.25 mD to 125 mD does not have great impact. This is mostly due to the limited effect of medium to high permeabilities on single-phase fluid flow over the short distance of the vertical extent of the reservoir. As can be seen in Fig. 4.15, the data do not always show a clear trend. A vertical permeability of 6.25 mD, for example, leads to a lower pressure in relatively small cells but to a higher pressure in medium size cells. There is no obvious physical explanation for the variations of pressure - they are probably fluctuations due to simulation instabilities.

It can be seen that only a significant reduction of the horizontal permeability has important impact on results obtained by the method. An even more dramatic increase in fluid pressure with smaller permeabilities is self-evident. The developing pressure accumulation in larger models due to lower horizontal permeabilities (Fig. 4.14) shows an increase relative to the base case. In models with lower horizontal permeabilities an increase of the model size has less impact on the pressure accumulation than on simulations with higher permeabilities.

The impact of permeability changes on single-phase fluid flow is much lower than on two-phase fluid flow where already minor changes can alter the flow behaviour of the phases. It should be noted that if the permeabilities are very low (e. g. due to the presence of extensive mud layers) pressure accumulations are expected to occur. But those reservoirs would not be suitable for CO_2 sequestration. The first sensitivity test shows that the proposed numerical method is not dependent on permeabilities over the range of interest for CO_2 storage operations.

The second sensitivity test shows that a change of the injection rate alters the storage capacity slightly. Higher injection rates lead to bigger pressure cells with greater pressure gradients and therefore decrease the storage capacity.

Although the calculated changes in capacity are not significant alone it should be taken into account that a combination of the parameters, for example a high injection rate and a low horizontal permeability, could decrease the storage capacity.

The model shows that, while permeability affects the pressure distribution within the sandstone reservoir as expected, the effects are not significant for the ranges of permeability that would be expected for a candidate reservoir. However, relative permeability does affect the flow of a non-wetting phase within the subsurface, and at present there are no published relative permeability curves for the Bunter Sandstone, or any other potential storage reservoirs in the North Sea. The physical distribution of the CO_2 within the reservoir, and the extent to which residual saturation trapping occurs, will be strongly affected by end-point saturations of the relative permeability curves.

The effect of the CO_2 flow through the reservoir on the pressure is relatively low. As the model results show, no pronounced pressure gradient could be observed, neither in the base case model nor during the sensitivity tests. The pressure in the compartment is therefore mainly dependent on the volume of the CO_2 and the application of different relative permeability curves with different residual saturation data will not alter the results significantly.

4.4.2 Mutual dissolution of CO_2 and brine

It is sometimes assumed that the mutual dissolution of CO_2 and brine is an important factor which controls the volume of CO_2 and the pressure in the storage site. The dissolution of brine into CO_2 can be neglected because the amount of brine which can dissolve into the CO_2 under the temperature and pressure conditions is much lower than the amount of brine that can dissolve into the CO_2. The impact of H_2O dissolving into CO_2 is higher at elevated temperatures. The solubility constant that controls the reaction increases with increasing temperature and more brine is allowed to dissolve into the CO_2. The impact of the increase in dissolution should not be overestimated because the total volume of CO_2 is tiny compared to the volume of brine and because CO_2 saturated with brine will dissolve into the brine eventually.

The dissolution of CO_2 into brine decreases slightly with increasing temperature but remains relatively constant over small temperature ranges (Spycher et al. 2003). If enough water is present, all CO_2 will dissolve at some point and it is generally accepted that the transition from supercritical CO_2 to dissolved CO_2 in water will have a pressure-reducing effect (Metz et al. 2005). But the dissolved CO_2 will increase the density and the volume of the water which leads to a pressure increase. Hence even after all the CO_2 has dissolved into the brine the pressure will not go back to its initial pre-injection level (van der Meer & van Wees 2006). In the simulation, after 30 years nearly 5.45 % of the CO_2 has dissolved into the brine. A minor amount of water has dissolved into the CO_2 and could have an impact on the pressure and therefore on the capacity. However, the modelled pressure decrease exceeds that which would occur in a real system. In the model the CO_2 enters many cells in a relatively short time and dissolves instantaneously. 'Real' CO_2 would take some time to dissolve in the pore water. However, the modelled pressure decline is small so that this effect is not thought to affect the conclusions of the study significantly.

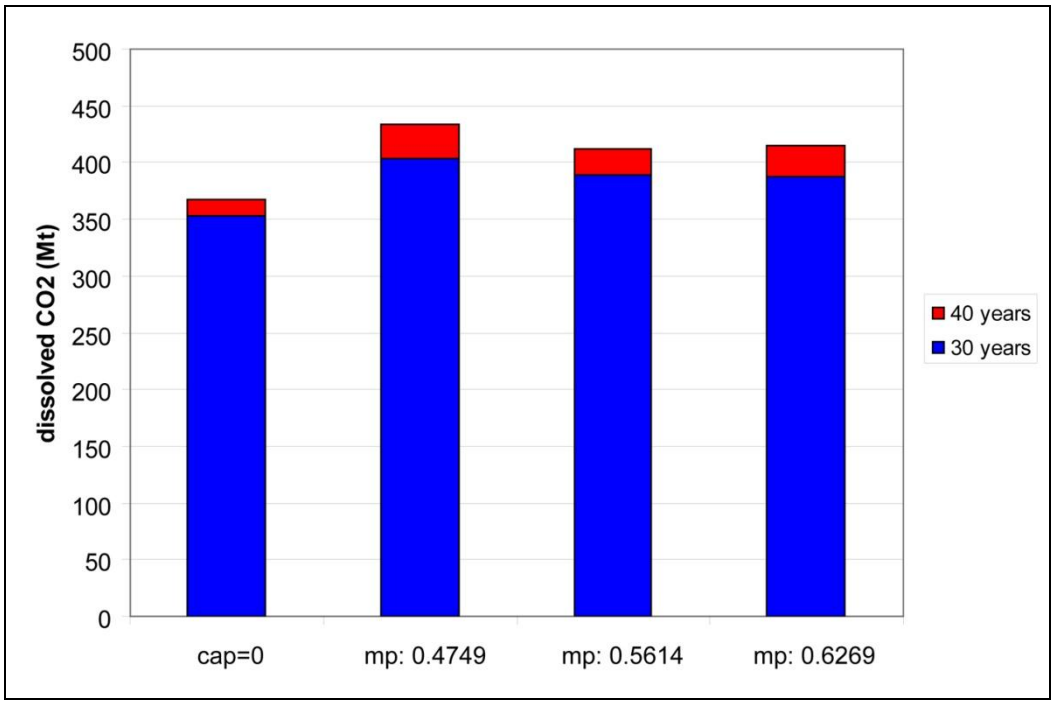

Figure 4.17: Mass of dissolved CO_2 for 30 years of injection and 10 years of recovery. Capillary pressure was modelled with van Genuchten (1980) and different coefficients (mp). The capillary pressure of the left model was set to zero.

Dissolution of CO_2 into brine is a sensitive parameter and if it has an effect on the storage calculation, values have to be chosen carefully. The variability of dissolution rates is presented here by varying the modelled capillary pressure curves (Equation (1); Fig. 4.4). Capillary pressure has significant impact on the spreading of the CO_2 plume at the top of the reservoir and can therefore increase or reduce the dissolution rate. Figure 4.17 illustrates the impact of different pore size distribution factors 'mp' which are used for modelled capillary pressures on the dissolution (see chapter 2.1 for additional information). If capillary pressure is neglected (set to 0), the lowest amount of CO_2 dissolves into the pore water and dissolution will definitely be underestimated. Variations of the parameter '*mp*' have limited impact on the mass of dissolved CO_2. Pruess et al. (2003) proposed several values for the parameter m dependent on the porous media; e. g. sand (0.6269), loamy sand (0.5614, used for this study) and sandy loam (0.4709). Although the post-injection dissolution rates vary moderately, the differences are relatively small and will not change the results of this study. After 30 years of injection, the amount of dissolved CO_2 decreases with an increase of the coefficient '*mp*'. This is not consistent for the 10 years of recovery where simulations with low and high value for '*mp*' ('*mp*': 0.4749 and '*mp*': 0.6269, respectively) calculate more dissolved CO_2 than the model with '*mp*': 0.5614.

A greater effect on the dissolution has a variation of the strength coefficient P_{c0}. Low permeability rocks generally have high strength coefficient (e. g. shale: 0.62 bar, Pruess et al. 2002) whereas a higher permeability is represented by a low strength coefficient (e. g. sand: 0.0358 bar, Pruess et al. 2002). Figure 4.18 shows the capillary pressure curves with strength coefficients ten times higher and ten times lower, relative to 0.0358 bar used for this study. It can be seen that a decrease of P_{c0} results in an almost vertical line near the residual water saturation whereas higher values create a curvature. Theoretically, the almost vertical blue line in Fig. 4.18 would be even steeper if more data points in the vicinity of the residual saturation were chosen.

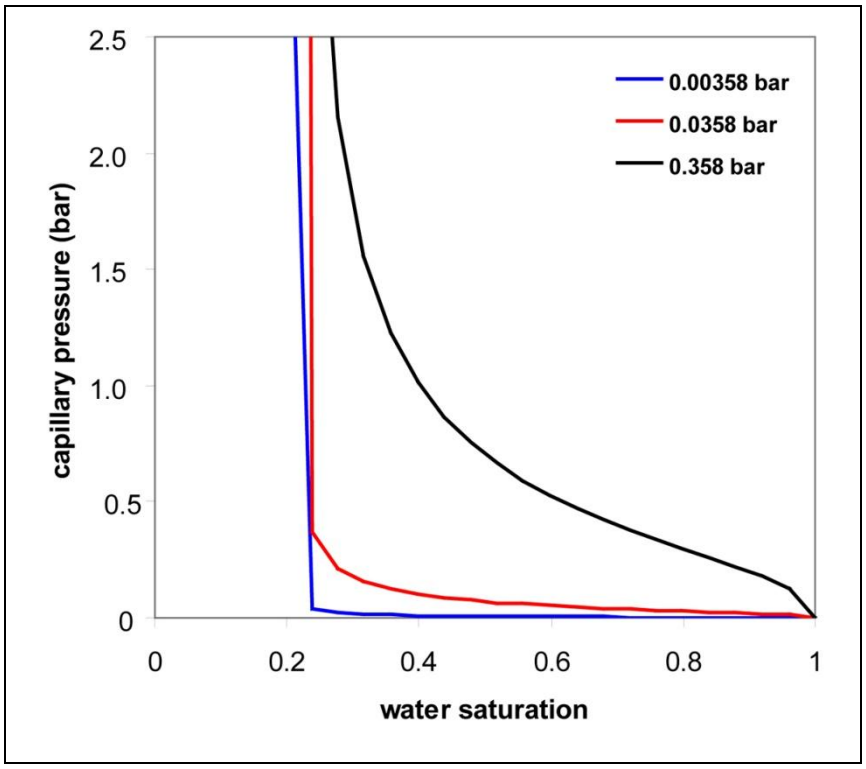

Figure 4.18: Capillary pressure curves, modelled with van Genuchten (1980), with different P_{c0}. Theoretically, the low P_{c0} curves would be even steeper if more data in the vicinity of the residual water saturation were taken into account.

Figure 4.19 shows that an increase of P_{c0} increases the amount of dissolved CO_2. Since the capillary pressure is not included in the equations defining the dissolution of CO_2 into water, it cannot influence the dissolution itself. Capillary pressure is a central part of the two phase fluid flow equation and determines the shape of the CO_2 plume. A higher P_{c0} changes the capillary pressure curve in a way that even for relatively high water saturation conditions the gas pressure has to be relatively high to replace more water. This results in cells which are not fully saturated (up to the residual water saturation) with water because it is energetically more efficient for the CO_2 to enter the adjacent cell than replacing more water from the initial cell. A low Pc_0 leads to a situation where the entering CO_2 does not need to have a high gas pressure to replace water until it reaches the residual saturation. Therefore, all cells are almost fully saturated with the gas phase.

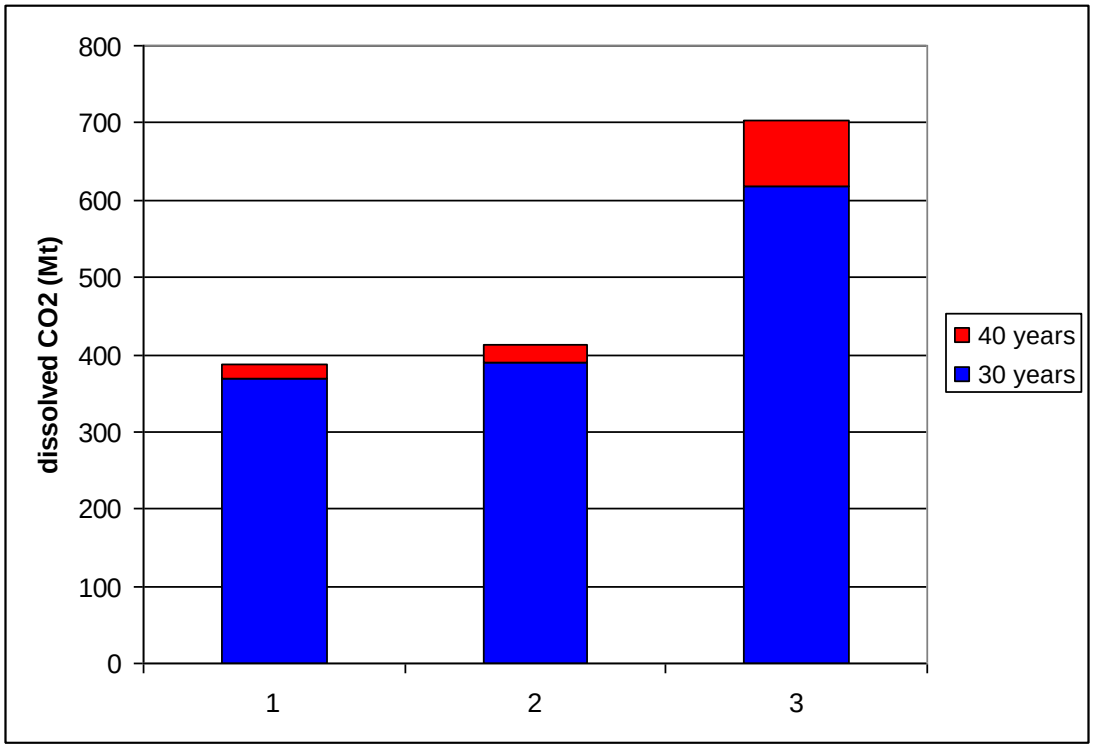

Figure 4.19: Mass of dissolved CO_2 for 30 years of injection and 10 years of recovery. Capillary pressure was modelled with van Genuchten (1980) and P_{c0}. Values for P_{c0} are 0.00358 bar (1), 0.0358 bar (2, used for this study) and 0.358 bar (3).

Figure 4.20 shows the gas saturation of cells transecting the CO_2-brine-interface. The steep capillary pressure curve (low P_{c0}) forces the gas to replace the water from the water filled cells almost entirely and the gas front penetrates the 'reservoir' like a piston. The shallower capillary pressure curve (high P_{c0}) allows the gas to enter the next cell without filling up the previous one. The gas water interface is now a shallow saturation gradient rather than a steep front.

A direct consequence of the gas front behaviour is that the plume of simulations with a shallow capillary pressure curve is wider and CO_2 has access to more cells. Since in the model CO_2 dissolves instantaneously until the water in the cell is fully saturated with CO_2, the amount of dissolved CO_2 is directly dependent on the number of cells that are reached by the gas. This is also the reason why, in simulations with neglected capillary pressure (P_c=0), the amount of dissolved CO_2 is lowest.

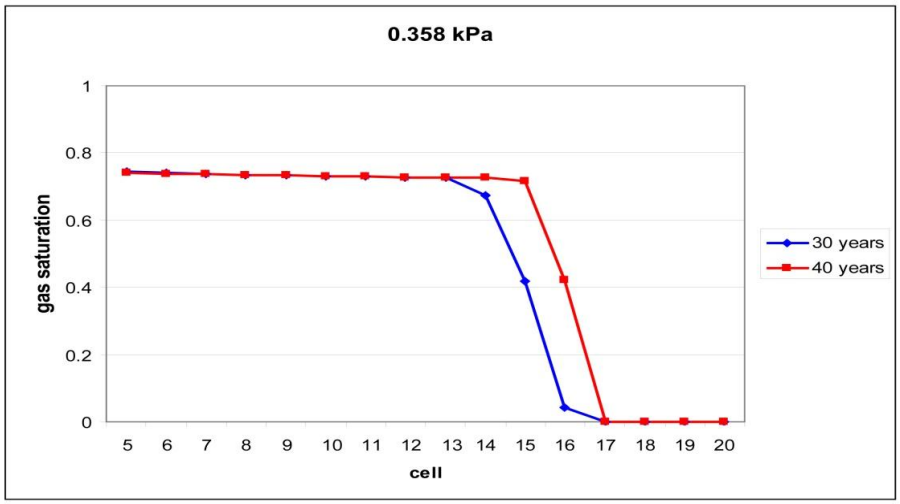

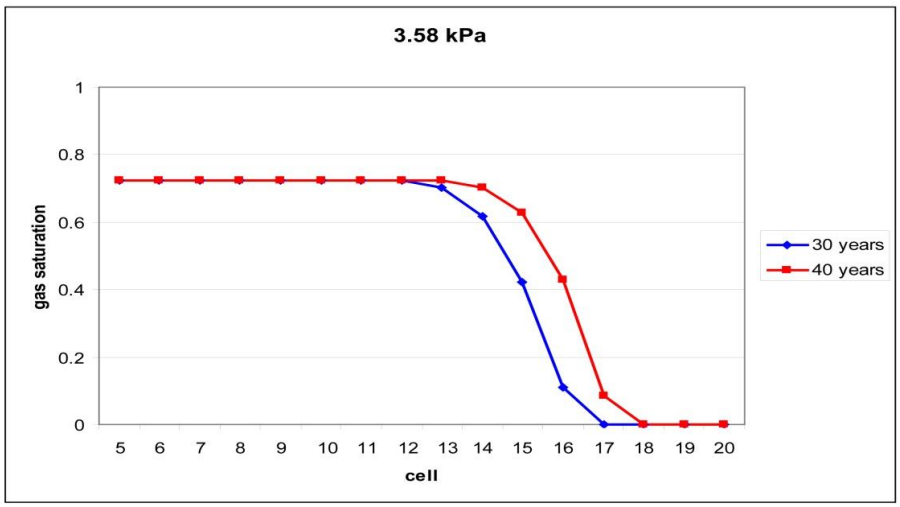

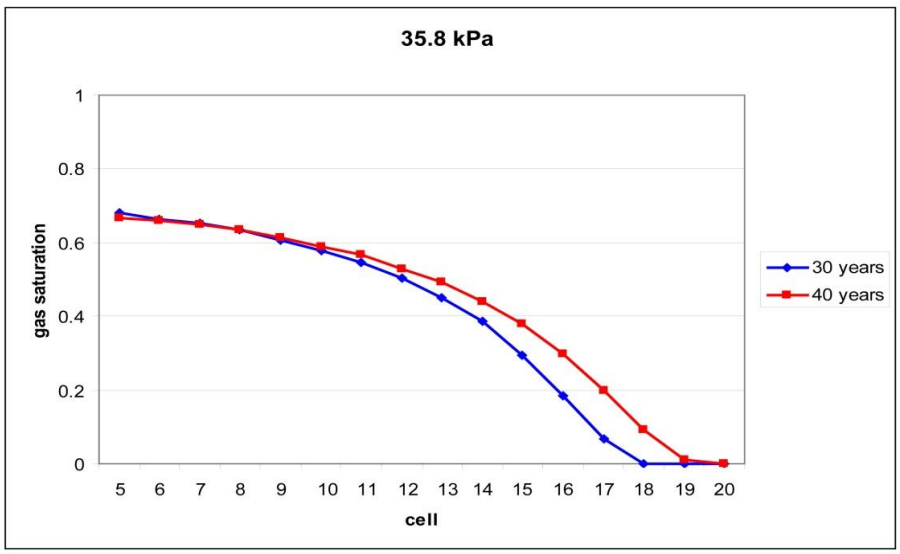

Figure 4.20: The graphs show the gas saturation of cells of the top layer of the model with increasing distance from the cell above the injection well. They illustrate that with decreasing

P_{c0} the gas water interface penetrates the cells piston-like and displaces most of the water. If P_{c0} is higher, more water will be retained in the cells and the plume becomes wider.

Figure 4.21 shows the impact of the different dissolution rates due to different capillary pressure curves on the average fluid pressure. It illustrates that, after injection ceases, the average fluid pressure still increases in simulation with low dissolution rates. The post injection pressure increase is not due to capillary pressure effects such as pressure gradients between the two phases. Simulations with no capillary pressure show the same trend. It is also not due to the development of the CO_2 plume. After 30 years, a part of the CO_2 is still present in deeper parts of the model cells. During the post injection period, this CO_2 rises to the top and becomes denser mainly due to the decreasing temperature. This process does not increase the average fluid pressure.

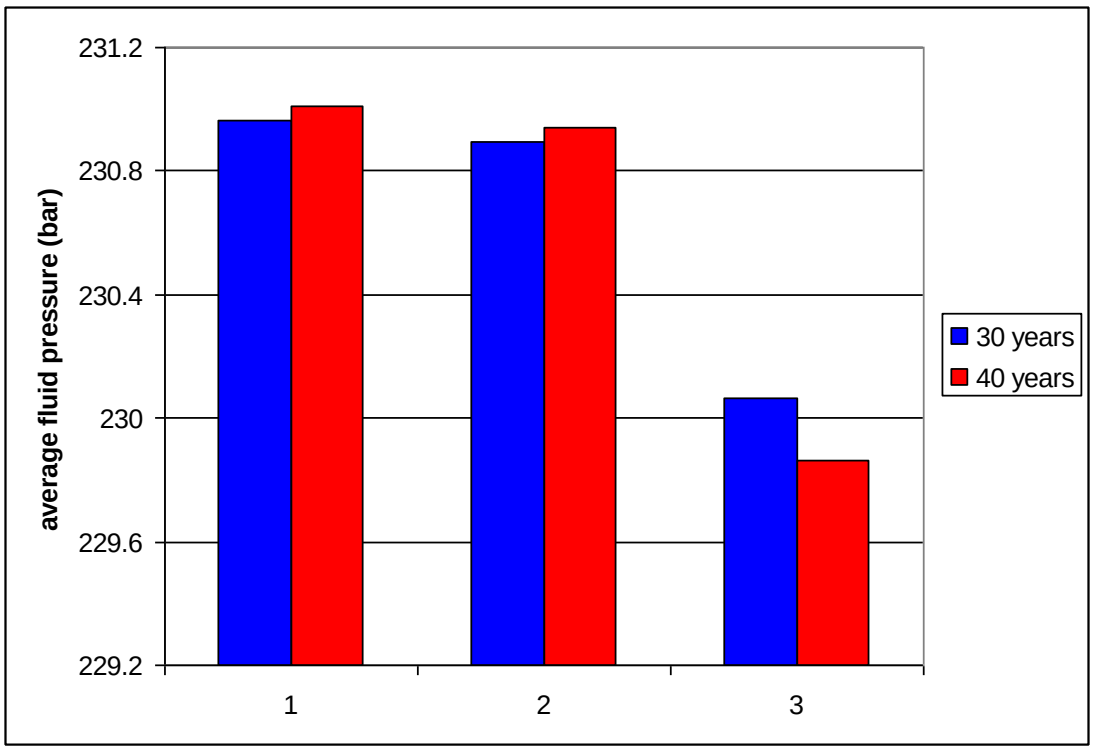

Figure 4.21: Average fluid pressure measured after 30 years of injection and 10 years of recovery. Capillary pressure was modelled with van Genuchten (1980). Values for P_{c0} are

0.00358 bar (1), 0.0358 bar (2, used for this study) and 0.358 kPa (3). Note the small impact of CO_2 dissolution on the pressure.

The most likely explanation of the pressure increase of the 'low-dissolution' models (and of the 'high-dissolution' model, although the effect is superposed by the pressure reducing dissolution) is a readjustment of the pressure after the breakdown of the CO_2 stream. Figure 4.22 illustrates the average fluid pressure and the fluid pressure of four cells in the simulated reservoir. The yellow shaded area represents the post-injection period when the pressure within the top cell above the injection point decreases. The same effect, only shorter and with greater decline, can be observed in the cell 1 1 14. The period represents the time after the CO_2 stream breaks down and brine flows 'back' into the former high pressure areas. This is a local effect and cannot be observed in cells which were not affected by the CO_2 stream directly. And indeed, cells on the other side of the modelled reservoir (here 77 77 1 and 77 77 14) have their maximum injection pressure at the beginning of year 31. This is the time when the average pressure reaches its maximum. Shortly after, the average pressure decreases slowly but steadily.

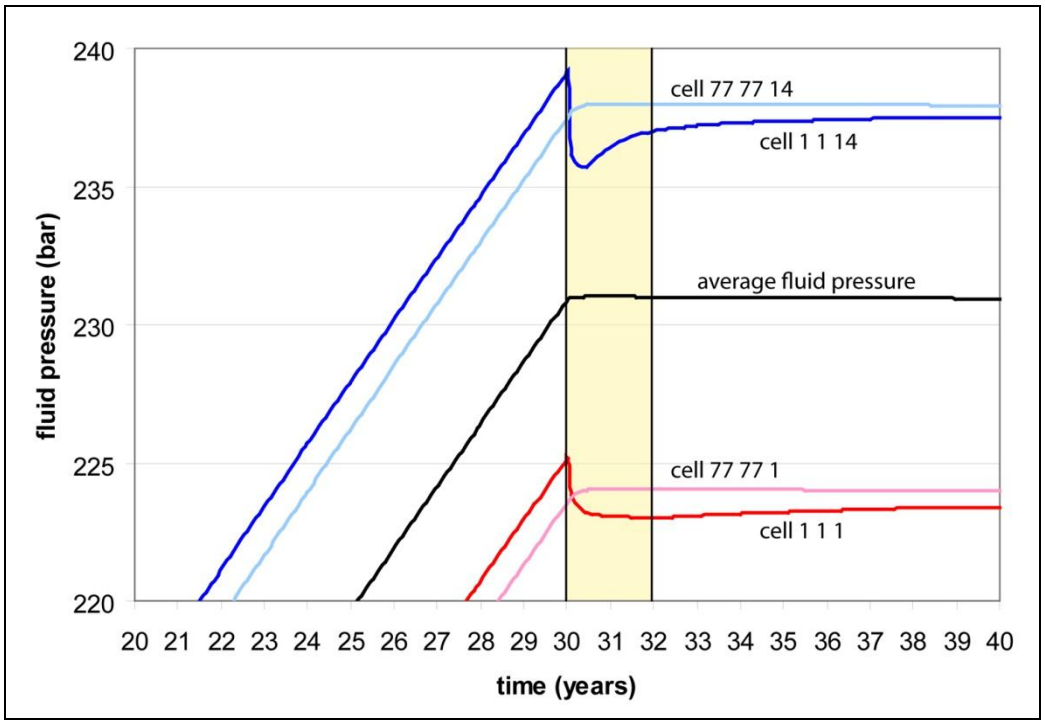

Figure 4.22: Average fluid pressure (black line) and fluid pressure development of four particular cells in the simulated reservoir with P_{c0} of 0.0358 bar: The cell at the bottom in which

the injection takes place (cell 1 1 14; blue), the cell at the bottom with maximum distance to the injection point (cell 77 77 14; light blue), the cell at the top of the simulated reservoir (cell 1 1 1; red; used for this study) and the cell at the top of the with maximum distance to the injection point (cell 77 77 1; light red). The yellow shaded area represents the time period when the pressure in cell 1 1 1 decreases after injection has ceased and before pressure rises again.

During the post-injection period, the pressure decreasing effect of CO_2 dissolution is too low in simulations with P_{c0} of 0.00358 and 0.0358 bar. The relatively high dissolution rate of the simulation with a P_{c0} of 0.358 bar lead to a decrease in pressure of 0.2 bar during the post-injection period. The overall pressure reducing effect is also very low. In the simulation with a P_{c0} of 0.0358 bar approximately 5.43 % of the CO_2 is dissolved into the water phase after 40 years. In the simulation with a P_{c0} of 0.358 bar approximately 9.86 % is dissolved during the same time. The average pressure difference of the two simulations after 40 years is 1.15 bar.

4.4.3 Discussion of the analytically derived results

The performed analytical approach (Zhou et al. 2008) provides a quick estimation of the CO_2 storage capacity of a saline aquifer. A comparison with numerical fluid pressure based methods give an excellent opportunity to justify the use of expensive engineering software. As mentioned before, the analytical method itself is only dependent on brine and pore compressibility, ‘maximum sustainable fluid pressure’ and the CO_2 volume at the particular pressure and temperature. Additionally, the calculation of CO_2 volume requires the application of an EoS.

4.4.4 Comparison of different methods

The storage capacity calculated with the simple analytical approach is approximately 6.55 Gt of CO_2. Dissolution is not taken into account. The stored CO_2 would occupy ~0.57 % of the total estimated pore space. By using a numerical simulator and the same method, a total amount of approximately 7.17 Gt of CO_2 would be injected.

Simulation results show that ~389.1 Mt of the CO_2 would dissolved into the pore water. This corresponds to 5.45 % of the entire injected CO_2. The storage capacity calculated with the numerical simulator is ~10 % higher.

Both the numerical approach and the analytical approach use the Peng-Robinson EoS. The calculated fluid properties (especially density and volume) of CO_2 should be similar and should not play a role in the variations of CO_2 capacity.

The sensitivity tests and the pressure map of the top layer of the reservoir show that there is only a small pressure gradient within the reservoir. Numerical simulation of the two phase fluid flow and the pressure flow do not have a significant effect and are not responsible for the differences.

The study shows that during the injection period the pressure reducing effect of CO_2 dissolution in brine does not have a significant effect. Although 5.45 % of the CO_2 in the numerical simulation is dissolved into the liquid phase, the pressure reducing effect is regarded to be low.

Brine compressibility was set to 0.000031 bar^{-1} in the analytical approach. Water compressibility, one of the most important parameters determining storage capacity, is calculated in Eclipse via the water density with the method proposed by Kell and Whalley (1975). To calculate the impact of salinity, the Ezrokhi method (Zaytsev & Aseyev 1993) is used. The analytical method uses a more recent equation (Batzle & Wang 1992). Although the differences in calculated densities of brine are usually relatively small, they might contribute to the differences in storage capacity.

The pore compressibility is 0.000045 bar^{-1} at a reference pressure of 150 bar. The storage capacity provided by the rock compressibility is supposed to be similar for both the numerical and the analytical approaches. Higher compressibility provides

more storage space if pressure increases due to CO_2 injection. This is obviously also true for porosity. No sensitivity tests have been conducted on that because the general trend of the results is clear.

4.4.5 Pressure as the limiting factor

The study shows that if fluid pressure cannot dissipate or dissipates very slowly during injection, pressure increase is the limiting factor for large-scale injection and storage of CO_2 in saline aquifers. Some important aspects, such as a full understanding of maximum reservoir fracture pressure estimation or a detailed geological description of large scale saline aquifers, are desirable. However, it is possible, at least as a first approach, to calculate the CO_2 storage capacity of poorly characterised aquifers. Whether the calculated capacity of the offshore UK Bunter Sandstone is a conservative or an optimistic approximation depends on how uncertainties are evaluated. For example, one of the main uncertainties is the permeability of under or overlying rock units. The proposed method assumes that there is no pressure dissipation from the Bunter Sandstone aquifer into either the underlying or overlying geological units. However, pressure migration through under or overlying rock units would increase the CO_2 storage capacity (Birkholzer et al. 2009; Zhou et al. 2008). Zhou et al. (2008) showed that a seal permeability of 10^{-4} to 10^{-2} mD provides a semi-open pressure system with a reduction of the pressure build-up during injection due to brine migration through the seal while CO_2 is still retained by the capillary entry pressure. The Bunter Sandstone is sealed by a thick sequence of mudstone and evaporates. While there is no permeability data available from these units, permeabilities are unlikely to be within the range defined by Zhou et al. (2008) and hence pressure migration through the seal during the injection is considered to be unlikely. The underlying rock formation beneath the Bunter Sandstone, the Bunter Shale, is mudstone-dominated. Geological features which could work as pressure migration channels (for example fluvial channel sandstones) are impossible to predict or to detect. Additionally, the underlying unit below the Bunter Shale, the Zechstein evaporates, contain significant halite and are effectively impermeable and

form the seal to the majority of the gas fields in the area. A hypothetical brine migration from the Bunter Sandstone into the Bunter Shale would therefore not lead to a general pressure equilibration but would rather increase the size of the aquifer. Pressure dissipation into the underlying formation beneath the Bunter Sandstone is therefore possible but cannot be predicted accurately and should therefore not be accounted in storage capacity estimates.

An alternative to the injection of pure CO_2 into saline aquifers is to inject CO_2-saturated brine which is denser than native brine and sinks to the bottom of the formation. Although the most obvious advantage of this method is an avoidance of buoyancy driven leakage it also reduces the increase of pressure in the aquifer, because CO_2 in solution occupies less volume than the brine and the free phase CO_2 together. The CO_2 would be dissolved into the brine in a mixing tank at the surface, prior to injection. Burton and Bryant (2009) calculated the brine required for the CO_2 disposal of a 500-MW-capacity power plant to range between 30,000 and 120,000 m^3 per day. The brine would be produced from the target aquifer and re-injected after the CO_2 has been dissolved. The main arguments against the injection of saturated brine are costs and energy consumption. Nevertheless it is the method which minimizes the risks of compromising the injection process due to fluid pressure increase and additionally prohibits an upward migration of the CO_2.

4.4.6 Comparison with a non-pressure based storage calculation

Holloway et al. (2006) calculated the CO_2 storage capacity of the offshore UK Bunter Sandstone to be 14.2 Gt (with an additional 0.4 Gt within the gas fields which is not relevant to our study). This capacity estimation assumes that a CO_2 saturation of 40 % is achievable within the known closed structures within the aquifer, with effectively infinite aquifer communication. The achievable saturation is based on numerical models which simulated the injection of CO_2 into one structure (Obdan & van der Meer 2003; Obdan et al. 2003). In the study, a method has been proposed to calculate CO_2 storage capacity of saline aquifers based on fluid pressure increase due

to CO_2 injection which is applicable to poorly characterised aquifers. The capacity of the offshore UK Bunter Sandstone calculated with this method will be reduced relative to a method with no pressure effects. The simulation results show that either 46 % (proposed analytical approach) or 50 % (proposed numerical approach) of the CO_2 calculated (14.2 Gt) by Holloway et al. (2006) can be successfully injected and stored. Given the different approaches used in our method and in the calculations of Holloway et al. (2006) it is encouraging that two estimations of the storage capacities of the Bunter Sandstone based on different concepts are still relatively similar.

4.5 Conclusions

This chapter has described a numerical method of calculating the CO_2 storage capacity of confined saline aquifers which is based on fluid pressure increase due to CO_2 injection. A case study utilising the new method was applied to an aquifer in the southern North Sea which could be a target for CO_2 sequestration. Subsequently, the results were compared with an analytical CO_2 storage calculation method introduced by Zhou et al. (2008).

The calculated capacity of the offshore UK southern North Sea Bunter Sandstone Formation is 6.55 to 7.17 Gt of CO_2 by using an analytical or a numerical approach respectively. Holloway et al. (2006) calculated the storage capacity of the same formation, with a method which did not take pressure into account, to be 14.2 Gt of CO_2, approximately twice as high as the capacity calculated in our study. The results here indicate that neglecting fluid pressure results in over-estimates of CO_2 storage capacity. Therefore, fluid pressure is vital in calculating the CO_2 storage capacity of saline aquifers. However, the storage capacity of the Bunter Sandstone Formation remains very high and it shall be emphasised here that if pressure is taken into account, the CO_2 capacity will only be reduced to ~50 %.

By comparing the results, the differences are relatively moderate and comprehensible. We conclude that the application of a numerical simulator for the well spacing method is not needed. The main reasons are:

- The proposed Peng-Robinson EoS does not require a complicated approach and can be simply solved with software such as MATLAB or EXCEL.
- Our model results show that the one and two phase fluid flow does not affect the results significantly. No significant pressure gradients could be observed. An ‘average pressure’ is therefore sufficient.

- Simulations have shown that the pressure decreasing effect of CO_2 dissolving into brine is negligible during the injection period and a 10 year post-injection period.

All important parameters, such as rock/fluid compressibility, density/volume of CO_2, pore-volume and pressure increase can be freely chosen and be added to Zhou's analytical approach (Zhou et al. 2008). This is regarded as a much more favourable way of calculating the storage capacity than the expensive and time consuming use of a numerical simulator.

5 How much CO_2 will be sequestered by mineral reaction during engineered CO_2 storage?

5.1 Introduction

5.1.1 Hypothesis

Precipitated carbonate minerals always contain CO_2. Therefore mineral trapping of CO_2 should be defined as enhanced carbonate precipitation as a consequence of an artificially or naturally increased CO_2 concentration. As a result, the 'trapped CO_2' incorporated in the carbonate crystal should be in an isotopic equilibrium with the CO_2 that triggered its precipitation. It should therefore be distinguishable from earlier carbonates which have precipitated out from CO_2 of a different origin. There are no engineered CO_2 storage sites that have stored CO_2 for a sufficient period of time to investigate mineral trapping, therefore researchers are dependent on computer simulations, experiments and the study of natural analogues.

The Fizzy field in the southern North Sea is a Rotliegend gas field with a present CO_2 concentration of ~50 mole %, according to analyses performed by Tullow Oil plc. Adjacent to the Fizzy field is the Orwell field, a Triassic gas field with wells and cores that reach the Rotliegend Formation. The pore fluid of the Rotliegend Orwell stratigraphy has a low CO_2 concentration (< 2 %, Wilkinson et al. 2009). Dolomite is the only abundant carbonate mineral in the Fizzy and Orwell Rotliegend rocks. Additionally, the Fizzy reservoir contains 0.1-0.8 vol. % of dawsonite (determined by XRD, Wilkinson et al. (2009)). It is presumed here that Orwell dolomite has never been in contact with the CO_2 currently present in Fizzy. This is a fair assumption because if CO_2 had been present in Orwell there is no likely reason why it would be almost entirely replaced by methane when this replacement did not occur in Fizzy. Orwell dolomite, as well as dolomite of comparable locations in the Rotliegend Formation of the southern North Sea, is supposed to have a diagenetic origin that is referred to here as an early precipitation stage (Purvis 1992; Sullivan et al 1990). The same dolomite presumably precipitated in all areas of the southern Permian Basin

with a similar depositional environment. Dolomite cement of the Rotliegend Formation of the Southern North Sea that precipitated during early diagenesis (including the Orwell Rotliegend Sandstone and the Fizzy field) is called 'diagenetic dolomite' in this study. The hypotheses is that during a time of high CO_2 concentration, which occurred only in Fizzy, a second precipitation stage produced a second dolomite generation, which is called 'sequestration dolomite' in this study. The later stage 'sequestration dolomite' will coat a core of earlier 'diagenetic dolomite' and will dissolve first, if the initial zonation is preserved (Fig. 5.1).

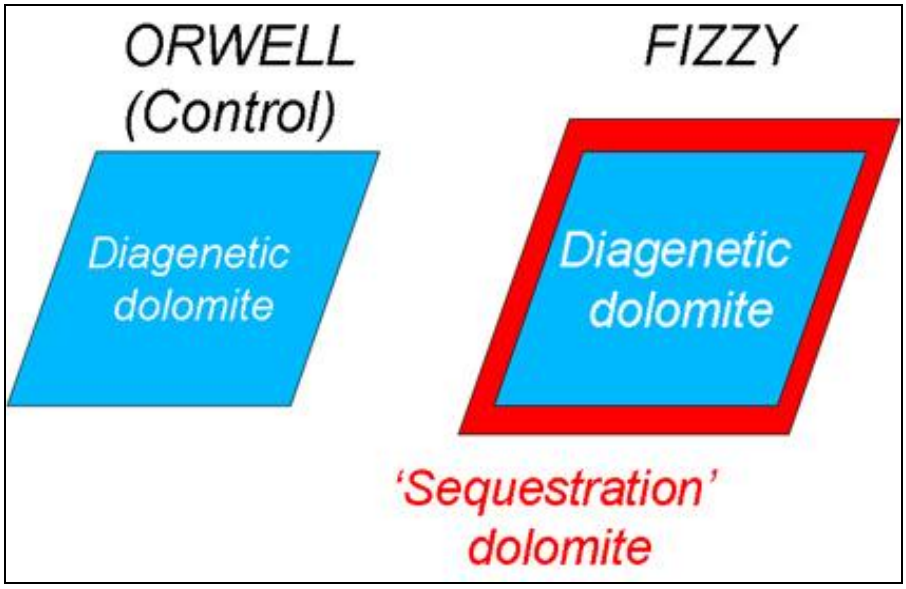

Figure 5.1: Schematic picture to illustrate the age relationship of 'diagenetic dolomite' and 'sequestration dolomite'. Note that 'sequestration dolomite' would only precipitate related to high CO_2 concentration reservoirs such as Fizzy. Due to the age relationship, 'sequestration dolomite' should coat a core of 'diagenetic dolomite' and dissolve earlier if the zonation is preserved.

During a previous study conducted by the SCCS (Scottish Carbon Capture & Storage) group at the University of Edinburgh a standard optical investigation was performed. Thin sections were made for conventional petrographic examination; all were stained for feldspars and carbonates. Rock chips and polished thin sections were studied using an SEM with EDS, back-scatter and CL, and both gas and water zones were studied (Fig. 5.2). Additionally, the whole rock isotopes samples from the Fizzy field and from the Rotliegend Formation underneath the Orwell field were

measured. No direct evidence for isotopic zonation could be found and only the deviation from the 'background' towards a calculated isotopic ratio for ‘sequestration dolomite’ of the Fizzy samples was found (Wilkinson et al. 2009). The application of the ion probe was considered but rejected because the dolomite cement in the rocks is too small.

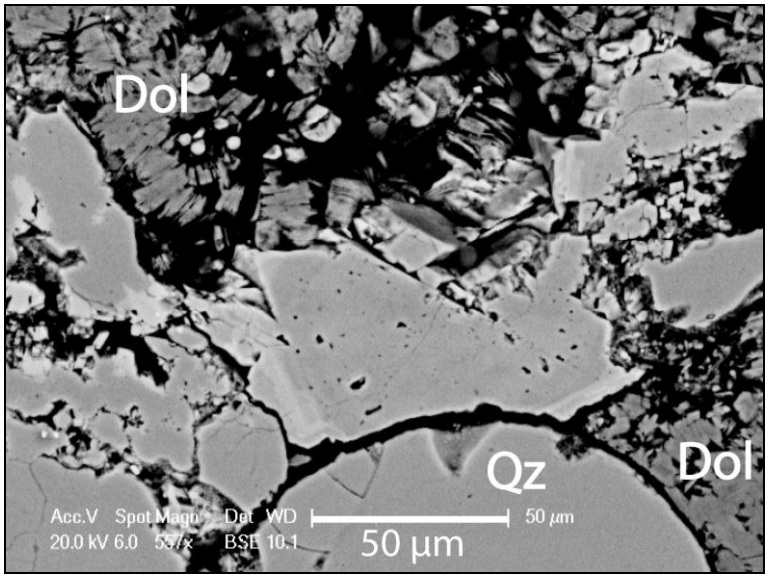

Figure 5.2: SEM-CL image of dolomite cement surrounding a Quartz grain (round grain at the bottom of the image) from the Orwell Field, which is very similar to that in the Fizzy accumulation. FOV=190 microns.

For this study we dissolved dolomite-rich Rotliegend rock samples of the Fizzy and Orwell fields in phosphoric acid. Evolving CO_2 was extracted stepwise and its carbon and oxygen isotope ratios were subsequently measured. The whole rock samples were crushed very gently in order to preserve any zonation of ‘diagenetic dolomite’ and ‘sequestration dolomite’ in the Fizzy cement. Comparison of the isotope data of the two locations should reveal whether ‘mineral trapping’ has occurred in the Rotliegend Formation in the southern North Sea.

5.1.2 Geological setting

All samples used in this study are from the Rotliegend Formation of the southern North Sea (Fig. 5.3). The Orwell field is actually a Triassic gas field. However, some wells were drilled into the deeper Rotliegend Formation and core material from that zone is available. Therefore, the so called ‘Orwell samples’ were taken from underneath the actual gas accumulation and were not derived from the gas field itself (Fig. 5.3).

The Fizzy gas accumulation was discovered in 1995 by the 50/26b-6 exploration well and was the first of several carbon dioxide and nitrogen rich gas field discoveries in the area (Underhill et al. 2009). The Rotliegend reservoir rocks were deposited in the vast southern Permian basin on top of the deformed Carboniferous units of the Variscan foreland (Ziegler 1990). Regional normal faulting and subsidence controlled the sedimentation rate in a desert like environment resulting in the formation of aeolian wadi and sabkha deposits (Glennie 1998). The cap rock of the Rotliegend reservoirs in the southern North Sea is the Zechstein Supergroup (Tucker 1991). It has proven its impermeability as a cap rock of many gas fields in the southern North Sea such as the Fizzy field. The extrapolation of its sealing capabilities from gas fields to adjacent areas remains controversial. The presence of the Triassic Orwell field, which lies relatively close to the Rotliegend Fizzy field, shows that there must have been fluid pathways which connected the Carboniferous source rocks with the Triassic Bunter Sandstone.

The main source rock of the North Sea gas fields within the southern Permian basin is the upper Carboniferous coal-rich Coal Measures Group (Westphalian Formation) which were deposited in the Variscan foreland (Glennie & Underhill 1998). Due to Mesozoic subsidence and deposition, the Coal Measures Group reached its maximum depth and maturity in the early part of the late Cretaceous (Glennie & Boegner 1981; Van Hoom 1987; Alberts & Underhill 1991).

The source of the Fizzy CO_2 remains unknown. Interestingly, Fizzy and other CO_2 rich fields in the area such as Oak and a third accumulation penetrated by well P/01-3 (Fig. 5.3) all lie adjacent to the boundary fault of a structure called the Fizzy Horst (Underhill et al. 2009). However, seismic sections of the area interpreted for their study do not show a structural link between the boundary faults and other faults of the Fizzy Horst structure such as, for example one main listric fault, deeper in the upper crust. Therefore, with the available information the local distribution of the CO_2 rich fields is not known. Because of the local distribution of the CO_2 rich fields, we attribute CO_2 enrichment in the Fizzy and adjacent gas accumulations of the area to a localized CO_2 source.

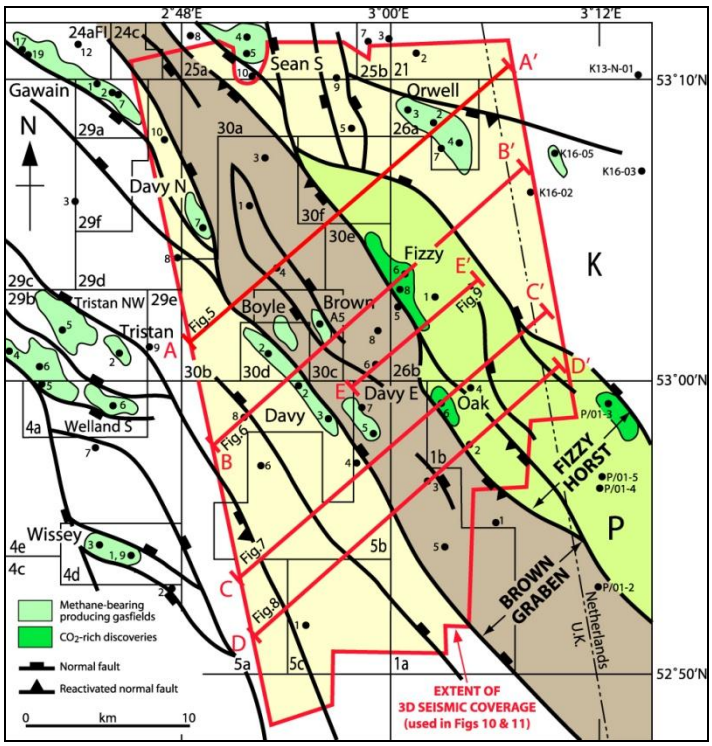

Figure 5.3: Location map showing the main structures in the vicinity of the gas accumulations. Also shown are the extent of 3D seismic data coverage used in a study published by Underhill et al. (2009). Seismic lines A-A' and B-B' are used here to explain the geology of the studied area. Figure is taken from Underhill et al. (2009).

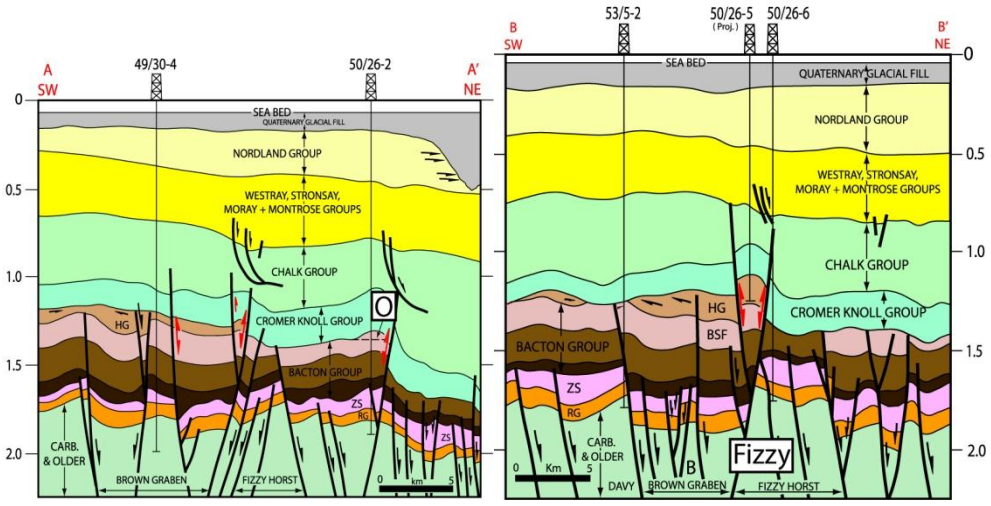

Figure 5.4: Interpreted SW-NE-striking sections through the Orwell field (section A-A'; O=Orwell) and the Fizzy field (section B-B'; Fizzy=Fizzy field). Orwell samples used for this study were taken from the Rotliegend Formation underneath the gas field. Y-axis in two way travel time (seconds). HG=Haisborough Group; BSF=Bunter Shale Formation; ZS=Zechstein Formation; RG=Rotliegend Formation; B=Brown Graben. For orientation see Fig. 5.3. Figure is taken from Underhill et al. (2009).

Wilkinson et al. (2009) propose thermal alteration of unspecified sediments as the CO_2 source. The main argument is the absence of other possibilities. A potential minimum age for the CO_2 could be inferred from the initiation of gradual cooling during the inversion which began during the Late Cretaceous. Hence, following this idea, the CO_2 has a minimum age of approximately 50 Ma years and should have migrated into the reservoir shortly after. Interestingly, the Rotliegend traps were formed during uplift of the inversion during the late Cretaceous and the Cenozoic and are younger than the migration of the hydrocarbons (Glennie & Boegner 1981). Alberts & Underhill (1991) explain this 'miss-timing between charge and trap formation' with hydrocarbons that had been trapped underneath the Zechstein Supergroup and subsequently migrated into the traps during or after their formation. However, any CO_2 generated by thermal alteration must be younger because otherwise it would be uniformly distributed in the Rotliegend Formation.

An alternative origin of the CO_2 is presented by Underhill et al. (2009). They propose that igneous and volcanic activity during the early Paleogene could have generated the gas (Underhill et al. 2009). They suggest that the creation of today's CO_2 gas fields predate the Cenozoic structural inversion and that CO_2 migrated via 'through-going, deep-seated, normal faults' into reservoirs that would have been hydrocarbon-rich if they had not been CO_2 charged before. Therefore the traps of the CO_2 gas fields must predate the hydrocarbon gas field traps.

Whatever the source of the CO_2, both theories suggest an age of approximately 50 Ma years (Wilkinson et al. 2009; Underhill et al. 2009). Hence, regardless of the source, the CO_2 should have been in contact with reactive minerals over geological timescales - far longer than any artificial CO_2 sequestration project will ever be monitored.

5.1.3 Samples used for this study

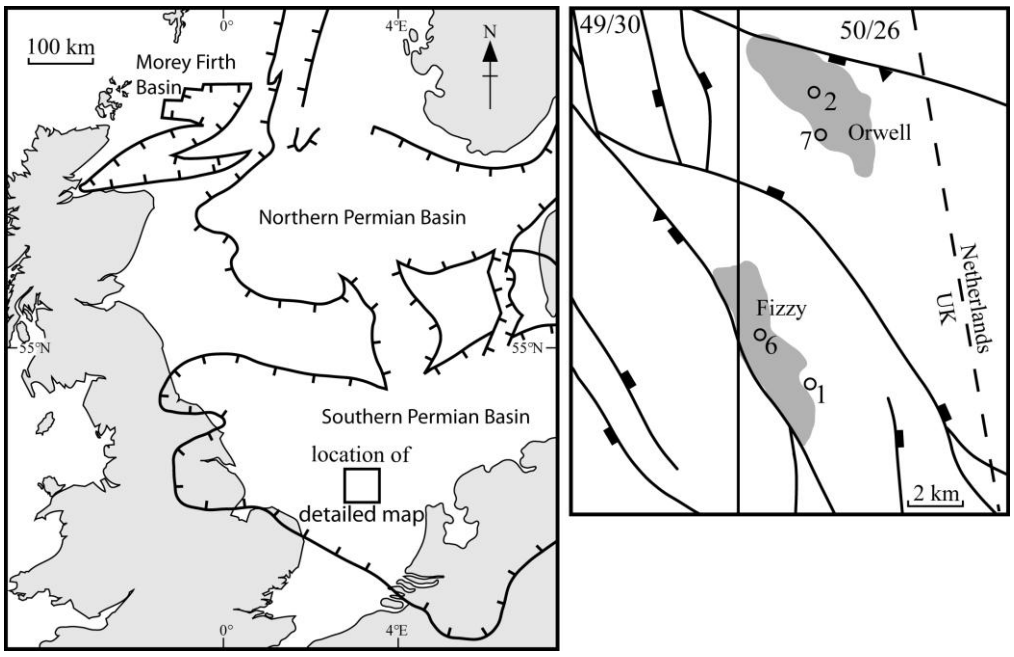

Figure 5.5: Location map for the Fizzy and Orwell gas accumulations in the North Sea. The enlargement shows parts of UK blocks 49/30 and 50/26 including wells identified by number. Also shown are the tectonic elements taken from Underhill et al. (2009).

Two wells from the Orwell field have 83 m (UK well numbers: 50/26a-2 and 50/26a-7; Fig. 5.5), and two wells from the Fizzy field have 86 m of core in total (UK well numbers: 50/26-1 and 50/26b-6; Fig. 5.5; Fig. 5.6). Information about the fluid zone is available for the Fizzy field samples. Since the Rotliegend Formation in the Orwell area does not contain any gas, the pore fluid should be dominantly brine. Further information on the origin of the samples is listed in Table 1. Seven samples from the Fizzy field from 6 core locations and four samples from the Orwell field were chosen. Three of the Fizzy field samples were derived from the gas cap and four from the water leg underneath the gas cap.

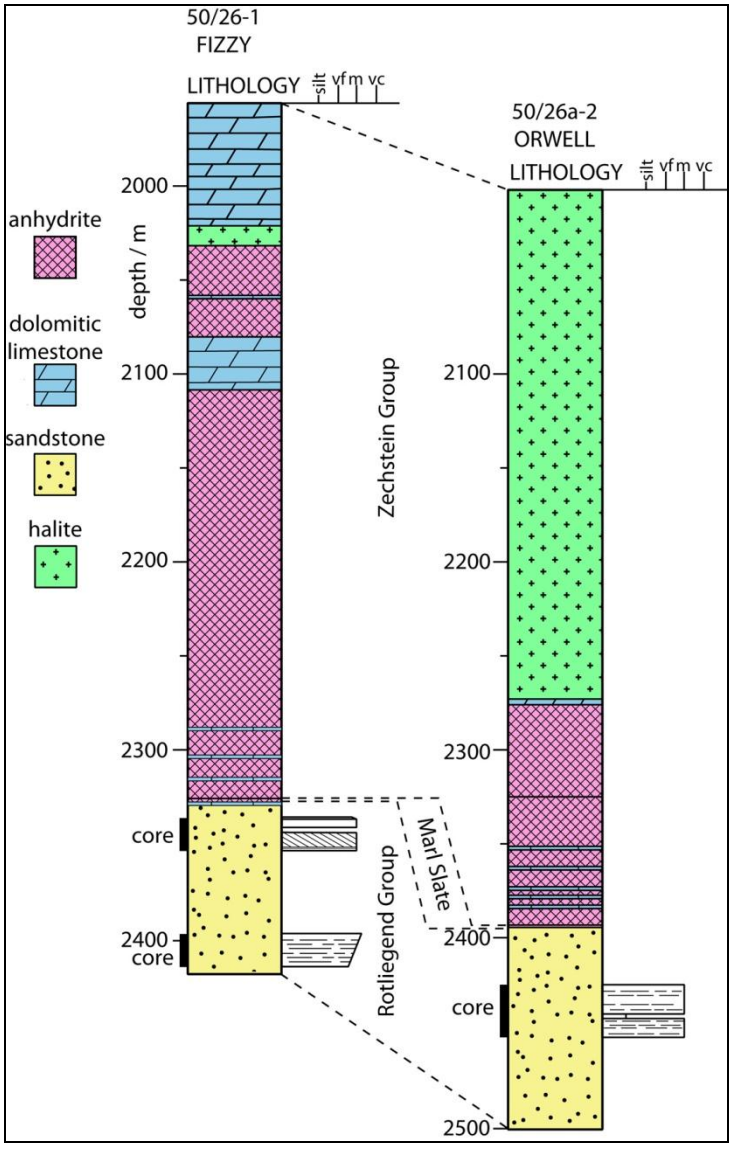

Figure 5.6: Stratigraphic log of the reservoir and seal of the Fizzy gas field and the Rotliegend and Zechstein Formation underneath the Triassic Orwell field. Grain sizes are shown only for cored sections. For well locations see Fig. 5.5. Taken from Wilkinson et al. (2009).

The mineralogy of the Rotliegend Sandstone from the Orwell and Fizzy fields is summarized in Table 2. The amount of dawsonite was determined by XRD analysis of whole rock samples. Further information is given in Wilkinson et al. (2009).

Number	Qz	Rock Frag.	K-Feldsp.	QOG	Dol.	Clay (Not Kaol.)	Kaol.	Gyp. and Anh.	Dawsonite	Poro.
1	51	12	7	1	14	0	3	0	0.6	12
4	51	19	6	2	8	2	1	0	0.3	9
5	59	16	2	1	5	2	1	0	0.5	14
8	50	14	6	1	10	0	3	2	0.1	13
9	57	17	5	2	2	0	4	3	0.5	9
10_1	60	19	3	2	1	0	2	2	0.1	10
10_2	60	19	3	2	1	0	2	2	0.1	10
11	42	11	19	1	11	0	0	5	Bel. det.	10
13	43	12	12	2	10	0	6	3	Bel. det.	10
14	40	13	17	0	11	0	4	1	Bel. det.	11
16	46	8	11	0	11	0	6	15	Bel. det.	3

Table 5.2: Composition of Rotliegend Sandstone from the Fizzy and Orwell fields, point count data. See Table 1 for origin of the samples. Dawsonite determined by XRD. Qz. = Quartz, Rock Frag. = Rock fragments, QOG = Quartz overgrows, Kaol. = Kaolinite, Gyp. = Gypsum, Anh. = Anhydrite, Bel. Det. = below detection, Poro. = Porosity. All data are taken from Wilkinson et al. 2009.

5.2 Methodology

5.2.1 Equipment and technique

All experiments were conducted at SUERC laboratories at East Kilbride. The extracted carbon dioxide was dried, purified and analysed on a VG Isogas SIRA 10 dual inlet, triple-collector isotope ratio mass spectrometer. All experimental work was performed at SUERC (Scottish Universities Environmental Research Centre) in East Kilbride (Scotland) under the supervision of Prof Tony Fallick.

All samples were dissolved in 103 % phosphoric acid; the carbon dioxide evolved from the dissolution is isolated, purified and quantified, and then analysed by the mass spectrometer. The relative abundances of the mass-to charge ratios at 44, 45 and 46 of evolved CO_2 are compared with those of a working standard reference gas of known isotopic composition. The raw delta values for carbon and oxygen isotopes can be calculated by using the equation:

$$\delta_{S-R} = \left(\frac{R_S}{R_R} - 1\right) 10^3 \quad (1)$$

Where *S* is the sample and *R* is the reference mass ratio. Adjusting the raw delta values with respect to the international V-PDB standard involves the equation:

$$\delta_{S-PDB} = \delta_{S-R} + \delta_{R-PDB} + 10^{-3}\delta_{S-R}\delta_{R-PDB} \quad (2)$$

All isotopic values of this study are reported relative to V-PDB. Isotopic values of studies of Sullivan et al. (1990) and Purvis (1992) are relative to the virtually identical PDB. For the correction of the raw values, a phosphoric acid fractionation

factor for dolomite at 100°C of 1.01186 was used (Rosenbaum & Sheppard 1986). Corrections were performed by using free online software: http://130.209.21.92:6622/sira10.php.

Three kinds of errors are involved in the measurement of isotopes in this study.

- Instrument error: The isotopic ratios of carbon and oxygen are determined with this error when an aliquot of pure carbon dioxide is presented to the mass spectrometer. The range of this error is typically less than plus or minus 0.05 per mil at one sigma (personal information from Prof Anthony Fallick).
- Chemistry error: A second error associated with acid hydrolysis chemistry by which carbon dioxide is released from the carbonate when mineralogically pure and isotopically homogeneous carbonates are involved. A generous estimate of this based on previous work at SUERC is plus or minus 0.1 per mil at one sigma (personal information from Prof Anthony Fallick).
- Especially for inhomogeneous samples, there is also a sample specific error that involves different carbonate phases or whether one phase armours another. Estimation of this error is difficult and certainly not constant from sample to sample. Also, in the case of the stepwise extraction experiments, the error might not be constant from step to step of the extraction.

The ‘instrument error’ and the ‘chemistry error’ should be taken into account but they are too small to be displayed on the graphs. Of importance is the sample specific error. Although this is a very important uncertainty, the quantification of this error is impossible because of the inhomogeneity of the samples in combination with the low number of experiments and the additional uncertainty due to the stepwise extraction. Important to bear in mind when interpreting the data is that all stepwise extraction data have a relatively similar uncertainty and that the focus should rather lie on trends and not on individual isotope values.

5.2.2 Sample preparation

It is essential for the stepwise dissolution method that the initial zonation of the carbonate crystals is preserved during the preparation procedure. Instead of grinding the rock and then separating the dolomite out, the samples were gently crushed and the whole rock sample was then analysed.

Material from the Orwell and the Fizzy (water) field contain between 1 and 15 vol. % of anhydrite and gypsum. There had been some concern that sulphur-bearing contaminant molecules would compromise the measurement of the isotopic ratios of carbon and oxygen. Hence, gypsum and anhydrite had to be removed from the sample. This was done by simply dissolving the crushed material in pure water. The solubility of the two minerals is between 2.0-2.5 grams per litre. Hence 2 grams of gently crushed rock material were left in 1 litre of pure water for 24 hours. Samples 8, 9, 10/1, 11, 13, 14, and 16 were washed; samples 1, 4, 5 and 10/2 were unwashed.

Further work has shown that neither the 'washing' of the sample nor the presence of anhydrite/gypsum affect the results recognisably. Fig. 5.7 shows bulk measurements of carbon and oxygen isotope ratios of four Orwell samples. Every sample was split in two, one was washed and the other was not. Three of the four pairs show almost identical results. One sample shows differences in the isotopic composition. Assuming the samples are relative heterogeneous, the data show that either the washing does not remove the gypsum and anhydrite or that the presence of anhydrite/gypsum does not change the measurement. Either way, there is no effect on the bulk analysis.

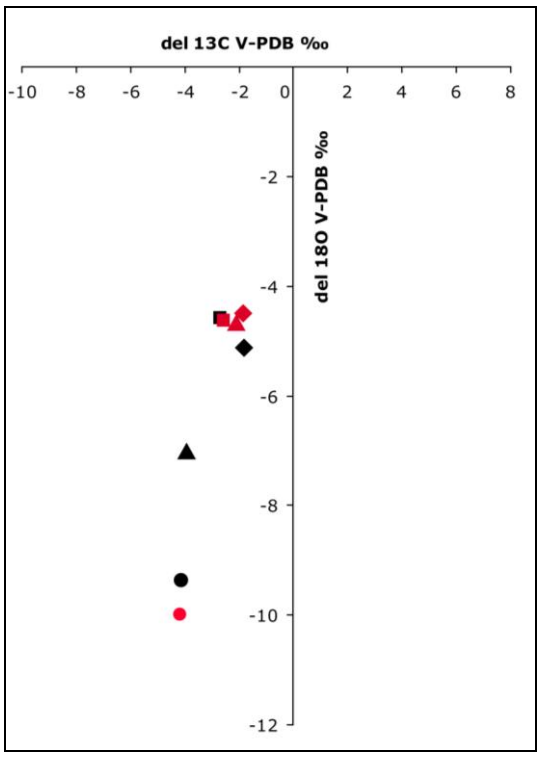

Figure 5.7: Stable carbon and oxygen isotope data from the dolomites from underneath the Orwell gas accumulation (see table 5.1 for origin of the samples). Two analyses were conducted on each sample. One is in its original crushed form and one was washed in pure water. Symbols identify the four samples (circles = 16; triangles = 13; diamonds = 14; squares = 11) and the colour shows whether the material was washed or not (black for washed and red for unwashed).

5.2.3 Whole rock analysis of the Orwell dolomite

To identify the carbon and oxygen isotope compositions of the 'diagenetic dolomite' four samples of two wells of the Orwell gas accumulation were crushed, dissolved and analysed. Three samples were taken from well 50/26a-7 and one from well 50/26-2. The crushed whole rock material was reacted over several days with 103 % phosphoric acid at 100˚C and the resultant CO_2 subsequently dried, purified, quantified and isotopically analysed (McCrea 1950).

5.2.4 Stepwise extraction and analysis of CO_2

The material that was chosen for the stepwise extraction experiments was reacted with phosphoric acid at 25˚C for two or three days. Table 3 shows the times of extraction for every experiment and whether the extraction and analysis was a success or a failure (explained below).

Sample	Day 1				Day 2		Day 3	
Orwell								
11w	11:40	12:20	15:10	17:50	09:35	16:35		
13	09:35	10:40	14:10	18:10	10:50	17:30		
14	10:10	11:00	14:40	18:28	09:40	16:40	09:50	16:40
16w	09:50	10:20	13:20	16:40	09:30	17:00	09:20	17:00
Fizzy (gas)								
8	09:50	10:40	14:30	17:35	09:20	16:20	09:35	16:20
9	09:15	10:20	13:50	17:50	10:30	17:10		
10w	09:30	10:00	13:00	16:20	09:10	16:45	09:55	16:50
10uw	10:10	10:40	13:40	17:20	09:50	17:15	09:30	17:15
Fizzy (water)								
1	09:30	10:15	13:45	17:15	09:00	16:00	09:15	16:00
4	09:00	10:00	13:30	17:30	10:10	16:50		
5uw	11:20	11:50	14:30	17:30	09:15	16:20		

Table 5.3: The list shows the timetable of the stepwise extractions of the experiments. Almost half of the first extractions failed because not enough dolomite could react in such a short time to give sufficient gas for isotopic analysis. Note that experiments ran for either two or for three days. Analysis of 'grey' extractions failed due to too small gas samples; 'orange' analyses failed because of air contamination.

The first CO_2 extraction was performed after a relatively short time period (20-50 minutes). The initial idea was to react traces of calcite that might have been too small

to be recognised under the microscope. Half of the first extractions failed because the amount of CO_2 was too small. The successful first extraction produced extremely negative (both carbon and oxygen) values (Swart et al. 1991). Air contamination was another reason why the extractions failed. After the last extraction the samples were placed on a hot block and spent at least three days there to guarantee that all the dolomite dissolved. Subsequently, the final extractions were performed.

5.3 Isotope geochemistry of 'diagenetic dolomite'

5.3.1 Isotopic composition of Rotliegend dolomite cement, southern North Sea

Dolomite is the most abundant cement in the Rotliegend Sandstone. Its precipitation requires a high Mg/Ca ratio which is common in evaporitic environments (e.g. Warren 2000). The precipitation of anhydrite and gypsum, a widespread process during evaporite formation, reduces the Ca concentration of the fluids which increases the Mg/Ca ratio. Purvis (1992) assumed that dolomite formation during the early burial of the formation is directly related to depth below the overlying Zechstein Formation. Close to the seal, where the Mg concentration is highest, dolomite cement is most abundant and consists of pore-lining rhombs (Purvis 1992) of dolomite which is likely to be linked to the vicinity to the Zechstein. With increasing depth, dolomite abundance decreases but the crystal size of the dolomite increases.

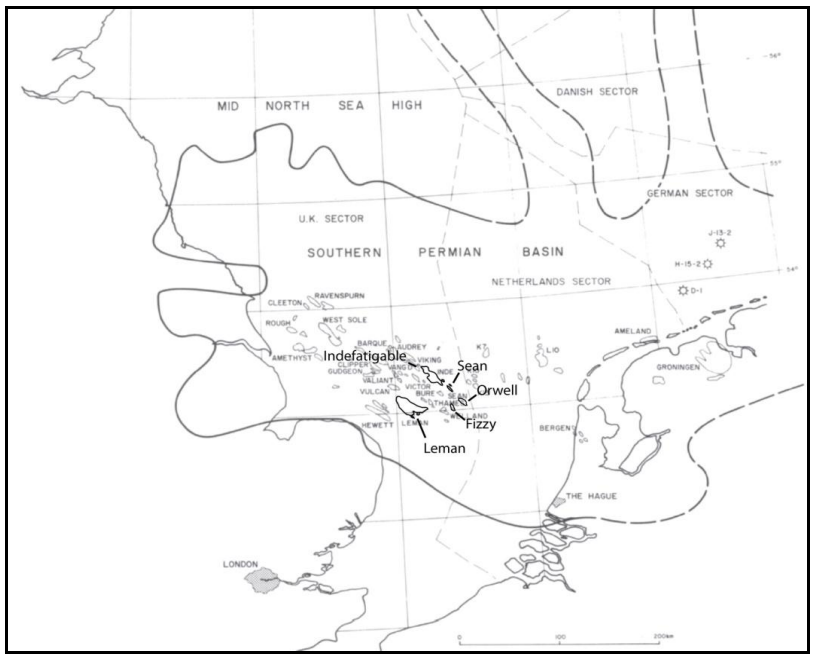

Figure 5.8: Southern North Sea provinces showing the southern Permian basin and the Rotliegend gas fields. Highlighted areas indicate gas accumulations with wells which were used for this study. (modified after Glennie and Provan (1990))

Two studies (Sullivan et al. 1990 and Purvis 1992) of oxygen and carbon isotope ratios of dolomite give a relatively good characterisation of the regional dolomite isotopic composition. They are taken directly from the vicinity of natural gas accumulations (Leman, Indefatigable and Sean Fields; Fig. 5.8) and data are available from both the gas cap and the water leg. The samples and the preparation are introduced here briefly in order to make the different data sets comparable. All isotopic analyses have been performed on either the bulk rock or on pure dolomite. The isotopic data which were taken from Sullivan et al. (1990) and Purvis (1992) were presented relative to PDB whereas the data of this study are presented relative to VPDB. A correction of the PDB values has not been conducted. The isotopic composition calculated will be a mixture of the earliest formed carbonate and the later, outer zones of a different composition (Purvis 1992).

Data set 1 (Sullivan et al. 1990)

Well no.	Depth (meters)	δ13C (‰ PDB)	δ18O (‰ PDB)	Type of dolomite
26_5	2033.00	-1.36	-5.50	Rhombic
27_2	2036.40	-1.28	-3.56	Rhombic
27_2	2053.40	-1.82	-4.22	Rhombic
26_25	2122.90	-1.44	-5.25	Poikilotopic

Table 5.4: Stable carbon and oxygen isotope data from dolomites of the Leman gas field.

Dolomite from four wells in the Leman gas field was extracted using 'standard petrographic techniques' (Sullivan et al. 1990; Table 5.4). The purity of the dolomite was verified by X-ray diffraction. Three of the dolomite samples consist of rhombic crystals (100-200 μm) and one is a poikilotopic phase (coarse crystals of cement enclose a number of smaller, detrital grains). Dolomite was left to react for 3 days at 25°C with 100% phosphoric acid, using the method outlined by McCrea (1950). CO_2

was extracted and analysed on a VG SIRA 10 mass spectrometer. Standard deviation of replicate analysis was less than 0.04 ‰ for carbon and 0.2 ‰ for oxygen isotope ratios. No information about whether the samples are from the gas or the water cap was provided.

Data set 2 (Purvis 1992)

Sample	Well no.	Depth (meters)	δ13C (‰ PDB)	δ18O (‰ PDB)	pore fluid
B-3	49_24_16	2640	-7.6	-11.9	water
E-10	49_19_2A	2588	-3.4	-6.1	gas
E-17	49_19_2A	2606	-4.4	-6.9	gas
F-3	49_19_3	2409	0.3	-6.6	gas
J-1	49_25_4	2580	-1.6	-5.9	gas
J-2	49_25_4	2583	-0.9	-4.7	gas
J-3	49_25_4	2594	-3.3	-8.2	gas
J-4	49_25_4	2601	-9.5	-10.9	gas
N-2	49_20_A2	2892	-4.5	-9.1	gas
N-4	49_20_A2	2905	-5	-7.8	gas
O-1	49_24_4	2624	-2.4	-9.1	water
O-2	49_24_4	2625	-2.7	-9.1	water

Table 5.5: Stable carbon and oxygen isotope data from dolomites of the Indefatigable and Sean gas fields.

Samples from seven wells located in or around the Indefatigable and Sean gas fields were analysed. 12 Dolomite samples were dissolved in 100 % phosphoric acid and analysed on a VG SIRA 10 mass spectrometer. Results were corrected using standard procedure (Craig 1957). Standard deviation of replicate analysis was less than 0.1 ‰ for both carbon and oxygen. The dolomite is more abundant near the top and occurs

in two forms: Pore-lining rhombs < 5 µm to > 120 µm, and less abundant anhedral, pore-filling cement. Concentric zonation of many rhombs show cores with a composition of $Ca_{0.52}Mg_{0.48}CO_3$ which become more ferroan towards the rims ($Ca_{0.5}Mg_{0.4}Fe_{0.1}CO_3$); sometimes the rims show ankerite composition (> 20 mole % iron). Anhedral cement has a $Ca_{0.53}Mg_{0.45}Fe_{0.02}CO_3$ composition. Information about the pore fluid was provided and is listed in Table 5.

5.3.2 Stable carbon and oxygen isotope data from dolomite of Rotliegend gas accumulation

Figure 5.9 shows the oxygen and carbon stable isotope ratios of dolomite from three different locations in the Rotliegend Formation of the southern North Sea. Although only some of the data overlap, there is a well defined area where the Rotliegend dolomite plots. No $\delta^{18}O$ ‰ PDB higher than -3 is recorded. For more negative $\delta^{18}O$ ‰ an appropriate $\delta^{13}C$ ‰ is expected that matches the $\delta^{13}C$ ‰ shown by Purvis (1992).

Some of the isotopic data of the two studies overlap. This implies a similar source of fluid from which the cement from the different gas fields precipitated. However, Purvis (1992) and Sullivan's (1990) data show significant differences, especially in terms of carbon isotopes. The Purvis data show the impact of fluids with rather low carbon isotope ratios.

Several sources of fluids could have influenced the isotopic signature of the dolomite. Two general facts have to be considered. Firstly, the dolomite was among the earliest diagenetic cements to be formed (Purvis 1992) and secondly, the Rotliegend Sandstone is sealed at the top by the Zechstein and at the bottom by the Carboniferous mudstones. Late migration of meteoric water as well as fluids coming from early Carboniferous units is not to be expected. Purvis (1992) and Sullivan

(1990) distinguish between different sources of fluids which could be responsible for the dolomite isotope ratios.

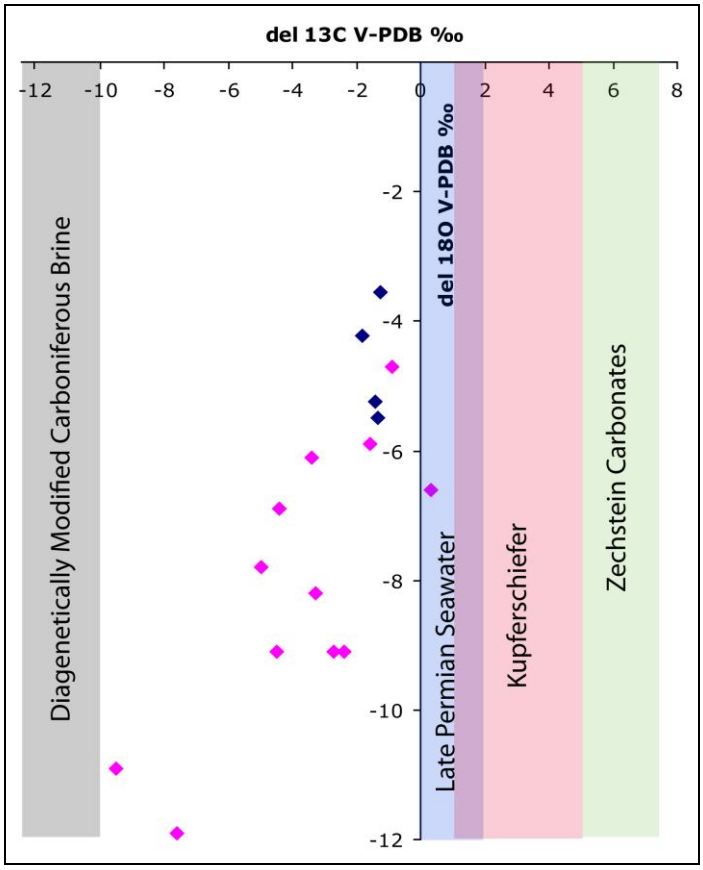

Figure 5.9: Stable carbon and oxygen isotope bulk rock data for the dolomites from the Leman gas field (dark blue, Sullivan et al. 1990) and the Indefatigable/Sean gas field (pink, Purvis 1992). Also shown are the carbon isotopes of different water sources in the area; see text for more information. The graph shows that in terms of carbon isotopes a combination of water sources is likely.

(i) Meteoric water that infiltrated the aeolian Rotliegend deposits. The arid environment did not support the growth of plants therefore only minor influence of organic matter on the pore fluid is assumed. Veizer et al. (1980) estimated the $\delta^{13}C$ values for late Permian seawaters to be between 0 and +2 ‰ (PDB).

(ii) Pore water descending from the overlying Kupferschiefer and the Zechstein units. Carbon isotopes of this unit are relatively heavy, between $\delta^{13}C$ =+1 and +5 ‰

(PDB) according to Magaritz et al. (1981) and Turner & Magaritz (1986). Studies on onshore Zechstein carbonates have shown even heavier carbon isotopes ($\delta^{13}C$ = 4.99 to 7.61 ‰ (PDB); Clark 1980).

(iii) Dewatering of the underlying Upper Carboniferous shales which contain organic- rich deltaic mudstone ($\delta^{13}C$ = -10 to -25 ‰ (PDB); Irvin at al. 1977).

The Rotliegend dolomite carbon isotope ratios are lower with respect to the expected meteoric pore water ratios and much lower with respect to the Zechstein isotope ratios. Different influences of organic rich fluids from below, probably due to regional geological distinctions, are likely to be responsible for the variations.

A linear correlation of carbon and strontium isotopes revealed that the source of the pore fluid was late Permian seawater that was contaminated with organic matter of the underlying Upper Carboniferous mudstones. The isotopes of subsequently precipitated Ankerit show that the influence of the organic matter increased with time (Sullivan et al. 1990).

5.4 Calculating the dolomite-CO_2 equilibrium

5.4.1 Introduction

If the dolomite in the Fizzy field precipitated because of an increased CO_2 concentration, the isotopic composition of the mineral should be in equilibrium with the CO_2 in the reservoir. The theoretical isotopic composition of a mineral in equilibrium with either a fluid or another mineral can be calculated with fractionation factors (*a*). As mentioned before, fractionation factors are usually experimentally derived but because it is very difficult to grow dolomite in the laboratory under conditions typical of the shallow subsurface, data of either high temperature experiments or experiments with microbes as catalysts must be used. This chapter describes the equilibrium constants which were used for this study.

5.4.2 Oxygen isotope equilibrium values

In 2005, Vasconcelos et al. published new fractionation factors for the dolomite water system using microbes as catalysts for dolomite precipitation experiments under low temperature conditions. The conclusion of their study is that for dolomite precipitation from pore water, the temperature dependent oxygen isotope fractionation factor is:

$$1000 \ln \alpha^{18}_{dol-water} = 2.73 \cdot (10^6 \cdot T_{(K)}{}^{-2}) + 0.26 \quad (3)$$

5.4.3 Carbon isotope equilibrium values

No carbon isotope fractionation factor for the dolomite-water system could be found in the literature. Wilkinson et al. (2009) used for their study fractionation factors for calcite/CO_2 after Deines et al. (1974) instead of dolomite fractionation factors. The carbon isotope fractionation can be calculated from:

$$1000 \ln a^{13}_{Cal-CO2} = 1.194 \cdot (10^6 \cdot T_{(K)}{}^{-2}) - 3.63 \quad (4)$$

An alternative way to express carbon isotope equilibrium data for a dolomite/CO_2 system is to calculate them via known fractionation factors. Deines (2004) presents an equation that calculates the relationship for the fractionation between Mg-calcite and calcite that would predict the computed dolomite-calcite fractionation for a Mg-mole fraction of 0.5. He determined the following relationship:

$$1000 \ln a^{13}_{Mg\_Ca-Cal} = \left[\begin{array}{l} 0.013702 - 0.10957 \cdot \frac{10^3}{T_{(K)}} + 1.35940 \cdot \frac{10^6}{T_{(K)}{}^2} \\ -0.329124 \cdot \frac{10^9}{T_{(K)}{}^3} + 0.0304160 \cdot \frac{10^{12}}{T_{(K)}{}^4} \end{array} \right] \cdot X^{1.5} \quad (5)$$

For dolomite, the mole fraction (X) would be 0.5. A fractionation factor for the calcite/CO_2 system has already been introduced earlier (Eq. 2). Because:

$$a^{13}_{Dol-Cal} = \frac{\delta^{13}C(dolomite) + 1000}{\delta^{13}C(calcite) + 1000} \quad (6) \text{ and } a^{13}_{Cal-CO2} = \frac{\delta^{13}C(calcite) + 1000}{\delta^{13}C(CO_2) + 1000} \quad (7)$$

, with

$$\delta^{13}C(sample) = \left(\frac{\left(\frac{^{13}C}{^{12}C} \right)_{sample}}{\left(\frac{^{13}C}{^{12}C} \right)_{standart}} - 1 \right) \cdot 1000\,‰ \quad (8)$$

, the theoretical dolomite in equilibrium with CO_2 can be calculated from:

$$\delta^{13}C(dolomite) = [a^{13}_{Dol-Cal} \cdot a^{13}_{Cal-CO2} \cdot (\delta^{13}C(CO_2) + 1000)] - 1000 \qquad (9)$$

5.4.4 Calculating the equilibrium graph

The theoretical isotopic composition of dolomite crystals in equilibrium with the pore fluid is given by:

$$a = \frac{\delta(dolomite) + 1000}{\delta(pore - fluid) + 1000} \qquad (10)$$

The oxygen isotopic composition of dolomite can be directly calculated with:

$$\delta^{18}O(dolomite) = a^{18}_{dol-water} * (1000 + \delta^{18}O(water)) - 1000 \qquad (11)$$

The carbon isotopic composition of dolomite can be calculated with:

$$\delta^{13}C(dolomite) = a^{13}_{dol-cal} \cdot a^{13}_{cal-CO2} \cdot (\delta^{13}C(CO_2) + 1000) - 1000 \qquad (12)$$

The carbon isotopic composition of two Fizzy CO_2 samples was measured and gave relatively similar results of $\delta^{13}C$ of -4.3‰ and -4.6‰ V-PDB. Fizzy pore water oxygen isotope data were not available. Instead, pore water oxygen isotope ratio from the Leman gas field, another Rotliegend gas field, were utilized for the calculation ($\delta^{18}O$ = 0.3 to 0.4 ‰ V-SMOW; Warren and Smalley 1992 ($\delta^{18}O$ = -29.6‰ and -30.3‰ V-PDB, respectively)). That is a reasonable simplification based on the concept that the oxygen incorporated in newly formed dolomite will be

derived primarily from the pore water and not from the dissolved CO_2. Fig. 5.10 shows the two theoretical isotopic compositions of dolomite in equilibrium with the CO_2 present in the Fizzy field. This study uses the equilibrium line based on the alternatively calculated carbon fractionation factors (Eq. 12)

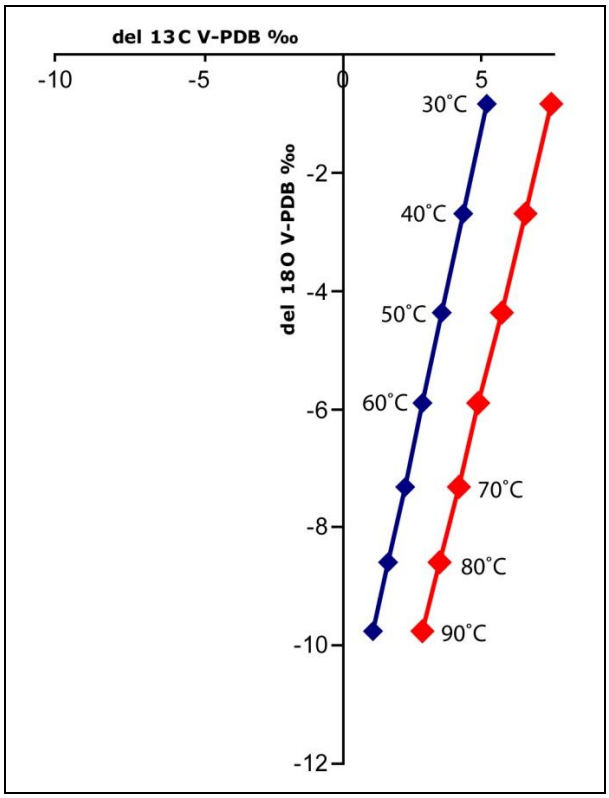

Figure 5.10: Graph that illustrates the two theoretical isotopic composition of dolomite in equilibrium with the Fizzy CO_2. One method uses carbon isotope values of calcite/CO_2 (blue). The second, alternative method uses calculated dolomite/CO_2 values (red).

5.5 Results

This chapter presents the results of the Orwell dolomite bulk analysis and the stepwise extraction method applied to rock samples of the Fizzy field and Orwell area. Results of the Fizzy field are subdivided into data taken from the Fizzy gas cap and the Fizzy water cap. Because the CO_2 should have been water saturated before it migrated into the reservoir and the residual water could not dissolve into the CO_2, it is likely that the rocks of the gas cap are still water-wet. Due to the high CO_2 concentration of the reservoir, the Fizzy pore water is assumed to have a high, if not saturated, CO_2 concentration.

All data are presented on a carbon and oxygen stable isotope diagram. The stepwise extraction data and the bulk data for the Orwell isotopes are presented with the theoretical line of dolomite in equilibrium with the present Fizzy CO_2.

5.5.1 Orwell bulk sample isotope data

Eight carbon and oxygen isotope analyses were conducted on four rock samples of the Orwell Rotliegend Sandstone. All Orwell bulk isotope data plot within the southern North Sea Rotliegend dolomite isotope ratio field defined earlier. The $\delta^{13}C$ and $\delta^{18}O$ results are shown in Fig. 5.7. The variation in $\delta^{13}C$ is relatively small; it ranges from $\delta^{13}C$ =-1.6 to -4.2 ‰ (V-PDB). Oxygen isotope values vary much more; from $\delta^{18}O$ = -4.5 to -10 ‰ (V-PDB) but five out of eight bulk measurements cluster relatively close together near a value of -2.1 ‰ ($\delta^{13}C$ V-PDB) and -4.7 ‰ (δ^{18}O V-PDB).

5.5.2 Stepwise extraction data of Orwell and Fizzy dolomite

This section describes the results of 11 experiments on the stepwise reaction of crushed rock material and subsequent extraction and isotope analysis of the CO_2

released. Yield information is given in percent of the reacted material assumed to be 100 % dolomite (this includes the mass of extractions that were discarded, but excludes the failed measurements).

The Orwell stepwise extraction data

The final extractions of all the four Orwell samples show the least negative oxygen isotope ratios (Fig. 5.11). The stepwise extraction data of sample 13 show a well-defined trend from negative $\delta^{18}O$ to less negative $\delta^{18}O$. This is certainly due to the fact that two out of six isotope analyses failed and one had to be discarded for sample 13. Therefore, there is a high probability that three points show a defined trend. In fact, sample 11, 14 and 16 with six, six and five valid measurements, respectively, show the same trend from negative to less negative, but each experiment essentially shows one data point with irregular $\delta^{18}O$.

The final extractions of samples 11, 13 and 16 have the least negative $\delta^{13}C$. The final extraction of sample 14 has $\delta^{13}C$ ‰ (V-PDB) 0.5 ‰ more negative than the second last extraction and less negative than all four previously extracted and analysed carbon isotope ratios. There is no general trend from more to less negative carbon isotope ratios. The variations in $\delta^{13}C$ are relatively small and vary by 6.3 ‰ ($\delta^{13}C$ V-PDB) for sample 11 (3.3 ‰ ($\delta^{13}C$ V-PDB) without the first extraction), 2.3 ‰ ($\delta^{13}C$ V-PDB) for sample 13, 2.9 ‰ ($\delta^{13}C$ V-PDB) for sample 14 and 2.5 ‰ ($\delta^{13}C$ V-PDB) for sample 16. The carbon values of sample 16 are within the expected range, however, the final extraction shows unusually positive $\delta^{13}C$ for the corresponding oxygen values.

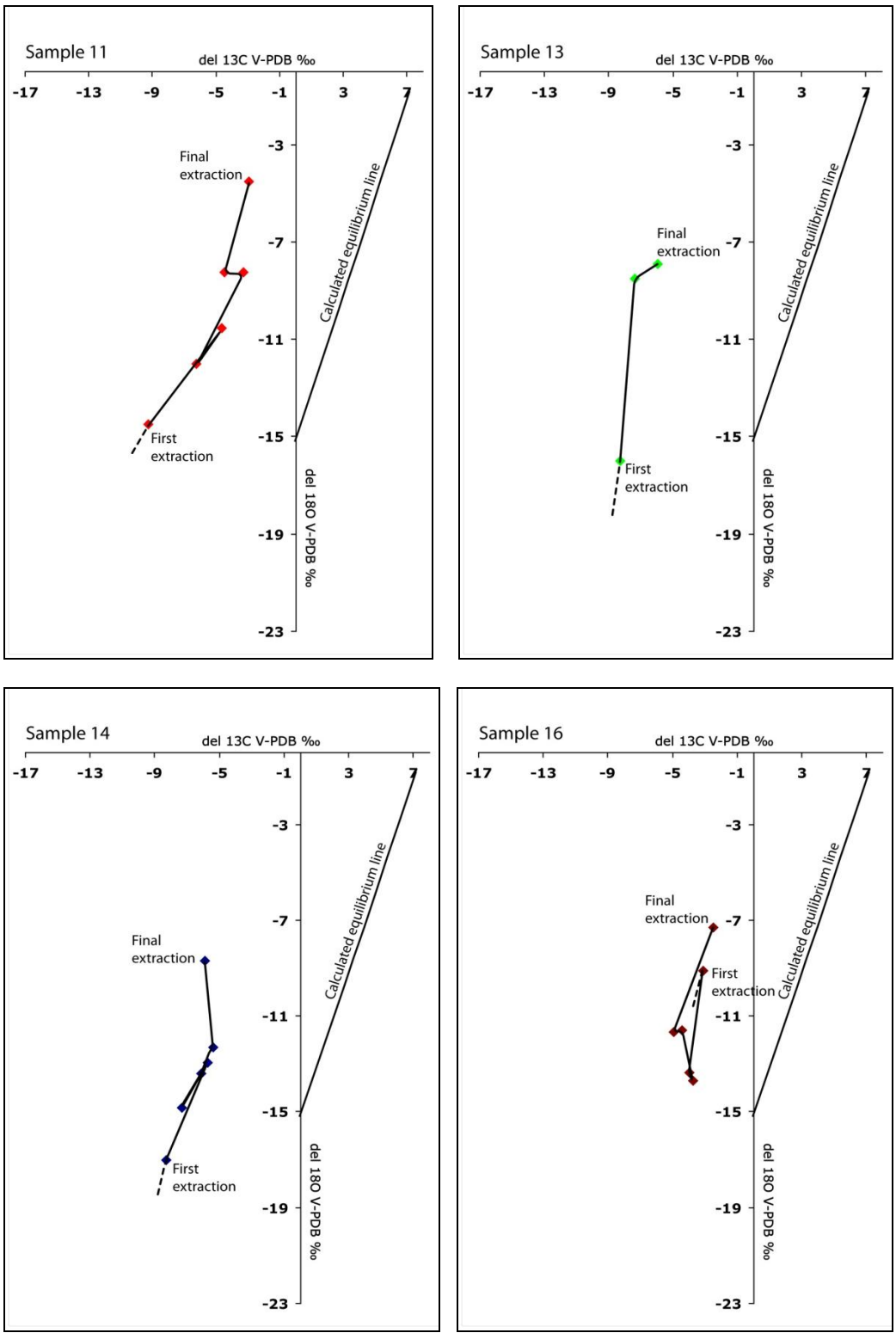

Figure 5.11: Stable C and O isotope data from stepwise extraction and analyses experiments for the dolomites from the Orwell Rotliegend Sandstone.

The Fizzy gas cap stepwise extraction data

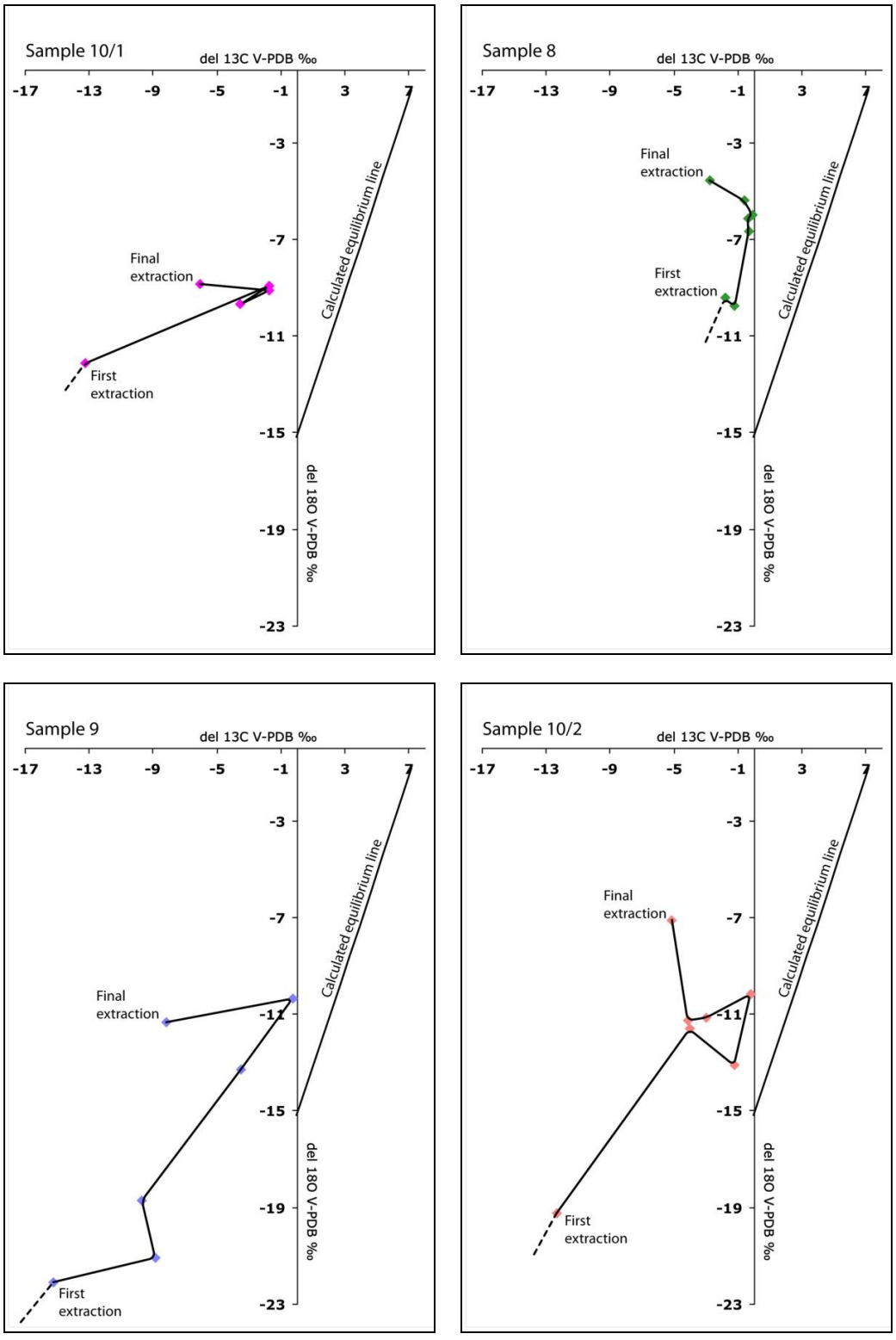

Figure 5.12: Stable carbon and oxygen isotope data from stepwise extraction and analyses experiments for the dolomites from the Fizzy filed gas cap.

Figure 5.12 shows the results of the stepwise extraction data of the dolomite derived from the gas cap of the Fizzy field. Yield data are available for samples 8 and 9 where the final extractions represent 89 % and 63 % of the material respectively.

The final extractions of all the fizzy gas cap samples (8, 10/1 and 10/2) show the least negative $\delta^{18}O$ of each experiment. The final extraction of sample 9 is more negative than the second last one (by 1 ‰ ($\delta^{18}O$ V-PDB)) but is less negative than the previously analysed extraction. All four experiments show a general trend from more negative $\delta^{18}O$ to less negative $\delta^{18}O$, although all show fluctuations that prevent an unambiguous trend.

All four experiments show relatively negative $\delta^{13}C$ for the last extractions. For sample 8, it is the most negative and for samples 10/1 and 10/2 the second most negative carbon isotope ratios. All experiments show a 'hook-like' trend from relatively negative $\delta^{13}C$ and $\delta^{18}O$ ratios to less negative oxygen and almost positive $\delta^{13}C$, before a change to no negative $\delta^{13}C$ in the final extraction. Sample 8 with the highest reaction rate, shows the smallest variation in $\delta^{13}C$ and $\delta^{18}O$ but has a distinct 'hook-like' trend. The data of the other three experiments, which have a much lower reaction rate, show more scatter (both for carbon and oxygen isotopes ratios).

Figure 5.13 shows the results of the stepwise extraction data of the dolomite derived from the water zone of the Fizzy field. Yield data are available for sample 4 and sample 1 where the final extraction represents 94 % and 55 % of the material respectively.

The final extractions of sample 4 and 5 show the least negative oxygen isotope ratios. The final extraction of sample 1 is 0.4 ‰ ($\delta^{18}O$ V-PDB) more negative that the second last extraction and less negative than all previous oxygen isotopes. As seen before, there is a general trend from more negative $\delta^{18}O$ to less negative $\delta^{18}O$ despite some fluctuations (see samples 4 and 5 which have low reaction rates).

The Fizzy pore water stepwise extraction data

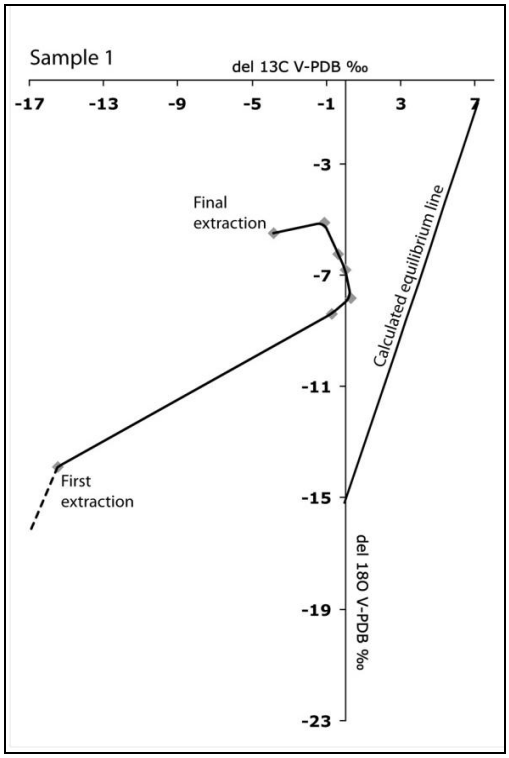

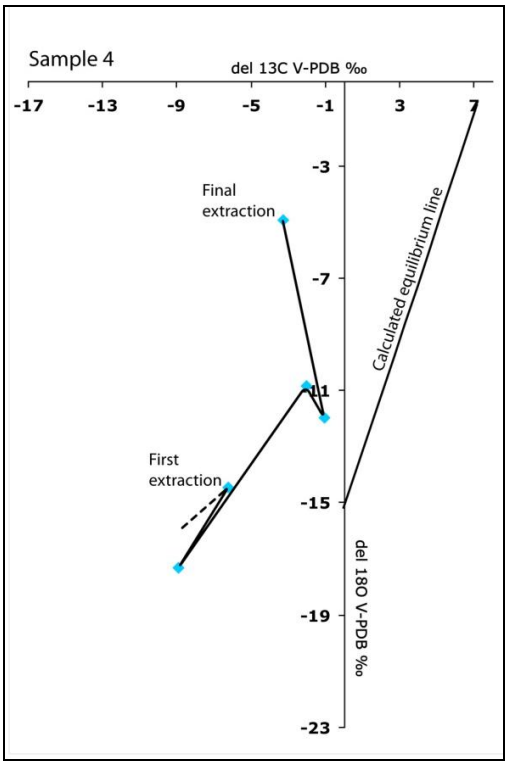

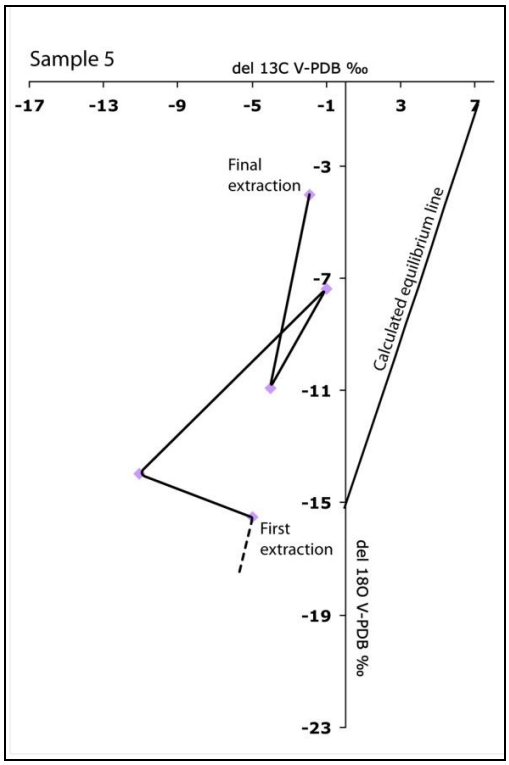

Figure 5.13: Stable C and O isotope data from stepwise extraction and analyses experiments for the dolomites from the Fizzy field water-zone.

Sample 1 is a good example of a 'hook-like' extraction path with negative $\delta^{13}C$ of the first evolved CO_2. Subsequent extractions show relatively constant $\delta^{13}C$ between -1.1 to +0.3 ‰ V-PDB and finally more negative values for the last extraction (-3.8 ‰ ($\delta^{13}C$ V-PDB)). The final extraction of Sample 5 has lower $\delta^{13}C$ than the two previous extractions. There is a path from very negative $\delta^{13}C$ to less negative $\delta^{13}C$ (-1.1 ‰ ($\delta^{13}C$ V-PDB)) and -2 ‰ ($\delta^{13}C$ V-PDB)) to more negative carbon isotope ratios for the final extraction, but the 'hook-like' trend is not as obvious as the one of sample 1. Sample 4 is the only sample of the Fizzy field that does not show the 'hook-like' trend. The $\delta^{13}C$ for the final extraction is less negative than the second last one.

5.5.3 Yield data of the stepwise extraction experiments

Yield data were recorded for six experiments, two for each location (Fizzy pore water 1, 4; Fizzy gas cap 8, 9; Orwell Rotliegend Sandstone 13, 14).

Fig. 5.14 shows the proportion (as a percentage) of reaction during and after the extraction time (1: 54 % of the dolomite reacted after the stepwise extraction; 4: 94 %; 8: 63 %; 9: 89 %; 13: 88 %; 14: 86 %). Four of the six samples have reaction trends that show that most of the dolomite reacts after the stepwise extraction procedure. Generally, the experiments with low reaction rates produce more scattered isotope data. The reaction rate seems to be random and the only constant is (if it is assumed that the results of two experiments set a trend) that the two Orwell Rotliegend samples have relatively low reaction rates.

Both samples from the Fizzy water cap region show a similar cumulative yield (1: 334.3; 4: 302.88) but a very different reaction history. The reaction rate of sample 1 is therefore higher than that of sample 4. The Fizzy gas cap samples have different cumulative yields (8: 415.2; 9: 52.56). The smaller yield of sample 9 can be explained with the low dolomite content of the sample (2 %). The two Orwell

Rotliegend Sandstone samples show relatively low cumulative yields (13: 103.4; 14: 58.32) although the original material should have a relatively high amount of dolomite (10 % and 11 %). The reaction rate of the two samples is relatively similar.

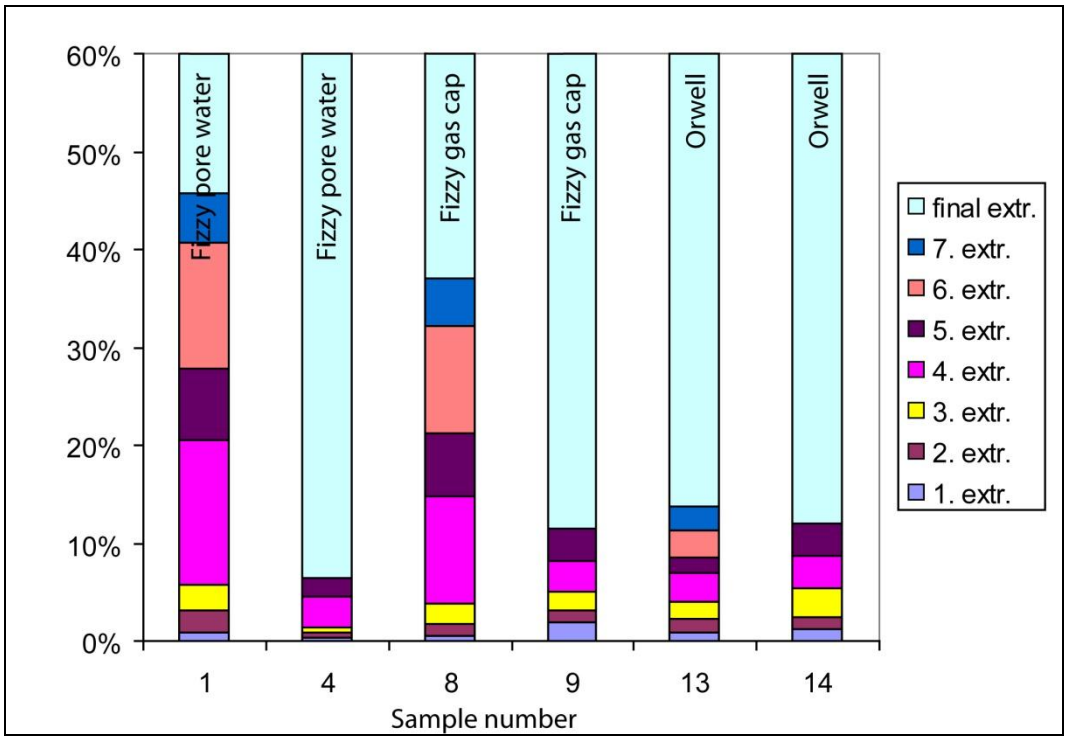

Figure 5.14: Graph showing the reacted dolomite in percent of the total dolomite per extraction. Three experiments lasted for two days (4, 9 and 14) and three for three days (1, 8 and 13)

5.6 Discussion

5.6.1 The Orwell dolomite as a reference for 'diagenetic dolomite'

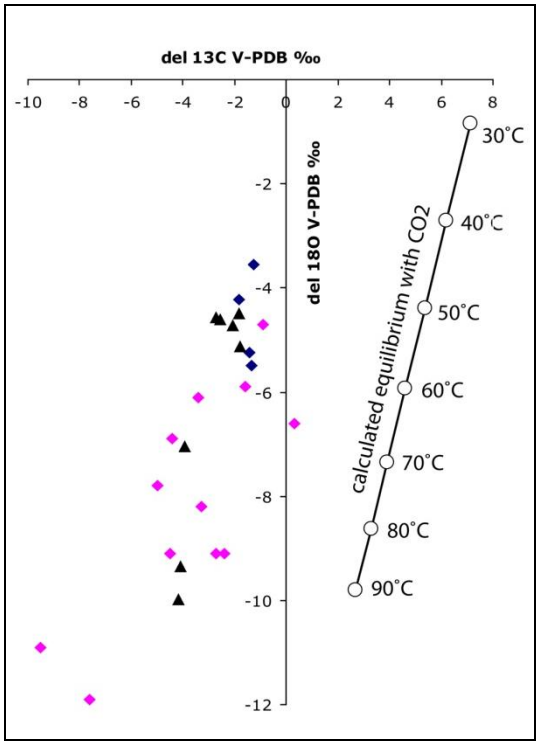

Figure 5.15: The graph shows whole rock stable isotope analysis of two studies taken from the literature (Sullivan et al. 1990; blue diamonds and Purvis 1992; pink diamonds) and data of this study (black triangles). The data match the literature values which are here used as a confirmation of the measurements.

Figure 5.15 shows the whole rock dolomite oxygen and carbon isotope ratios of the two studies conducted by Purvis (1992) and Sullivan et al. (1990) together with the results of this study. The results of this study fit into the general trend of the southern North Sea Rotliegend dolomite. The majority of the new data scatter around an oxygen ratio of $\delta^{18}O$ =-5 ‰ (V-PDB) which is in the range of the data presented by Sullivan et al. (1990). The theoretical fractionation factors show that the $\delta^{18}O$ require higher formation temperatures, for example 90˚C for oxygen isotope ratios of ~-10 ‰ (V-PDB). The very negative oxygen data of the Purvis (1992) study predict dolomite formation at a depth of approximately 3 km. This is not consistent with the

subsidence history curve presented in his paper (for details see Bulat and Stoker (1987) modified by Purvis (1990)) which assumes dolomite formation depth of less than 2 km. One explanation for the unusually low oxygen ratios of the Orwell whole rock samples is that the material was not ground but gently crushed. Therefore, an incomplete reaction cannot be dismissed. Given the fact that Purvis (1992) found even more negative oxygen isotope ratios, the interpretation of the variations as sample heterogeneities is preferred here.

Note the lack of data between the new Orwell dolomite, which is interpreted as 'diagenetic dolomite', and the calculated dolomite-Fizzy CO_2 equilibrium line (which is where the 'sequestration dolomite' might be assumed to plot.

The isotopic data of Purvis (1992) and Sullivan (1990) and the new Orwell dolomite overlap. This implies a similar source of fluid out of which the cement from the different gas fields precipitated. Although Purvis claims that his and Sullivan's (1990) data show a 'large overlap' (Purvis 1992), significant differences, in terms of carbon and oxygen isotopes, are obvious and might preserve a greater impact of fluids with lower isotope ratios.

The dolomite carbon isotope ratios are slightly lower to much lower with respect to the estimated pore water isotope ratios and much lower with respect to the Zechstein isotope ratios. Different influences of organic rich fluids from depth, probably due to regional geological distinctions, are likely to be responsible for the variations.

To define an area in which the 'diagenetic dolomite' would plot we used only data of the Orwell Rotliegend Sandstone and extended it for lower oxygen isotope ratios (according to Purvis (1990)). The two main reasons why the literature isotope data are not directly involved in the definition of the 'diagenetic dolomite' is that firstly, only the Orwell Field is regionally and tectonically in the vicinity of the Fizzy field and different fluid sources are unlikely. Secondly, small systematic errors of isotope

data are usually due to varying calibration of the analytical process. This is generally not a problem as long as the error is consistent but here we consider it to be safer to use only our own data.

Figure 5.16 illustrates the area which characterises the 'diagenetic dolomite' and the calculated equilibrium line for dolomite in equilibrium with the Fizzy CO_2 (which represents the 'sequestration dolomite').

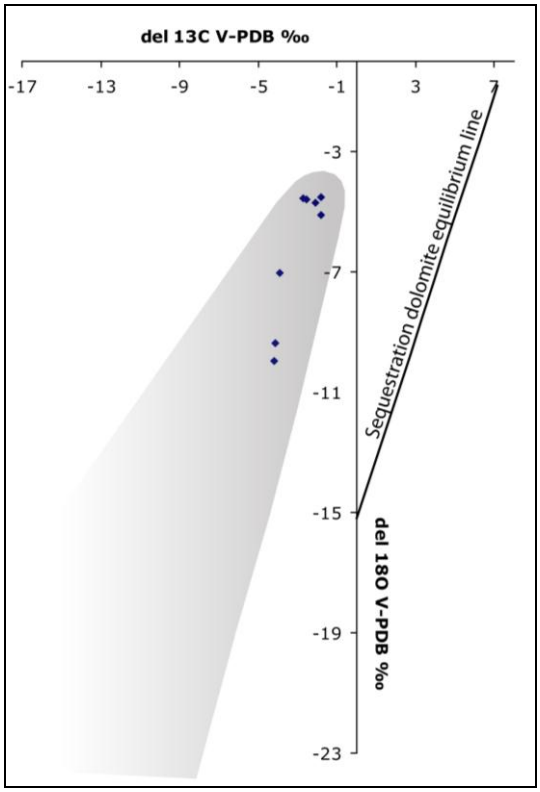

Figure 5.16: Graph showing the area of 'diagenetic dolomite' (grey field) defined by the Orwell Rotliegend Sandstone whole rock isotope data (blue diamonds). Note the shade fades towards lower oxygen isotope ratios to show that very low oxygen isotope ratios are supposed to be more and more unlikely. The line to the right is the calculated line on which dolomite should plot that precipitated in equilibrium with CO_2 currently present in the Fizzy field.

5.6.2 Comparison of the Orwell and Fizzy stepwise extraction data

The results of the stepwise extraction experiments of the Fizzy dolomite and the Orwell dolomite are illustrated in Fig. 5.17. The Fizzy data scatter more which could be coincidental, or due to the greater number of data points. Since around twice as many data points are available for the Fizzy field a broader variation can be expected. However, there is an intriguing gathering of data in the gap between the 'diagenetic dolomite' area and the 'sequestration dolomite' line which seems to represent a systematic difference between the two locations.

The rock samples have been carefully crushed and not ground in order to maintain any zonation of the dolomite cement. Theoretically, the rim of the cement should react first and its isotopic signature should be reported during the early stages of the stepwise extraction. Because the reaction rates of the samples vary, even the path of two chemically identical samples will produce different results although the bulk isotopic composition might be similar. For example, the core of the cement, which is supposed to be represented by the final extraction, can represent between 55 % and 95 % of the material, depending on the reaction rate of each sample.

The carbon and oxygen isotopic ratios of the core of the Orwell and the Fizzy dolomite lie in the area that is defined to be the 'diagenetic dolomite' (Fig. 5.17). Therefore, the core, which represents the early dolomite cement, precipitated during the diagenesis of the Rotliegend Formation. As a confirmation of the accuracy of the results, all core data, bar one Orwell data point lie on a straight line. This line, which runs almost parallel to the calculated line for dolomite precipitation in equilibrium with Fizzy CO_2, can therefore be seen as a line that represents the stable isotope ratio of dolomite that precipitated in equilibrium with the porewater CO_2 that was present in the area during early diagenesis.

The stepwise extraction data of the Orwell Rotliegend Sandstone all lie (bar one exception) in the 'diagenetic dolomite' area (Fig. 5.17). The precipitation of the cement has therefore not been significantly influenced by CO_2 that is currently present in the Fizzy field. All core oxygen isotope ratios are less negative than those of previously extracted CO_2. The carbon isotope ratios of the Orwell data do not change significantly but there is a general trend from more to less negative carbon isotope ratios. We conclude that only one isotopic composition of CO_2, which could consist of several sources, was involved in the precipitation of the Orwell dolomite cement. Hence, it can be assumed that both the rims and the cores consist of 'diagenetic dolomite'.

The stepwise extraction data of the Fizzy field do not lie only in the area of the 'diagenetic dolomite' (Fig. 5.17). Several stepwise extraction data points lie in the gap between the 'diagenetic dolomite' area and the 'sequestration dolomite' line. Unlike the Orwell data, the second last extraction and the final extraction very often show a change to more negative carbon isotope ratios, with sometimes only a minor change in oxygen isotope ratios. The stepwise extraction data, which plot towards the 'sequestration dolomite' line, are interpreted to have precipitated in the presence of the Fizzy CO_2. The reason, why no extraction produced isotope ratios that lie directly on the equilibrium line, is presumably related to the limitation of the method. No clear separation of 'diagenetic' and 'sequestration dolomite' in the rims of the dolomite crystals is possible and only mixtures of the two dolomites can be detected. Additionally, despite careful treatment, many crystals might have broken with a proportion of the 'diagenetic dolomite' reacting at the beginning as well. However, the cloud of isotope data to the right of the core data illustrate undoubtedly that the precipitation of the rims of the Fizzy dolomite was influenced by an additional type of CO_2, most likely the current Fizzy field CO_2, which is represented by the 'sequestration dolomite equilibrium line'. The different trends of the Orwell dolomite and the Fizzy dolomite are shown in Fig. 5.18.

The fractionation factors of carbon and oxygen isotopes can have an influence on the stepwise extraction experiments and should be taken into account. The method of

producing CO_2 from the reaction of dolomite and phosphoric acid for stable carbon and oxygen isotope analysis is:

$$CaMg(CO_3)_2 + 2H_3PO_4 \leftrightarrow 2(Ca,Mg)HPO_4 + 2CO_2 + 2H_2O \quad (13)$$

Because all the reaction products contain oxygen, isotope fractionation takes place between the CO_2 and the water. As a result, the oxygen isotopic composition of the CO_2 is different to the oxygen isotopic composition of the carbonate. The fractionation is temperature dependent and also highly dependent on the composition of the carbonate mineral. However, this well known fractionation can be compensated for using phosphoric fractionation factors. Carbon isotopes are not affected by the reaction because the entire carbon of the carbonates goes into the CO_2.

Walters et al. (1971) found that the O^{18}/O^{16} ratio of CO_2 from carbonate dissolution in phosphoric acid at 25°C increases during a stepwise extraction experiment on "essentially monomineralic" samples. The first reacting carbonate has "as much as 3 ‰ lighter than CO_2 from the last reacting carbonate, for either calcite or dolomite". They propose three mechanisms which could cause the change in $\delta^{18}O$:

- The particle size of the reacting carbonate (also discovered by Fritz and Fontes 1966).
- Particle surface strain caused by crushing or grinding.
- Kinetic isotope fractionation associated with diffusion of the reacting products away from the reaction particle surfaces.

According to our method, the particle size of the dolomite varies a lot and the overwhelming mass of the dolomite should not be ground but some might have been ground between the quartz grains and could have a very small grain size. Hence none of the mechanisms can be excluded. Some of the early data show very low oxygen isotope ratios relative to their average isotopic ratio that cannot be explained by the fractionation proposed by Walters et al. (1971). A closer look on their method shows

that the amount of dissolved material per extraction was not equal and their results did not reveal the yield per extraction accurately. But it is very clear that the first extractions usually represent far more (>5 % of the reaction completion) material than the first extractions of our study. By assuming that the proposed three per mil lighter oxygen ratios are essentially an average of the early extractions of evolving CO_2, most of the very low oxygen isotope values of the early extractions can be explained. Walters et al. (1971) would have recognized them as well if their early extractions had represented less material. There is no direct evidence for that, but it is a logical explanation for the rather unexpected results. However, small heterogeneity of the dolomite or minor traces of other carbonates cannot be excluded.

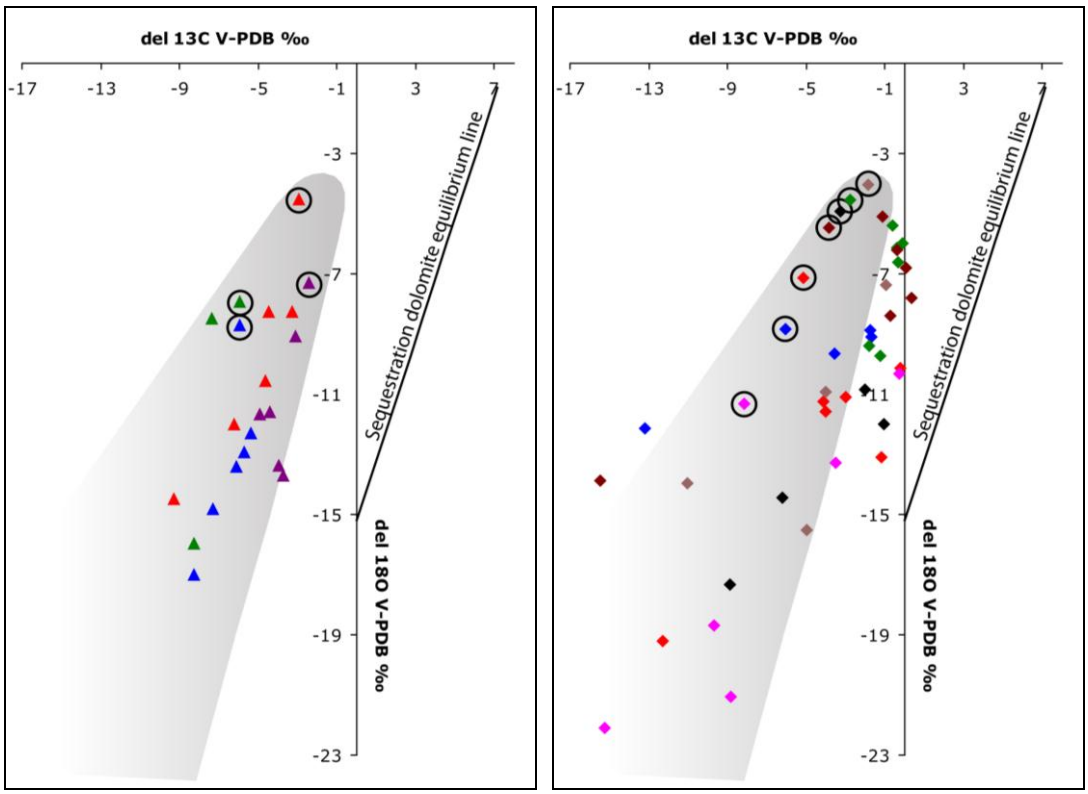

Figure 5.17: The two graphs show the stable isotope stepwise extraction data of the Orwell field (left) and the Fizzy field (right). The data of the final extraction, which represents the majority of the carbonate in the samples, are in black circles. See result chapter for description of the data.

Although we could not find information in the literature, the previously introduced mass weight dependent fractionation might be relevant for carbon as well. An early release of lighter carbon followed by a subsequent release of heavier carbon might therefore be expected. We consider this fractionation of the carbon to be smaller than any fractionation of oxygen because the mass difference of the $^{13}C/^{12}C$ system is half that in the $^{18}O/^{16}O$ system. The general trend of the Orwell dolomite seems to go from negative to less negative carbon isotope ratios which could be explained by fractionation. However the Fizzy dolomite carbon isotope ratios become generally more negative with progressing reaction time, a trend that clearly contradicts this type of fractionation.

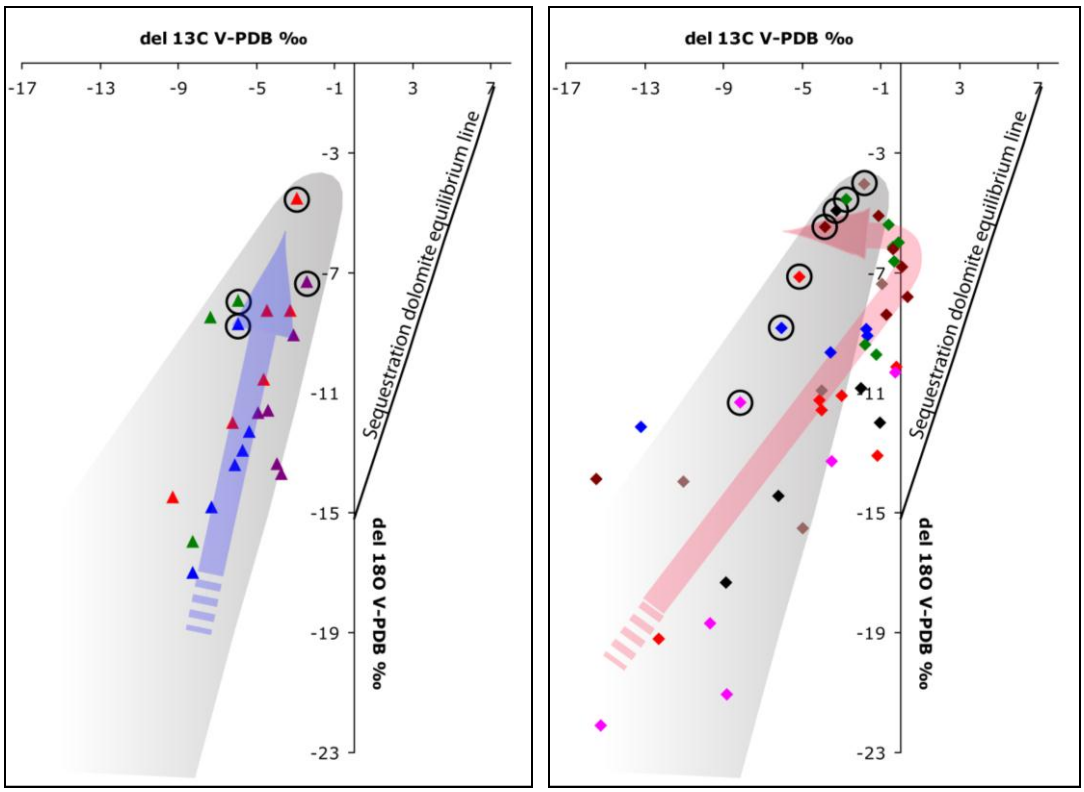

Figure 5.18: The two graphs show the overall trend of the stable isotope stepwise extraction data of the Orwell field (left) and the Fizzy field (right).

It is important here to keep in mind that any kind of fractionation will have an impact on both the Orwell and the Fizzy dolomite. Hence fractionation factors might change

the overall results and the subsequent interpretation of the data but it will not explain the two different trends of the Orwell dolomite and the Fizzy dolomite.

5.6.3 Interpretation of the yield data

The two samples from the Fizzy pore water region have comparable yields (1: 334.3 micromoles (µmoles); 4: 302.88 µmoles) but different reaction rates (Fig. 5.14). The two samples from the Fizzy gas cap have different yields (8: 415.2 µmoles; 9: 52.56 µmoles). The extremely low yield of sample 9 is related to the low dolomite content of the original material (~2 %). The reaction rate is defined to be the mass of reacted material over time. Several parameters have influence on the reaction rate such as temperature, surface area, diffusion coefficient, degree of ordering of dolomite and concentrations. If all those parameters are similar, the samples with high overall yield should have a reaction pattern with very low relative yield during the stepwise extraction and high yield for the final extraction. This pattern is shown by sample 9. Samples with low yield should show high amounts of reacted material during the stepwise extraction and a relatively low yield for the final extraction. The pattern is shown by sample 8. Although CO_2 has been extracted two times more from sample 8 than from sample 9, the yields are not consistent with the theory. In fact, they rather show the opposite trend, so the Fizzy gas cap samples 8 and 9 are an example for a reaction rate which must have been influenced by additional parameters.

The two Orwell field samples show low accumulated yield (13 :103.4 µmoles; 14: 58.32 µmoles; Fig 5.14) which is surprising because the original material should have a relatively high amount of dolomite (10 % and 11 %, Table 2). The reaction rates of the two Orwell samples are relatively similar.

It is unknown why the yields and the reaction rate vary. Four possible reasons for the inconsistency are proposed here.

(i) The Bunter Sandstone is relatively heterogeneous. The compositions of the cored and sampled sections were made by point-count analysis and represent only a fraction of the sampled material. Therefore, variations of the dolomite content are always possible.

(ii) The ‘Fizzy gas cap’ and the ‘Orwell’ samples were washed because of their high Gypsum/Anhydrite content. It is possible that some of the dolomite dissolved in the pure water as well. Sample 8 would contradict this explanation because it has a high yield even though it has been washed. The Rotliegend Sandstone contains a significant amount of clay minerals. During washing the clay became suspended and gathered near the water surface. Although some clay was lost while the water was being removed, some clay might have coated the dolomite crystals and retarded their dissolution. We tried to avoid this effect by washing the dried samples with acetone but we cannot guarantee that this prevents the dolomite from dissolving.

(iii) The material was gently crushed and, depending on the intensity of the crushing and the stability of the samples, the grain size of the dolomite cement accumulation might vary. Since surface area is a key parameter determining the reaction rate, highly crushed dolomite cement will dissolve much quicker.

(iv) Phosphoric acid at 25°C is relatively viscous. The mixing with the crushed material can be relatively slow depending on the grain size of the samples. Especially clay rich and fine grained samples did not mix very well with the acid and sometimes, during the early stages of dissolution, fractions of the material seemed to remain unaffected by the acid. As Swart et al. (1991) suggested, in relatively high velocity phosphoric acid CO_2 bubbles become trapped in the acid and might take longer to dissolve. This could lead to an unfinished dissolution especially if extraction occurs at low temperatures.

5.6.4 Mass balance of the stepwise extraction data

As a confirmation of the reliability of the stepwise extraction data, a mass balance calculation was conducted. All six experiments with available yield data were used for the calculation. The mass balance of the data shows that the sum of the stepwise extraction represents a reasonable average which is comparable with the Orwell whole rock isotopic data and the published data by Sullivan et al. (1990) and Purvis (1992). Due to a lack of Fizzy whole rock data, special focus lies on comparison with the Orwell whole rock data because they were taken adjacent to the Fizzy field and are supposed to consist of 'diagenetic dolomite'. Because the Fizzy field dolomite may also contain a certain amount of 'sequestration dolomite', it is expected that the calculated overall carbon isotope ratio will plot towards slightly heavier carbon isotope ratios compared to the Orwell data.

The calculated data (Fig. 5.19) show that all six calculated isotopic ratios lie in the vicinity of Orwell whole rock or published data (Sullivan et al. 1990; Purvis 1992). They all represent the southern North Sea Rotliegend dolomite and no obvious artefacts are evident.

However, by comparing the Fizzy mass balance data with the Orwell whole rock data, differences are apparent. The pore water and one of the gas cap data points plot very close to the Orwell whole rock data and lie in the range for the expected oxygen and carbon isotope ratios. Sample 1 and 8 lie slightly to the right of the Orwell whole rock data. This suggests that a fraction of 'sequestration dolomite' could be present. This has already been revealed by the 'hook-like' stepwise dissolution path. The two Orwell samples do not plot in the vicinity of the Orwell whole rock data and show more negative carbon isotope ratios. The two remaining Orwell stepwise extraction data (sample 11 and 16; no yield data available) seem to have slightly heavier carbon isotope ratios and would plot closer to the whole rock data. Because extractions and isotopic analysis on samples 13 and 14 were conducted during the same session, a

systematic error of the carbon isotope ratios could be the reason for the inconsistency. However, experiments and analysis on samples 13 and 14 were conducted in one session together with samples 1, 4, 8 and 9. These data do not show any inconsistencies such as unusual low carbon isotope ratios. Because a systematic error on only two samples is extremely unlikely, the variations are presumably due to rock heterogeneities.

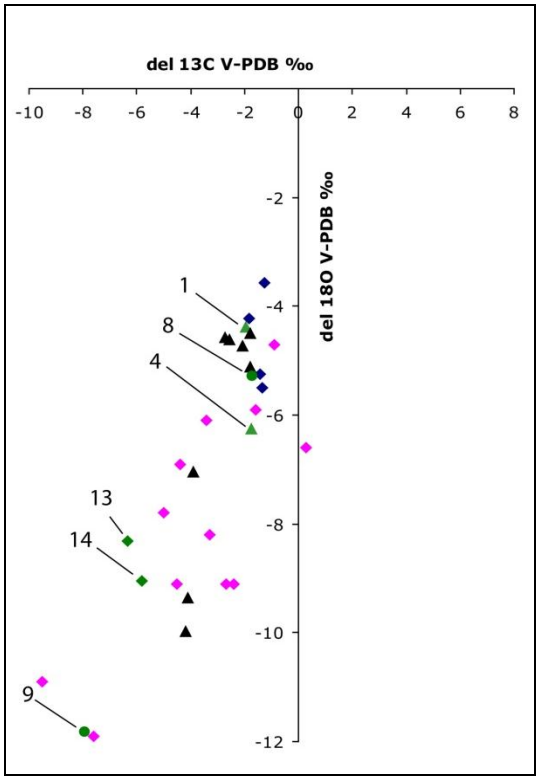

Figure 5.19: Mass balanced data in comparison with published data from Sullivan et al. (1990; blue diamonds), Purvis (1992; pink diamonds) and the whole rock Orwell data of this study (black triangles). Mass balanced data are available for Fizzy pore water (green triangles), Fizzy gas cap (green circles) and Orwell (green diamonds). Sample numbers added for orientation.

Sample 9 still lies in the range of Purvis (1992) data but is far more negative in carbon and oxygen than the Orwell whole rock data. Both the overall yield of the experiment and the fraction of dolomite in the sample were very low. Therefore, the isotope ratios and the low yield do not necessarily have to be due to incomplete reaction. A more likely explanation is that dolomite precipitation (of both ‘diagenetic

dolomite' and 'sequestration dolomite') in parts of the Rotliegend Sandstone have been incomplete due to, for example, low permeability and porosity. Hence, dolomite might not be in equilibrium with later low temperature pore water and have precipitated out of early high temperature pore water.

5.6.5 How much of the dolomite is actually stored CO_2?

The main issue with calculating the amount of CO_2 which has precipitated due to the high CO_2 concentration in the Fizzy field is how to distinguish between 'diagenetic dolomite' and 'sequestration dolomite'. To quantify the amount of 'stored CO_2' we applied a method that is primarily based on carbon isotope ratios. As seen before, these are less affected by isotopic fractionation during analysis and have previously been used to identify the existence of 'sequestration dolomite'.

The method we propose is based on two assumptions:

(i) The 'core' (the isotopic ratios of the final extraction) consists of only 'diagenetic dolomite'. This is confirmed by the linear relationship of the core data which plot along a line ('diagenetic dolomite equilibrium line', Fig. 5.20) almost parallel to the line which represents the theoretical equilibrium of Fizzy CO_2 with precipitated dolomite ('sequestration dolomite equilibrium line', Fig. 5.20). The position of the 'diagenetic dolomite equilibrium line' is shifted towards lighter carbon isotope ratios compared to the 'sequestration dolomite equilibrium line' because the isotopic composition of the CO_2 was different.

(ii) The 'rims' (the isotopic ratios of the stepwise extractions) represent the 'sequestration dolomite' and an unknown proportion of 'diagenetic dolomite'.

The key to quantifying the amount of dolomite which precipitated due to the high CO_2 concentration is to reveal the dolomite ratio in the rims.

The method that is proposed here uses average isotopic ratios for rim dolomite as is shown for sample 1. An alternative way would be the use of the data of the single extraction before the 'final extraction' as a representation of the rim dolomite. This way is too dependent on the isotopic composition of one single extraction, especially if the amount of extracted CO_2 was tiny, and could lead to biased results. An average value should give a more accurate representation of the isotopic composition of the rim dolomite.

All stepwise extractions except the final extractions represent the isotopic composition of the rims. However, some of the early extractions show extremely negative carbon and oxygen isotope ratios, presumably related to finely ground dust. For the quantification of the 'sequestration dolomite' we used only extraction data that represents the 'rims' with $\delta^{13}C$ heavier than -5 ‰ (V-PDB) and $\delta^{18}O$ heavier than -13.5 ‰ (V-PDB) to avoid the incorporation of outliers in the method (see Fig. 5.20). Additionally, sample 4 was not taken into account because it does not show clear evidence for CO_2 sequestration.

The average isotopic composition of the rim dolomite can be used to estimate a ratio of the amount of 'sequestration dolomite' and 'diagenetic dolomite' in the rims. If the average isotopic composition is close to the 'sequestration dolomite equilibrium line', the rim dolomite consists mostly of 'sequestration dolomite'. If the average composition is close to the 'diagenetic dolomite equilibrium line', the rim dolomite consists mostly of 'diagenetic dolomite'. By knowing how much of the dolomite is actually defined to be rim dolomite, the amount of 'sequestration dolomite' can be calculated. If the amount of rim dolomite is relatively small, it should consist mostly of 'sequestration dolomite' because only small parts of the outer rim have been dissolved. If the amount of rim dolomite is relatively high, a more evenly distributed mixture of 'sequestration' and 'diagenetic dolomite' can be expected.

A way to calculate the ratio of 'sequestration' and 'diagenetic dolomite' is to draw a straight line through the core isotopic ratio, and the average rim isotopic ratio to the 'sequestration dolomite equilibrium line' (Fig. 5.20). The length (in percentage) of the lines between the core value and the average isotopic composition of the rim relative to a line that connects the core value and the 'calculated 'sequestration dolomite equilibrium line' provides the fraction of 'sequestration dolomite' in the rims.

This method was used for the following calculation of the amount of 'sequestration dolomite'. By combining the 'sequestration dolomite' fraction with the amount of rim material (as percentage of the entire material) the amount of 'sequestration dolomite' in the three samples, can be found to lie between 7 % and 22 % (sample 1: 22 %; sample 8: 15 %; sample 9: 7 %). Because the stepwise extraction of sample 4 does not provide evidence for 'sequestration dolomite' in the rim we conclude that, according to our method, between 0 % and 22 % of the dolomite in the Fizzy field precipitated due to the high CO_2 concentration.

To calculate the fraction of CO_2 that is actually 'trapped' in the dolomite, the amount of CO_2 in the system has to be calculated. The mass of CO_2 in the pore space of one cubic meter of Fizzy gas cap can be calculated as follows:

$$Mass_{CO2}(gas-phase) = \phi \cdot S_G \cdot W_{CO2} \cdot \rho_{CO2} \quad (14)$$

$$Mass_{CO2}(aqeous-phase) = \phi \cdot S_L \cdot Sol_{CO2} \quad (15)$$

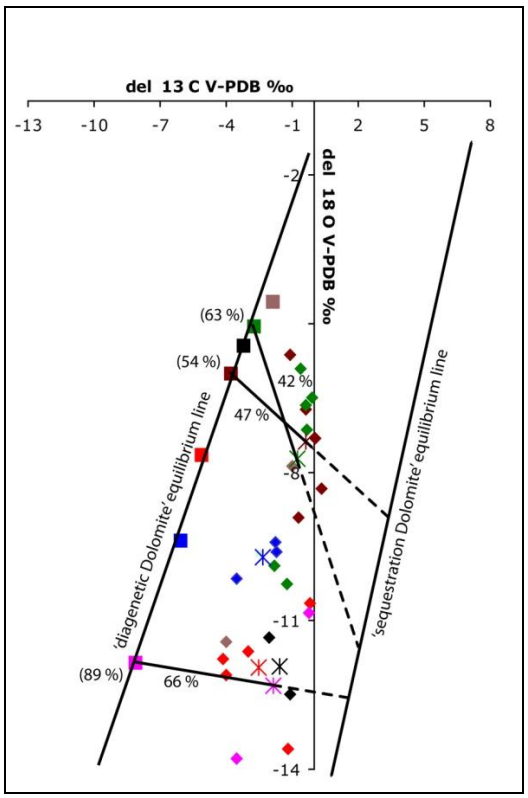

Figure 5.20: Graph illustrating the method of how to quantify the ratio of 'sequestration dolomite' to total dolomite. All data which were used for the calculation are illustrated. Several lines are shown: To the right the 'sequestration dolomite' line on which the isotope ratios of dolomite in equilibrium with the Fizzy field CO_2 should plot. To the left the 'diagenetic dolomite' line which represents the Rotliegend dolomite of the region which precipitated during the early diagenesis. This line is defined by the isotopic ratios of the cores (squares). The average isotopic composition of the rim dolomite is used for the calculation. See text for more information.

The porosity is given in percent (ϕ =0.223; source: Tullow Oil (unpublished data); taken from Wilkinson et al. 2009), S is the saturation of the liquid or the gaseous phase in the pore space (0.32 and 0.68, respectively; source: Tullow Oil (unpublished data); taken from Wilkinson et al. 2009), W_{CO2} is the fraction of CO_2 in the gaseous phase in weight percent (70.2 %: source: Tullow Oil (unpublished data)). Fluid properties were calculated for 80°C and 253 bar using the NIST database (http://webbook.nist.gov/chemistry/fluid/). The calculation was based on the idea that CO_2 and methane are the only gaseous phases; Sol_{CO2} is the mass of CO_2 dissolved in

the pore water under the given conditions (in kg/m^3, calculated after Spycher and Pruess (2005); taken from Wilkinson et al. 2009).

The CO_2 in the dawsonite and in the 'sequestration dolomite' can be calculated from:

$$Mass_{CO2}(dawsonite) = \rho_{rock} \cdot Vol_{dawsonite} \cdot F_{CO2(dawsonite)} \quad (16)$$

$$Mass_{CO2}(dolomite) = \rho_{rock} \cdot Vol_{dolomite} \cdot F_{CO2(dolomite)} \cdot f^* \quad (17)$$

The whole rock density is 2400 kg/m^3 (as an assumption for North Sea basins), $Vol_{(mineral)}$ is the fraction of dawsonite and dolomite in the whole rock measured by point count analysis and XRF (0.004 and 0.071, respectively; taken from Wilkinson et al, 2009) and F_{CO2} is the weight fraction of CO_2 in the mineral. The factor f^* represents the fraction of 'sequestration dolomite' relative to the entire dolomite. Hence, the fraction of sequestered CO_2 in dolomite relative to the entire volume of CO_2 which is presumably related to the currently high CO_2 concentration is, according to the three samples, between 7 and 19 %. If sample 4, which does not show clear evidence for sequestration, is taken into account, the fraction of sequestered CO_2 in dolomite lies between 0 and 19 %.

5.6.6 'Net gain' of natural CO_2 sequestration in Fizzy

The data suggest that relatively recent dolomite precipitation due to high CO_2 concentrations has occurred. Between 0 and 22 % of the dolomite precipitated during the last 50 Ma years. Hence, if, according to Wilkinson et al. (2009), the dolomite content of the Fizzy rocks is 7.2 %, then the overall percentage of Fizzy's 'diagenetic dolomite' is between 5.6 and 7.2 %.

According to Wilkinson et al. (2009), the adjacent Orwell field contains an average of 12 % dolomite. In other words, even with 'sequestration dolomite' the overall amount of Orwell dolomite is almost twice as high as it is for Fizzy. There are two possible explanations for this. Firstly, less dolomite precipitated in the Fizzy area during the diagenesis. No data for permeability is available but the porosity of each of the two gas accumulations is within a similar range. In fact, the porosity of the Orwell field (8.2 %; Fizzy porosity =10.7 %) is slightly lower, probably due to the enhanced dolomite cementation. Therefore the cement precipitation could not vary because of constrained fluid circulation. Due to the relatively small lateral distance between Fizzy and Orwell, chemical variations in the pore water are also unlikely but cannot be ruled out.

The second explanation is carbonate dissolution followed by precipitation. It is well known that an increase in CO_2 concentration leads to an acidification of water which dissolves carbonate minerals (e. g. Rochelle et al. 2004; Xu et al., 2007). At the same time, dissolution of carbonate consumes H^+ ions and buffers the pH. Once it has equilibrated, precipitation of secondary carbonate might start. Although the slightly higher porosity of the Fizzy reservoir rock would support this theory, Wilkinson et al. (2009) did not find any evidence for dissolution.

If the lower carbonate content of the Fizzy field relative to the Orwell field was because of the dissolution of almost half of the dolomite as a response to the invading CO_2, the actual 'net gain' would be negative and more CO_2 would be released by dissolution than trapped by precipitation of 'sequestration dolomite'. To answer the important question, whether CO_2 related dissolution took place, is not a part of the study but clearly mineral sequestration does not inevitably mean a reduction in CO_2.

5.6.7 Dawsonite precipitation instead of 'sequestration dolomite'?

One important difference of the Fizzy field reservoir rocks and the Orwell Rotliegend rocks is a small amount of dawsonite in Fizzy. Dawsonite is commonly associated with high subsurface CO_2 concentrations (Wopfner & Hoecker 1987). According to Wilkinson et al. (2009) its occurrence in Rotliegend rocks of the southern North Sea is extremely unusual. Because it is linked to high CO_2 concentration, it is almost certain that Fizzy dawsonite precipitation was triggered by the late Cretaceous CO_2 flush and precipitated simultaneously with the 'sequestration dolomite'. Dawsonite is still a relatively poorly investigated mineral. To our knowledge, neither fractionation factors for the dawsonite – water/CO_2 system nor dissolution constants for subsurface conditions have been experimentally or theoretically investigated. We can therefore only assume the impact of dawsonite on the experimental results.

If dawsonite dissolved simultaneously with the 'sequestration dolomite', analysis of evolving CO_2 would provide a mixture of two reactions: the reaction of dolomite and the reaction of dawsonite with phosphoric acid. If the stable carbon and oxygen isotope ratios of the CO_2 evolving from dawsonite dissolution were relatively heavy, they could be responsible for the 'hook-like' reaction path. The amount of dawsonite in the Fizzy rock samples is relatively low and dawsonite would have had to release extremely heavy carbon isotope ratios to produce the sometimes quite distinct shift towards heavy carbon isotopes. Although that seems to be unlikely, we cannot eliminate that dawsonite reaction might have some impact on the data and the amount of 'sequestration dolomite' may actually be exaggerated.

5.7 Conclusions

- A stepwise CO_2 extraction and carbon and oxygen isotope analysis of dolomite cement from a natural Rotliegend CO_2 reservoir and an adjacent non-CO_2 gas accumulation in the southern North Sea has successfully been conducted. Early extractions generally give lower oxygen and carbon ratios. With progressing time, isotopic ratios become generally higher if the dolomite precipitated from one isotopic composition of CO_2.
- Results of this study show that carbonates were precipitated due to high CO_2 concentration in Fizzy. Stepwise extraction experiments conducted on dolomite cement from the Fizzy field, a natural CO_2 reservoir, strongly suggest precipitation of two generations of dolomite. The first early dolomite generation ('diagenetic dolomite') cemented the Rotliegend Sandstone during the early diagenisis of the formation, whereas the second younger dolomite ('sequestration dolomite') precipitated due to the high CO_2 concentration.
- According to our method, between 0 and 22 % of the dolomite in the Fizzy field precipitated due to the high CO_2 concentration. Therefore, between 0 and 19 % of the CO_2, which is related to the relatively recent high CO_2 concentration, is 'trapped' in the 'sequestration dolomite'. The wide range of this estimation is mainly related to the rock heterogeneity.
- Uncertainties are high, mainly related to the limited number of experiments and the heterogeneities of the Rotliegend reservoir rocks. Additional uncertainties such as possible dawsonite dissolution require more research and a better understanding.
- Fizzy contains less dolomite and has a higher porosity than the adjacent Orwell field. Further research should reveal whether the invading CO_2 acidified the Fizzy trap and dissolved a significant part of the carbonate. The subsequent precipitation of dolomite and dawsonite incorporated less CO_2 than might have been previously released. Hence CO_2 migration into the reservoir would have increased the amount of free CO_2, not decreased it.

6 Overall conclusions and future work

When CO_2 is injected into a brine filled reservoir, several chemical and physical effects have to be considered to guarantee safe long term storage. This PhD thesis investigated aspects concerning the injection and the long term fate of CO_2 in the subsurface. The key conclusions of this study are:

- The fracture strength of subsurface formations is sensitive to high fluid pressure. Considering the simulation conditions used for this study presented in chapter 3 a pore pressure increase of ~37.5 % relative to hydrostatic will compromise formation stability. The determination of a fracture pressure is an important uncertainty.
- Generally, the injection pressure reduction effect of mutual dissolution varies and should be accounted for. To model it realistically, both dissolution coefficients and fluid properties need to be determined as accurately as possible as dissolution is determined by a combination of fluid flow and the dissolution itself.
- Simulated mutual dissolution of H_2O is always an overestimation because it occurs instantaneously. However, the degree of overestimation can be reduced if the grid is sufficiently small.
- Fluid pressure is vital in calculating the CO_2 storage capacity of saline aquifers. However, the storage capacity of the Bunter Sandstone Formation based on fluid pressure remains very high. It shall be emphasised here that if fluid pressure is taken into account, the CO_2 capacity will only be reduced to ~50 % compared to a capacity estimation made by Holloway et al. (2006) using a method that did not take fluid pressure into account.
- By comparing the results of two CO_2 capacity calculations, one based on fluid pressure using a numerical simulator and the other using a simple analytical approach (Zhou et al. 2008) the differences between them are

relatively moderate. It was concluded that the application of a numerical simulator is not needed. The main reasons are:

1. The proposed Peng-Robinson EoS does not require a complicated approach and can be simply solved with software such as MATLAB or EXCEL.
2. The model results of chapter 4 show that the difference between one and two phase fluid flow does not affect the results significantly. No significant pressure gradients could be observed. An 'average pressure' is therefore sufficient.
3. Simulations have shown that the pressure decreasing effect of CO_2 dissolving into brine is negligible both during the injection period and throughout a 10 year post-injection period.

- Carbonates were precipitated due to high CO_2 concentration in the Fizzy field, a natural CO_2 reservoir in the southern North Sea. Stepwise extraction experiments conducted on dolomite cement from the Fizzy field strongly suggest precipitation of two generations of dolomite. The first early dolomite generation ('diagenetic dolomite') cemented the Rotliegend Sandstone during the early diagenesis of the formation, whereas the second younger dolomite ('sequestration dolomite') precipitated due to the high CO_2 concentration.
- According to the proposed method, between 0 and 22 % of the dolomite in the Fizzy field precipitated due to the high CO_2 concentration. Therefore, between 0 and 19 % of the CO_2, which is related to the relatively recent high CO_2 concentration, is 'trapped' in the 'sequestration dolomite'. The wide range of this estimat**e** ~~ion~~ is mainly related to the rock heterogeneity.

Although some aspects concerning CO_2 storage in the subsurface have been successfully investigated, many answers remain unknown. This is certainly due to the fact that the concept and implementation of CO_2 storage are still relatively immature. Although many years of enhanced oil and gas recovery experience can provide important knowledge on CO_2 injection and short term storage, prediction and

prognosis are still uncertain and have to be assessed carefully. There is very limited data available on issues concerning high pressures (higher than the initial pre-injection pressure) during long term storage.

One of the greatest uncertainties is presumably the geological description of large scale saline aquifers. A combination of seismic data, core analysis and pressure data is needed to characterise an aquifer sufficiently. It should also be taken into consideration that all of these methods have their limitations.

The accuracy of the results of chapter 3 and chapter 4 depend on the accurate determination of the fracture pressure. The studies use leak-off pressure data from the central North Sea to calibrate a fracture gradient for the southern North Sea. This is dangerous because the central North Sea has (as most of the basins worldwide) has a relatively unique geology. Especially in deeper areas, the fracture pressure is very high and can even exceed the lithostatic gradient due to pore pressure stress coupling and resulting increase in rock tensile strength in the Jurassic and the Triassic Formations. To improve the prediction of the fracture pressure of saline aquifers, the following proposals could be used.

- The leak-off pressure tests and limited tests of as many wells as possible should be analysed. It is important to consider that those tests only provide the fracture pressure of low-permeability rocks. For CO_2 storage purposes they define the fracture pressure of potential cap rocks and not of reservoir rocks.
- If no direct fracture pressure data **is** available, the fracture pressure gradient can be modelled using parameters such as the Poisson ratio or lithology related coefficient (e.g. Matthews & Kelly 1967; Daines 1982). Due to poro-elastic behaviour of rocks, an accurate pressure prediction of the cap rock is also necessary.

An additional improvement of chapter 3 would be a realistic application of Forchheimer flow and sensitivity tests on reservoir heterogeneity.

This thesis presents strong evidence for dolomite precipitation due to ~~an~~ enhanced CO_2 concentration in the Rotliegend Formation of the southern North Sea. To reduce uncertainties and to achieve a better understanding of the process of mineral trapping the following next steps are proposed:

- One of the major uncertainties is the position of the 'sequestration dolomite equilibrium line'. As mentioned in chapter 5, no carbon isotope fractionation factor for the dolomite-water system could be found in the literature. The use of Deines (2004) seems to be an alternative, but more experimental research is necessary to make more reliable predictions.
- One of the assumptions is that the dawsonite in the Fizzy field does not have any impact on the isotopic trend of the stepwise extraction data. To our knowledge no fractionation factors for dawsonite exist. More experimental research in this is area is required.
- Finally, the source and date of the CO_2 charge in the Fizzy field is still unknown.

The presented future work proposal represent only a tiny fraction of what is needed to achieve a better understanding of the chemical and physical processes which may occur when CO_2 is injected into the subsurface. Generally, the research on storage requires a multidisciplinary approach in disciplines of geology, geophysics, geochemistry, reservoir engineering, petroleum geology and many more. Only if the research of several disciplines is combined can real progress can be achieved.

7 Reference

Adam, N.K. 1968. The physics and chemistry of surfaces. Dover publications, New York. Unabridged and corrected republication of the third (1941) edition.

Adamson, A.W. 1979. A textbook of physical chemistry. 2nd edition. Academic Press, New York.

Alberts, M.A. & Underhill, J.R. 1991. The effect of Tertiary structuration on Permian gas prospectivity, Cleaver Bank area, southern North Sea, UK. In: Spencer, A.M. (ed.): Generation, Accumulation and Production of Europe's Hydrocarbons. Special Publication of the European Association of Petroleum Geoscientists Memoir, 1, 161–173.

Allan, P.A. & Allan, J.R. 2005. Basin Analysis. Blackwell Publishing, Oxford.

Arts, R., Eiken, O., Chadwick, R.A., Thibeau, S. & Nooner, S. 2008. Ten years' experience of monitoring CO_2 injection in the Utsira Sand at Sleipner, offshore Norway, First Break, 26, 65-72.

Bachu, S., Gunther, W.D. & Perkins, E.H. 1994. Aquifer disposal of CO_2: Hydrodynamic and mineral trapping. Energy Conversion Management, 35/4, 269– 279.

Baker, J.C., Bai, G.P., Hamilton, P.J., Golding, S.D. & Keene, J.B. 1995. Continental style carbon dioxide seepage recorded by dawsonite in the Bowen-Gunnedah-Sydney basin system, Eastern Australia. Journal of Sedimentary Research, 65/3, 522-530.

Bando, S., Takemura, F., Nishio, M., Hihara, E. & Akai, M. 2004. Viscosity of aqueous NaCl solutions with dissolved CO_2 at (30 to 60)°C and (10 to 20) MPa. Journal of Chemical & Engineering Data, 49, 1328-1332.

Batzle, M. & Wang, Z. 1992. Seismic properties of pore fluids. Geophysics, 57, 1396–1408.

Bear, J. 1979. Hydraulics of Groundwater. McGraw-Hill, New York

Bell, J.S. 1990. The stress regime of the Scotian shelf offshore eastern Canada to 9 kilometres depth and implication for rock mechanics and hydrocarbon migration. In: Maury, V. & Formaintroux, D. (eds): Rock at great depth. Rotterdam, Netherlands, Balkema, 1243-1265.

Bennion, D.B. & Bachu, S. 2006. Dependence on temperature, pressure, and salinity of the IFT and relative permeability displacement characteristics of CO_2 injected in deep saline aquifers. Paper SPE 102138.

Bentham, M. 2006. An assessment of carbon sequestration potential in the UK – Southern North Sea case study. Tyndall Centre for Climate Change Research Working Paper 85.

Berg, R.R. 1975. Capillary pressure in stratigraphic traps. AAPG Bulletin, 59/6, 939-956.

Bergamo, P.E.S., Grimstad, A.-A. & Lindeberg, E. 2011. Simultaneous CO_2 injection and water production to optimise aquifer storage capacity. International Journal of Greenhouse Gas Control, 5, 555-564.

Bergman, M., Winter, E.M., 1995. Disposal of carbon dioxide in aquifers in the U.S. Energy Conversion Management, 36, 523–526.

Biot, M.A. 1941. General theory of three-dimensional consolidation. Journal of Applied Geophysics, 12, 155-164.

Birkholzer, J.T. & Zhou, Q. 2009. Basin-scale hydrologic impacts of CO_2 storage: Capacity and regulatory implications. International Journal of Greenhouse Gas Control, 3, 745-756.

Birkholzer, J.T., Zhou, Q. & Tsang, C.-F. 2009. Large-scale impact of CO_2 storage in deep saline aquifers: A sensitivity study on pressure response in stratified systems. International Journal of Greenhouse Gas Control, 3, 181-194.

Bradshaw, J., Bachu, S., Bonijoly, D., Burruss, R., Holloway, S., Christensen, N.P. & Mathiassen, O.M. 2007. CO_2 storage capacity estimations: Issues and development of standards. International Journal of Greenhouse Gas Control, 1, 62-68.

Breckels, I.M. & van Eekelen, H.A.M. 1982. Relationship between horizontal stress and depth in sedimentary basins. Journal of Petroleum Technology, 34, 2191-2198.

Brooks, R.H. & Corey, A.T. 1964. Hydraulic properties of porous media. Hydrology paper 3. Civil Engineering Department, Colerado State University, Fort Collins, Colorado.

Brown, E.T. & Hoek, E., 1978. Trends in relationships between in situ stresses and depth. International Journal of Rock Mechanics, 15, 211–225.

Buckley, S.E. & Leverett, M.C. 1942. Mechanism of fluid displacement in sands. Transaction of the AIME, 146, 107-116.

Bulat, J. & Stoker, S.J. 1987. Uplift determination from interval velocity studies, UK southern North Sea. In: Brooks, J. & Glennie, K. W. (eds.): Petroleum Geology of North West Europe, Graham and Trotman, London, 293-305.

Burton, M. & Bryant, S.L. 2009. Eliminating buoyant migration of sequestered CO_2 through surface dissolution: Implementation, costs and technical challenges. Paper SPE 110650.

Byerlee, J.D. 1967. Frictional characteristics of granite under high confining pressure. Jouirnal of Geophysical Research, 72, 3639-3648.

Byerlee, J.D.1978. Friction of rocks. Pure and Applied Geophysics, 116, 615–626.

Cameron, T.D.J., Crosby, A., Balson, P.S., Jeffery, D.H., Lott, G.K., Bulat, J. & Harrison, D.L. 1992. The geology of the southern North Sea. United Kingdom Offshore Regional Report. British Geological Survey and HMSO, London.

Cavanagh, A.J., Haszeldine, R.S. & Blunt, M.J. 2010. Open or closed? A discussion of mistaken assumptions in the Economides pressure analysis of carbon sequestration. Journal of Petroleum Science and Engineering, 74, 107-110.

Chadwick, R.A., Arts, R., Bernstone, C., May, F., Thibeau, S. & Zweigel, P. 2008. Best Practice for the Storage of CO_2 in Saline Aquifers. British Geological Survey Occasional Publication, 14, Keyworth, Nottingham.

Chadwick, R.A., Noy, D.J. & Holloway, S. 2009. Flow processes and pressure evolution in aquifers during the injection of supercritical CO_2 as a greenhouse gas mitigation measure. Petroleum Geoscience, 15, 59-73.

Chadwick, R.A., Noy, D., Arts, R. & Eiken, O. 2009. Latest time-laps seismic data from Sleipner yield new insights into CO_2 plume developement. 9th International Conference on Greenhouse Gas Control Technologies, Washington DC, USA. ISSN: 18766102.

Clark, D.N. 1980. The diagenesis of Zechstein carbonate sediments. In: Fuechtbauer, H. & Peryt, T.M. (eds.): The Zechstein basin. Contributions to Sedimentology, 9, 167-203.

Class, H., Ebigbo, A., Helmig, R., Dahle, H., Nordbotten, J.M., Celia, M.A., Audigane, P., Darcis, M., Ennis-King, J., Fan, Y., Flemisch, B., Gasda, S., Krug, S., Labregere, D., Jin, M., Sbai, A., Thomas, S.T. & Trenty, L. 2009. A benchmark-study on problems related to CO_2 storage in geological formations. Computational Geosciences, 13/4, 409-434.

Clochard, V., Delepine, N., Labat, K. & Ricarte, P. 2010. CO_2 plume imaging using 3D pre-stack stratigraphic inversion: A case study on the Sleipner field. First Break, 28, 91-96.

Cooke-Yarborough, P. 1991. The Hewett Field, Blocks 48/28-29-30, 52/4a, UK 572 North Sea. In: Abbotts, I.L. (ed.): United Kingdom Oil and Gas Fields, 25 years 573 Commemorative Volume. Memoirs 14. Geological Society, London, 574 pages, 433–441.

Corey, A.T. 1954. The interrelation between gas and oil relative permeabilities. Producers Monthly, 38-41.

Cox, P.M., Betts, R.A., Jones, C.D., Spall, S.A. & Totterdell, I.J. 2000. Acceleration of global warming due to carbon-cycle feedbacks in a coupled climate model: Nature, 408, 194-187.

Craig, H. 1957. Isotopic standards for carbon and oxygen and correction factors for mass-spectrometric analysis of carbon dioxide. Geochemica et Cosmochimica Acta, 12, 133-149.

Crowley, T.J. 2000. Causes of climate change over the past 1000 years. Science, 289, 270-277.

Curtis, C.D. 1978. Possible links between sandstone diagenesis and depth related geochemical reactions occurring in enclosing mudstones. Journal of the Geological Society, 135, 107-117.

Daines, S.R., 1982. Prediction of fracture pressures for wildcat wells. Journal of Petroleum Technology, 34/4, 863–872.

Dake, L.P. 1983. Fundamentals of reservoir engineering. Elsevier Science, 462 pages.

Deines, P., Langmuir, D. & Harmon, R.S. 1974. Stable carbon isotope ratios and existence of a gas-phase in evolution of carbonate ground waters: Geochimica et Cosmochimica Acta, 38, 1147–1164.

Deines, P. 2004. Carbon isotope effects in carbonate systems. Geochemica et Cosmochimica Act, 68/12, 2659-2679.

Detournay, E., Cheng, A.H.-D., Roegiers, J.C. & McLennan, J.D. 1989. Poroelasticity considerations in in situ stress determination by hydraulic fracturing, International Journal of Rock Mechanics, 26, 507-513.

Detournay, E. & Cheng, A.H.-D. 1993. Fundamentals of poroelasticity. In: Fairhurst, C. (ed): Comprehensive Rock Engineering: Principles, Practice and Projects, Vol. II, Analysis and Design, Pergamon Press, 113-171.

Domenico, S.N., 1984, Rock lithology and porosity determination from shear and compressional wave velocity, Geophysics, 1188-1195.

Doughty, C. & Pruess, K. 2004. Modeling supercritical carbon dioxide injection in heterogeneous porous media, Vadose Zone Journal, 3, 837 - 847.

Duan Z. & Sun R. 2003. An improved model calculating CO_2 solubility in pure water and aqueous NaCl solutions from 257 to 533 K and from 0 to 2000 bar. Chemical Geology, 193, 257–271.

Ehlig-Economides, C. & Economides, M.J. 2010. Sequestering carbon dioxide in a closed underground volume. Journal of Petroleum Science and Engineering, 70, 123-130.

Engelder, T. & Fischer, M.P. 1994. Influence of poroelastic behaviour on the magnitude of minimum horizontal stress, S_h, in overpressured parts of sedimentary basins. Geology, 22, 949-952.

Etheridge, M.A., Wall, V.J. & Vernon, R.H. 1983. The role of the fluid phase during regional metamorphism of calcareous sediments in the Waterville-Vassalboro area, south-central Maine. Contributions to Mineralogy and Petrology, 57, 119-143.

Fairhurst , C. 1964. Measurement of in situ rock stresses, with particulare reference to hydraulic fracturing. Rock Mech. Eng. Geol., 2, 129-47.

Falkowski, P., Scholes, R.L., Boyle, E., Canadell, J., Canfield, D., Elser, J., Gruber, N., Hibbard, K., Hoegberg, P., Linder, S., Mackenzie, F.T., Moore III, B., Pedersen, T., Rosenthal, Y., Seitzinger, S., Smetacek, V. & Steffen, W. 2000. The global carbon cycle: A test of our knowledge of earth as a system: Science, 290, 291-296.

Fenghour, A., Wakeham, W.A. & Vesovic, V. 1999. The viscosity of Carbon Dioxide. Journal of Physical and Chemical Reference Data, 27/1, 34-44.

Fertl, W.H., Chilingarian, G.V. &. Rieke, H.H. 1976. Elsevier, Amsterdam (1976).

Firoozabadi, A. & Katz, D.L. 1979. An analysis of high-velocity gas flow through porous media. Journal of Petroleum Technology, 31/2, 211-216.

Folk, R.L. & Land L.S. 1975. Mg/Ca ratio and salinity: Two controls over crystallisation of dolomite. American Association of Petroleum Geologists Bulletin, 59, 60-68.

Fritz, P. & Fontes, J.C. 1966. Fractionment isotopique pendant l'attaque acide des carbonates naturels: role de la granulometrie. Comptes rendus de l'Académie des Sciences, 263, 1345-1348.

Forchheimer, P. 1901. Wasserbewegung durch Boeden. Zeitung des Vereins Deutscher Ingenieure, 45, 1781-1788.

Gaarenstroom, L., Tromp, R.J., de Jong, M.C. & Brandenburg, A.M. 1993. Overpressure in the central North Sea: implications for trap integrity and drilling safety. In: Parker, J. R. (ed): Petroleum Geology of Northwest Europe. Proceedings of the 4th Conference 2. The Geological Society, London, 1305-1313.

Gercek, H. 2006. Poisson's ratio values for rocks. International Journal of Rock Mechanics and Mining Sciences, 44, 1–13.

Ghanbari, S., Al-Zaabi, Y., Pickup, G.E., Mackay, E., Gozalpour, F. & Todd, A.C. 2006. Simulation of CO_2 storage in saline aquifers. Chemical Engineering Research and Design, 84/9, 764-775.

Glennie, K.W. 1998. Lower Permian–Rotliegend. In: Glennie, K.W. (ed.): Petroleum Geology of the North Sea: Basic concepts and recent advances. Blackwell Science, Oxford, 137–173.

Glennie, K.W. & Boegner, P. 1981. Sole Pit inversion tectonics. In: Illing, L.V. & Hobson, D.G. (eds.): The Petroleum Geology of the Continental Shelf of N.W. Europe. Heyden, London, 110–120.

Glennie, K.W. & Underhill, J.R. 1998. The development and evolution of structural styles in the North Sea. In: Glennie, K.W. (ed.): Petroleum Geology of the North Sea Basin: Basic concepts and recent advances. Blackwell Science, Oxford, 42–84.

Götze, J. 1998. Geochemistry and provenance of the Altendorf feldspathic sandstone in the Middle Bunter of the Thuringian basin (Germany). Chemical Geology, 150, 43-61.

Goldsmith, J.R. & Graf, D.L. 1958a. Structural and compositional variations in some natural dolomites. Journal of Geology, 66, 678-693.

Graboski, M.S. & Daubert, T.E. 1978. Modified Soave equation of state for phase equilibrium calculations. Industrial and Engineering Chemistry Process Design and Development, 19/3, 501-505.

Gunter, W.D., Wiwchar, B. & Perkins, E.H. 1997. Aquifer disposalof CO_2-rich greenhouse gases: Extension of the time scale of experiment for CO_2-sequestering reactions by geochemical modelling. Mineralogy and Petrology, 59, 121-140.

Gunter, W.D., Perkins, E.H. & Hutcheon, I. 2000. Aquifer disposal of acid gases: Modelling of water-rock reactions for trapping of acid wastes. Applied Geochemistry, 15, 1085-1095.

Haimson, B. & Fairhurst, C. 1967. Initiation and extension of hydraulic fractures in rocks. Society of Petroleum Engineers Journal. 7, 310-318.

Han, W.H. & McPherson, B. 2008. Comparison of two different equations of state for application of carbon dioxide sequestration. Advances in Water Resources, 31, 877-890.

Hardie, L.A 1987. Dolomitization; a critical view on some current views. Journal of Sedimentary Petrology, 57/1, 166-183.

Hebach, A., Oberhof, A. & Dahmen, N. 2004. Density of water + carbon dioxide at elevated pressures: Measurements and correlation. Journal of Chemical & Engineering Data, 49/4, 950-953.

Heinemann, N., Wilkinson, M., Pickup, G.E., Haszeldine, R.S. & Cutler, N.A. 2012. CO_2 storage in the offshore UK Bunter Sandstone Formation. International Journal of Greenhouse Control, 6, 210-219.

Hillis, R.R. 2001. Coupled changes in pore pressure and stress in oil fields and sedimentary basins. Petroleum Geoscience, 7, 419-425.

Holditch, S.A. & Morse, R.A. 1976. The effects of non-Darcy flow on the behaviour of hydraulic fractured gas wells, Journal of Petroleum Technology, 28/10, 1196-1179.

Holloway, S., Vincent, C.J., Bentham, M.S. & Kirk, K.L. 2006. Top-down and bottom-up estimates of CO_2 storage capacity in the United Kingdom sector of the southern North Sea basin. Environmental Geosciences, 13, 71-84.

Hough, E.W., Rzasa, M.J. & B.B. Wood. 1951. Interfacial tensions of reservoir pressures and temperatures, apparatus and the water-methane system, AIME Petroleum Transaction, 192, 57-60.

Hubbert, M.K. & Willis, D.G. 1957. Mechanics of hydrologic fracturing. AIME Petroleum Transactions, 210, 153-168.

Hurter, S., Labregere, D. & Berge, J. 2007. Simulations for CO_2 injection projects with compositional simulator. SPE 108540

Hsu, K.J. 1967. Chemistry of dolomite formation. Elsevier Dev. Sediment., 9b, 169-191.

IPCC: 2001, Intergovernmental Panel on Climate Change, Third Assessment Report. Cambridge University Press.

Irwin, H., Curtis, D.D. & Coleman, M.L. 1977. Isotopic evidence for source of diagenetic carbonates formed during burial of organic-rich sediments. Nature, 269, 209-213.

ISRM. Terminology (English, French, German), 1975. Lisbon, 83 pages.

Jaeger, J.C. & Cook, N.G.W. 1969. Fundamentals of rock mechanics. Barnes and Noble, New York and London.

Jaeger, J.C, Cook, N.G.W. & Zimmerman, R.W. 2007. Fundamentals of rock mechanics. Wiley-Blackwell, Oxford.

Jenkins, D.A.L. 2001. Potential impacts and effects of climate change. In: Gerhard. L. C., Harrison, W. E. & Hanson, B. M. (eds.): Geologic Perspectives of Global Climate Change. Studies in Geology. American Association of Petroleum Geologists, Tulsa, OK, 47, 337-359.

Jimenez, J.A. & Chalaturnyk, R.J. 2002. Are disused hydrocarbon reservoirs safe for geological storage of CO_2? In: Kaya, Y., Ohyma, K., Gale, J. & Suzuki, Y. (eds.): GHGT-6: Sixth international conference on Greenhouse Gas Control Technologies, Kyoto, Japan, 30 September – 4 October.

Johnson, J.W., Nitao, J.J. & Knauss, K.G. 2004. Reactive transport modelling of CO_2 storage in saline aquifers to elucidate fundamental processes, trapping mechanisms and sequestration partitioning. In: Baines, S. & Worden, R. (eds.): Geological storage of carbon dioxide. Geological Society Special Publication, 233, 107-128.

Juanes, R., Spiteri, E.J., Orr Jr., F.M. & Blunt, M.J. 2006. Impact of relative permeability hysteresis on geological CO_2 storage. Water Resources Research. 42, W12418.

Jueza, J. 1966. An equation of state for water and steam, steam tables in the critical region and in the range from 1,000 to 100,000 bars. Rozprav. Ceskoslovenske Akad. VED Rada TV, 76, 3-121.

Kell, G.S. & Whalley, E. 1974. Reanalysis of the density of liquid water in the range 0-150 C and 0-1 kbar. The Journal of Chemical Physics, 62/9, 3496-3503.

Kerrick, D.M. & Jacobs, G.K. 1981. A modified Redlich-Kwong equation for H_2O, CO_2 and H_2O-CO_2 mixtures at elevated pressures and temperatures. American Journal of Science, 281, 735-767.

Ketter, F.J. 1991. The Esmond, Forbes, and Gordon Fields, Blocks 43/8a, 43/13a, 43/15a, 43/20a, UK North Sea. In: Abbotts, I.L. (ed): United Kingdom Oil and Gas Fields, 25 years Commemorative Volume, Geological Society, London, Memoirs, 14, 425–432.

Kestin, J., Khalifa, H.E. & Correia, R.J., 1981. Tables of the dynamic and kinematic viscosity of aqueous NaCl solutions in the temperature range 20–150°C and the pressure range 0.1–35 MPa. Journal of Physical and Chemical Reference Data, 10, 41–71.

King, M.B., Mubarak, A., Kim, J.D. & Bott, T.R. 1992.The mutual solubilities of water with supercritical and liquid carbon dioxide. Journal of Supercritical Fluids, 5, 296−302.

Kopp, A., Class, H. & Helmig, R. 2008. Investigations on CO_2 storage capacity in saline aquifers Part 1. Dimensional analysis of flow processes and reservoir characteristics. International Journal of Greenhouse Gas Control, 3/3, 263-276.

Kuempel, H.-J. 1991. Poroelaticity: parameters reviewed. Geophysical Journal International, 105, 783-799.

Land, L.S. 1980. The isotopic and trace element geochemistry of dolomite: The state of the art. In: Zenger, D.H., Dunham, J.B. & Ethington, R.L (eds.), Concepts and Models of Dolomitization. Spec. Publ. –SEPM, 28, 87-110.

Land, L.S. 1998. Failure to precipitate dolomite at 25 degrees C from dilute solution despite 1000-fold oversaturation after 32 years. Aquatic Geochemistry, 4/3-4, 361-368.

Leveille, G.P., Knipe, R., More, C., Ellis, D., Dudley, G., Jones, G., Fisher, Q.J. & Allinson, G. 1997. Compartmentalization of Rotliegendes gas reservoir by sealing faults, Jupiter field area, southern North Sea. In: Ziegler, K, Turner, P. & Daines, S.R. (eds.): Petroleum Geology of the southern North Sea: Future Potential. Geological Society Special Publication, 123, 87-104.

Lindeberg, E. & Bergmo, P. 2002. The long-term fate of CO_2 injected into an aquifer. In: Proceeding of the 6th International Greenhouse Gas Control Technologies, Kyoto, October 2002.

Lindeberg, E., Vuillaume, J.-F. & Ghaderi, A. 2009. Determination of the CO_2 storage capacity of the Utsira Formation. Energy Procedia, 1, 2777-2784.

Magaritz, M., Turner, P. & Kadling, K-C. 1981. Carbon isotope change at the base of the Upper Permian Zechstein sequence, Journal of Geology, 16, 243-254.

Mathews, WR. & Kelly, J. 1967. How to predict formation pressure and fracture gradient. Oil and Gas Journal, 65/8, 92-106.

Mathias, S.A., Hardisty, P.E., Trudell, M.R. & Zimmerman, R.W. 2009. Approximate solutions for pressure buildup during CO_2 injection in brine aquifers. Transport through porous Media, 79, 265-284.

Mathias, S.A., Hardisty, P.E., Trudell, M.R. & Zimmerman, R.W. 2009. Screening and selection of sites for CO_2 sequestration based on pressure buildup. International Journal of Greenhouse Gas Control, 3, 577-585.

McCrea, J. M. 1950. On the isotopic chemistry of carbonates and a paleo-temperature scale. Journal of Chemical Physics, 18, 849-857.

McCrone, C.W., Gainski, M. & Lumsden, P.J. 2003. The Indefatigable Field, Blocks 49/18, 49/19, 49/23, 49/24, UK North Sea. In: Gluyas, J. G. and Hichens, H. M. (eds): United Kingdom Oil and Gas Fields, Commemorative Millennium Volume. Geological Society, London, Memoir, 20, p. 741-747.

McWhorter, D.B. & Kueper, B.H. 1996. Mechanics and Mathematics of the Movement of Dense, Non-Aqueous Phase Liquids (DNAPLs) in Porous Media. Chapter 3, Dense Chlorinated Solvents and Other DNAPLs in Groundwater, Edited by J.F. Pankow and J.A. Cherry, Waterloo Educational Services.

Metz, B., Davidson, O., De Coninck, H., Loos, M. & Mayer, L. 2005. IPCC special report on carbon dioxide capture and storage. Cambridge University Press.

Morrow, D.W. 1978. Dolomitization of lower Palaeozoic burrow-fillings. Journal of Sedimentary Petrology, 48, 295-306.

Moss, B., Barson, D., Rakhit, K., Dennis, H. & Swarbrick, R. 2003. Formation pore pressures and formation waters. In: Evans, D., Graham, C., Armour, A. and Bathurst, P. (eds): The Millennium Atlas: Petroleum Geology of the Central and Northern North Sea. Geological Society, London.

Mualem, Y. 1976a. A new model for predicting the hydraulic conductivity of undersaturated porous media. Water Resources Research, 12, 513-522.

Nghiem, L., Sammon, P., Grabenstetter, J. & Ohkuma, H. 2004. Modeling CO_2 storage in aquifers with fully coupled geochemical EoS compositional simulator. Society of Petroleum Engineers Journal, 2004:89474

Nordbotten, J.M., Celia, M.A. & Bachu, S. 2004. Analytical solutions for leakage rates through abandoned wells. Water Resources Research, 40, W04204.

Nordbotten, J.M., Celia, M.A. & Bachu, S. 2005. Injection and storage of CO_2 in deep saline aquifers: Analytical solution for CO_2 plume evolution during injection. Transport in Porous Media, 58, 339-360.

Obdam, A. & van der Meer, L.G. H. 2003. GESTCO: Reservoir simulation for selected case studies. TNO-report No. NITG 03-091-A: Utrecht, Netherlands, TNO-NITG.

Obdam, A., van der Meer, L.G.H., May, F., Kervevan, C., Bech, N. & Wildenborg, A. 2003. Effective CO_2 storage capacity in aquifers, gas fields, oil fields and coal fields. In: Gale, J. and Kaya, Y. (eds): Greenhouse gas control technologies, Pergamon, Amsterdam.

Orr, F.M. 2004. Storage of carbon dioxide in geologic formations: Journal of Petroleum Technology, 90-97.

Paterson, M.S. & Wong, T.-F. 2005. Experimental Rock Deformation – The Brittle Field, 2nd ed., Springer Verlag, Berlin and New York.

Peng, D.-Y. & Robinson, D.B. 1976. A new two constant equation of state. Industrial & Engineering Chemistry Fundamentals, 15/1, 59-64.

Prausnitz J.M., Lichtenthaller R.N. & De Azedevo E.G. 1986. Molecular thermodynamics of Fluid Phase Equilibria. Prentice Hall, New York.

Pruess, K., Oldenburg, C. & Moridis, G. 1999. TOUGH2 User Guide, version 2.0. Lawrence Berkeley National Laboratory Report LBNL-43134.

Pruess, K., Garcia, J., Kovcek, T., Oldenburg, C., Rutqvist, J., Steefel, C. & Xu, T. 2002. Intercomparison of numerical simulation codes for geological disposal of CO_2. LBNL-51817.

Pruess, K., Xu, T., Apps, J. & Garcia, J. 2003. Numerical modeling of aquifer disposal of CO_2. Paper SPE 83695.

Pruess, K., Garcia, J., Kovcek, T., Oldenburg, C., Rutqvist, J., Steefel, C. & Xu, T. 2002. Intercomparison of numerical simulation codes for geological disposal of CO_2. LBNL-51817.

Pruess, K., Xu, T., Apps, J. & Garcia, J. 2003. Numerical modeling of aquifer disposal of CO_2. Paper SPE 83695.

Pruess, K. 2008. Leakage of CO_2 from geologic storage: Role of secondary accumulation at shallow depth. International Journal of Greenhouse Gas Control, 2, 37-46.

Pruess, K. & Mueller, N. 2009. Formation dry-out from CO_2 injection into saline aquifers: 1. Effects of solids precipitation and their mitigation. Water Resources Research, 45.

Purcell, W.R. 1949. Capillary pressures – their measurement using mercury and the calculation of permeability. Transaction of the AIME, 186, 39-48.

Purvis, K. 1992. Lower Permian Rotliegend sandstones, southern North Sea: a case study of sandstone diagenesis in evaporite-associated sequences. Sedimentary Geology, 77, 155-171.

Raleigh, C.B., Healy, J.H. & Bredehoeft, J.D. 1976. An experiment in earthquake control at Rangely, Colorado. Science, 191, 1230-1237.

Reeder, R. J. & Wenk, H.R. 1979. Microstructures in low temperature dolomites. Geophysical Research Letters, 6, 77-80.

Rhys, G.H. 1974. A proposed standard lithostatigraphic nomenclature for the southern North Sea and an outline structural nomenclature for the whole of the (UK) North Sea. A report on

the joint Oil Industry – Institute of Geological Sciences Committee on the North Sea Nomenclature. Report of the Institute of Geological Sciences, 74/8.

Redlich, O. & Kwong, J.N.S. 1949. On the thermodynamics of solutions. V. An equation of state. Chemical Reviews, 44, 233-244.

Riaz, A., Hesse, M., Tchelepi, H.A. & Orr, F.M. 2006. Onset of convection in a gravitationally unstable diffusive boundary layer in porous media. Journal of Fluid Mechanics, 548, 87-111.

Rochelle, C.A., Czernichowsky-Lauriol, I. & Milodowski, A.E. 2004. The impact of chemical reactions on CO_2 storage in geological formations: A brief review. In: Baines, S. J. & Worden, R. H. (eds.): Geological Storage of Carbon Dioxide. Geological Society, London, Special Publications, 233, 87-106.

Rosenbaum, J. & Sheppard, S.M.F. 1986. An isotopic study of siderites, dolomites and ankerites at high temperatures. Geochemica et Cosmochimica Acta, 50/6, 1147-1150.

Rutqvist, J. & Tsang, C.F. 2002. A study of caprock hydromechanical changes associated with CO_2 injection into a brine formation. Environmental Geology, 42, 296-305.

Rutqvist, J., Birkholzer, J., Cappa, F. & Tsang, C.-F. 2007. Estimating maximum sustainable injection pressure during geological sequestration of CO_2 using coupled fluid flow and geomechanical fault-slip analysis. Energy Conversion and Management, 48, 1798-1807.

Scheidecker, A. E. 1960. On the connection between tectonic stresses and well fracturing data. Geofis. Pur. Appl., 46, 66-76.

Schmitt, D.R. & Zoback, M.D. 1989. Poroelastic effects in the determination of the maximum horizontal principle stress in hydraulic fracturing tests – a proposed breakdown

equation employing a modified effective stress relation for tensile failure. International Journal of Rock Mechanics, 26, 499-506.

Schowalter, T.T. 1979. Mechanics of secondary hydrocarbon migration and entrapment. AAPG Bulletin, 63, 723-760.

Sibson, R.H., 1981. Controls on low-stress hydro-fracture dilatancy in thrust, wrench and normal fault terrains. Nature, 289, 665-667.

Sibson, R.H. 1990. Conditions for fault-valve behavior. In: Knipe, R. J. & Rutter, E. H. (eds): Deformation Mechanisms, Rheology and Tectonics. Geological Society of London, Special Publication, 54, 15-28.

Singh, V., Cavanagh, A., Hansen, H., Nazarian, B., Iding, M. & Ringrose, P. 2010. Reservoir modeling of CO_2 plume behavior calibrated against monitoring data from Sleipner, Norway, SPE 134891-PP.

Soave, G. 1972. Equilibrium constants from a modified Redlich-Kwong equation of state. Chemical Engineering Science, 27, 1197-1203.

Smith, H.J., Fischer, H., Wahlen, M., Mastroianni, D. & Deck, B. 1999. Dual modes of the carbon cycle since the last glacial maximum: Nature, 400, 248-150.

Span, R. & Wagner, W. 1996 A new equation of state for CO_2 covering the fluid region from the triple-point temperature to 1100°K at pressures up to 800MPa. Journal of Physical and Chemical Reference Data, 25/6, 1509-1596.

Spycher, N., Pruess, K. & Ennis-King, J. 2003 CO_2-H_2O mixtures in the geological sequestration of CO_2. I. Assessment and calculation of mutual solubilities from 12 to 100 C and up to 600 bar. Geochemica et. Cosmochimica Acta, 67/16, 3015-3031.

Spycher, N. & Pruess, K. 2005. CO_2-H_2O mixtures in the geological sequestration of CO_2. II. Partitioning in chloride brines at 12–100°C and up to 600 bar. Geochimica et Cosmochemica Acta, 69/13, 3309-3320.

Stein, R.S. 1982. Modified Redlich-Kwong equation of state for phase equilibrium calculations. Industrial and Engineering Chemistry Process Design and Development, 21, 564-569.

Stone, H.L. 1970. Probability model for estimation three-phase relative permeability. Journal of Petroleum Technology, 20, 214-218.

Sullivan, M.D. 1991. Diagenetic study of the lower Permian Rotliegend sandstone, Leman Field, southern North Sea: Unpublished PhD thesis, University of Glasgow, UK.

Sullivan, M.D., Haszeldine, R.S. & Fallick, A.E. 1990. Linear coupling of carbon and strontium isotopes in Rotliegend Sandstone, North Sea: Evidence for cross-formational fluid flow. Geology, 18, 1215-1218.

Swarbrick, R.E., Lahann, R.W. and O'Conner, S. 2011. Pore pressure – stress coupling: Evidence from deep boreholes. Tectonic Studies Group Technical Programme.

Swart, P.K., Burns, S.J. & Leder J.J. 1991. Fractionation of the stable isotopes of oxygen and carbon is carbon dioxide during the reaction of calcite with phosphoric acid as a function of temperature and technique. Chemical Geology, 86/2, 89-96.

Tegetmeier, A., Dittmar, D., Fredenhagen, A. & Eggers, R, 2000. Density and volume of water and triglyceride mixtures in contact with carbon dioxide. Chemical Engineering and Processing, 39, 399-405.

Touret, J. & Bottinga, Y. 1979. Equation d'etat pour le CO_2; application aux inclusions carboniques. Bull. Mineralogie, 102, 577-583.

Tucker, M.E. 1991. Sequence stratigraphy of carbonate–evaporite basins: models and application to the Upper Permian (Zechstein) of northeast England and adjoining North Sea. Journal of the Geological Society, London, 148, 1019–1036.

Turner, P. & Magaritz, M. 1986. Chemical and isotopic studies of a core of Marl Slate from NE England: influence of freshwater influx into the Zechstein Sea. In: Harwood G. M. & Smith D. B. (eds.): The English Zechstein and related topics. Geological Society, London, Special Publications, 22, 19-29.

Ukaegbu, C., Gundogan, O., Mackay, E., Pickup, G., Todd, A. & Gozalpour, F. 2009. Simulation of CO_2 storage in a heterogenous aquifer. Proceedings of the Institution of Mechanical Engineers, Part A: Journal of Power and Energy 2009, 223-249.

Underhill, J.R., Lykakis, N. & Shafique, S. 2009. Turning exploration risk into a carbon storage opportunity in the UK Southern North Sea. Petroleum Geoscience, 15, 291-304.

van der Meer, L.G.H. & van Wees, J. D. 2006. Limitations to storage pressure in finite saline aquifers and the effect of CO_2 solubility on storage pressure. Paper SPE 103342.

van der Meer, B. & Egberts, P. 2008. Calculating subsurface CO_2 storage capacities. The Leading Edge, 27/4, 502-505.

van der Meer, L.G.H., 1995. The CO_2 storage efficiency of aquifers. Energy Conversion Management, 36, 513–518.

Van Hoorn, B. 1987. Structural evolution, timing and tectonic style of the Sole Pit Inversion. Tectonophysics, 137, 239–284.

Van Genuchten, M.T. 1980. A closed-form equation for predicting the hydrolic conductivity of undersaturated soils. Soil science society of America Journal, 44/5, 892-898.

Vandeweijer, V., van der Meer, B., Kramers, L., Neele, F., Maurand, N., Le Gallo, Y., Bossie-Codreanu, D., Schaefer, F., Evans, D., Kirk, K, Bernstone, C., Stiff, S. & Hull, W. 2009. CO_2 Storage in saline aquifers: In the southern North Sea and northern Germany. Energy Procedia, 1, 3079-3086.

Vasconcelos, C., McKenzie, J.A., Warthmann, R. & Bernasconi, S.M. 2005. Calibration of the $\delta^{18}O$ paleothermometer for dolomite precipitated in microbial cultures and natural environments. Geology, 33/4, 317-320.

Veizer, J., Holser, W.T. & Wilgus, C.K. 1980. Correlation of $^{13}C/^{12}C$ and $^{34}S/^{32}S$ secular variations. Geochemica et Cosmochimica Acta, 44, 579-587.

Vera, J. H. & Prausnitz, J.M. 1972. Generalized van der Waals theory for dense fluids. Chemical Engineering Journal, 3, 577-583.

Vesovic, V., Wakeham, W.A., Olchowy, G.A., Sengers, J.V., Watson, J.T.R. & Millat, J. 1990. The transport properties of Carbon Dioxide. Journal of Physical and Chemical Reference Data, 19/3, 763-808.

Wagner, W. & Pruss, A. 2002. The IAPWS formulation 1995 for the thermodynamic properties of ordinary water substance for general and scientific use. Journal of Physical and Chemical Reference Data, 31/2, 387-535.

Walters (jr), L.J., Claypool, G.E. & Choquette, P. W. 1971. Geochemica et Cosmochimica Act, 86, 129-140.

Warren, J. 2000. Dolomite: Occurrence, evolution and economically important associations. Earth-Science Reviews, 52, 1-81.

Warren, E.A. & Smalley, P.C. 1992. North Sea formation water atlas. Geological Society of London Memoir, 15, 208 p.

Wilkinson, M., Haszeldine, R.S., Fallick, A.E., Odling, N., Stoker, S. & Gatliff, R. 2009. CO_2-mineral reaction in a natural analogue for CO_2 storage: Implications for modelling. Journal of Sedimentary Research, 79, 486-494.

Xu, T., Apps, J, A., Pruess, K. & Yamamoto, H. 2007. Numerical modeling of injection and mineral trapping of CO_2 with H_2S and SO_2 in a sandstone formation: Chemical Geology, 242, 319-346.

Zeng, Z. & Grigg, R. 2006. A criterion for non-darcy flow in porous media. Transport in Porous Media, 63, 57-69.

Zhou, Q., Birkholzer, J.T., Tsang, C.-F. & Rutqvist, J. 2008. A method for quick assessment of CO_2 storage capacity in closed and semi-closed saline formations. International Journal of Greenhouse Gas Control, 2, 626-639.

Ziegler, P.A. 1990. Geological Atlas of Western and Central Europe (2nd edn.). Shell Internationale Petroleum Maatschappij, The Hague.

Ziegler, K. 2006. Clay minerals of the Permian Rotliegend group in the North Sea and adjacent areas. Clay minerals, 41, 355-393

Zimmerman, R.W. 2000. Coupling in poroelasticity and thermoelasticity. International Journal of Rock Mechanics, 37, 79-87.

Zudkevitch, D. & Joffe, J. 1970. Correlation and prediction of vapour-liquid equilibria with the Redlich-Kwong equation of state. American Institute of Chemical Engineers, 16/1, 112-119.

Websites:

National Institute of Standards and Technology website:
http://webbook.nist.gov/chemistry/fluid/

http://www.geos.ed.ac.uk/sccs/storage/howstored.html